Modeling the Performance and Hydrodynamic Behavior of a Countercurrent Multistage Fluidized Bed Adsorber

by

Morteza Davarpanah

A thesis submitted in partial fulfillment of the requirements for the degree of

Doctor of Philosophy

in

Environmental Engineering

Department of Civil and Environmental Engineering
University of Alberta

Abstract

Fluidized bed (FB) adsorbers provide excellent gas-solid contact at low pressure drops which allows for effective handling of large flow rates. However, the design, operation, and modeling of FB adsorbers could be challenging due to the complex processes involved. The goal of this research is to model the adsorptive and hydrodynamic behavior of multi-stage countercurrent FB adsorbers. The models proposed are versatile and responsive to changes in design and operating parameters including changes in the scale, weir height, temperature, humidity, adsorbent feed rate, air flow rate, initial concentration, the number of stages, and the type of adsorbent and adsorbate.

This research can be sectioned into two main parts. The performance of FB systems is studied in the first part. A two-phase model is developed to describe the adsorption of volatile organic compounds (VOCs) on beaded activated carbon (BAC) in a lab-scale fluidized bed adsorber. The model is then modified to capture the effect of adsorbent apparent densities (or heel buildup) and further refined to consider any changes in the FB scale. Next, the impact of humidity and temperature on the adsorption of VOC on BAC is investigated. Later, the intensification of the adsorption process in FB systems is discussed. Last in the first part, is a thorough study on the performance of the model using various formulas for the calculation of different parameters (bubble diameter, interphase mass transfer rate, etc.), where a generic set of formulas is proposed.

The hydrodynamics of FB systems are studied in the second part, where Computational Fluid Dynamics (CFD) is used to simulate one stage of the lab-scale FB. A presentation of the variables essential for the hydrodynamic study of the FB (solid volume fraction, air turbulent viscosity, etc.) is given in this section, followed by a comparison between the CFD simulation results and those of (semi)empirical formulas describing different hydrodynamic parameters (minimum fluidization velocity, bubble diameter, etc.).

The results indicate that the two-phase model shows good agreement with the experimental results obtained over a wide range of operating conditions (adsorbent feed rate, air flow rate, initial concentration, etc.). A sensitivity analysis of the two-phase model shows that internal diffusion within the adsorbent is rate-limiting for adsorption. It is also shown that the main characteristics of adsorbents (pore diameter, porosity, and adsorption capacity) can be correlated to their apparent densities to simulate the performance of BACs with different service lifetimes (degree of exhaustion as a result of heel buildup) in lab- and industrial-scale adsorbers using a two-phase model.

The effect of humidity on the adsorption of 1,2,4-trimethylbenzene (TMB) on BAC shows a drop in overall removal efficiency (ORE) starting at RH=75% which eventually plateaued at RHs close to 100% after decreasing ORE by 7.6 %. A small reduction (1.7%) in ORE is also observed when increasing the adsorption temperature from 22 to 50 ˚C in dry condition. The intensification simulations show that increasing the adsorbent feed rate is effective when there is a need for more adsorption sites (e.g. at high inlet concentrations). Reducing air flow rate at constant VOC load is always effective especially when there are enough adsorption sites available (e.g. high adsorbent feed rate, and low VOC loads and RHs). Similarly and under the same condition, increasing the number of stages can improve the FB performance. Also, the application of 3 adsorbers of 2 stages instead of 1 adsorber of 6 stages can improve the ORE by 34.5%.

The effect of different empirical equations on the performance of the model shows that although the best set of formulas depends on the adsorbent-adsorbate system, a generic set of formulas can be achieved with reasonably accurate predictions for a large dataset of FB experiments. According to the CFD simulations, the minimum fluidization velocity and bed voidage at minimum

fluidization velocity are 0.194 m/s and 0.476, respectively. It is also shown that Yasui-Johnson's formula for estimating the bubble diameter yields the closest overall results to those of the CFD.

In summary, different modeling and simulation methods are used to shed light on the adsorptive and hydrodynamic behavior of FB systems. The results of this research can pave the way for optimizing the design and operation of FB adsorbers, leading to cost savings and performance improvements.

Preface

The work presented in this dissertation was planned, designed, conducted, analyzed, interpreted, and compiled by myself, and was fully reviewed and supervised by Dr. Zaher Hashisho in the Department of Civil and Environmental Engineering at the University of Alberta. My colleagues in the Air Quality Characterization Lab in the Department of Civil and Environmental Engineering at the University of Alberta, and collaborators from our industrial sponsor, Ford Motor Company, assisted me in the following areas:

Chapter 3:

- This chapter has been published as: Davarpanah, M.; Hashisho, Z.; Phillips, J. H.; Crompton, D.; Anderson, J. E.; Nichols, M., Modeling VOC adsorption in a multistage countercurrent fluidized bed adsorber. Chemical Engineering Journal 2020, 394, 124963
- Mr. David Crompton, Mr. John Phillips, Dr. James E. Anderson, and Dr. Mark Nicholas contributed to manuscript edits

Chapter 4:

- This chapter has been published as: Davarpanah, M.; Hashisho, Z.; Crompton, D.; Anderson, J. E.; Nichols, M., Modeling VOC adsorption in lab- and industrial-scale fluidized bed adsorbers: Effect of operating parameters and heel build-up. Journal of Hazardous Materials 2020, 400, 123129
- Mr. David Crompton, Dr. James E. Anderson, and Dr. Mark Nicholas contributed to manuscript edits

Chapter 5:

- Mr. Keivan Rahmani assisted me in the fluidized bed experiments for the effect of humidity
- MS. Samineh Kamravaei conducted the fluidized bed experiments for the effect of temperature

Chapter 6:

- Dr. Mohammad Feizbakhshan conducted the fluidized bed experiments

Chapter 8:

- The CFD simulations in this chapter were closely reviewed by Dr. Petr Nikrityuk
- Dr. Hongbo Shi conducted the model verification

I dedicate this dissertation to the University of Alberta students and professors who lost their lives in the Flight PS 752 tragedy. This dissertation is also dedicated to healthcare professionals, first responders and essential workers who are working hard to ensure the health, safety and comfort of our communities during the COVID-19 pandemic.

Acknowledgement

The completion of this thesis would not have been possible without many sources of support. I would first like to start by expressing my deepest gratitude to my supervisor, Dr. Zaher Hashisho, for his guidance, support, and invaluable comments and feedback during my PhD studies. I would also like to extend my gratitude and appreciation to my supervisory committee members, Dr. Rajender Gupta and Dr. Petr Nikrityuk whose perspectives and expertise contributed to strengthening this work. I am also very thankful to my collaborators, co-authors, colleagues and anyone who assisted me in this research.

I would like to acknowledge financial support from Ford Motor Company, the Natural Sciences and Engineering Research Council of Canada, Air & Waste Management Association, and the Faculty of Graduate Studies and Research at the University of Alberta. Last, but by no means least, I would like to say a special thank you to my friends and family who have always supported me during graduate school and throughout life.

Table of contents

List of Tables

List of Figures

1. Chapter 1: Introduction and research objectives

1.1. General Introduction

Volatile organic compounds (VOCs) are carbon-containing chemicals in the gas or vapor phase which can cause serious health problems for humans (from headaches to liver damage and cancer) as primary pollution (Leslie, 2000, Kampa and Castanas, 2008). When combined with nitrogen oxides, they can produce secondary pollutions such as photochemical smog which contributes to urban air pollution (Parmar and Rao, 2008, Kim, 2011).

In 2015, Canada received a "D" grade on six indicators including VOC emissions, ranking 16th out of 17 peer countries (Emmanuel, 2015). Statistics show that VOC emissions in Canada in 2015 were 1,858 kilotons (Government of Canada, 2020). The oil and gas industry, as well as the paint and solvent sector, have been the highest contributors accounting for 37% and 17% of total VOC emissions, respectively (Government of Canada, 2020). Driven by continued demand for fossil fuel energy, there is an increasingly urgent need for reducing VOC emissions.

Many technological alternatives have been investigated to solve the issue of VOC emissions, among which adsorption in a fluidized bed adsorber has attracted considerable attention due to its high efficiency and ability to treat large flow rates. The fluidized bed system offers excellent gas-solid mass transfer and temperature control due to the rigorous mixing of solid particles in the bed (Davarpanah et al., 2020, Davarpanah et al., 2020). It is, hence, a good candidate for process intensification in adsorption processes when the external mass-transfer resistance is high (Hymore and Laguerie, 1984). The drawback of wide residence time distribution of gas and solid in traditional fluidized beds can also be minimized in the countercurrent multistage configuration (Hymore and Laguerie, 1984, Roy et al., 2009).

Despite all the advantages, fluidized bed systems are difficult to understand experimentally due to the complexity of interconnected transfer phenomena (Hymore and Laguerie, 1984, Werther and Hartge, 2004). The lack of proper understanding of fluidized bed systems, hence, makes the operation, design, and scale-up of fluidized beds challenging tasks to deal with.

The use of modeling and simulation tools is the best way to understand the intricate effect of parameters on each other and the whole process. The results of modeling can help engineers to not only design an efficient system but also optimize the operation of the system in various conditions, leading to savings on costs and efforts (Davarpanah et al., 2020, Davarpanah et al., 2020).

A good model must be able to account for several changes typical in operation and scale-up processes such as changes in operating parameters (gas flow rate, adsorbent feed rate, initial concentration), temperature and humidity, adsorbent apparent density (as they develop heel buildup during cyclic adsorption/desorption steps), and bed geometry (diameter, bed height, weir height, stage orifices) (Davarpanah et al., 2020).

The application of the two-phase model (which is the most well-known theory describing the adsorption process in a fluidized bed), along with Computational Fluid Dynamics (CFD) can provide a good understanding of adsorptive and hydrodynamic behavior of fluidized beds. The importance of the two-phase model appears in the study of the adsorption process in large-scale fluidized beds when theoretical and empirical correlations describing gas-solid hydrodynamic and adsorptive interactions make computations too complicated and time-consuming for 3D CFD simulations (Davarpanah et al., 2020). The main objective of CFD, however, is to obtain a realistic flow structure to be able to get a better insight into the interactions between the fluid and dispersed phases that are usually unknown and difficult to predict.

1.2. Problem Statement

The performance of the adsorption process is enhanced when it is carried out in a countercurrent multistage fluidized bed adsorber. This configuration maximizes solid-gas contacts, reduces the effect of gas bypassing, and narrows the residence time distribution of solids (Davarpanah et al., 2020, Davarpanah et al., 2020). Despite all the advantages, understanding the effects of all parameters controlling fluidized bed operation can be challenging due to the complexity of transfer phenomena and their interconnected effects. Moreover, while studying hydrodynamics and adsorption processes, many parameters (e.g. different interactive forces and kinetics parameters) are difficult to measure experimentally, hence, not often reported in the literature (Davarpanah et al., 2020). Thus, more studies are required to advance the knowledge of the design and operation of fluidized beds. In recent years, together with rapid advancements of numerical algorithms and computing power, modeling and simulation have appeared to be viable tools to span the gaps between experiments and theoretical solutions.

1.3. Goal and Objectives

The goal of this research is to model the adsorptive and hydrodynamic behavior of a multi-stage countercurrent fluidized bed adsorber. In this regard, the objectives of this research can be summarized as follows:

Objective 1: Developing a model to predict the adsorptive behavior of a lab-scale fluidized bed

- ***Objective 1.1:*** To investigate the effect of different design and operating conditions (e.g. adsorbent feed rate, gas velocity, initial concentration, and weir height), as well as the sensitivity of the model towards input parameters (e.g. adsorption capacity, the number of stages, adsorbent diameter, and diffusion coefficients).

- ***Objective 1.2:*** To predict the effect of adsorbent heel buildup (as adsorbents are used in the bed) on the adsorption process and evaluate the model for any changes in the fluidized bed scale.
- ***Objective 1.3:*** To improve the model to take into account the effect of temperature and humidity.
- ***Objective 1.4:*** To investigate different intensification approaches used for the optimization of the design and operation of fluidized bed adsorbers.
- ***Objective 1.5:*** To investigate the performance of the model using different empirical/semi-empirical formulas for the calculation of different parameters (e.g. bubble diameter, interphase mass transfer flow rate, and mass transfer coefficient) and propose a generic set of formulas which would maximize the prediction accuracy for a large adsorption dataset.

Objective 2: Determining the hydrodynamic behavior of one stage of the lab-scale fluidized bed using CFD simulation in 3D.

- ***Objective 2.1:*** To investigate the parameters essential for hydrodynamic studies such as solid volume fraction and, turbulent viscosity, time-averaged solid volume fraction, and volume-averaged solid velocity.
- ***Objective 2.2:*** To compare the CFD simulation results with those of empirical/semi-empirical formulas describing minimum fluidization velocity, bed voidage at minimum fluidization velocity, bubble diameter, and bubble velocity inside the fluidized bed.

1.4. Research significance

Although some efforts have been made to model the adsorptive behavior of fluidized bed systems, most studies have dealt with chemical reactions with constant rates at a given temperature along the bed (Mohanty et al., 2009, Mohanty and Meikap, 2011). The models developed in this study, however, account for the adsorption kinetics and consider the residence time of solids on each stage.

Moreover, to the best of our knowledge, no or few studies have dealt with:

- Modeling the adsorption process in an industrial fluidized bed using a two-phase model.
- Modeling the effect of heel buildup on the adsorption process in a fluidized bed.
- Modeling the binary adsorption in a fluidized bed.
- Studying the intensification of the adsorption process in a fluidized bed at design and operation levels
- Studying the performance of the model using different formulas for calculation of different parameters (bubble diameter, interphase mass transfer flow rate, etc.).
- Comparing the CFD simulation results with empirical/semi-empirical formulas describing the hydrodynamic behavior of the bed.

The outcome of this research could provide researchers, designers, and operation engineers with a better understanding of the hydrodynamic and adsorptive behavior of fluidized beds, leading to cost savings and performance improvements in industrial operations. The numerical models proposed are responsive to changes in the type of adsorbent and adsorbate, bed geometry, and operating parameters; and can, therefore, be applied to different what-if scenarios at minimum cost.

1.5. Thesis Outline

This dissertation consists of nine chapters. Chapter 1 presents a general overview of VOC emissions and fluidized bed operation, followed by problem statement, research objectives and significance, and thesis outline. Chapter 2 provides an in-depth literature review of the adsorption process in fluidized beds with an emphasis on the classification of particles and flow regimes, followed by a review of different mathematical models describing the behavior of fluidized bed

systems along with their strengths and limitations. Theoretical and experimental methodologies, as well as the results and discussion, are presented in Chapters 3 to 8.

Chapter 3 presents a modeling approach for adsorption in fluidized beds which takes into account the residence time distribution of the adsorbent particles, as well as adsorption kinetics. The model is used to describe the adsorption of 1,2,4-trimethylbenzene (TMB) on beaded activated carbon (BAC) in a lab-scale multistage countercurrent fluidized bed adsorber. Chapter 4 attempts to model the effect of changes in operating parameters on the adsorption of a mixture of industrial solvents onto BAC with different apparent densities (and adsorption capacities). The model is then used to predict the performance of an industrial-scale fluidized bed adsorber.

The competitive adsorption of VOC and water vapor is measured and modeled in Chapter 5. A thermodynamic approach is also used to take into account the effect of temperature on the adsorption of VOC onto BAC. Chapter 6 investigates the intensification of the adsorption systems to optimize the design and operation of adsorbers for efficient VOC emissions control.

Chapter 7 studies the performance of the model using different empirical and semi-empirical formulas for calculation of different parameters (bubble diameter, interphase mass transfer flow rate, etc.), and proposes a generic set of formulas which maximizes the accuracy of prediction for a large adsorption dataset (with a range of different adsorbates, adsorbents, operating conditions, and scales). The CFD simulation of one stage of the lab-scale fluidized bed is the topic of Chapter 8. Variables essential for the hydrodynamic study of the fluidized bed (solid volume fraction, air turbulent viscosity, time-averaged solid volume fraction, etc.) are presented, followed by a comparison between the CFD simulation results and the results of empirical/semi-empirical formulas describing different parameters (minimum fluidization velocity, bubble diameter, etc.). Finally, a summary of findings and recommendations for future work are presented in Chapter 9.

1.6. References

Davarpanah, M., Hashisho, Z., Crompton, D., Anderson, J.E., Nichols, M., 2020. Modeling VOC adsorption in lab- and industrial-scale fluidized bed adsorbers: Effect of operating parameters and heel build-up. *Journal of Hazardous Materials*, **400**: 123129.

Davarpanah, M., Hashisho, Z., Phillips, J.H., Crompton, D., Anderson, J.E., Nichols, M., 2020. Modeling VOC adsorption in a multistage countercurrent fluidized bed adsorber. *Chemical Engineering Journal*, **394**: 124963.

Emmanuel, O.K. (2015). The impact of economic growth and trade on the environment: the canadian case. 33rd USAEE/IAEE North American Conference. Pittsburgh, PA, USA.

Government of Canada (2020). Canada's Air Pollutant Emissions Inventory Report 2020.

Hymore, K., Laguerie, C., 1984. Analysis and modelling of the operation of a counterflow multistage fluidized bed adsorber for drying moist air. *Chemical Engineering and Processing: Process Intensification*, **18**: 255-267.

Kampa, M., Castanas, E., 2008. Human health effects of air pollution. *Environmental Pollution*, **151**: 362-367.

Kim, B.R., 2011. VOC Emissions from Automotive Painting and Their Control: A Review. *Environmental Engineering Research*, **16**: 1-9.

Leslie, G.B., 2000. Health Risks from Indoor Air Pollutants: Public Alarm and Toxicological Reality. *Indoor and Built Environment*, **9**: 5-16.

Mohanty, C.R., Malavia, G., Meikap, B.C., 2009. Development of a Countercurrent Multistage Fluidized-Bed Reactor and Mathematical Modeling for Prediction of Removal Efficiency of Sulfur Dioxide from Flue Gases. *Industrial & Engineering Chemistry Research*, **48**: 1629-1637.

Mohanty, C.R., Meikap, B.C., 2011. Modeling the operation of a three-stage fluidized bed reactor for removing CO2 from flue gases. *Journal of Hazardous Materials*, **187**: 113-121.

Parmar, G.R., Rao, N.N., 2008. Emerging Control Technologies for Volatile Organic Compounds. *Critical Reviews in Environmental Science and Technology*, **39**: 41-78.

Roy, S., Mohanty, C.R., Meikap, B.C., 2009. Multistage Fluidized Bed Reactor Performance Characterization for Adsorption of Carbon Dioxide. *Industrial & Engineering Chemistry Research*, **48**: 10718-10727.

Werther, J., Hartge, E.-U., 2004. Modeling of Industrial Fluidized-Bed Reactors. *Industrial & Engineering Chemistry Research*, **43**: 5593-5604.

2. Chapter 2: Literature review

2.1. Nomenclature

Symbol	Description	Units
Ar	Archimedes number	-
C_0	TMB concentration at bed entry	ppm_v
D	bed diameter	m
$d_{b,\,max}$	maximum stable bubble diameter	m
d_p	adsorbent mean diameter	m
F_g	air flow rate	SLPM
g	standard gravity	m/s^2
H	weir height	m
n_0	number of orifices on the distributor	-
RE	removal efficiency	%
Re_{mf}	Reynolds number at u_{mf}	-
RH	relative humidity	%
u_0	superficial gas velocity	$m\ s^{-1}$
u_k	minimum turbulent velocity	$m\ s^{-1}$
u_{mb}	minimum bubbling velocity	$m\ s^{-1}$
u_{mf}	minimum fluidization velocity	$m\ s^{-1}$
u_{ms}	minimum slugging velocity	$m\ s^{-1}$
u_{tr}	transport velocity	$m\ s^{-1}$
V_T^*	terminal settling velocity of a spherical particle of diameter $2.7d_p$ in a stagnant gas having the physical properties of the fluidizing gas	$m\ s^{-1}$
ε_{mf}	void fraction at u_{mf}	-
μ_g	gas viscosity	$kg\ m^{-1}\ s^{-1}$
ρ_g	gas density	$kg\ m^{-3}$
ρ_p	adsorbent density	$kg\ m^{-3}$
ϕ	adsorbent shape factor	-

2.2. Fluidized bed

2.2.1. Definition

The term “fluidization” describes a certain method of contacting solids and fluids (Leva, 1959). In a fluidized bed, the upward gas or liquid stream, which might be inert or contain species consumed in a reaction, is passed through a bed of solid particles. There is a certain flow rate for the fluid at which the individual particles are somewhat disengaged from each other. This suspended bed which resembles a liquid of high viscosity is called the fluidized bed (Missen et al., 1999). The agitation and mixing achieved by means of the moving fluid ensures high heat and mass transfer rates and the gap between particles delivers less resistance for the fluid passage (Kunii and Levenspiel, 1969). Hence, fluidized beds are frequently used in processes with high mass-transfer resistance or pressure drops e.g. adsorption and drying (Kim et al., 2013, Girimonte et al., 2017), or processes with a high enthalpy of reaction which require temperature uniformity and effective heat transfer e.g. polymerization and combustion (Harshe et al., 2004, Schulzke et al., 2018). Fluidized beds are commonly used in chemical, petroleum, metallurgical, and energy industries (Kunii and Levenspiel, 1969, Saxena and Vadivel, 1988).

2.2.2. Advantages and disadvantages

The advantages and disadvantages of fluidized beds may be considered relative to the characteristics of fixed beds. In general, high agitation in fluidized beds leads to significant operational advantages, although it introduces some unfavorable effects which need to be considered (Leva, 1959).

2.2.2.1. Advantages

- Continuous mode of operation with respect to the fluid and the solid in fluidized beds allows the treatment of large flow rates (Missen et al., 1999). Cyclic adsorption-desorption

in a fluidized bed adsorber or regeneration of deactivated catalysts in a fluidized bed reactor are some examples of the continuous operation in fluidized beds (Missen et al., 1999).

- Excellent fluid-solid contact and uniform distribution of the fluid stream inside fluidized beds increase the mass transfer rate and minimize clogging and fluid channeling, leading to a more efficient process (Kunii and Levenspiel, 1969). In the adsorption process, for example, fluidized beds show faster adsorption kinetics and sharper breakthrough curves compared to fixed beds as a result of higher mass transfer coefficients (Kamravaei et al., 2017).
- Uniformity of temperature throughout the bed in fluidized bed operation gives better control over the temperature-dependent processes. Unlike fixed beds, the high degree of turbulence in fluidized beds results in relatively high heat transfer coefficients and uniform temperature throughout the bed which can prevent the formation of hot spots and bed fires (Delage et al., 2000, Sanders, 2003, Yazbek et al., 2006).
- Fluidized beds offer lower pressure drops compared to fixed beds especially when relatively small particles are to be used inside the bed which, in turn, leads to a decrease in operational costs (Davidson and Harrison, 1963).

2.2.2.2. Disadvantages

- High agitation and bubble break-up inside fluidized beds can lead to erosion of pipes and internal parts, as well as attrition of solid particles which might lead to the necessity of entrainment and/or elutriation, recovery equipment (e.g. cyclones), and more frequent maintenance (Leva, 1959, Missen et al., 1999).
- The formation of large bubbles in fluidized beds decreases the efficient contact between the fluid and solid, causing a bypassing effect which decreases the process efficiency. Adsorbent/catalyst holdup and lower conversion in reactions are some diverse impacts of poor fluid-solid contact (Missen et al., 1999). The formation of large bubbles can be prevented by using multistage fluidized beds with effective air distributors (Leva, 1959).
- Most importantly, compared to fixed beds, the prediction of the behavior of fluidized beds is much more difficult which means more complex design, scale-up, and operation of fluidized beds (Davarpanah et al., 2020).

2.2.3. Applications of fluidized beds in the adsorption process

Adsorption is one of the processes which can benefit from the advantages of fluidized beds. Many studies were carried out on the application of fluidized bed adsorbers in the adsorption of different chemicals on a variety of adsorbents.

Hamed et al. (Hamed et al., 2010) compared the performance of fluidized and fixed bed adsorbers in the adsorption of humidity on silica gel and reported 20% higher removal efficiency for the fluidized bed as a result of faster mass transfer rate. Reichhold and Hofbauer (Reichhold and Hofbauer, 1995) reported the experimental adsorption-desorption of CO_2, SO_2, and gaseous organic solvents on several adsorbents in an internally circulating fluidized bed. Some other studies have been conducted on the application of fluidization in the adsorption of VOCs on polymeric adsorbents (Song et al., 2005) and heterogeneous alumina-catalyst adsorbents (Dolidovich et al., 1999). Kamravaei et al. (Kamravaei et al., 2017) compared the adsorption/desorption of VOCs in fixed and fluidized bed adsorbers and reported 30% less heel buildup inside the pores of the activated carbon used in fluidized bed configuration (Kamravaei et al., 2017).

Roy et al. (Roy et al., 2009) investigated the effect of different variables including the type of adsorbent, superficial gas velocity, inlet concentration, and weir height on CO_2 removal efficiency in a multistage fluidized bed. They reported higher removal efficiency at lower air flow rates, lower inlet concentrations, and higher weir heights. The effect of operating conditions has been experimentally investigated by many other researchers (Chiang et al., 2000, Song et al., 2005, Mohanty et al., 2009, Hamed et al., 2010).

While there are numerous experimental studies on the performance of fluidized beds at different operating conditions, only a few studies have investigated the intricate effect of variables on each

other and the performance of the system (Hymore and Laguerie, 1984, Mohanty and Meikap, 2011).

2.3. Fluidized bed modeling

Fluidized beds are widely used in many processes including adsorption, combustion, gasification, covering particles, drying, and granulation (Philippsen et al., 2015). However, the development of fluidized beds is somewhat limited by the lack of knowledge on the details of operational variables and their interconnected effects. The calculations of mass and heat transfers are complex and difficult to achieve when they are intimately contingent on the intricate patterns of gas-solid contacting and mixing inside the fluidized bed (de Lasa, 2012). Because of this, there is a growing demand for modeling and simulation tools incorporating mathematical models which allow the description and analysis of the processes involved in a fluidized bed operation.

Generally, mathematical models describing the fluidized bed can be classified as macro- and micro-scale models (Davarpanah et al., 2020). The macro-scale modeling of the gas flow in fluidized beds started by Davidson and Harrison (Davidson and Harrison, 1963) and Kunii and Levenspiel (Kunii and Levenspiel, 1969) with analysis of bubble motion, system instability, and mass transfer. Based on these models, many other authors studied this subject to develop more realistic models (Kato and Wen, 1969, Geldart, 1973, Mori and Wen, 1975, Haider and Levenspiel, 1989).

More recently, computational Fluid Dynamics (CFD) has been used as a micro-scale modeling tool to predict the behavior of fluidized beds. CFD uses a variety of complex theoretical, empirical, and semi-empirical correlations based on mass, heat, and momentum transfer to describe different

phenomena inside the bed. As a result, it requires powerful computers and long processing times (Philippsen et al., 2015).

There are several mathematical models and correlations in the literature which describe a fluidized bed process. The application of these models, however, depends on the process conditions, and hence, there is no model with universal applicability (Yang, 2003). Before discussing different simulation approaches, it is essential to provide some basic understanding of some key aspects of the physical behavior of fluidized beds. To that end, Geldart's classification of particles is discussed in this section, followed by different flow regimes and their criteria. Then, different mathematical models are reviewed in two classes of "two- and three-phase models" and "computational fluid dynamics".

2.3.1. Particle classification

The characteristics of the particles can influence the hydrodynamics of fluidization. A widely used classification for particles according to their fluidization behavior when fluidized by air at ambient conditions was offered by Geldart (Geldart, 1973):

- Group A: particles with small sizes (30-150 μm) and/or low particle densities (<1.4 g/cm^3). While no bubbles are observed initially at the minimum fluidization velocity (u_{mf}), they appear at air velocities higher than u_{mf} (Philippsen et al., 2015). The fluidization is smooth and homogeneous; hence, the bubbles growth and bubble rising speed are easy to control. Fluid-cracking catalysts are typically in this category (Poulopoulos and Inglezakis, 2006).
- Group B: Particles with medium sizes (40-500 μm) and densities between 1.4 and 4 g/cm^3. The bubbles usually appear at the beginning of the fluidization and grow bigger as they rise through the bed (Philippsen et al., 2015). Glass beads (ballotini) and coarse sand are typically in this category (Poulopoulos and Inglezakis, 2006).
- Group C: Very small and cohesive particles (<30 μm) (Philippsen et al., 2015). Fluidization is difficult for this group of particles. Channeling and slug regime is observed in fluidized

beds filled with particles in group C. Talc, flour, and starch are examples of materials in this category (Poulopoulos and Inglezakis, 2006).

- Group D: Large particles (> 500 μm) (Philippsen et al., 2015). Fluidization is difficult and usually non-uniform. This group of particles can produce deep spouting beds. Roasted coffee beans, lead shot, and some roasted metal ores are examples of particles in group D (Poulopoulos and Inglezakis, 2006).

2.3.2. Flow regimes in the bed

The hydrodynamics of fluidized beds are generally characterized by the balance of forces between solid particles and gas velocity. It is often possible to set the required fluidization regime by controlling the gas velocity (Philippsen et al., 2015). The sequence of several distinct fluidization regimes that might be exhibited when increasing the gas flow through a bed of particulate solids is shown in Figure 2-1.

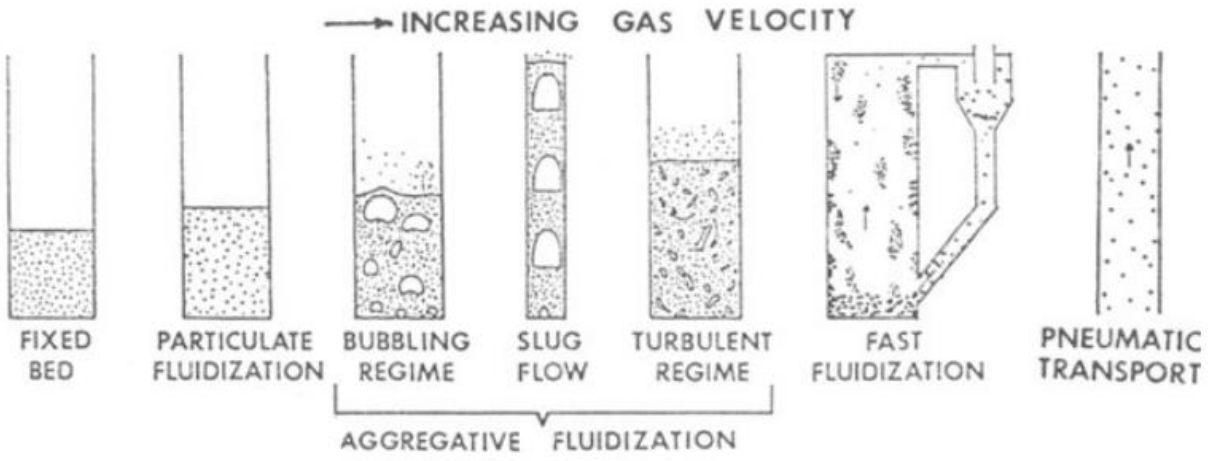

Figure 2-1. Different hydrodynamic regimes inside the bed according to the gas velocity extent (de Lasa, 2012).

Consider an upward gas flow through a bed of solid particles initially fixed in a vessel. At relatively low gas velocities, the gas percolates through the void spaces between particles without disturbing the bed. At this level, no visual change is observed in the state of the bed, although it

slightly expands as fluid velocity increases (Kunii and Levenspiel, 1969, Poulopoulos and Inglezakis, 2006, de Lasa, 2012). As the gas velocity increases further, a point is reached at which the drag force imparted by the upward fluid is equal to the weight of the particles. This point known as minimum fluidization is when the particles begin to suspend, and the bed acquires fluid-like properties (Kunii and Levenspiel, 1969, Poulopoulos and Inglezakis, 2006, de Lasa, 2012).

When the gas velocity exceeds the minimum fluidization velocity, bubbles that contain no or few solid particles are formed at or close to the gas distributor from which they rise towards the surface. On their way to the surface, bubbles coalesce into each other forming bigger bubbles, which may then split and recombine. The formation, rise, coalescence, and break-up of bubbles imposes a great deal of agitation in the system which results in the bubbling fluidization (Kunii and Levenspiel, 1969, Poulopoulos and Inglezakis, 2006, de Lasa, 2012). Industrial reactors often operate in this regime, with typical values of gas velocities 5–30 times required for minimum fluidization (Poulopoulos and Inglezakis, 2006). It is worth mentioning that for particles in group A the transition between particulate fluidization and bubbling fluidization with increasing the gas velocity is relatively short (de Lasa, 2012).

When the bubbles grow as large as the vessel diameter, they fill most of the bed cross-sectional area and the bed exhibits a slugging regime. In slugging fluidization, voids are bullet-shaped slugs, rising in sequence. The bed surface rises steadily and then collapses as the slugs rise and break at the surface (Kunii and Levenspiel, 1969, Poulopoulos and Inglezakis, 2006, de Lasa, 2012). This effect is undesirable since it may cause dangerous vibrations that damage the system. This regime is usually seen in beds with big height and small diameter. The vertical mixing of solids in this regime is not as effective as the bubbling regime (de Lasa, 2012).

Increasing the gas velocity beyond a certain point would result in a transitional regime called turbulent fluidization. Instead of distinct bubbles, turbulent motions of solid clusters and voids of gas in various sizes are observed inside the bed (de Lasa, 2012). The vigorous splashing of particles assures particle mixing in the horizontal and vertical directions. The upper surface of the bed is difficult to notice visually, although it can be determined by X-ray measurements and pressure profiles (de Lasa, 2012).

A further increase in gas velocity leads to substantial entrainment of solid particles inside the bed column. Solid particles are then collected in a cyclone and are sent downwards in strands along the outer wall of the column. This circulation of solids introduces excellent particle mixing in both the vertical and horizontal directions. Depending on the gas velocity, the solids volume fraction in the bed is typically 2-20%, for a fixed value of particle feed rate and recirculation rate (de Lasa, 2012).

Increasing the gas velocity to values greater than the terminal velocity leads to a pneumatic transport of solids and the fluidized bed becomes an entrained bed in which disperse and dilute solid phase exists. In this regime all regions of the bed are similarly subject to the gas flow and no distinct area is observed (de Lasa, 2012).

Different regimes in a fluidized bed can also be characterized by the relation between the pressure drop and gas velocity (Philippsen et al., 2015). A gas stream loses pressure when it passes through a porous bed. Starting from fixed particles in a bed, the pressure drop increases linearly as the gas velocity increases until a point where the pressure drop balances with the weight of the particles. This equilibrium point is known as the minimum fluidization velocity (Philippsen et al., 2015). In the bubbling regime, the pressure drop remains almost constant even with increasing the gas velocity. When the gas velocity is higher than the terminal velocity of the particles, the bed

pressure drop decreases as the pneumatic transport starts (Poulopoulos and Inglezakis, 2006, de Lasa, 2012).

2.3.3. Flow regimes criteria

Most gas-solid fluidized beds work in the range of aggregative fluidization (bubbling regime, slug flow, and turbulent regime). The quantitative criteria for determining the hydrodynamic regime in the range of aggregative fluidization are presented in this section in relation to the gas velocity and the pressure drop. While the former is indicated by the solid and gas properties, the latter can be measured by pressure transducers.

2.3.3.1. Bubbling regime

All the following criteria must be satisfied for the bubbling regime to prevail (de Lasa, 2012):

a) Superficial gas velocity (u_0) higher than the minimum fluidization velocity (u_{mf}). The minimum fluidization velocity can be easily estimated by the following relation:

$$\frac{1.75}{\phi\varepsilon_{mf}^3}\mathrm{Re}_{mf}^2+\frac{150\left(1-\varepsilon_{mf}\right)}{\phi^2\varepsilon_{mf}^3}\mathrm{Re}_{mf}-\mathrm{Ar}=0 \tag{2-1}$$

$$\mathrm{Re}_{mf}=\frac{\rho_g d_p u_{mf}}{\mu_g},\ \mathrm{Ar}=\frac{\rho_g\left(\rho_p-\rho_g\right)gd_p^3}{\mu_g^2}$$

b) Superficial gas velocity higher than the minimum bubbling velocity (u_{mb}):

$$u_{mb}=2.07d_p\rho_g^{0.06}\mu_g^{-0.347}\exp(0.71u_{mf}) \tag{2-2}$$

c) Superficial gas velocity lower than the minimum slugging velocity (u_{ms}) and minimum turbulent velocity (u_k). If $u_{mb}<u_0<u_k$ but other conditions for the slugging regime are not satisfied, the bubbling regime is prevalent.

$$u_{ms}=u_{mf}+0.07\sqrt{gD} \tag{2-3}$$

$$u_k = 7.0 u_{mf} \sqrt{\rho_p d_p} - 0.77 \tag{2-4}$$

The bubbling regime is also associated with irregular pressure fluctuations with large amplitude and frequency in the range of 0.5 to 5 Hz depending on bed height (de Lasa, 2012).

2.3.3.2. Slugging regime

All of the following criteria must be satisfied for the slug flow to prevail (de Lasa, 2012):

a) Bed height must be 1.5 or 2 times the bed diameter. To be exact, the following condition should be met:

$$H \geq 3.5D\left(1 - n_0^{-0.5}\right) \tag{2-5}$$

b) Superficial gas velocity higher than the minimum slugging velocity (u_{ms}) .

c) The maximum stable bubble diameter similar to or higher than the bed diameter.

$$d_{b,\max} = 2.0\left(V_T^*\right)^2 / g \tag{2-6}$$

where V_T^* is the terminal settling velocity of a spherical particle of diameter $2.7d_p$ in a stagnant gas having the physical properties of the fluidizing gas.

d) Superficial gas velocity lower than the minimum turbulent velocity (u_k)

Slugging regime is also associated with fluctuations with large amplitude and regular frequency, typically between 0.2-1 Hz. Sound emission and column vibration are also other indications of the slugging regime (de Lasa, 2012).

2.3.3.3. Turbulent regime

The gas velocity must fall between the minimum turbulent velocity and transport velocity (u_{tr}) (de Lasa, 2012). Typical reported values of u_{tr} are 1.5 m/s for silica-alumina cracking catalyst (d_p=49 μm and ρ_p=1070 kg/m^3), and 3.8 m/s for hydrated alumina particles (ρ_p=2460 kg/m^3). There is insufficient data to allow u_{tr} to be correlated in a general way (de Lasa, 2012).

Turbulent fluidization is associated with irregular pressure fluctuations with a smaller amplitude and a larger frequency (>5 Hz). Time-averaged pressure profiles also show a distinct change in slope, indicating the upper bed surface (de Lasa, 2012).

2.3.4. Mathematical models

2.3.4.1. Two- and three-phase models

The macro-scale description of gas-solid interphase exchange is usually given by a two-phase model (bubble–emulsion) or a three-phase model (bubble–cloud/wake–emulsion). The two-phase model is comprised of a dense phase (emulsion or particulate phase) and a dilute phase (bubble) which is out of any particles. This model was first developed by Toomey and Johnstone (Toomey and Johnstone, 1952) assuming the emulsion phase to be perfectly mixed and the gas in the bubble phase to be in plug flow. The bed was considered in minimum fluidization condition and heterogeneous reactions were assumed to occur only in the emulsion phase (Toomey and Johnstone, 1952).

To further develop the two-phase model, Davidson and Harrison (Davidson and Harrison, 1963) assumed that the emulsion phase (in addition to the bubble phase) was in plug flow. They also assumed that the bubble diameter was constant throughout the process and the mass transfer had both diffusive and convective contributions. Contrary to this assumption, Partridge and Rowe (Partridge and Rowe, 1965) considered only the diffusive term of mass transfer equations. In an attempt to change the modeling domain, Kato and Wen (Kato and Wen, 1969) proposed a modeling approach that considered compartments equal in height with bubble diameter.

According to Kunii and Levenspiel (Kunii and Levenspiel, 1969), at high bubble velocities and in relatively high beds (>0.3 m), the emulsion phase does not maintain the minimum fluidization conditions, and solid recirculation is observed around bubbles. This area around the fast bubbles

which contains a relatively low fraction of solids is called cloud or wake. Based on this idea, Kunii and Levenspiel (Kunii and Levenspiel, 1969) developed the three-phase model (bubble cloud/wake and emulsion), where the cloud phase introduces a new transfer resistance between the bubble and the emulsion phase.

Unlike the two-phase model, the three-phase model does not assume the minimum fluidization condition for the emulsion phase, and the mass transfer between bubble and emulsion is studied through two steps of bubble–cloud and cloud–emulsion. Heterogeneous reactions occur in both the emulsion and the cloud phase (Kunii and Levenspiel, 1969). Although Kunii and Levenspiel's model covers a wider operational condition in the fluidized bed process, it has the disadvantage of computational implementation (Philippsen et al., 2015). Most industrial fluidized beds work in the operational range congruent with the assumptions of the two-phase model. In these conditions, the application of the three-phase model not only has no advantages over the two-phase model but also increases the calculation error in some cases (Davarpanah et al., 2020). In an attempt to develop Kunii and Levenspiel's model, Grace (Grace, 1986) proposed a model that was different in two major ways: (i) reactive particles could exist in the bubble phase, and (ii) fluidizing gas passes through the bed completely in bubble form.

Chavarie and Grace (Chavarie and Grace, 1975) studied the catalytic decomposition of ozone in a fluidized bed and compared the results of mathematical models suggested by Davidson and Harrison (Davidson and Harrison, 1963), Partridge and Rowe (Partridge and Rowe, 1965), Kunii and Levenspiel (Kunii and Levenspiel, 1969) and Kato and Wen (Kato and Wen, 1969), against experimental data. According to the results, the bubbling bed model of Kunii and Levenspiel (Kunii and Levenspiel, 1969) could approximate the performance of the fluidized bed studied better than any other models investigated. van Lare (van Lare, 1991) investigated the effect of

particle size on mass transfer in a fluidized bed using the two-phase model, along with van Deemter's model (van Deemter, 1961). The results showed that bubble–emulsion mass transfer coefficient, and therefore, heterogeneous reaction conversions are highest for particles in group B (even higher than those for smaller particles) (van Lare, 1991).

Wanderley (Wanderley, 2010) modeled the production of ethylene dichloride from an oxychlorination reaction in a bubbling fluidized bed using a phenomenological model based on the two-phase theory. They considered a system of one-dimensional flow in the axial direction at a steady state and studied the effects of fluid dynamics variables as well as the bubble–emulsion mass transfer on the overall conversion. The study showed that the model along with the simplifying assumptions adopted could adequately describe the industrial reactor. The process was found to be very sensitive to operating pressure, the temperature of the cooling water, minimum fluidization height, the catalyst particle diameter as well as the bubble size and the reactor diameter. Except for the bubble diameter, an increase in the other parameters improved the conversion reaction. Smaller bubbles and lower gas velocities would improve the mass transfer in the bubble–emulsion interface, hence, increase the conversion rate. The diffusion coefficient was also shown to play a more important role in determining the reactor conversion than the residence time (Wanderley, 2010).

2.3.4.2. Computational fluid dynamics (CFD)

The numerical simulation of the fluidized bed is conducted by means of classical conservation equations of mass, energy, and momentum, using correlations describing the interactions between solid and gas phases. There are a variety of commercial codes such as CFX, FLUENT, and MFIX, which use the finite volumes method to model different phenomena e.g. fluid mechanics, heat transfer, combustion, and gasification in fluidized beds (Philippsen et al., 2015).

In general, there are two widely used modeling approaches for gas-particle flows: (i) Euler-Euler method, also known as Two-Fluid Model (TFM), and (ii) Euler-Lagrange method, also quoted in the literature as Discrete Particle Model (DPM) (Stroh et al., 2016). The gas phase is considered continuous in both models, and the main difference is how the solid phase is treated.

2.3.4.2.1. Euler-Euler approach

In the Euler-Euler approach, the solid phase is considered continuous and coupling between phases is achieved through shared pressure and interphase forces including the drag force, lift force, and virtual mass force. The balance between computational costs, level of details, and potential of applicability are the main advantages of this approach (Stroh et al., 2016).

Many researchers used the Euler-Euler approach to simulate fluidized bed systems. Studying a cold flow circulating fluidized bed, Samuelsberg and Hjertager (Samuelsberg and Hjertager, 1996) showed that the numerical predictions of particle velocities at different gas mass flow rates using TFM had a good agreement with experimental data measured by laser Doppler anemometry. Du et al. (Du et al., 2006) compared the effect of different drag models (Gidaspow (Gidaspow, 1994) model, the Syamlal and O'Brien (Syamlal and O'Brien, 1988) model, the Richardson and Zaki (Richardson and Zaki, 1954) model, the Di Felice (Di Felice, 1994) model and the Arastoopour et al. (Arastoopour et al., 1990) model) on the numerical predictions of velocity profiles and solid flow patterns in a spouted bed and showed that Gidaspow model could best predict the experimental data amongst several drag models investigated. Kuipers et al. (Kuipers et al., 1993) simulated the hydrodynamics of a fluidized bed using the 2D Euler–Euler approach. They showed that the computed bubble size was not greatly influenced by the bed rheology. However, the bubble shape appeared to be quite sensitive to the bed rheology.

The main challenge of the Euler-Euler model, however, is how to model the kinetic and collisional transport of the particles (gas-particle, particle-particle, and particle-wall interactions) while representing the solid phase as an interpenetrating continuum. Therefore, many assumptions are needed to be made regarding the gas-particle drag correlations and the rheology of the solid phase. Closure and modeling terms with empirical nature are also required for the estimation of some parameters (Almohammed et al., 2014).

The kinetic theory of granular flow (KTGF) has been widely accepted as an essential model for simulating the flow properties of the solid. KTGF is based on the theory of non-uniform dense gases described by Chapman et al. (Chapman et al., 1990). This approach allows the determination of the pressure and viscosity of the solids in terms of empirical relations that consider the energy dissipation due to particle-particle collisions by means of restitution coefficient.

Goldschmidt et al. (Goldschmidt et al., 2001) studied the effect of the coefficient of restitution using the Euler–Euler approach along with KTGF and showed that the hydrodynamics of fluidized beds with dense fluidizing gases strongly depend on the energy dissipated in the particle-particle collisions. Huilin et al. (Huilin et al., 2003) later confirmed this result and showed that considering the effect of particle-particle interactions was essential for obtaining realistic simulations using a fundamental hydrodynamics model. Hydrodynamics of a two-dimensional gas-solid fluidized bed reactor was studied at different restitution coefficients by Taghipour et al. (Taghipour et al., 2005). They found that the sensitivity of the model to the restitution coefficient was higher at gas velocities below that required for minimum fluidization.

The influence of the particle diameter on the hydrodynamics of a fluidized bed was simulated by Mineto et al. (Mineto et al., 2008) using the Euler–Euler method along with KTGF. The maximum and the minimum values of granular temperature were observed in the bubble and dense

regions, respectively. They reported that the cohesive forces are negligible for particles with an average diameter of 500 μm when the central bubbles are well distributed and have low velocities. However, the cohesive forces were found to be the main factor in the stability of the flow for particles with an average diameter of 125 μm.

Using the Euler–Euler approach and KTGF, Papadikis et al. (Papadikis et al., 2008) simulated the fast pyrolysis process of biomass in a fluidized bed. They reported that the drag force was an important parameter defining the particle motion. Comparing 2-D and 3-D simulations, the authors stated that even though 2-D simulations are generally preferred due to computational power limitations, 3-D simulations are to be used when heat, mass and momentum transfer phenomena are studied.

Souza (Souza, 2009) investigated the diffusive effect of the numerical discretization of the convection terms on the simulation of a fluidized bed using the Euler–Euler model and KTGF. They noted that the first-order method (first-order upwind) is highly diffusive and requires refined meshes. The high order method of Superbee showed results with a better agreement with the experiments and allowed for the use of coarser mesh. The diffusive effects of the numerical discretization for the Superbee method decreased with increasing the number of iterations. It was also discussed that high-order discretization methods tend to produce numerical oscillations near high gradients, and hence, require the application of a flow restrictor (Souza, 2009).

2.3.4.2.2. Euler-Lagrange approach

In the Euler-Lagrange approach, the motion of each individual element is computed based on the first principles of hydrodynamics. This approach, hence, does not require additional closure equations for the solid phase and allows simulation of different particle types with various sizes, shapes, and densities (Stroh et al., 2016). The Euler-Lagrange model can also give more detailed

information such as bubble positions, solid size distribution, and solid age distribution compared to the Euler-Euler model (Xue et al., 2017). However, for modeling gas-solid flows based on the Euler-Lagrange model, an accurate description of the particle-particle and particle-wall collisions is still required (Almohammed et al., 2014).

The particle collisions can be modeled by either (i) stochastic particle collision models or (ii) deterministic particle collision models (Almohammed et al., 2014, Stroh et al., 2016). The stochastic particle collision approach, usually cited as the Multi-Phase Particle In Cell (MP-PIC) was originally developed by Andrews and O'Rourke (Andrews and O'Rourke, 1996) and further improved by Snider (Snider, 2001). This model considers billions of particles to be represented by fewer parcels (also known as computational particles) and the particle properties are interpolated to and from an Eulerian grid using interpolation functions (Snider et al., 1998). MP-PIC approach is mainly used for the dilute gas-solid flows, and the simplifications applied were reported to produce unrealistic results such as solid volume fractions greater than unity in the control volume in some cases (Almohammed et al., 2014). Sommerfeld (Sommerfeld, 2001) introduced an MP-PIC inter-particle collision model and compared the numerical predictions with results from large-eddy simulations. Some other researchers also used the MP-PIC approach to simulate fluidized systems (Snider et al., 1998, Zhao et al., 2006, Snider, 2007).

For Euler-Lagrange simulations with deterministic collision detection, two models are widely recognized: (i) the hard-sphere model and (ii) the soft-sphere model. In the hard-sphere model, single binary collisions are considered as instantaneous processes. In the soft-sphere model, also known as the discrete element method (DEM), the particles can overlap each other or penetrate the wall (Almohammed et al., 2014).

Rhodes et al. (Rhodes et al., 2001) studied the influence of the magnitude of the cohesive interparticle force on fluidization characteristics in a two-dimensional fluidized bed (height 0.2 m, width 0.08 m) using DEM. It was shown that applying a cohesive interparticle force on particles in Group D or B would lead to non-bubbling fluidization for the gas velocities between the minimum fluidization velocity and the minimum bubbling velocity, which associates with particles in Group A.

Almohammed et al. (Almohammed et al., 2014) conducted comparative research on the influence of two gas flow rates on the hydrodynamics of a spouted bed using Euler-Euler and Euler-Lagrange deterministic models. Numerical results were compared to experimental observations in terms of bubble diameter, bed height, and bed expansion. Based on the results, at a gas mass flow rate of 0.005 kg/s, the characteristics of the bubble formation and the bed expansion predicted using both techniques were in very good agreement with experimental observations. However, when the gas mass flow rate is increased to 0.006 kg/s the Euler-Euler model showed some deviations from the experimental results compared to the DEM.

Although the deterministic collision models show much better agreement with the experimental data than stochastic collision models, the particle trajectories in both models are calculated for each particle/parcel individually which makes them impractical for simulating industrial systems due to their high computational demands (Stroh et al., 2016).

2.3.4.3. Important parameters in modeling the adsorption process in fluidized beds

When considering the isothermal adsorption process in fluidized bed systems, there are several important parameters such as minimum fluidization velocity, bubble diameter, bubble rising velocity, and interphase mass transfer coefficients, which frequently appear in formulas describing the hydrodynamics and kinetics of the adsorption process in a fluidized bed (Davidson and

Harrison, 1963, Kunii and Levenspiel, 1969, de Lasa, 2012). These parameters are all dependent on the gas, solid and bed properties, each of which will be described in this section.

2.3.4.3.1. Gas properties

According to the two- and three-phase models, the gas properties can influence the adsorption rate constant, interphase mass transfer rate, minimum fluidization velocity, and the adsorption equilibrium isotherm.

The adsorption rate constant is directly affected by the gas molecular weight, the gas diffusivity in air, and the gas density. When the gas molecular weight increases, the adsorption rate constant decreases due to a decrease in molecular quadratic velocity (Hymore and Laguerie, 1984). Increasing the gas diffusivity, however, increases the adsorption rate constant (Hymore and Laguerie, 1984). Higher gas density (assuming that the molecular weight is constant) can also increase the adsorption rate constant (Hymore and Laguerie, 1984).

The gas diffusivity is one of the important factors in the calculations of the interphase mass transfer rate. Other parameters in determining the interphase mass transfer rate are bubble diameter, bubble rising velocity, and minimum fluidization velocity, which are all functions of gas, solid and bed properties (Davidson and Harrison, 1963).

The minimum fluidization velocity which is perhaps the most important parameter in the calculations of the two- and three-phase models is affected by the gas density and viscosity (de Lasa, 2012). Although the effect of these parameters is contingent on the range of other parameters such as solid diameter and density, increasing the gas density and viscosity would decrease the minimum fluidization velocity in the practical range of operation.

The forces holding the adsorbate molecules to the atoms on the surface of the adsorbent in the physical adsorption process are identified as dispersive and electrostatic (coulombic) forces, the latter exists only on polar surfaces (Yang, 1987). The dispersive forces exist between any two atoms or molecules and arise from the rapid fluctuation of electron density in each atom, which induces an electrical moment in the neighbor, and therefore, creates an attraction field. The electrostatic forces originate in the ionic atoms and polar groups on the surface of the adsorbent (Yang, 1987). Considering the nature of the adsorptive forces, the adsorption of various adsorbates on a given solid might exhibit different adsorption isotherms. The adsorption isotherm is an important factor in the calculations of fluidized bed since it is frequently incorporated in the estimations of the adsorption capacity and kinetics.

It was previously reported that two adsorbates that are different in nature such as water and 1,2,4-Trimethylbenzene (TMB) would exhibit totally different isotherms on BAC (see Figure 2-2) (Amdebrhan, 2018, Laskar et al., 2019). When dealing with VOC only, less difference is expected in the adsorption isotherms. Laskar (Laskar et al., 2019) measured the adsorption isotherms of different VOCs including toluene, n-butanol, TMB, acetone, and 2-propanol and showed that non-polar VOCs (toluene, n-butanol, TMB) generally have a higher adsorption affinity towards BAC than the polar VOCs (acetone, and 2-propanol). However, the isotherm shapes were almost identical (Brunauer-Deming-Deming-Teller type I) and the maximum adsorption capacity for all adsorbates fell in the small range of 0.484-0.515 cm^3/g (Laskar et al., 2019).

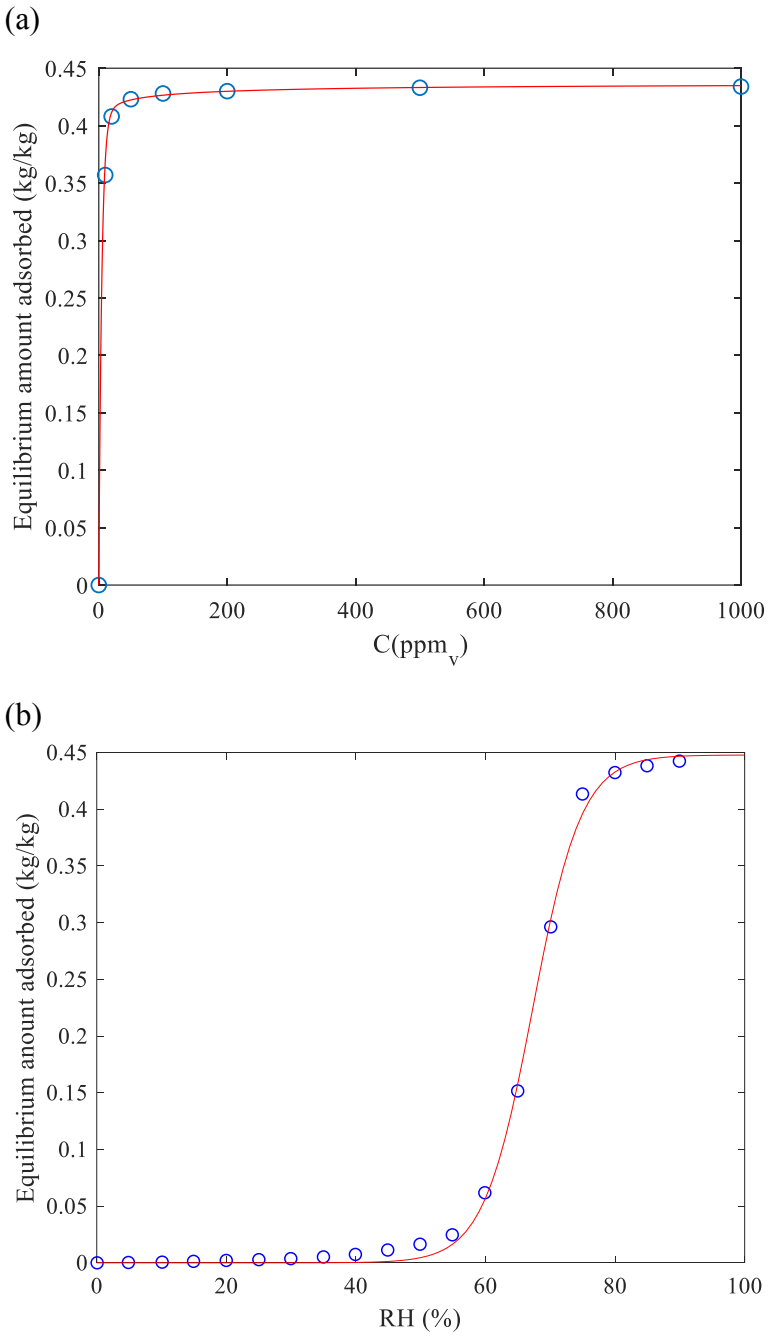

Figure 2-2. The equilibrium adsorption isotherms of (a) TMB (Amdebrhan, 2018) and (b) water vapor (Laskar et al., 2019) on BAC at room temperature.

When the CFD calculations of the hydrodynamics of the bed are concerned, the exact effect of gas properties, in many cases, depends on the formulas and methods used. However, it can be said

that increasing the gas density and gas viscosity normally increases the drag force imparted on the solids which translates into lower minimum fluidization velocities (Ansys, Release 19.2).

2.3.4.3.2. Solid properties

In fluidized bed modeling, the physical properties of the solid including the solid diameter, solid density, and solid porosity are used to determine the minimum fluidization velocity, the adsorption rate constant, and the average bubble diameter. The minimum fluidization velocity and the average bubble diameter allow the determination of interphase mass transfer rate and the bubble rise velocity which are often used in the calculations of the fluidized bed systems.

The minimum fluidization increases with an increase in the solid diameter and/or solid density. The adsorption rate constant is affected by the solid pore diameter and solid diameter. Knudsen diffusion coefficient is proportional to the solid pore diameter, while the internal mass transfer coefficient is inversely proportional to the square of the solid diameter (Davarpanah et al., 2020).

The effect of solid properties on the average bubble diameter depends on the formulas used. In some formulas, the average bubble diameter is directly proportional to the solid diameter and density. Conventional formulas for the calculation of the bubble diameter are provided in the literature (Mori and Wen, 1975, Hatzantonis et al., 2000).

Similar to the adsorbate properties, the adsorbent properties are important in determining the adsorption equilibrium isotherms. Porous media are very complex and except for solids with well-defined structures i.e. synthetic zeolites, the understanding of the characteristics of solids with complex structures is still far from complete (Do, 1998).

Among the practical solids used in industries, activated carbon (AC) is one of the most commonly used solids for the removal of VOCs, owing to its high surface area, porosity, and

micropore volume (Do, 1998). The structure of activated carbon is composed of an amorphous structure and a graphite-like microcrystalline structure, the latter provides adsorption capacity in the form of a slit-shaped channel (Do, 1998). Despite the advantages of ACs, there are some limitations in specific applications such as regeneration difficulties for solvents with high boiling points (> 150°C), surface hydrophobicity, the possibility of polymerization or oxidation of some solvents in AC pores, and the risk of bed fire (Parmar and Rao, 2008, Amdebrhan, 2018). These limitations have urged the development of new adsorbents (Liu et al., 2009).

Recently, polymeric adsorbents have attracted attention as an alternative to the AC due to their controllable pore structure, stable physical-chemical properties, and ease of regeneration (Choung et al., 2001, Tsyurupa and Davankov, 2006, Long et al., 2009). A hypercrosslinked polymer produced by means of crosslinking microporous resin can deliver favorable adsorptive properties such as narrow pore size distribution (PSD), as well as controllable pore structure and internal surface area (Choung et al., 2001).

Another important class of solids used as widely as AC is zeolite which can be found naturally or made synthetically (Do, 1998). Compared to natural zeolite, the application of synthetic zeolite is more common in the industries because synthetic zeolite can be engineered for more specificity (Do, 1998). Zeolite has a crystal structure with a fixed pore size which can selectively adsorb the target molecules, and that is the reason that a zeolite adsorbent is sometimes called a molecular sieve (Amdebrhan, 2018). The book by Ruthven (Ruthven, 1984) provides a good overview of different types of zeolites.

Given the difference in their physical and chemical properties, adsorbents might show different affinity towards a specific molecule, hence, exhibit different equilibrium isotherms.

Figure 2-3 compares the adsorption capacity of beaded activated carbon (BAC), a polymeric adsorbent (Dowex Optipore® V–503), and Zeolite (ZEOcat F603, ZEOCHEM®) in adsorption of TMB in the range of 0-1000 ppm_v (Amdebrhan, 2018). Both the amount adsorbed as well as the local slope of the isotherm in the range of fluidized bed operation are important in the calculations of the two- and three-phase models. The removal efficiency in the fluidized bed experiments for the adsorption of TMB on BAC, a polymeric adsorbent (Dowex Optipore® V–503), and Zeolite (ZEOcat F603, ZEOCHEM®) at various adsorbent feed rates are compared in Figure 2-4 when the inlet concentration (C_0) and air flow rate (F_g) are 100 ppm_v and 300 SLPM, respectively.

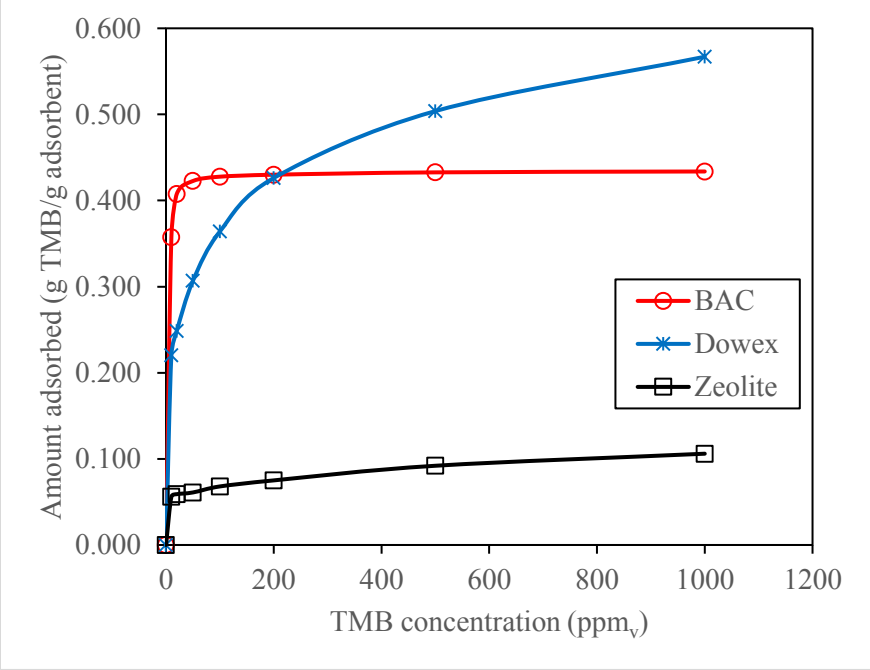

Figure 2-3. A comparison of the adsorption capacity of BAC, a polymeric adsorbent (Dowex Optipore® V–503), and Zeolite (ZEOcat F603, ZEOCHEM®), and Zeolite in adsorption of TMB (Amdebrhan, 2018).

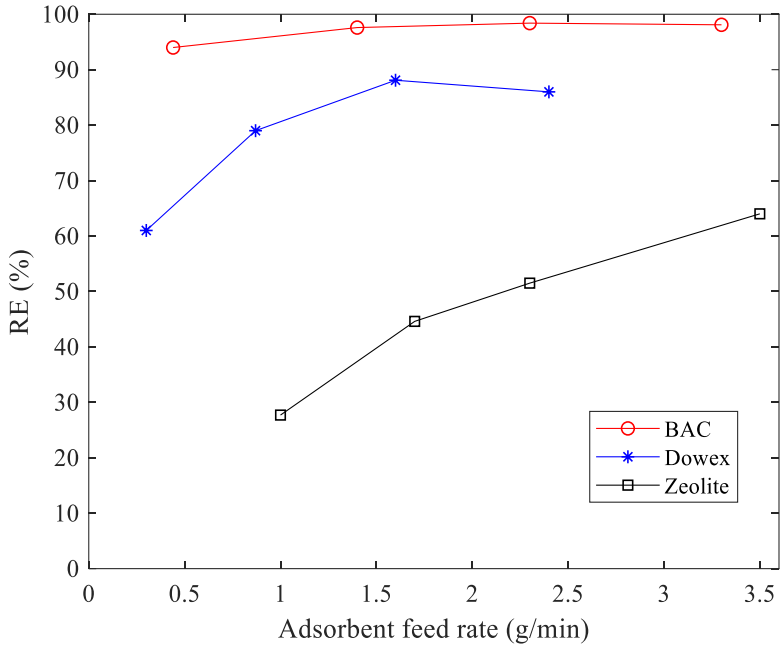

Figure 2-4. A comparison of removal efficiency achieved in fluidized bed operation for the adsorption of TMB on BAC, a polymeric adsorbent (Dowex Optipore® V–503), and Zeolite (ZEOcat F603, ZEOCHEM®) at F_g=300 SLPM and C_0=100 ppm_v (Kamravaei et al., 2016, Davarpanah et al., 2020).

The effect of the solid properties on the CFD calculations of the hydrodynamics of the bed is reflected in equations of momentum transfer, solid pressure, solid collisional viscosity, bulk viscosity, solid kinetic viscosity, and collision dissipation of energy (Ansys, Release 19.2). Increasing the particle density is expected to increase the minimum fluidization velocities. The CFD formulas and equations used in this study will be presented later.

2.3.4.3.3. Bed properties

The bed properties including the cross-section area of the bed, the number of stages, the stage configuration, the number of orifices on the distributors, and the weir height on each stage can influence the efficiency of the fluidized bed. A larger cross-section area and a higher number of orifices are expected to improve the efficiency of the fluidized bed by facilitating the mass transfer

in the bed (Davarpanah et al., 2020). The impacts of the number of stages, the stage configuration, and the weir height are complex and will be discussed in the next chapters.

The detailed effect of bed geometry on the hydrodynamic regime inside a fluidized bed is complex and requires a thorough investigation. Afrooz et al. (Afrooz et al., 2017) used CFD simulations to compare the hydrodynamics of a swirl tube reactor with that of a conventional straight tube reactor. They found that the usage of the swirl tube reactor design not only resulted in better lateral solid mixing inside the bed but also increased the residence time of the particles inside the bed (Afrooz et al., 2017).

2.4. References

Afrooz, I.E., Sinnathambi, C.M., Chuang, D.L., Karuppanan, S., 2017. CFD simulation of bubbling fluidized bed: Effects of bed column geometry on hydrodynamics of gas–solid mixing. *Materialwissenschaft und Werkstofftechnik*, **48**: 226-234.

Almohammed, N., Alobaid, F., Breuer, M., Epple, B., 2014. A comparative study on the influence of the gas flow rate on the hydrodynamics of a gas–solid spouted fluidized bed using Euler–Euler and Euler–Lagrange/DEM models. *Powder Technology*, **264**: 343-364.

Amdebrhan, B.T. (2018). Evaluating the Performance of Activated Carbon, Polymeric, and Zeolite Adsorbents for Volatile Organic Compounds Control. Department of Civil and Environmental Engineering, University of Alberta. **Master of Science**.

Andrews, M.J., O'Rourke, P.J., 1996. The multiphase particle-in-cell (MP-PIC) method for dense particulate flows. *International Journal of Multiphase Flow*, **22**: 379-402.

Ansys (Release 19.2). Ansys fluent theory guide. USA, ANSYS Inc.

Arastoopour, H., Pakdel, P., Adewumi, M., 1990. Hydrodynamic analysis of dilute gas—solids flow in a vertical pipe. *Powder Technology*, **62**: 163-170.

Chapman, S., Cowling, T.G., Burnett, D. (1990). The mathematical theory of non-uniform gases: an account of the kinetic theory of viscosity, thermal conduction and diffusion in gases, Cambridge university press.

Chavarie, C., Grace, J.R., 1975. Performance Analysis of a Fluidized Bed Reactor. II. Observed Reactor Behavior Compared with Simple Two-Phase Models. *Industrial & Engineering Chemistry Fundamentals*, **14**: 79-86.

Chiang, B.-C., Wey, M.-Y., Yang, W.-Y., 2000. Control of Incinerator Organics by Fluidized Bed Activated Carbon Adsorber. *Journal of Environmental Engineering*, **126**: 985-992.

Choung, J.-H., Lee, Y.-W., Choi, D.-K., Kim, S.-H., 2001. Adsorption Equilibria of Toluene on Polymeric Adsorbents. *Journal of Chemical & Engineering Data*, **46**: 954-958.

Davarpanah, M., Hashisho, Z., Crompton, D., Anderson, J.E., Nichols, M., 2020. Modeling VOC adsorption in lab- and industrial-scale fluidized bed adsorbers: Effect of operating parameters and heel build-up. *Journal of Hazardous Materials*, **400**: 123129.

Davarpanah, M., Hashisho, Z., Phillips, J.H., Crompton, D., Anderson, J.E., Nichols, M., 2020. Modeling VOC adsorption in a multistage countercurrent fluidized bed adsorber. *Chemical Engineering Journal*, **394**: 124963.

Davidson, J.F., Harrison, D. (1963). Fluidized Particles. New York, Cambridge University Press.

de Lasa, H. (2012). Chemical Reactor Design and Technology: Overview of the New Developments of Energy and Petrochemical Reactor Technologies. Projections for the 90's, Springer Science & Business Media.

Delage, F., Pré, P., Le Cloirec, P., 2000. Mass Transfer and Warming during Adsorption of High Concentrations of VOCs on an Activated Carbon Bed: Experimental and Theoretical Analysis. *Environmental Science & Technology*, **34**: 4816-4821.

Di Felice, R., 1994. The voidage function for fluid-particle interaction systems. *International Journal of Multiphase Flow*, **20**: 153-159.

Do, D.D. (1998). Adsorption Analysis: Equilibria And Kinetics. London, Imperial College Press.

Dolidovich, A.F., Akhremkova, G.S., Efremtsev, V.S., 1999. Novel technologies of VOC decontamination in fixed, moving and fluidized catalyst-adsorbent beds. **77**: 342-355.

Du, W., Bao, X., Xu, J., Wei, W., 2006. Computational fluid dynamics (CFD) modeling of spouted bed: Assessment of drag coefficient correlations. *Chemical Engineering Science*, **61**: 1401-1420.

Geldart, D., 1973. Types of gas fluidization. *Powder Technology*, **7**: 285-292.

Gidaspow, D. (1994). Multiphase flow and fluidization: continuum and kinetic theory descriptions, Academic press.

Girimonte, R., Formisani, B., Testa, F., 2017. Adsorption of CO2 on a confined fluidized bed of pelletized 13X zeolite. *Powder Technology*, **311**: 9-17.

Goldschmidt, M.J.V., Kuipers, J.A.M., van Swaaij, W.P.M., 2001. Hydrodynamic modelling of dense gas-fluidised beds using the kinetic theory of granular flow: effect of coefficient of restitution on bed dynamics. *Chemical Engineering Science*, **56**: 571-578.

Grace, J.R., 1986. Contacting modes and behaviour classification of gas—solid and other two-phase suspensions. *The Canadian Journal of Chemical Engineering*, **64**: 353-363.

Haider, A., Levenspiel, O., 1989. Drag coefficient and terminal velocity of spherical and nonspherical particles. *Powder Technology*, **58**: 63-70.

Hamed, A.M., Abd El Rahman, W.R., El-Emam, S.H., 2010. Experimental study of the transient adsorption/desorption characteristics of silica gel particles in fluidized bed. *Energy*, **35**: 2468-2483.

Harshe, Y.M., Utikar, R.P., Ranade, V.V., 2004. A computational model for predicting particle size distribution and performance of fluidized bed polypropylene reactor. *Chemical Engineering Science*, **59**: 5145-5156.

Hatzantonis, H., Yiannoulakis, H., Yiagopoulos, A., Kiparissides, C., 2000. Recent developments in modeling gas-phase catalyzed olefin polymerization fluidized-bed reactors: The effect of bubble size variation on the reactor's performance. *Chemical Engineering Science*, **55**: 3237-3259.

Huilin, L., Yurong, H., Gidaspow, D., 2003. Hydrodynamic modelling of binary mixture in a gas bubbling fluidized bed using the kinetic theory of granular flow. *Chemical Engineering Science*, **58**: 1197-1205.

Hymore, K., Laguerie, C., 1984. Analysis and modelling of the operation of a counterflow multistage fluidized bed adsorber for drying moist air. *Chemical Engineering and Processing: Process Intensification*, **18**: 255-267.

Kamravaei, S., Shariaty, P., Hashisho, Z., Phillips, J.H., Anderson, J.E., Nichols, M., Crompton, D. (2016). Performance of a Multistage Fluidized Bed Adsorber Using Polymeric Adsorbent to Capture Volatile Organic Compounds. AIChE Annual Meeting. San Francisco, CA, USA.

Kamravaei, S., Shariaty, P., Jahandar Lashaki, M., Atkinson, J.D., Hashisho, Z., Phillips, J.H., Anderson, J.E., Nichols, M., 2017. Effect of Beaded Activated Carbon Fluidization on

Adsorption of Volatile Organic Compounds. *Industrial & Engineering Chemistry Research*, **56**: 1297-1305.

Kato, K., Wen, C.Y., 1969. Bubble assemblage model for fluidized bed catalytic reactors. *Chemical Engineering Science*, **24**: 1351-1369.

Kim, H.S., Matsushita, Y., Oomori, M., Harada, T., Miyawaki, J., Yoon, S.H., Mochida, I., 2013. Fluidized bed drying of Loy Yang brown coal with variation of temperature, relative humidity, fluidization velocity and formulation of its drying rate. *Fuel*, **105**: 415-424.

Kuipers, J.A.M., van Duin, K.J., van Beckum, F.P.H., van Swaaij, W.P.M., 1993. Computer simulation of the hydrodynamics of a two-dimensional gas-fluidized bed. *Computers & Chemical Engineering*, **17**: 839-858.

Kunii, D., Levenspiel, O. (1969). Fluidization engineering. New York, Wiley.

Laskar, I.I., Hashisho, Z., Phillips, J.H., Anderson, J.E., Nichols, M., 2019. Competitive adsorption equilibrium modeling of volatile organic compound (VOC) and water vapor onto activated carbon. *Separation and Purification Technology*, **212**: 632-640.

Leva, M. (1959). Fluidization. New York, McGraw-Hill.

Liu, P., Long, C., Li, Q., Qian, H., Li, A., Zhang, Q., 2009. Adsorption of trichloroethylene and benzene vapors onto hypercrosslinked polymeric resin. *Journal of Hazardous Materials*, **166**: 46-51.

Long, C., Li, A., Wu, H., Zhang, Q., 2009. Adsorption of naphthalene onto macroporous and hypercrosslinked polymeric adsorbent: Effect of pore structure of adsorbents on thermodynamic and kinetic properties. *Colloids and Surfaces A: Physicochemical and Engineering Aspects*, **333**: 150-155.

Mineto, A., Souza, M., Silva, R., Cabézas-Gomes, L., Montagnoli, A., Navarro, H. (2008). Particle diameter influence on simulation ofgas–solid flow in bubbling fluidized bed. 7th Brazilian conference on dynamics, control and applications.

Missen, R.W., Mims, C.A., Saville, B.A. (1999). Introduction to chemical reaction engineering and kinetics, Wiley New York.

Mohanty, C.R., Malavia, G., Meikap, B.C., 2009. Development of a Countercurrent Multistage Fluidized-Bed Reactor and Mathematical Modeling for Prediction of Removal Efficiency of Sulfur Dioxide from Flue Gases. *Industrial & Engineering Chemistry Research*, **48**: 1629-1637.

Mohanty, C.R., Meikap, B.C., 2011. Modeling the operation of a three-stage fluidized bed reactor for removing CO2 from flue gases. *Journal of Hazardous Materials*, **187**: 113-121.

Mori, S., Wen, C.Y., 1975. Estimation of bubble diameter in gaseous fluidized beds. *AIChE Journal*, **21**: 109-115.

Papadikis, K., Bridgwater, A.V., Gu, S., 2008. CFD modelling of the fast pyrolysis of biomass in fluidised bed reactors, Part A: Eulerian computation of momentum transport in bubbling fluidised beds. *Chemical Engineering Science*, **63**: 4218-4227.

Parmar, G.R., Rao, N.N., 2008. Emerging Control Technologies for Volatile Organic Compounds. *Critical Reviews in Environmental Science and Technology*, **39**: 41-78.

Partridge, B., Rowe, P. (1965). Chemical reaction in a bubbling gas-fluidised bed, UK Atomic Energy Authority Research Group.

Philippsen, C.G., Vilela, A.C.F., Zen, L.D., 2015. Fluidized bed modeling applied to the analysis of processes: review and state of the art. *Journal of Materials Research and Technology*, **4**: 208-216.

Poulopoulos, S.G., Inglezakis, V.J. (2006). Adsorption, ion exchange and catalysis: design of operations and environmental applications, Elsevier.

Reichhold, A., Hofbauer, H., 1995. Internally circulating fluidized bed for continuous adsorption and desorption. *Chemical Engineering and Processing: Process Intensification*, **34**: 521-527.

Rhodes, M.J., Wang, X.S., Nguyen, M., Stewart, P., Liffman, K., 2001. Use of discrete element method simulation in studying fluidization characteristics: influence of interparticle force. *Chemical Engineering Science*, **56**: 69-76.

Richardson, J.F., Zaki, W.N., 1954. Sedimentation and fluidisation: Part I. *Transactions of the Institution of Chemical Engineers*, **32**: 35-53.

Roy, S., Mohanty, C.R., Meikap, B.C., 2009. Multistage Fluidized Bed Reactor Performance Characterization for Adsorption of Carbon Dioxide. *Industrial & Engineering Chemistry Research*, **48**: 10718-10727.

Ruthven, D.M. (1984). Principles of adsorption and adsorption processes, John Wiley & Sons.

Samuelsberg, A., Hjertager, B.H., 1996. An experimental and numerical study of flow patterns in a circulating fluidized bed reactor. *International Journal of Multiphase Flow*, **22**: 575-591.

Sanders, R.E., 2003. Designs that lacked inherent safety: case histories. *Journal of Hazardous Materials*, **104**: 149-161.

Saxena, S.C., Vadivel, R., 1988. Wall effects in gas-fluidized beds at incipient fluidization. *The Chemical Engineering Journal*, **39**: 133-137.

Schulzke, T., Westermeyer, J., Giani, H., Hornsby, C., 2018. Combustion of Refined Renewable Biomass Fuel (RRBF) in a bubbling fluidized bed. *Renewable Energy*, **124**: 84-94.

Snider, D.M., 2001. An Incompressible Three-Dimensional Multiphase Particle-in-Cell Model for Dense Particle Flows. *Journal of Computational Physics*, **170**: 523-549.

Snider, D.M., 2007. Three fundamental granular flow experiments and CPFD predictions. *Powder Technology*, **176**: 36-46.

Snider, D.M., O'Rourke, P.J., Andrews, M.J., 1998. Sediment flow in inclined vessels calculated using a multiphase particle-in-cell model for dense particle flows. *International Journal of Multiphase Flow*, **24**: 1359-1382.

Sommerfeld, M., 2001. Validation of a stochastic Lagrangian modelling approach for inter-particle collisions in homogeneous isotropic turbulence. *International Journal of Multiphase Flow*, **27**: 1829-1858.

Song, W., Tondeur, D., Luo, L., Li, J., 2005. VOC Adsorption in Circulating Gas Fluidized Bed. *Adsorption*, **11**: 853-858.

Souza, M. (2009). Numerical effects onthe simulation of gas–solid flow in bubbling fluidized bedusing the kinetic theory of granular flow, São Paulo State University.

Stroh, A., Alobaid, F., Hasenzahl, M.T., Hilz, J., Ströhle, J., Epple, B., 2016. Comparison of three different CFD methods for dense fluidized beds and validation by a cold flow experiment. *Particuology*, **29**: 34-47.

Syamlal, M., O'Brien, T.J., 1988. Simulation of granular layer inversion in liquid fluidized beds. *International Journal of Multiphase Flow*, **14**: 473-481.

Taghipour, F., Ellis, N., Wong, C., 2005. Experimental and computational study of gas–solid fluidized bed hydrodynamics. *Chemical Engineering Science*, **60**: 6857-6867.

Toomey, R.D., Johnstone, H.F., 1952. Gaseous Fluidization of Solid Particles. *Chemical Engineering Progress*, **48**: 220-226.

Tsyurupa, M.P., Davankov, V.A., 2006. Porous structure of hypercrosslinked polystyrene: State-of-the-art mini-review. *Reactive and Functional Polymers*, **66**: 768-779.

van Deemter, J.J., 1961. Mixing and contacting in gas-solid fluidized beds. *Chemical Engineering Science*, **13**: 143-154.

van Lare, C.E.J. (1991). Mass transfer in gas fluidized beds: scaling, modeling and particle size influence, Technische Universiteit Eindhoven.

Wanderley, P. (2010). Modeling andsimulation of an oxychlorination reactor in fluidized bed forthe production of 1,2-dichloroethane., Universidade Federal de Alagoas.

Xue, J., Chen, F., Yang, N., Ge, W. (2017). A Study of the Soft-Sphere Model in Eulerian-Lagrangian Simulation of Gas-Liquid Flow. International Journal of Chemical Reactor Engineering. **15**.

Yang, R.T. (1987). Gas Separation by Adsorption Processes, Butterworth-Heinemann.

Yang, W.-c. (2003). Handbook of fluidization and fluid-particle systems, CRC press.

Yazbek, W., Pré, P., Delebarre, A., 2006. Adsorption and Desorption of Volatile Organic Compounds in Fluidized Bed. *Journal of Environmental Engineering*, **132**: 442-452.

Zhao, P., Snider, D., Williams, K. (2006). Computational particle-fluid dynamics simulations of a commercial-scale turbulent fluidized bed reactor. AIChE Annual Meeting.

3. Chapter 3*: Modeling VOC adsorption in a multistage countercurrent fluidized bed adsorber

3.1. Abstract

The adsorption of 1,2,4-trimethylbenzene (TMB) on beaded activated carbon (BAC) in a six-stage countercurrent fluidized bed adsorber was simulated employing a two-phase model, assuming the gas in particulate phase to be either in plug flow (EGPF model) or in perfectly mixed flow (EGPM model). A rather simple model considering equilibrium state on each stage (Equilibrium model) was also used for comparison. Simulation results were compared with experimental data obtained at different values of adsorbent feed rate, superficial gas velocity, TMB initial concentration, and weir height (which influences the effective bed height). The results demonstrate that the Equilibrium model overpredicts the overall removal efficiencies when the adsorbate-adsorbent system is far from an equilibrium condition. On the other hand, both EGPF and EGPM show good agreement with the experimental results over industrially relevant operating conditions. Stage-wise removal efficiencies show that the EGPF model tends to predict removal efficiency better than EGPM when the weir height is high. The sensitivity analysis of the EGPM model indicates that internal diffusion within the BAC is rate-limiting for adsorption, while BAC diameter strongly influences the overall removal efficiency and can be optimized for different conditions. The effect of changes in BAC adsorption capacity on overall removal efficiency depends on the number of available adsorption sites, as well as proximity to an equilibrium condition. The model developed in this study is also able to predict the effect of the number of

* This chapter has been published as an original paper: Davarpanah, M.; Hashisho, Z.; Phillips, J. H.; Crompton, D.; Anderson, J. E.; Nichols, M., Modeling VOC adsorption in a multistage countercurrent fluidized bed adsorber. Chemical Engineering Journal 2020, 394, 124963. Reproduced with permission from Elsevier.

stages on the overall removal efficiency of the adsorber. The results of this study could pave the way for optimizing the design and operation of fluidized bed adsorbers, leading to cost savings and performance improvements.

3.2. Nomenclature

Sym.	Description	Value /Formula	Units	Source
A	cross-section area of bed	Table 3-1	m^2	measured
Ar	Archimedes number	Table 3-3	-	(Abasaeed and Al-Zahrani, 1998)
a_p	external surface area per unit volume of particles	Table 3-3	m^{-1}	(Seader and Henley, 2006)
b	Langmuir coefficient	1.19×10^5	kg/kg	measured
C	TMB concentration	Eq. (3-5)	kg TMB/kg air	calculated
C^*	TMB concentration in air in equilibrium condition	Table S1	kg TMB/kg air	measured
C_0	TMB concentration at bed entry	Table 3-2	ppm_v, kg TMB/kg air	measured
C_b	TMB concentration in bubble phase	Eqs. (3-8) and (3-16)	kg TMB/kg air	calculated
C_p	TMB concentration in particulate phase	Eqs. (3-10) and (3-17)	kg TMB/kg air	calculated
d_b	mean bubble diameter	Table 3-3	m	(Cai et al., 1994)
D_e	internal mass transfer coefficient	Eq. (3-39)	$m^2\ s^{-1}$	(Seader and Henley, 2006)
D_g	TMB diffusivity in air	Table 3-1	$m^2\ s^{-1}$	(Tang et al., 2014)
D_k	Knudsen diffusion coefficient	Eq. (3-40)	$m^2\ s^{-1}$	(Seader and Henley, 2006)
D_s	surface diffusion coefficient	Eq. (3-41)	$m^2\ s^{-1}$	(Seader and Henley, 2006)
d_p	adsorbent mean diameter	Table 3-1	m	(Tefera et al., 2014)

d_{pore}	mean diameter of pores in adsorbent	Table 3-1	m	measured
E	cumulative fraction of solids on the stages	Eq. (3-22)	-	(Hymore and Laguerie, 1984)
F_g	air flow rate	Table 3-2	SLPM, kg hr^{-1}	measured
F_p	adsorbent feed rate	Table 3-2	g min^{-1}, kg hr^{-1}	measured
g	standard gravity	9.8	m/s^2	(Abasaeed and Al-Zahrani, 1998)
H	weir height	Table 3-2	mm, m	measured
H_{mf}	height of bed on each stage at u_{mf}	Table 3-3	m	(Hymore and Laguerie, 1984)
i	index of the stage number	-	-	-
IP	ionization potential	8.27	eV	(Tefera et al., 2014)
k	adsorption rate constant	Eq. (3-33)	s^{-1}	(Seader and Henley, 2006)
k'	coefficient	Eq. (3-12)	-	calculated
k_c	external mass transfer coefficient	Eq. (3-34)	m s^{-1}	(Poulopoulos and Inglezakis, 2006)
m	slope of the isotherm	Eq. (3-32)	kg air/kg BAC	calculated
M	TMB molecular weight	Table 3-1	g mol^{-1}	(Tefera et al., 2014)
m_1	coefficient	Eq. (3-18)	-	calculated
m_2	coefficient	Eq. (3-19)	-	calculated
N_b	number of bubbles per unit volume of bed	Table 3-3	m^{-3}	(Hymore and Laguerie, 1984)
Q	mass transfer flow rate between a bubble and the particulate phase	Table 3-3	m^3 s^{-1}	(Hatzantonis et al., 2000, Poulopoulos and Inglezakis, 2006)
q	TMB content of adsorbent	N/A	kg TMB/kg BAC	N/A

q^*	TMB content of adsorbent in equilibrium condition	Table S1	kg TMB/kg BAC	measured
q_m	adsorbent maximum capacity	0.4377	kg/kg	calculated
r_{mic}	adsorbent mean micropore width	1.02	nm	(Tefera et al., 2014)
R	Gas constant	8.314×10^{-3}	kJ K^{-1} mol^{-1}	-
RE	removal efficiency	Eq. (3-3)	-	(Hymore and Laguerie, 1984)
Re	Reynolds number	Eq. (3-37)	-	(Poulopoulos and Inglezakis, 2006)
Re_{mf}	Reynolds number at u_{mf}	Table 3-3	-	(Abasaeed and Al-Zahrani, 1998)
Sh	Sherwood number	Eqs. (3-35) and (3-36)	-	(Poulopoulos and Inglezakis, 2006)
Sc	Schmidt number	Eq. (3-38)	-	(Poulopoulos and Inglezakis, 2006)
t	particles residence time	-	s	-
T	temperature	Table 3-1	K	measured
u_0	superficial gas velocity	F_g/A	m s^{-1}	calculated
u_b	velocity of bubble rising through a bed	Table 3-3	m s^{-1}	(Kunii and Levenspiel, 1969)
u_{mf}	minimum fluidization velocity	Table 3-3	m s^{-1}	(Abasaeed and Al-Zahrani, 1998)
V_b	bubble volume	Table 3-3	m^3	(Hymore and Laguerie, 1984)
W	mass of adsorbent on each stage	Table 3-3	kg	(Hymore and Laguerie, 1984)
X	coefficient	Eq. (3-11)	-	calculated
y	axis along the bed	-	m	-
α	coefficient	Eq. (3-31)	-	(Hymore and Laguerie, 1984)
α'	polarizability	15.87	$\times10^{-24}$ cm^3	(Tefera et al., 2014)

β	fraction of gas flowing as bubbles	Eq. (3-6)	-	(Hymore and Laguerie, 1984)
ΔH_{ads}	heat of adsorption	Eq. (3-42)	kJ mol^{-1}	(Giraudet et al., 2006)
ΔH_{vap}	heat of vaporization	39.2	kJ mol^{-1}	(Tefera et al., 2014)
ε_{mf}	void fraction at u_{mf}	Table 3-3	-	(Hymore and Laguerie, 1984)
ε_p	adsorbent internal porosity	Table 3-1	-	(Tefera et al., 2014)
γ	surface tension	28.70	mN m^{-1}	(Tefera et al., 2014)
μ_g	gas viscosity	Table 3-1	kg m^{-1} s^{-1}	(Keenan et al., 1983)
ρ_g	gas density	Table 3-1	kg m^{-3}	(Keenan et al., 1983)
ρ_p	adsorbent density	Table 3-1	kg m^{-3}	(Tefera et al., 2014)
τ	mean residence time of solids on each stage	Eq. (3-23)	s	(Hymore and Laguerie, 1984)
τ'	tortuosity	Table 3-3	-	(Poulopoulos and Inglezakis, 2006)
ϕ	adsorbent shape factor	Table 3-1	-	measured

3.3. Introduction

Fluidized bed systems offer excellent gas-solid mass transfer and temperature control when applied to several gas purification and separation processes due to the rigorous mixing of solid particles and air in the bed. Handling large gas flow rates is also possible owing to their low pressure drops. A fluidized bed system, hence, is a good candidate for process intensification when the external mass-transfer resistance or the pressure drop is high (e.g. adsorption and drying processes) (Kim et al., 2013, Girimonte et al., 2017) or when temperature uniformity and heat transfer are important (e.g. polymerization and combustion processes) (Harshe et al., 2004,

Schulzke et al., 2018). The wide residence time distribution of the gas and solid, which is the main disadvantage of traditional fluidized beds can be minimized with the use of countercurrent multistage beds, leading to a more efficient process (Hymore and Laguerie, 1984, Choi et al., 2002, Roy et al., 2009).

Despite these advantages, understanding the effects of all the parameters controlling fluidized bed operation can be challenging (Hymore and Laguerie, 1984, Werther and Hartge, 2004). Adsorption in a fluidized bed depends on the particle fluid dynamics as well as the mass, momentum and heat transfer processes, and varying parameters can strongly influence the overall removal efficiency of the adsorber. For example, changing just a single parameter such as the diameter of adsorbent particles affects the efficiency of the adsorber due to changes in dynamics of the fluidized bed, the mass of adsorbent on each stage, and the solid-gas mass transfer.

Modeling and simulation tools are effective ways to understand the intricate effects of different parameters on the behavior of a system. They also allow for studying what-if scenarios at minimum cost which eventually leads to time and cost savings.

The simplest model to calculate the removal efficiency in a fluidized bed is probably the Equilibrium model presented by Kunii and Levenspiel (Kunii and Levenspiel, 1969). The model was based on a mass balance with the assumption that the solid particles in a stage in a fluidized bed are in equilibrium with the leaving gas. Although in some cases the Equilibrium model could show acceptable predictions of experimental results, the deviation from experimental results is large in processes in which kinetics control the mass transfer between solid and gas (Hymore and Laguerie, 1984).

To take into account the adsorption kinetics, Toomey and Johnstone (Toomey and Johnstone, 1952) introduced the first two-phase model, which assumed that the fluidized bed consisted of an

emulsion phase (also known as particulate phase) and a particle-free bubble phase formed by the gas in excess of that required for minimum fluidization. In this model, emulsion and bubble phases were considered in perfectly-mixed and plug flow regimes, respectively. Davidson and Harrison (Davidson and Harrison, 1963) developed a more sophisticated two-phase model that could account for the detailed hydrodynamic behavior of a fluidized bed and described the particulate and bubble phases as plug flows.

Depending on the process studied, other authors also used different assumptions and formulas to the two-phase model to describe the contribution of different phenomena taking place in a fluidized bed such as mass transfer and bubble motion. Lu et al. (Lu et al., 2004) presented new mechanisms and a kinetic model for dimethyl ether synthesis in a fluidized bed reactor modeled with a two-phase model. Hymore and Laguerie (Hymore and Laguerie, 1984) developed a correction factor to describe the diffusion of vapor in the pores of alumina particles for simulation of the adsorption process in a fluidized bed reactor using the two-phase model.

Although an important effort has been made to improve the knowledge of the behavior of fluidized beds, most papers investigating multi-stage fluidized beds have focused on chemical reactions with constant rates at a given temperature along the bed (zero-order kinetics) (Mohanty et al., 2009, Mohanty and Meikap, 2011). However, concentration-dependent kinetics in the adsorption processes could add to the complexity of the model since the concentration variation along the bed is influenced by the residence time of the adsorbent.

The objective of this study is to model the operation of a multistage countercurrent fluidized bed adsorber taking into consideration the residence time distribution of the adsorbent particles, as well as adsorption kinetics. The particulate phase was modeled in both perfectly-mixed and plug flow regimes. The Equilibrium model was also applied to show the deviation of the system from

equilibrium. The validity of the models was verified by comparing simulations with experimental data for adsorption of 1,2,4-trimethylbenzene (TMB) on beaded activated carbon (BAC).

3.4. Experimental setup

The multistage fluidized bed adsorber used in this study is schematically shown in Figure 3-1. The adsorber is comprised of 6 plexiglass cylindrical compartments (10.4 cm height and 7.6 cm inner diameter) separated by perforated trays which allow the passage of air but not the passage of solid particles. The solid particles are fed at the top of the adsorber using a volumetric feeder (Schenck AccuRate) connected to a speed controller. The volumetric feeder was calibrated before the experiments. There is a protruding downcomer (4 mm) on each stage which allows for solid transfer to the stage below while maintaining the desired amount of solid on each stage. The continuous transport of solid particles to stages below occurs by gravity. The stream of air can easily pass through the perforated trays over the cross-sectional area of the bed and does not prevent particle transport through the downcomers.

The adsorbate gas stream was generated using a syringe pump (Chemyx Inc, Nexus 6000) which injected TMB into a stream of dry compressed air. The flow of the compressed air was set using a mass flow controller (Alicat Scientific). There was an air distributor compartment at the bottom to ensure uniform distribution of air in the inlet, and ports for sampling adsorbent particles and gas concentration along the adsorber. The sampling ports were connected to a flame-ionization detector (FID, Baseline Mocon, Series 9000) and controlled by solenoid valves. The inlet TMB concentration was stabilized before the experiments started. All adsorption experiments were duplicated and carried out at constant temperature (21°C). Table 3-1 summarizes the main characteristics of the system modeled.

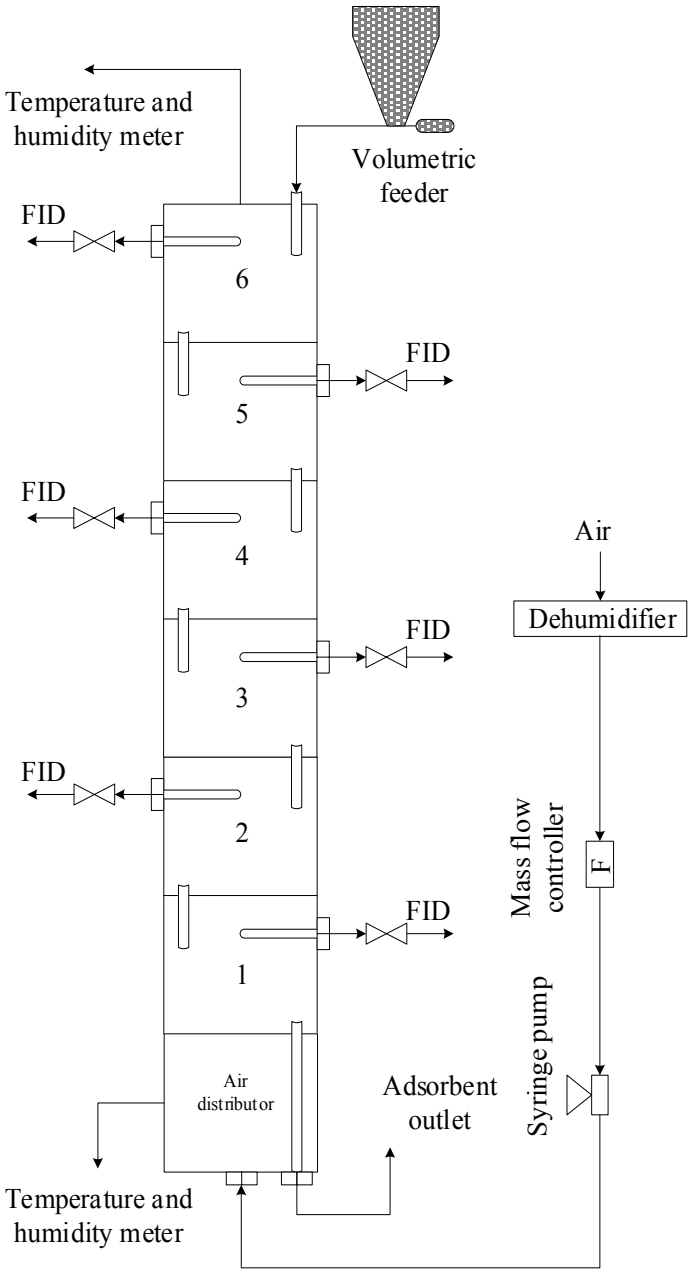

Figure 3-1. Schematic diagram of the fluidized bed adsorber set-up.

Table 3-1. System properties.

Parameter	Value	Unit	Source
Adsorber cross-section area, A	4.56×10^{-3}	m^2	measured
Adsorbent mean diameter, d_p	7.5×10^{-4}	m	(Tefera et al., 2014)
Adsorbent apparent density, ρ_p	601	kg m^{-3}	(Tefera et al., 2014)
Adsorbent mean diameter of pores, d_{pore}	1.9×10^{-9}	m	measured
Adsorbent internal porosity, ε_p	0.56	-	(Tefera et al., 2014)
Adsorbent shape factor, ϕ	1	-	measured
Temperature, T	294	K	measured
TMB molecular weight, M	120.19	g mol^{-1}	(Tefera et al., 2014)
TMB diffusivity in air, D_g	6.45×10^{-6}	m^2 s^{-1}	(Tang et al., 2014)
Air density, ρ_g	1.20	kg m^{-3}	(Keenan et al., 1983)
Air viscosity, μ_g	1.82×10^{-5}	kg m^{-1} s^{-1}	(Keenan et al., 1983)

The proposed models were validated using experimental data reported by Kamravaei et al. (Kamravaei, 2015, Kamravaei, 2016). To evaluate the models in a broader range of parameters, some experiments were carried out at high air flow rates with the same set-up, procedures, and characterization instruments. This was done to understand the limits of the models. In these experiments, the injection rate of TMB was kept constant while the air flow rate was increased. The TMB injection rate was calculated based on the ideal gas law, using the density and molecular weight of TMB (876 kg/m^3 and 120.19 g/mol, respectively). The design and operating parameters used to verify the models are summarized in Table 3-2.

Table 3-2. Experimental parameters for adsorption of TMB on BAC in the fluidized bed.

Changing parameter	Exp. no.	BAC feed rate, F_p (g min^{-1})	Gas flow rate, F_g (SLPM)	Weir height, H (mm)	Initial Conc, C_0 (ppm$_v$)	TMB Injection rate (μL min^{-1})
Adsorbent feed rate	1*	0.44	300	4	100	168
	2	1.40	300	4	100	168
	3	2.30	300	4	100	168
	4	3.30	300	4	100	168
Air flow rate	5	0.44	200	4	100	112
	6	0.44	250	4	100	140
	7	0.44	300	4	100	168
	8	0.44	350	4	100	196
Initial concentration	9	0.44	300	4	50.0	84.1
	10	0.44	300	4	100	168
	11	0.44	300	4	150	252
	12	0.44	300	4	200	336
	13	0.44	300	4	300	504
Air flow rate and initial concentration**	14	0.44	200	4	150	168
	15	0.44	250	4	120	168
	16	0.44	300	4	100	168
	17	0.44	350	4	85.7	168
	18	0.44	400	4	75.0	168
	19	0.44	450	4	66.7	168
Weir height	20	0.44	300	2	100	168
	21	0.44	300	4	100	168

22	0.44	300	6	100	168
23	0.44	300	8	100	168

* Reference case.

** TMB injection rate is kept constant.

3.5. Mathematical model

3.5.1. Equilibrium model

Assuming each stage of the fluidized bed as a theoretical plate on which the solids are in equilibrium with leaving gas, the mass balance on the i^{th} stage could be stated as:

$$F_p\left(q_i^* - q_{i-1}^*\right) = F_g\left(C_{i+1}^* - C_i^*\right) \tag{3-1}$$

where q^* and C^* are equilibrium concentration of TMB on BAC and in air, respectively, and F_p and F_g are adsorbent feed rate and air flow rate, respectively (Kunii and Levenspiel, 1969, Hymore and Laguerie, 1984).

The adsorption isotherm of TMB on BAC at 21ºC was measured (Amdebrhan, 2018) and the results were fitted with the Langmuir model (Figure 3-2). The linear form of Langmuir isotherm is written as:

$$\frac{1}{q^*} = \frac{1}{q_m} + \frac{1}{bq_m C^*} \tag{3-2}$$

where q_m and b are the adsorbent maximum equilibrium capacity and the Langmuir affinity coefficient, respectively. The isotherm parameters were determined by fitting the experimentally measured isotherm with the Langmuir model (Figure 3-2 (b)).

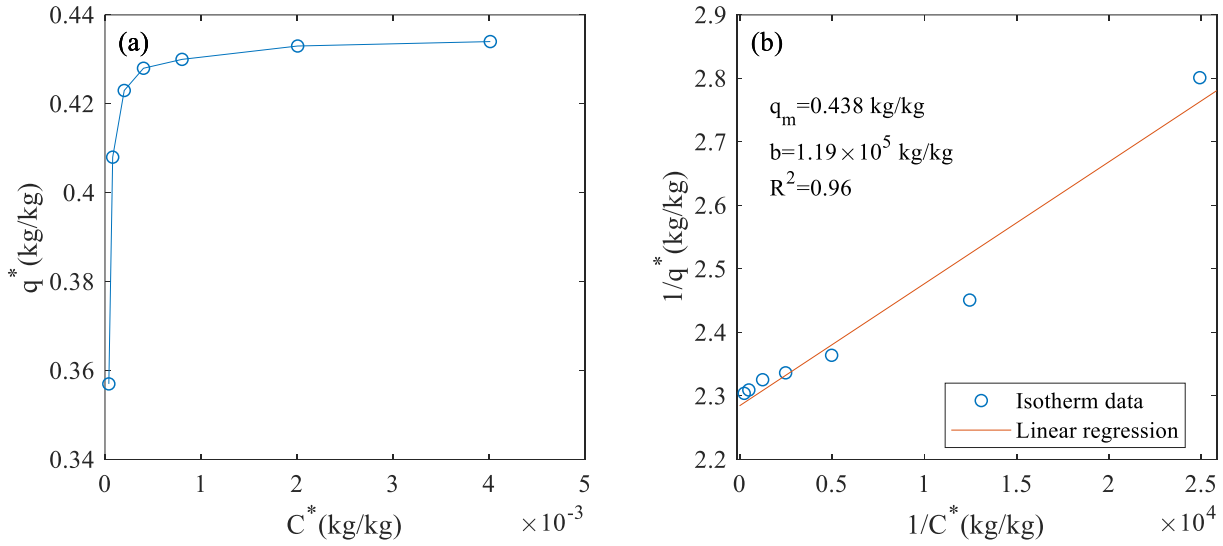

Figure 3-2. (a) Adsorption isotherm and (b) Langmuir fitting for adsorption of TMB on BAC (Amdebrhan, 2018).

Finally, the removal efficiency (RE) was calculated according to the following equation:

$$\mathrm{RE}(\%) = \frac{C_0 - C_i^*}{C_0} \times 100 \tag{3-3}$$

where C_0 is TMB concentration in the inlet gas stream.

3.5.2. Two-phase model

The two-phase model was first introduced by Toomey and Johnstone (Toomey and Johnstone, 1952). Their model considered heterogeneous reactions in an emulsion phase undergoing perfect mixing in the minimum fluidization condition, and a gas bubble phase in plug flow. Other researchers further developed the model for different conditions (Davidson and Harrison, 1963, Hymore and Laguerie, 1984).

3.5.2.1. Assumptions

The following assumptions were made while developing the two-phase model:

1. The fluidized bed adsorber is divided into two phases: an emulsion or particulate phase (a dense suspension of particles in air) and a bubble phase without particles.
2. The gas flow rate in the particulate phase is equal to that required for minimum fluidization and the gas in excess of that passes through the bed in the form of bubbles.
3. As bubbles rise in the bed, they exchange gas with the particulate phase. The interphase mass transfer is the result of diffusion and bulk flow of the gas.
4. While the bubble phase is assumed to be in plug flow regime, the gas in the emulsion phase could be in either perfectly mixed (EGPM) or in plug flow (EGPF) regime. This assumption results in two distinct models demonstrated in Figure 3-3.

Additional assumptions:

1. Temperature is constant during the experiments.
2. Solid particles are spherical and well-mixed on each stage due to the fluidization.
3. Bubbles are spherical and of constant size.
4. All stages are identical and fluidized under the same condition.
5. The radial concentration gradients are negligible in both particulate and bubble phases.

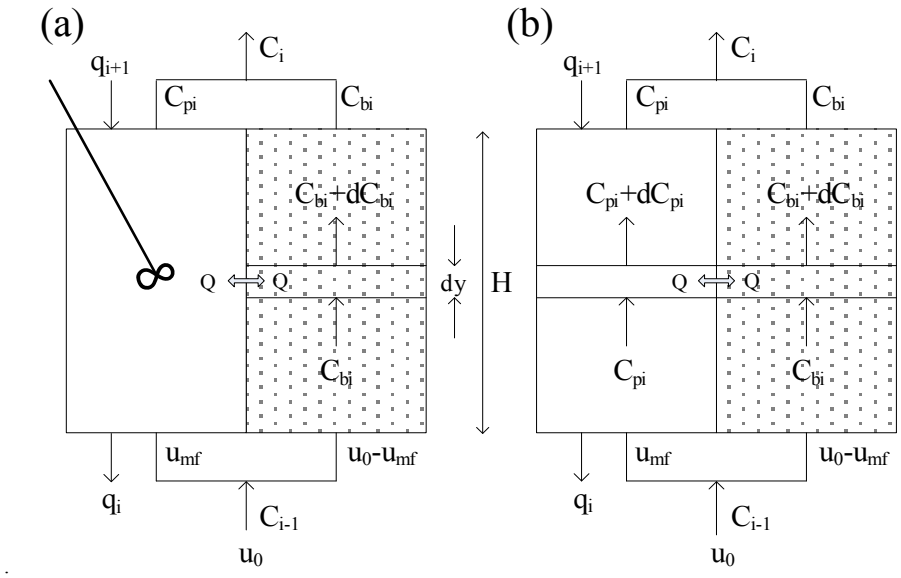

Figure 3-3. Schematic diagram of (a) EGPM and (b) EGPF (adopted from (Hymore and Laguerie, 1984)).

3.5.2.2. Mass balance for TMB at the exit

Writing the mass balance of TMB at the top of the bed results in:

$$u_0 C_i = \left(u_0 - u_{mf}\right) C_{bi}\Big|_{y=H} + u_{mf} C_{pi} \tag{3-4}$$

Rearranging the equation, the concentration of TMB leaving the i^{th} stage is given by the following equation:

$$C_i = \beta C_{bi}\Big|_{y=H} + (1-\beta) C_{pi} \tag{3-5}$$

where β is the fraction of gas flowing as bubbles:

$$\beta = 1 - \frac{u_{mf}}{u_0} \tag{3-6}$$

3.5.2.3. Mass balance for gas in the bubble phase

The equation below is obtained by writing a material balance on a single rising bubble:

$$Q\left(C_{pi} - C_{bi}\right) = u_b V_b \frac{dC_{bi}}{dy} \tag{3-7}$$

where Q is the interphase mass transfer flow rate, u_b is bubble rise velocity, V_b is bubble volume, and C_{pi} and C_{bi} are TMB concentrations in particulate and bubble phases, respectively.

Integration of Eq. (3-7) with respect to y, using the boundary condition $C_{bi}=C_{i-1}$ at $y=0$, results in:

$$C_{bi}(y) = C_{pi} + \left(C_{i-1} - C_{pi}\right) exp\left(\frac{-Qy}{u_b V_b}\right) \tag{3-8}$$

3.5.2.4. Mass balance for gas perfectly mixed in the particulate phase

Regarding the adsorbate in the particulate phase, the following is taken into account to develop the mass balance:

1- The adsorbate entering at the bottom and leaving at the top with flow rates $u_{mf} A \rho_g C_{i-1}$ and $u_{mf} A \rho_g C_{pi}$, respectively.

2- The adsorbate entering the particulate phase from bubbles and leaving the particulate phase to bubbles with flow rates $N_b Q A \rho_g \int_0^H C_{bi} dy$ and $N_b Q A \rho_g C_{pi} H$, respectively; where N_b is the number of bubbles per unit volume of bed.

3- The adsorbate consumed in the adsorption process with flow rate $W k_i \left(q_i^* - \bar{q}_i \right)$; where W is the mass of solids on each stage, k is the adsorption rate constant, $\bar{q}_i$ is the average TMB content of the particles on the i^{th} stage, and q_i^* is that in equilibrium with C_{pi}. To simplify the mathematical calculations, it is assumed that the adsorption isotherm is linear in the range of (q_i^*, $\bar{q}_i$). Hence, $k_i \left(q_i^* - \bar{q}_i \right) = m_i k_i \left(C_{pi} - \bar{C}_{pi}^* \right)$, where m_i is the local slope of the isotherm in the range of (q_i^*, $\bar{q}_i$) (Hymore and Laguerie, 1984, Arnaldos and Casal, 1987).

Writing the material balance using the terms above yields:

$$N_b V_b u_b \left(C_{i-1} - C_{pi} \right) \left[1 - \exp\left(\frac{-QH}{u_b V_b} \right) \right] + u_{mf} \left(C_{i-1} - C_{pi} \right) = \left(\frac{W m_i k_i}{A \rho_g} \right) \left(C_{pi} - \bar{C}_{pi}^* \right) \tag{3-9}$$

Solving Eq. (3-9) for C_{pi} will result in the following equation:

$$C_{pi} = \bar{C}_{pi}^* + \left(C_{i-1} - \bar{C}_{pi}^* \right) \left(\frac{1 - \beta \exp(-X)}{1 - \beta \exp(-X) + k_i'} \right) \tag{3-10}$$

where

$$X = \frac{QH}{u_b V_b} \tag{3-11}$$

$$k_i' = \frac{Wm_i k_i}{A\rho_g u_0} \tag{3-12}$$

where H is the weir height, m is the slope of the isotherm, k is adsorption rate constant, A is the cross-section area of the bed, ρ_g is the air density, and u_0 is the superficial air velocity.

3.5.2.5. Mass balance for gas in plug flow in the particulate phase

Considering a material balance on an infinitesimal height "*dy*" in the particulate phase, we will have:

$$u_{mf}\frac{dC_{pi}}{dy} + \left(u_0 - u_{mf}\right)\frac{dC_{bi}}{dy} + \frac{Wmk}{A\rho_g H}\left(C_{pi} - \bar{C}_{pi}^*\right) = 0 \tag{3-13}$$

$$\left(1-\beta\right)\frac{dC_{pi}}{dy} + \beta\frac{dC_{bi}}{dy} + \frac{k_i'}{H}\left(C_{pi} - \bar{C}_{pi}^*\right) = 0 \tag{3-14}$$

$$H^2\left(1-\beta\right)\frac{d^2C_{bi}}{dy^2} + H\left(X + k'\right)\frac{dC_{bi}}{dy} + k_i' X C_{bi} = k_i' X \bar{C}_{pi}^* \tag{3-15}$$

Solving Eq. (3-15) with boundary conditions $\frac{dC_b}{dy} = 0$ at $y = 0$ and $C_b = C_0$ at $y = 0$ results in Eqs. (3-16) and (3-17).

$$C_{bi} = \frac{C_{i-1} - \bar{C}_{pi}^*}{m_{1i} - m_{2i}}\left(m_{1i}\exp\left(-m_{2i}y\right) - m_{2i}\exp\left(-m_{1i}y\right)\right) + \bar{C}_{pi}^* \tag{3-16}$$

$$C_{pi} = \frac{C_{i-1} - \bar{C}_{pi}^*}{m_{1i} - m_{2i}}\left[m_{1i}\left(1 - \frac{H}{X}m_{2i}\right)\exp\left(-m_{2i}H\right) - m_{2i}\left(1 - \frac{H}{X}m_{1i}\right)\exp\left(-m_{1i}H\right)\right] + \bar{C}_{pi}^* \tag{3-17}$$

where,

$$m_{1i} = \frac{1}{2}\frac{X + k_i'}{H\left(1-\beta\right)} - \frac{1}{2}\left[\left(\frac{X + k_i'}{H\left(1-\beta\right)}\right)^2 - \left(\frac{4k_i'X}{H^2\left(1-\beta\right)}\right)\right]^{\frac{1}{2}} \tag{3-18}$$

$$m_{2i} = \frac{1}{2}\frac{X + k_i'}{H\left(1-\beta\right)} + \frac{1}{2}\left[\left(\frac{X + k_i'}{H\left(1-\beta\right)}\right)^2 - \left(\frac{4k_i'X}{H^2\left(1-\beta\right)}\right)\right]^{\frac{1}{2}} \tag{3-19}$$

It should be noted that when considering plug flow for gas in the particulate phase, the concentration of TMB in the particulate phase varies along the bed, and therefore, an average concentration should be calculated according to Eq. (3-20):

$$\bar{C}_{pi} = \frac{1}{H}\int_0^H C_{pi}dy \tag{3-20}$$

3.5.2.6. Mass balance for solids

Adsorbent particles are assumed to be perfectly mixed on each stage and their residence time distribution (RTD) can be described by the RDT function of a continuous stirred tank reactor (CSTR) (Levenspiel, 1972):

$$E_i\left(t\right) = \frac{1}{\tau}\exp\left(-\frac{t}{\tau}\right) \tag{3-21}$$

The fraction of solids with residence times $t_1, t_2, ..., t_i$ on the first, second and i^{th} stage are equal to (Hymore and Laguerie, 1984):

$$E_i\left(t_1,t_2,...,t_i\right)=\frac{1}{\tau}\exp\left(-\frac{1}{\tau}\sum_{j=1}^{i}t_j\right) \tag{3-22}$$

where τ is the mean residence time of solids on each stage and can be calculated using the following equation:

$$\tau=\frac{W}{F_p} \tag{3-23}$$

The rate of increase in TMB concentration for this fraction of particles is given by:

$$\frac{dq_i}{dt}=k_i\left(q_i^*-q_i\right) \tag{3-24}$$

After integrating Eq. (3-24), q_i can be calculated by:

$$q_i=q_i^*-\left(q_i^*-q_{i0}\right)\exp\left(-k_it_i\right) \tag{3-25}$$

where q_{i0} is the TMB content of the particle when entering the i^{th} stage:

$$q_{i0}=q_{i-1}\left(t_1,t_2,...,t_{i-1}\right) \tag{3-26}$$

Substituting Eq. (3-26) into Eq. (3-25) will result in:

$$q_i=q_{i-1}\exp\left(-k_it_i\right)+q_i^*\left[1-\exp\left(-k_it_i\right)\right] \tag{3-27}$$

Eq. (3-27) can be written as a mathematical series:

$$q_i=q_0\exp\left(-\sum_{j=1}^{i}k_jt_j\right)+\sum_{j=1}^{i}\left\{q_i^*\left[1-\exp\left(-k_jt_j\right)\right]\exp\left(-\sum_{k=j+1}^{i}k_kt_k\right)\right\} \tag{3-28}$$

The average TMB content of particles leaving the i^{th} stage can be calculated by:

$$\bar{q}_i = \int_{\tau_1=0}^{\infty} \int_{\tau_2=0}^{\infty} \ldots \int_{\tau_i=0}^{\infty} q_i E_i\left(t_1, t_2, \ldots, t_i\right) \mathrm{d}t_1 \mathrm{d}t_2 \ldots \mathrm{d}t_i \tag{3-29}$$

After integrating Eq. (3-29), $\bar{q}_i$ can be obtained using the following equation (Hymore and Laguerie, 1984):

$$\bar{q}_i = q_0 \prod_{j=0}^{i} \alpha_j + \sum_{j=1}^{i} q_j^* \left(1-\alpha_j\right) \prod_{k=j+1}^{i} \alpha_k \tag{3-30}$$

where,

$$\alpha_j = \frac{1}{1+k_j \tau} \tag{3-31}$$

Knowing $\bar{q}_i$, it is now possible to calculate $\bar{C}_{pi}^*$ using the adsorption isotherm.

3.5.2.7. Estimation of adsorption rate

Assuming that the overall adsorption rate is described using the Linear Driving Force model:

$$\frac{dq_i}{dt} = k_i\left(q_i^* - q_i\right) = k_i m_i \left(C_i - C_i^*\right) \tag{3-32}$$

For the adsorption of TMB on BAC, the following steps are considered:

1. Transfer of TMB from bulk gas flow to the external surface of adsorbent (external diffusion).
2. Transfer of TMB from the external surface into the pores of the adsorbent (internal diffusion).
3. Transfer of TMB from one adsorption site to another (surface diffusion) which is considered a part of the internal diffusion (Seader and Henley, 2006).
4. Adsorption of TMB onto the pore surfaces.

Unlike chemical adsorption which involves valence bond formation, physical adsorption onto the porous surface (#4) is essentially instantaneous since it is only reliant on the collision frequency and orientation of TMB with the porous surface (Seader and Henley, 2006). Thus, only the first three steps need to be considered for modeling rates in this system.

According to Seader and Henley (Seader and Henley, 2006), a suitable relationship for describing the factor *km* in Eq. (3-32) is:

$$\frac{1}{km} = \frac{1}{k_c a_p} + \frac{d_p^2}{60 D_e} \tag{3-33}$$

where k_c is the external mass transfer coefficient, a_p is the external surface area per unit mass of particles, d_p is adsorbent particle diameter, and D_e is the internal mass transfer coefficient.

The external mass transfer coefficient could be described by Eqs. (3-34)-(3-38) (Poulopoulos and Inglezakis, 2006):

$$k_c = \frac{D_g \mathrm{Sh}}{d_p} \tag{3-34}$$

$$\mathrm{Sh} = \frac{0.7}{\varepsilon_{mf}} \mathrm{Re}\,\mathrm{Sc}^{\frac{1}{3}} \text{ when } 0.22<\mathrm{Re}<1 \tag{3-35}$$

$$\mathrm{Sh} = \frac{0.86}{\varepsilon_{mf}} \mathrm{Re}^{\frac{1}{2}}\,\mathrm{Sc}^{\frac{1}{3}} \text{ when } 5<\mathrm{Re}<10 \tag{3-36}$$

$$\mathrm{Re} = \frac{d_p \rho_g u_{mf}}{\mu_g} \tag{3-37}$$

$$\mathrm{Sc} = \frac{\mu_g}{\rho_g D_g} \tag{3-38}$$

The internal mass transfer coefficient accounts for diffusion of adsorbate in air (D_g), Knudsen diffusion (D_k), as well as surface diffusion (D_s), given by the following equations (Seader and Henley, 2006):

$$D_e = \frac{\varepsilon_p}{\tau'}\left[\left(\frac{1}{\frac{1}{D_g}+\frac{1}{D_k}}\right)+D_s\frac{\rho_p m}{\varepsilon_p}\right] \tag{3-39}$$

$$D_k = 48.5 d_{pore}\left(\frac{T}{M}\right)^{0.5} \tag{3-40}$$

$$D_s = 1.6\times10^{-6}\exp\left(\frac{-0.45(-\Delta H_{ads})}{2RT}\right) \tag{3-41}$$

The heat of adsorption, ΔH_{ads}, is calculated using the model previously developed for adsorption of VOC onto activated carbon (Giraudet et al., 2006):

$$-\Delta H_{ads} = 103.2 + 1.16\alpha' + 0.76\Delta H_{vap} - 3.87IP - 0.7\gamma - 26.19 r_{mic} \tag{3-42}$$

where ΔH_{ads} is the heat of adsorption, α' is polarizability, ΔH_{vap} is the heat of vaporization, γ is surface tension, IP is ionization potential, and r_{mic} is the adsorbent mean micropore width.

Equations (3-5), (3-8) and (3-10) for EGPM model and equations (3-5), (3-16) and (3-17) for EGPF model could be solved to calculate TMB concentration leaving the i^{th} stage. Table 3-3 lists formulas used for calculating the remaining model parameters.

Table 3-3. Correlations used in the calculations of two-phase models.

Parameter	Formula	Reference
Mean bubble diameter, d_b	$d_b = 0.21(u_0 - u_{mf})^{0.42} H^{0.8} \times \exp\left(-0.25(u_0 - u_{mf})^2 - 0.1(u_0 - u_{mf})\right)$	(Cai et al., 1994)
Bubble rise velocity, u_b	$u_b = u_0 - u_{mf} + 0.711(gd_b)^{\frac{1}{2}}$	(Kunii and Levenspiel, 1969)
Interphase mass transfer, Q	$Q = \left(\frac{1}{3}u_{mf} + \left(\frac{4\varepsilon_{mf} D_g u_b}{\pi d_b}\right)^{\frac{1}{2}}\right) \times \pi d_b^2$	(Hatzantonis et al., 2000, Poulopoulos and Inglezakis, 2006)
Minimum fluidization velocity, u_{mf}	$\frac{1.75}{\phi\varepsilon_{mf}^3}\mathrm{Re}_{mf}^2 + \frac{150(1-\varepsilon_{mf})}{\phi^2\varepsilon_{mf}^3}\mathrm{Re}_{mf} - \mathrm{Ar} = 0$ $\mathrm{Re}_{mf} = \frac{\rho_g d_p u_{mf}}{\mu_g}$ $\mathrm{Ar} = \frac{\rho_g(\rho_p - \rho_g) g d_p^3}{\mu_g^2}$	(Abasaeed and Al-Zahrani, 1998)
Bed voidage at minimum fluidization, ε_{mf}	$\varepsilon_{mf} = \frac{1}{6}(6 - \pi) = 0.472$	(Davidson and Harrison, 1963)
Mass of adsorbent on each stage, W	$W = \rho_p H_{mf} A(1 - \varepsilon_{mf})$	(Hymore and Laguerie, 1984)
Bed height at minimum fluidization, H_{mf}	$H_{mf} = H\left(1 - \frac{u_0 - u_{mf}}{u_b}\right)$	(Hymore and Laguerie, 1984)
Bubble volume, V_b	$V_b = \frac{\pi d_b^3}{6}$	(Hymore and Laguerie, 1984)
Number of bubbles per unit bed volume, N_b	$N_b = \frac{u_0 - u_{mf}}{u_b V_b}$	(Hymore and Laguerie, 1984)
External specific surface area per unit of volume, a_p	$a_p = \frac{6}{d_p}$	(Seader and Henley, 2006)
Tortuosity, τ	$\tau' = 1 - \frac{1}{2}\ln\varepsilon_p$	(Poulopoulos and Inglezakis, 2006)

3.6. Results and discussion

A computer program was developed in Matlab R2018b to solve the equations. The following results were obtained and compared with experiments.

3.6.1. Effect of design and operating parameters on overall removal efficiency

Figure 3-4 compares the experimental overall removal efficiencies to ones calculated using the Equilibrium and two-phase models at different adsorbate feed rates, air flow rates, initial concentrations, and weir heights.

The Equilibrium model overestimates the removal efficiencies, except in 3 sets of experiments conducted at high TMB initial concentrations (exp. no. 11-13 in Table 3-2). As mentioned before, the Equilibrium model considers each stage of the fluidized bed as an ideal plate where the gas stream leaving the stage is in equilibrium with the adsorbent (Kunii and Levenspiel, 1969). This assumption is not always valid since the operating parameters might not provide the condition of equilibrium. For most conditions used in this study, the Equilibrium model fails to have a good prediction because:

1. The presence of the bubble phase and therefore the possibility of gas bypass and particulate-bubble mass transfer are neglected.
2. The influence of in-phase mass transfer is neglected.
3. The recirculation of solid particles, which introduces a residence time distribution within a stage, is not taken into account.

Hymore and Laguerie (Hymore and Laguerie, 1984) defined plate efficiency as a scale to evaluate how far from the equilibrium each stage of a fluidized bed is working, with 0% indicating no adsorption and 100% representing the equilibrium condition on the plate. They stated that while

the assumption of the infinitely-rapid rate of adsorption in the Equilibrium model creates 100% plate efficiency, the real efficiencies of plates in the adsorption of water vapor on alumina particles lie within the range of 25% to 75%.

When the adsorbent feed rate is low and TMB concentration is high (experiment no. 11-13) the equilibrium condition is reached (Figure 3-4 (c)). It should be noted that the TMB concentration is not the only factor that can determine if the system with a given adsorbent feed rate is operating close to the equilibrium condition. The air flow rate is also an important factor affecting the fluidization regime and thereby mass and heat transfers in a fluidized bed.

The experiments conducted at different air flow rate while maintaining the injection rate constant (no. 14-19) show that the removal efficiency decreases as air flow rate increases and this reduction is more significant at air flow rates higher than 300 SLPM. This is because high fluidization increases the chance of solids falling down the downcomers, and therefore, at any time, there would be less amount of adsorbent on stages leading to decreased overall removal efficiencies.

The two-phase models, on the other hand, show good agreement with experimental data in most cases. A better demonstration of the deviation of predicted results from experimental data for each model is presented in Figure S1 in Supplementary Information. Except at very high air flow rates (F_g=350-450 SLPM), both EGPM and EGPF models could successfully predict the changes in overall removal efficiency with similar accuracy, suggesting relatively robust behavior of both models with respect to parameter changes under these conditions.

However, at air flow rates higher than 350 SLPM, the discrepancy between the two-phase models and the experimental data increases. A possible explanation is that the two-phase assumption in the model is met only when the operating velocity is 3-8 times the minimum

fluidization velocity (Mohanty et al., 2009, Mohanty and Meikap, 2011). At higher values of the u_0/u_{mf}, a third phase called "cloud and wake" arises (Missen et al., 1999, Philippsen et al., 2015) where the gas recirculates and penetrates slightly into the particulate phase to form a transitional cloud region around the bubble (Philippsen et al., 2015). In experiments no. 18 and 19, the ratio of u_0/u_{mf} is 7.5 and 8.4, respectively, thus the large deviation from experimental data may be due to the violation of the first assumption of the two-phase model.

To overcome this drawback of the two-phase model at high superficial velocity, Kunii and Levenspiel (Kunii and Levenspiel, 1969) presented a three-phase model accounting for the cloud/wake region. However, industrial fluidized-bed adsorbers usually operate at superficial gas velocities 3-6 times the minimum fluidization velocity and the two-phase model is effective in most practical applications (McAuley et al., 1994). Moreover, the three-phase model includes a greater number of empirical parameters which could increase the estimation error, potentially without providing a significant advantage over the two-phase model in these applications (Harshe et al., 2004).

Excluding the data from experiments no. 18 and 19, which may involve three-phase flow, the correlation coefficients of EGPM and EGPF models for predicting the overall removal efficiencies are R^2=0.95 and 0.93, respectively.

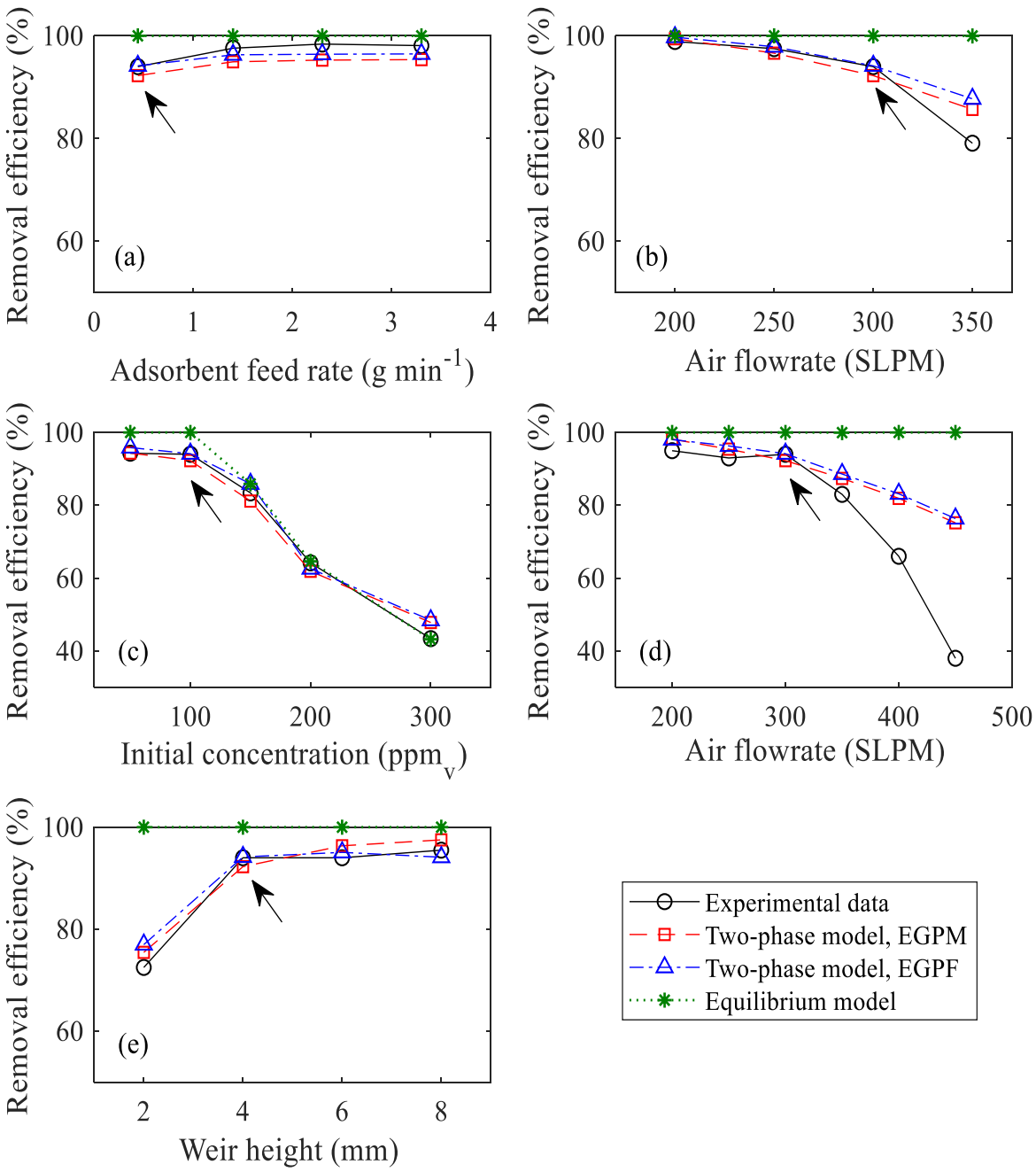

Figure 3-4. Experimental and predicted removal efficiencies (RE) as a function of (a) adsorbent feed rate (exp. no. 1-4), (b) gas flow rate (exp. no. 5-8), (c) initial concentration (exp. no. 9-13), (d) gas flow rate (exp. no. 14-19), and (e) weir height (exp. no. 20-23). Arrows in the figure indicate the reference case.

3.6.2. Effect of design and operating parameters on stage-wise concentration

The stage-wise comparison of TMB concentration between experimental data and the predicted results using EGPM and EGPF models are depicted in Figure 3-5, and in Table S2 in Supplementary Information. In general, there is good agreement between experimental and predicted stage-wise concentrations where the operating parameters are well within the acceptable range of the two-phase model (i.e. all cases except experiments no. 18 and 19). The failure of the two-phase model in predicting the concentration along the bed when the air flow rates are high can be seen in experiments no. 18 and 19. As stated before, this deviation may be due to the violation of the basic two-phase assumption in these models. In some other cases such as 13, 17, and 23, there is a larger discrepancy in the middle stages even though there is good agreement between the measured and predicted concentrations at the last stage of the bed (i.e., giving the overall removal efficiency). This deviation from experimental results might be due to model error and/or experimental error.

Model error is mainly due to the simplifying assumptions in both governing equations and empirical parameters. The existence of two phases only, neglecting radial concentration gradients, constant bubble diameter along the bed, and linear adsorption isotherm in the range of q_i^* and $\overline{q}_i$ are a few examples of the assumptions made in developing the model. As for the experimental error, the ingress of the fluidized adsorbent particles into the inlet fitting of the gas sampling line can bias the measured concentrations. Although a mesh was placed at the inlet fitting of the sampling line, a single adsorbent particle being stuck on the mesh might cause an error in measured concentrations.

For both the EGPM and EGPF models, several experiments exhibit TMB concentrations that are not reduced from the inlet levels in the lower (air inlet) adsorber stages, e.g. cases with low adsorbent feed rate and high TMB concentration (experiments no. 11-13). In these cases, the adsorbents in the lower stages are saturated and the equilibrium condition is reached. These results are consistent with those of the Equilibrium model.

Two other cases with BAC saturation are the ones with a high air flow rate (experiment 19) and a high weir height (experiment 23). As mentioned before, in experiment 19, the amount of adsorbent on each stage is very low due to the high fluidization. Such a low amount of adsorbent in the bottom stage (which is partially filled) could not really contribute to TMB removal. The BAC saturation in the bottom stage for experiment 23 is most likely due to experimental/measurement error.

By comparing EGPM and EGPF models, it is seen that the general trends of both models are quite similar except in experiment no. 23 where the weir height is at its highest value, 8 mm. In that case, the experimental results are somewhat better fit by the EGPF model than the EGPM model, but both tend to underestimate the actual concentrations in most stages. An increase in the ratio of effective bed height to bed diameter in a bubbling bed could lead to a plug flow regime for gas in the particulate phase (Kunii and Levenspiel, 1969, Lu et al., 2004). High u_0/u_{mf} in our system, on the other hand, could raise the possibility of gas reverse flow in the particulate phase leading to the fluidized bed approaching a perfectly-mixed regime (Kunii and Levenspiel, 1969, Lu et al., 2004). The increase in bed height by increasing the weir height to 8 mm results in a proportional increase in overall effective bed height (the sum of the adsorbent layer thickness on each stage). Consequently, the gas in the particulate phase may approach the plug flow regime.

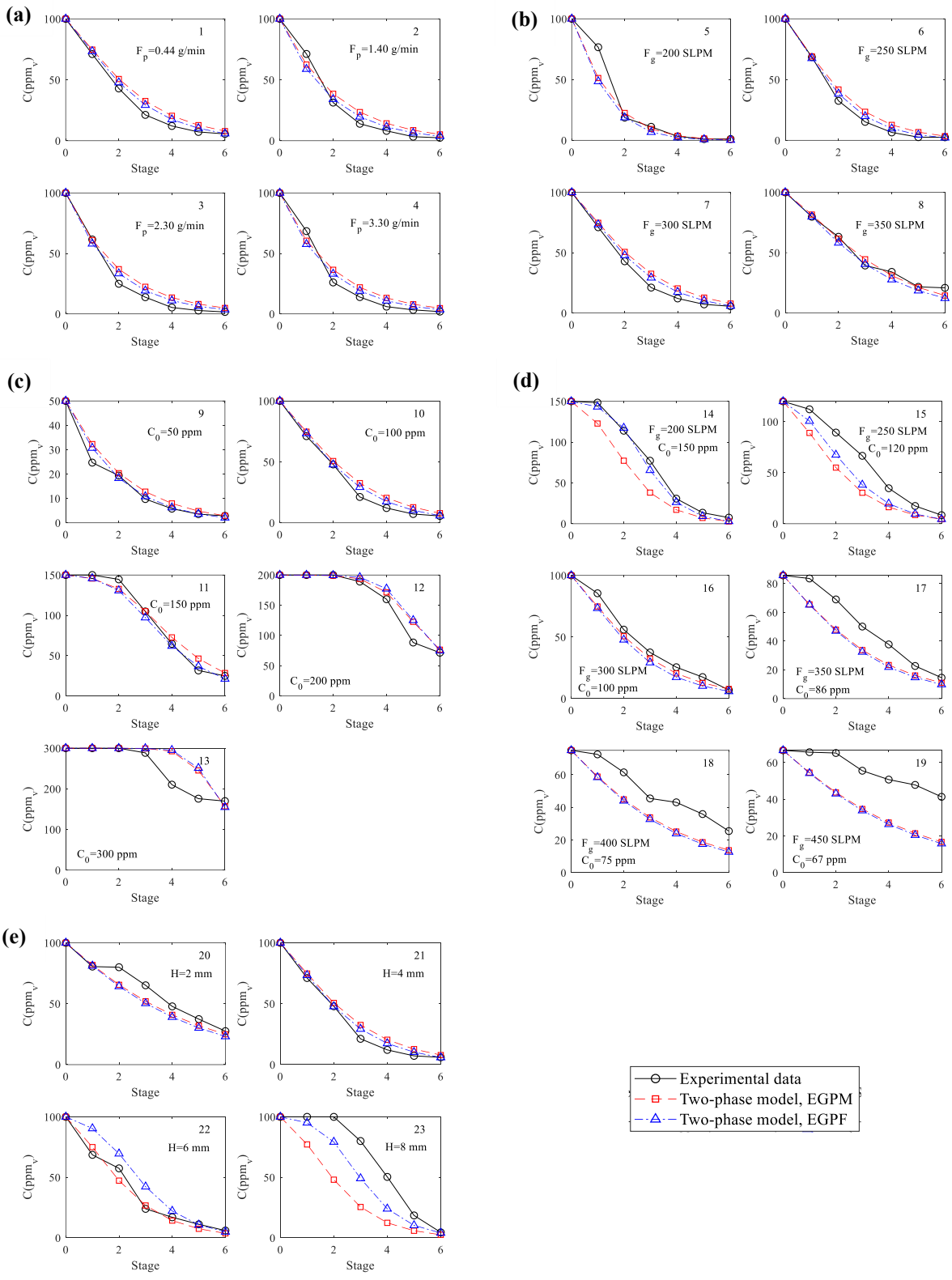

Figure 3-5. Stage-wise comparison of experimental vs. EGPM and EGPF prediction of TMB concentration in the fluidized bed in varying (a) adsorbent feed rate, (b) air flow rate, (c) initial

concentration, (d) air flow rate, and initial concentration, and (e) weir height. The experiment number from Table 3-2 is shown on the top-right side of each diagram. Reference scenario is F_p=0.44 g min-1, F_g=300 SLPM, H=4 mm, and C_0=100 ppm_v. Concentration at stage 0 denotes the inlet concentration.

3.6.3. Sensitivity analysis

Adsorption in a fluidized bed is very sensitive to changes in design, operation and kinetic parameters. Hence, having a good understanding of the system's sensitivity to the deviations of different parameters from their nominal values is important in process operation and optimization. It also gives information essential for process scale-up and intensification. The sensitivity of EGPM model to internal mass transfer coefficient, particle diameter, and adsorption capacity is shown in Figure 3-6.

It can be seen in Figure 3-6 (a) that the extent of sensitivity to the internal mass transfer coefficient differs from case to case. The increase in overall removal efficiency by doubling the internal mass transfer coefficient is comparatively lower when the calculated removal efficiency is closer to 100% (e.g. experiments no. 5, 14, 15, 22, and 23) or the condition is closer to equilibrium (experiments no. 11-13). In both cases, the adsorption process is controlled by the low driving force resulting from the low concentration difference between the gas-phase adsorbate and available adsorption sites.

The sensitivity of the model to other mass transfer coefficients (e.g. external mass transfer coefficients, surface diffusion coefficient, and interphase mass transfer flow rate between bubble and particulate phases) is presented in Figure S2 in Supplementary Information. In a nutshell, the results suggest that the internal diffusion is the rate-controlling step in the adsorption process, and the contribution of the surface diffusion to the internal diffusion is negligible. The model is also

sensitive to interphase mass transfer resistance, a parameter greatly affected by superficial velocity and solid particle diameter.

The sensitivity of the model to the adsorbent particle diameter, d_p, for all the experiments is shown in Figure 3-6 (b). Adsorbent diameter is one of the most influential parameters affecting the performance of a fluidized bed because it directly and indirectly affects the minimum fluidization velocity and adsorption rate constant, as well as other parameters. Figure S3 in Supplementary Information shows the interdependence of several parameters of the two-phase model on the particle diameter. The general trend shows that doubling (in most cases) or halving (in a few cases) the adsorbent particle diameter could reduce the overall removal efficiency, suggesting an optimum value for this parameter in each set of experiments.

The reference scenario (experiment no. 1) was chosen for additional sensitivity analysis on adsorbent particle diameter (Figure 3-6 (c)). For the reference condition, the removal efficiency is highest when the diameter of adsorbent particles is ~0.6 mm and declines for greater and smaller sizes.

The effect of the adsorption capacity was investigated by doubling or halving q_m (maximum adsorption capacity) in the Langmuir isotherm while keeping other characteristics of the adsorbent (such as pore diameter) constant for the various cases (Figure 3-6 (d)). In cases 2-4 when adsorbent feed rates are 3.2, 5.2, and 7.5 times the reference scenario, respectively, there is no significant change in removal efficiency by halving or doubling adsorption capacity. In these cases, RE is not limited by adsorption capacity. After halving the adsorption capacity, the adsorbent feed rate is still high enough to compensate for the reduced adsorption capacity. Doubling the adsorption capacity has also little effect on RE since the available adsorption sites are already sufficient.

When close to equilibrium (experiments no. 11-13), however, the removal efficiency is greatly influenced by doubling the adsorption capacity. This is simply because adding adsorption sites provides the driving force necessary for further adsorption which does not exist in equilibrium condition. These results are consistent with those of the Equilibrium model in terms of showing the cases in an equilibrium state. The rest of the experiments (1, 5-10 and 14-23) were conducted at the lowest of these adsorbent feed rates (0.44 g min^{-1}) and with TMB concentrations mostly lower than 150 ppm. In these cases, doubling the adsorption capacity yields a marginal increase in removal efficiencies because, unlike experiments 11-13, these experiments are not limited by the adsorption capacity. However, (unlike experiments 2-4) halving the adsorption capacity markedly reduces the removal efficiency as a result of insufficient adsorption sites.

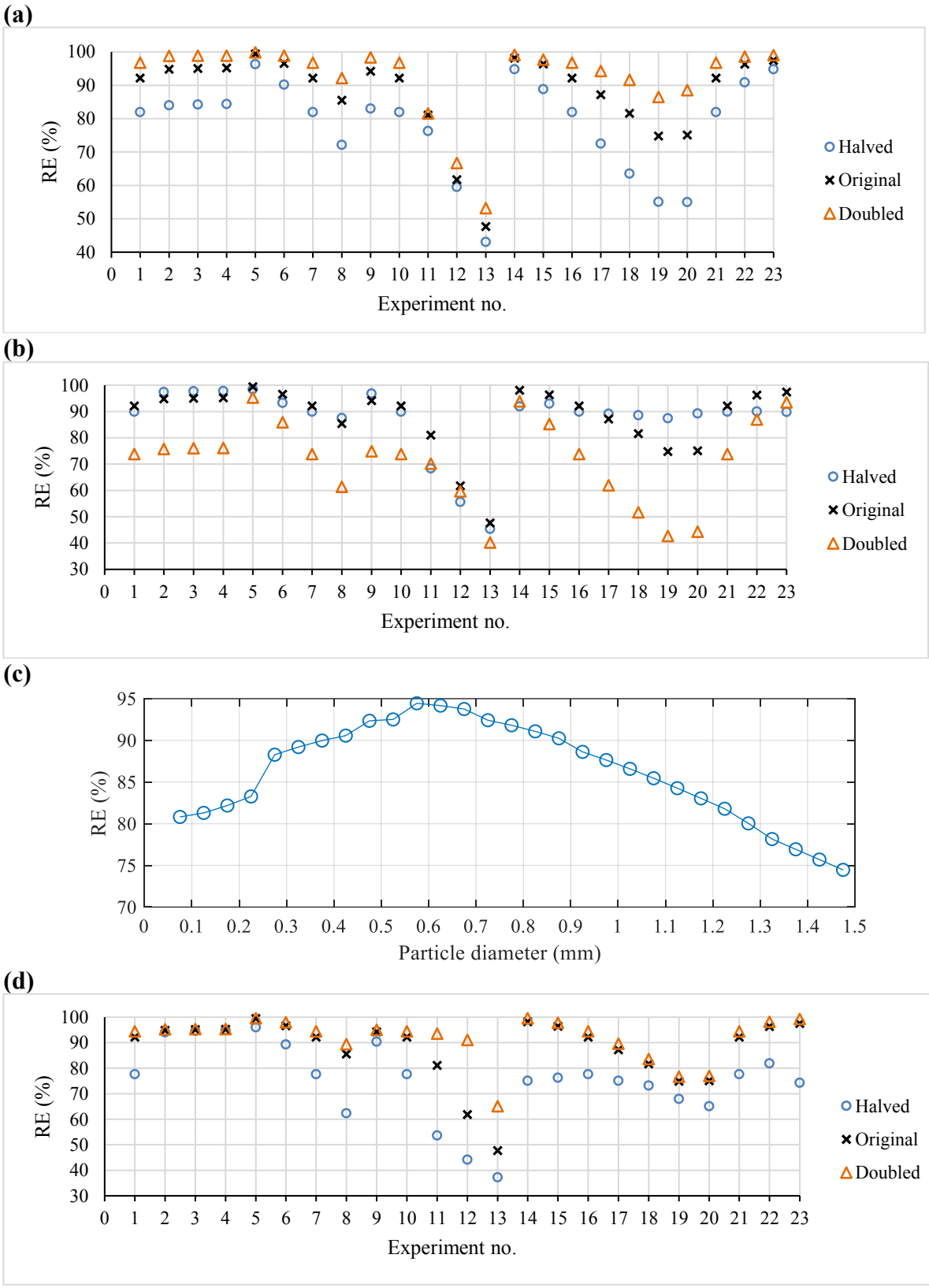

Figure 3-6. The sensitivity of EGPM model to (a) internal diffusion coefficient, (b) particle diameter, (c) particle diameter for the reference condition, and (d) adsorption capacity.

Figure 3-7 illustrates the effect of the number of stages used in the fluidized bed configuration on the overall removal efficiency for the reference scenario. Experimental removal efficiencies for 2-stage, 4-stage, and 6-stage fluidized beds were also measured and presented in Figure 3-7 for comparison. From the experimental results, an increase in the number of stages from 2 to 4 enhances the removal efficiency by 22.8%, while this enhancement after adding 2 more stages (i.e. from 4 to 6) is only 3.4%. The reduction in the increment of the removal efficiency with the increase in the number of stages can be due to slow kinetics and the lack of concentration difference (the driving force) between the adsorbate and the adsorbent sites. Introducing more virgin adsorbent to the bed (i.e. increasing the adsorbent feed rate) and increasing the contact time (reducing the inlet air flow rate) can facilitate reaching high REs when capturing VOCs at low concentrations as depicted in Figure 3-4 (a), (b) and (d).

The model is reasonably sensitive to the number of stages with a more significant change in the removal efficiency at lower numbers of stages. The calculated values are also very close to the experimental values, suggesting good prediction by the model. It is shown that almost 10 stages are predicted to be required for achieving 99% removal efficiency for the reference condition.

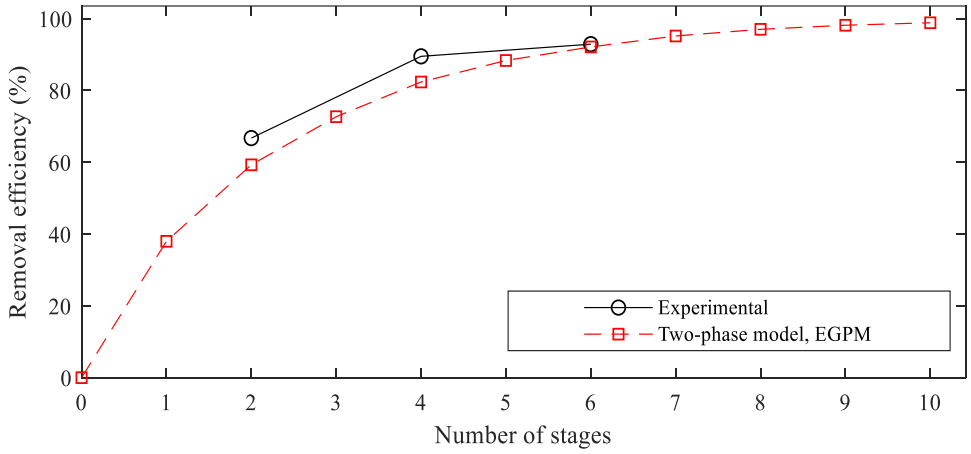

Figure 3-7. Sensitivity of EGPM model to the number of stages for the reference scenario.

3.6.4. Conclusion

A two-phase model was developed and used to predict the removal efficiency for adsorption of TMB on BAC in a multistage countercurrent fluidized bed. Two model variants were considered: perfectly-mixed flow and plug flow for the gas in the emulsion (particulate) phase. The results were compared to experimental data in different design and operating parameters and compared to those of an Equilibrium model. The main conclusions can be summarized as follows:

- The Equilibrium model has a good prediction of the experimental results only when the system is in an equilibrium state. In order to achieve an equilibrium state in an adsorption process with fast kinetics carried out in a countercurrent fluidized bed, the adsorbent feed rate needs to be low and the initial concentration needs to be high.
- EGPM and EGPF models generally matched the experimental data except at very high superficial velocities where the underlying model assumption of two phases is not valid.
- EGPM and EGPF models provided similar accuracy compared to the experimental data, though the assumption of plug flow for gas in the particulate phase (EGPF model) leads to slightly better predictions than the assumption of perfectly-mixed flow (EGPM model) based on stage-wise measurements of removal efficiency.
- Sensitivity analysis demonstrates that the EGPM model is highly sensitive to the internal diffusion and interphase mass transfer coefficients, but is insensitive to the external and surface diffusion coefficients.
- The adsorbent particle diameter is an important parameter in the calculation of removal efficiency using the two-phase model and could be optimized to enhance the removal efficiency for specific operating conditions.
- The impact of adsorption capacity on removal efficiency depends on the number of adsorption sites available and the proximity to the equilibrium state.
- The model can also predict the effect of the number of stages on removal efficiency.

The two-phase models developed in this study accurately simulate the adsorption of TMB on BAC in a lab-scale multistage fluidized bed. These models may provide guidance for the design and operation of fluidized bed adsorbers with different adsorbents and adsorbates as well.

3.7. References

Abasaeed, A.E., Al-Zahrani, S.M., 1998. Modeling of Fluidized Bed Reactors for the Polymerization Reaction of Ethylene and Propylene. *Developments in Chemical Engineering and Mineral Processing*, **6**: 121-134.

Amdebrhan, B.T. (2018). Evaluating the Performance of Activated Carbon, Polymeric, and Zeolite Adsorbents for Volatile Organic Compounds Control. Department of Civil and Environmental Engineering, University of Alberta. **Master of Science**.

Arnaldos, J., Casal, J., 1987. Study and modelling of mass transfer in magnetically stabilized fluidized beds. *International Journal of Heat and Mass Transfer*, **30**: 1525-1529.

Cai, P., Schiavetti, M., De Michele, G., Grazzini, G.C., Miccio, M., 1994. Quantitative estimation of bubble size in PFBC. *Powder Technology*, **80**: 99-109.

Choi, K.-B., Park, S.-I., Park, Y.-S., Sung, S.-W., Lee, D.-H., 2002. Drying characteristics of millet in a continuous multistage fluidized bed. *Korean Journal of Chemical Engineering*, **19**: 1106-1111.

Davidson, J.F., Harrison, D. (1963). Fluidized Particles. New York, Cambridge University Press.

Giraudet, S., Pré, P., Tezel, H., Le Cloirec, P., 2006. Estimation of adsorption energies using the physical characteristics of activated carbons and the molecular properties of volatile organic compounds. *Carbon*, **44**: 2413-2421.

Girimonte, R., Formisani, B., Testa, F., 2017. Adsorption of CO2 on a confined fluidized bed of pelletized 13X zeolite. *Powder Technology*, **311**: 9-17.

Harshe, Y.M., Utikar, R.P., Ranade, V.V., 2004. A computational model for predicting particle size distribution and performance of fluidized bed polypropylene reactor. *Chemical Engineering Science*, **59**: 5145-5156.

Hatzantonis, H., Yiannoulakis, H., Yiagopoulos, A., Kiparissides, C., 2000. Recent developments in modeling gas-phase catalyzed olefin polymerization fluidized-bed reactors: The effect of

bubble size variation on the reactor's performance. *Chemical Engineering Science*, **55**: 3237-3259.

Hymore, K., Laguerie, C., 1984. Analysis and modelling of the operation of a counterflow multistage fluidized bed adsorber for drying moist air. *Chemical Engineering and Processing: Process Intensification*, **18**: 255-267.

Kamravaei, S., Shariaty, P. Jahandar Lashaki, M., Atkinson, J.D., Hashisho, Z., Phillips, J.H., Anderson, J.E., and Nichols, M (2016). Effect of Beaded Activated Carbon Fluidization on Adsorption of Volatile Organic Compounds. AIChE Annual Meeting. San Francisco, CA, USA.

Kamravaei, S., Shariaty, P. Jahandar Lashaki, M., Atkinson, J.D., Hashisho, Z., Phillips, J.H., Anderson, J.E., and Nichols, M. Crompton, D (2015). Effect of Operational Parameters on the Performance of a Multistage Fluidized Bed Adsorber. AIChE Annual Meeting. Salt lake City, UT, USA.

Keenan, J., Chao, J., Kaye, J., 1983. Gas Tables International Version-Thermodynamic Properties of Air, Products of Combustion and Component Gases. *Compressible Flow Functions*.

Kim, H.S., Matsushita, Y., Oomori, M., Harada, T., Miyawaki, J., Yoon, S.H., Mochida, I., 2013. Fluidized bed drying of Loy Yang brown coal with variation of temperature, relative humidity, fluidization velocity and formulation of its drying rate. *Fuel*, **105**: 415-424.

Kunii, D., Levenspiel, O. (1969). Fluidization engineering. New York, Wiley.

Levenspiel, O. (1972). Chemical reaction engineering. New York, Wiley.

Lu, W.-Z., Teng, L.-H., Xiao, W.-D., 2004. Simulation and experiment study of dimethyl ether synthesis from syngas in a fluidized-bed reactor. *Chemical Engineering Science*, **59**: 5455-5464.

McAuley, K.B., Talbot, J.P., Harris, T.J., 1994. A comparison of two-phase and well-mixed models for fluidized-bed polyethylene reactors. *Chemical Engineering Science*, **49**: 2035-2045.

Missen, R.W., Mims, C.A., Saville, B.A. (1999). Introduction to chemical reaction engineering and kinetics, Wiley New York.

Mohanty, C.R., Malavia, G., Meikap, B.C., 2009. Development of a Countercurrent Multistage Fluidized-Bed Reactor and Mathematical Modeling for Prediction of Removal Efficiency of Sulfur Dioxide from Flue Gases. *Industrial & Engineering Chemistry Research*, **48**: 1629-1637.

Mohanty, C.R., Meikap, B.C., 2011. Modeling the operation of a three-stage fluidized bed reactor for removing CO2 from flue gases. *Journal of Hazardous Materials*, **187**: 113-121.

Philippsen, C.G., Vilela, A.C.F., Zen, L.D., 2015. Fluidized bed modeling applied to the analysis of processes: review and state of the art. *Journal of Materials Research and Technology*, **4**: 208-216.

Poulopoulos, S.G., Inglezakis, V.J. (2006). Adsorption, ion exchange and catalysis: design of operations and environmental applications, Elsevier.

Roy, S., Mohanty, C.R., Meikap, B.C., 2009. Multistage Fluidized Bed Reactor Performance Characterization for Adsorption of Carbon Dioxide. *Industrial & Engineering Chemistry Research*, **48**: 10718-10727.

Schulzke, T., Westermeyer, J., Giani, H., Hornsby, C., 2018. Combustion of Refined Renewable Biomass Fuel (RRBF) in a bubbling fluidized bed. *Renewable Energy*, **124**: 84-94.

Seader, J.D., Henley, E.J. (2006). Separation process principles, John Wiley & Sons, Inc.

Tang, M., Cox, R., Kalberer, M., 2014. Compilation and evaluation of gas phase diffusion coefficients of reactive trace gases in the atmosphere: volume 1. Inorganic compounds. *Atmospheric Chemistry and Physics*, **14**: 9233-9247.

Tefera, D.T., Hashisho, Z., Philips, J.H., Anderson, J.E., Nichols, M., 2014. Modeling Competitive Adsorption of Mixtures of Volatile Organic Compounds in a Fixed-Bed of Beaded Activated Carbon. *Environmental Science & Technology*, **48**: 5108-5117.

Toomey, R.D., Johnstone, H.F., 1952. Gaseous Fluidization of Solid Particles. *Chemical Engineering Progress*, **48**: 220-226.

Werther, J., Hartge, E.-U., 2004. Modeling of Industrial Fluidized-Bed Reactors. *Industrial & Engineering Chemistry Research*, **43**: 5593-5604.

4. Chapter 4*: Modeling VOC Adsorption in Lab- and Industrial-Scale Fluidized Bed Adsorbers: Effect of Operating Parameters and Heel Build-Up

4.1. Abstract

Scale-up and optimization of fluidized beds are challenging due to the difficulty in accounting for the interrelated effect of various phenomena, which are typically described by empirical and/or semi-empirical equations. In this study, a two-phase model was introduced to simulate the adsorption of VOCs on beaded activated carbon (BAC) in a lab-scale fluidized bed adsorber. The model assumes the presence of a bubble phase free from adsorbent particles, and an emulsion phase composed of the adsorbent particles and interstitial gas. The versatility of the proposed model was then evaluated using data from an industrial scale adsorber with different operating conditions, adsorbent properties, and bed geometry. The response of the model to the operating conditions (adsorbent feed rate, air flow rate, and initial concentration) showed better agreement with the experimental lab-scale data when the emulsion gas in the two-phase model was considered in plug flow than in perfectly-mixed flow (R^2= 0.96 compared to 0.91). To simulate the performance of BACs with different service lifetimes (degree of exhaustion as a result of heel developed inside their pores), the main characteristics of the BACs (pore diameter, porosity, and adsorption capacity) were first correlated to their apparent densities. The model could accurately predict the experimental lab-scale VOC concentrations in each stage (R^2=0.92) as well as overall removal efficiencies (R^2=0.99) for BACs ranging from virgin to fully-spent. Finally, the model

* This chapter has been published as an original paper: Davarpanah, M.; Hashisho, Z.; Crompton, D.; Anderson, J. E.; Nichols, M., Modeling VOC adsorption in lab- and industrial-scale fluidized bed adsorbers: Effect of operating parameters and heel build-up. Journal of Hazardous Materials 2020, 400, 123129. Reproduced with permission from Elsevier.

was used to predict the performance of an industrial-scale fluidized bed adsorber for VOC removal at different operating conditions and apparent densities. Predicted and measured VOC removal efficiencies were in good agreement (R^2=0.94). Although the model was verified for adsorption of VOCs on BAC, the modeling approach presented in this study could be used for describing adsorption in different adsorbate-adsorbent systems in multistage counter-current fluidized bed adsorbers.

4.2. Nomenclature

Sym.	Description	Value /Formula	Units	Source
A	cross-section area of bed	4.56×10^{-3} (lab-scale), 23.24 (industrial-scale)	m^2	measured
AD	apparent density (bulk bed density)	Table 4-2, Table 4-4	kg m^{-3}	measured
Ar	Archimedes number	Table 4-3	-	(Abasaeed and Al-Zahrani, 1998)
b	Langmuir coefficient	Table S3	kg/kg	measured
C	VOC concentration	Eq. (4-4)	kg VOC/ kg air	calculated
C^*	VOC concentration in air in equilibrium condition	Figure 4-2	kg VOC/ kg air	measured
C_0	VOC concentration at bed entry	Table 4-2, Table 4-4	ppm_v, kg VOC/ kg air	measured
C_b	VOC concentration in bubble phase	Eqs. (4-6), (4-13)	kg VOC/ kg air	calculated
C_e	VOC concentration in emulsion phase	Eqs. (4-8), (4-14)	kg VOC/ kg air	calculated
d_b	mean bubble diameter	Table 4-3	m	(Yasui and Johanson, 1958,

				Mori and Wen, 1975)
D_e	internal mass transfer coefficient	Eq. (4-26)	$m^2\ s^{-1}$	(Seader and Henley, 2006)
D_g	VOC diffusivity in air	6.5×10^{-6}	$m^2\ s^{-1}$	(Tang et al., 2014)
D_k	Knudsen diffusion coefficient	Eq. (4-28)	$m^2\ s^{-1}$	(Seader and Henley, 2006)
d_p	adsorbent mean diameter	7.5×10^{-4}	m	(Tefera et al., 2014)
d_{pore}	average pore diameter	Eq. (4-29)	nm	(Khan, 2010)
E	cumulative fraction of solids on the stages	Eq. (4-18)	-	(Hymore and Laguerie, 1984)
F_g	air flow rate	Table 4-2, Table 4-4	SLPM, kg hr^{-1}	measured
F_p	adsorbent feed rate	Table 4-2, Table 4-4	g min^{-1}, kg hr^{-1}	measured
g	standard gravity	9.8	m/s^2	(Abasaeed and Al-Zahrani, 1998)
H_w	weir height	4×10^{-3} (lab-scale), 12.7×10^{-3} (industrial-scale)	m	measured
H_{mf}	height of bed on each stage at u_{mf}	Table 4-3	m	(Hymore and Laguerie, 1984)
k	adsorption rate constant	Eq. (4-25)	s^{-1}	(Seader and Henley, 2006)
k'	coefficient	Eq. (4-10)	-	calculated
m	slope of the isotherm	Eq. (4-24)	kg air/kg BAC	calculated
M	VOC molecular weight	107	g mol^{-1}	(Tefera et al., 2014)
m_1	coefficient	Eq. (4-15)	-	calculated
m_2	coefficient	Eq. (4-16)	-	calculated
N_b	number of bubbles per unit volume of bed	Table 4-3	m^{-3}	(Hymore and Laguerie, 1984)

Q	mass transfer flow rate between a bubble and the emulsion phase	Eq. (4-23)	$m^3\ s^{-1}$	(Davidson and Harrison, 1963, Kunii and Levenspiel, 1969, Hatzantonis et al., 2000)
q	VOC content of adsorbent	N/A	kg VOC/ kg BAC	N/A
q^*	VOC content of adsorbent in equilibrium condition	Figure 4-2	kg VOC/ kg BAC	measured
q_m	adsorbent maximum capacity	Table S3	kg/kg	measured
RE	removal efficiency	Eq. (4-36)	-	(Hymore and Laguerie, 1984)
Re_{mf}	Reynolds number at u_{mf}	Table 4-3	-	(Abasaeed and Al-Zahrani, 1998)
S_{BET}	BET surface area	Table 4-1, Eq. (4-31)	$m^2\ g^{-1}$	(Fayaz et al., 2019)
t	particles residence time	-	s	-
T	temperature	294.15	K	measured
u_0	superficial gas velocity	F_g/A	$m\ s^{-1}$	calculated
u_b	velocity of bubble rising through a bed	Table 4-3	$m\ s^{-1}$	(Kunii and Levenspiel, 1969)
u_{mf}	minimum fluidization velocity	Table 4-3	$m\ s^{-1}$	(Abasaeed and Al-Zahrani, 1998)
V_{ads}	total volume of nitrogen adsorbed at relative pressure close to one	Table 4-1, Eq. (4-30)	$cm^3\ g^{-1}$	(Fayaz et al., 2019)
V_b	total volume in a single bubble	Table 4-3	m^3	(Hymore and Laguerie, 1984)
V_{pore}	total pore volume	Table 4-1, Eq. (4-35)	$cm^3\ g^{-1}$	(Fayaz et al., 2019)
W	mass of adsorbent on each stage	Table 4-3	kg	(Hymore and Laguerie, 1984)
X	coefficient	Eq. (4-9)	-	calculated

y	distance axis along the bed	-	m	-
α	coefficient	Eq. (4-22)	-	(Hymore and Laguerie, 1984)
β	fraction of gas flowing as bubbles	Eq. (4-5)	-	(Hymore and Laguerie, 1984)
ε_{mf}	void fraction at u_{mf}	Table 4-3	-	(Hymore and Laguerie, 1984)
ε_b	bulk bed porosity	Eq. (4-34)	-	(Tefera et al., 2014)
ε_p	adsorbent internal porosity	Eq. (4-32)	-	(Tefera et al., 2014)
μ_g	gas viscosity	1.82×10^{-5}	kg m^{-1} s^{-1}	(Keenan et al., 1983)
ρ_g	gas density	1.20	kg m^{-3}	(Keenan et al., 1983)
ρ_p	adsorbent density	Eq. (4-33)	kg m^{-3}	(Tefera et al., 2014)
τ	mean residence time of solids on each stage	Eq. (2-1)	s	(Hymore and Laguerie, 1984)
τ'	tortuosity	Eq. (4-27)	-	(Poulopoulos and Inglezakis, 2006)
ϕ	adsorbent shape factor	1	-	measured

4.3. Introduction

Volatile organic compounds (VOCs) are commonly present in solvent-based paints and inks and are released into the air upon application and drying (Na et al., 2004). VOC emissions can be effectively and economically controlled by activated carbon adsorbers (Zhang et al., 2017). Compared to a fixed bed adsorber, a fluidized bed offers large gas-solid contact, reduced pressure drops, and a continuous process with a greater ability for operational control (Hymore and Laguerie, 1984, Mohanty et al., 2009, Roy et al., 2009).

Despite all the advantages, the scale-up process of a fluidized bed is reported to be challenging because of the interconnection of the complex processes involved, as well as the limited number of relevant studies and experimental data (Hymore and Laguerie, 1984, Werther and Hartge, 2004). In fact, the scale-up of fluidized beds is obscure enough that despite a history of over 50 years in the chemical industry, many tend to believe that "it is still more of an art than an exact science" (Inglezakis and Poulopoulos, 2006).

Modern process design, however, is informed by modeling and simulation tools to fill this gap. A good model must be able to take into account a number of changing variables typical for the scale-up process such as bed geometry (diameter, height, tray orifices, and downcomers), operating parameters (gas flow rate, adsorbent feed rate, and inlet concentration), and adsorbent apparent density as it accumulates a heel over cyclical adsorption/desorption steps (Werther and Hartge, 2004).

Micro-scale modeling (e.g., Molecular Dynamics (Gallas et al., 1992) and Computational Fluid Dynamics (Loha et al., 2013)) could provide accurate predictions for many processes. However, theoretical and empirical correlations employed in micro-scale models which describe the gas-solid hydrodynamic and adsorptive interactions, make computations too complicated and time-consuming to handle the large geometry of an industrial bed (Werther and Hartge, 2004, Khan et al., 2014).

Two-phase and three-phase models are the most common macro-scale models used to describe the behavior of fluidized beds. The two-phase model consists of an emulsion phase and a bubble phase, the latter is assumed to be free of solids (Toomey and Johnstone, 1952). However, in very high air velocities (higher than 8 times the minimum fluidization velocity) gas bubbles carry a considerable amount of solids behind them. This region, called the wake, is considered in three-

phase models (Mohanty et al., 2009, Mohanty and Meikap, 2011). Nevertheless, most industrial adsorbers operate at air velocity 3-6 times the minimum fluidization velocity where the assumptions of the two-phase model are valid (McAuley et al., 1994).

The two-phase model was first introduced by Toomey and Johnstone (Toomey and Johnstone, 1952), and later developed by Davidson and Harrison (Davidson and Harrison, 1963), and Kunii and Levenspiel (Kunii and Levenspiel, 1969), in which bubble motion was incorporated and the diffusive and convective contributions of mass transfer were taken into account. Many other researchers also contributed to the development of the model by investigating the effect of bubble growth and coalescence (Mori and Wen, 1975, Darton et al., 1977, Cai et al., 1994), the residence time distribution of solids (Hymore and Laguerie, 1984), etc.

Mohanty et al. (Mohanty et al., 2009, Mohanty and Meikap, 2011) employed a two-phase model to simulate a bubbling countercurrent multistage fluidized-bed reactor used for the adsorption of carbon dioxide (Mohanty and Meikap, 2011) and sulfur dioxide (Mohanty et al., 2009) by hydrated lime particles. They assumed the bubble phase to be in plug flow and emulsion phase to be either in plug flow or in perfectly mixed flow, and then compared the model results with experimental data as the operating parameters changed. Garnavi et al. (Garnavi et al., 2006) proposed a two-phase model that considered bubble size variations along the bed height for the simulation of a fluidized bed dryer and studied the impact of the gas velocity, gas temperature, solid particle size, and solid mean residence time on the drying process.

However, to the best of our knowledge, no research has dealt with modeling the adsorption process in an industrial fluidized bed using a two-phase model. This might be due to the complexity of developing a model versatile enough to account for details of industrial-scale operation which is usually different from the controlled operation of lab-scale adsorbers. For example, there were

studies considering the adsorption process in a lab-scale fluidized bed as a reaction with a constant rate determined by the Arrhenius equation (Mohanty et al., 2009, Roy et al., 2009, Mohanty and Meikap, 2011). The assumption of constant adsorption rate in these studies makes the model specific to the lab-scale systems simulated, while a more inclusive model sensitive to scale-up is required for simulating industrial-scale beds.

This study presents a modeling approach based on the two-phase model to describe adsorption in multistage fluidized bed adsorbers. The model attempts to simulate the effect of changes in operating parameters on the adsorption of a mixture of industrial solvents onto beaded activated carbon (BAC) with different apparent densities (and adsorption capacities). This model is then utilized to predict the performance of an industrial-scale fluidized bed adsorber and a comparison is made against actual operating data.

4.4. Process description

4.4.1. Materials

Adsorption isotherms in this study were measured at room temperature using a microbalance (CAHN C-1000). The adsorbents were Beaded Activated Carbon (BAC) (average particle size of 7.5×10^{-4} m) ranging from virgin to fully-spent BAC. As the BAC experiences adsorption and desorption cycles, a heel accumulates which, in turn, reduces the adsorption capacity of the BAC and increases its apparent density. Samples of different use history are identified as BAC-X where X is the apparent density in kg/m^3. The properties of the tested adsorbents are listed in Table 4-1. The adsorbate was a solvent mixture (SM) meant to simulate the emissions from automotive painting booths. The mixture consists of petroleum naphtha- light aromatic, *n*-butanol, trimethylbenzene, each >10% by weight, as well as other organic chemicals (e .g. *n*-butyl acetate, butyl propionate, *n*-heptane, *n*-propyl propionate, ethyl 3- ethoxypropionate, trimethyl

orthoacetate, isopropanol, *n*-propylbenzene, isobutanol, each 1 to 10% by weight). SM molecular weight and diffusivity in air were calculated as a mole-weighted average. This assumption is later supported by a sensitivity analysis.

Table 4-1. Adsorbents properties (Fayaz et al., 2019).

Adsorbent	Apparent density, AD (kg m^{-3})	BET surface area, S_{BET} (m^2 g^{-1})	Total volume of nitrogen adsorbed at relative pressure ≈1, $V_{ads,}$ (cm^3 g^{-1})	Total pore volume, V_{pore} (cm^3 g^{-1})
BAC-606*	606	1,350	411.5	0.57
BAC-707	707	859	286.5	0.41
BAC-746	746	720	253.5	0.37
BAC-807**	807	376	182.3	0.25

* virgin (before the first cycle)

** completely spent (after the last cycle)

Prior to the measurement, BAC samples were heated in an oven in air at 120 °C for 3 hours to remove residual moisture. Approximately 20 mg of adsorbent was placed into the sample pan and exposed to the gas-phase SM at different concentrations in nitrogen. The concentration was increased to the next step once equilibrium was reached, as indicated by <0.1% change in weight per hour. To produce adsorbate vapor streams, a syringe pump continuously injected the appropriate amount of SM into a 300 SCCM stream of nitrogen (grade 5.0). The adsorption capacity was calculated using the weights of adsorbent before and after adsorption at each concentration step.

4.4.2. Fluidized bed setup

All lab-scale fluidized bed data used in this study are listed in Table 4-2 and (except one) was previously reported (Kamravaei, 2015). The fluidized bed setup is shown in Figure 4-1. The

adsorber is a 1:5,000 scaled-down version of an industrial-scale fluidized bed adsorber used for controlling emissions from an automotive painting booth and consists of 6 cylindrical compartments (10.4 cm height and 7.6 cm inner diameter) tightly connected and sealed using nuts and bolts and an elastomeric O-ring in between. Trays separate the compartments and upward-protruding downcomers (walls surrounding a 4-mm diameter opening in the tray) on trays allow for solid transfer to the stages below while maintaining the desired amount of adsorbent on each stage. A volumetric feeder (Schenck AccuRate) at the top of the adsorber was used to adjust the solid flow rate. To reach the desired concentration, a syringe pump (New Era, NE-300) equipped with a 50 ml syringe (SGE) injected the liquid solvent mixture into a stream of dry and filtered compressed air, which was regulated using a mass flow controller (Alicat Scientific). An air distributor at the bottom of the bed was designed to ensure a well-distributed inlet gas flow.

The sampling tubes were placed horizontally and pulled air from the center of the column on each stage. The concentration of VOC was measured using a flame-ionization detector (FID, Baseline Mocon, series 9000). Solenoid valves (controlled by LabVIEW software) allowed for switching between the streams of sampling tubes. A data acquisition system logged the FID readings. The experiments were started after the inlet SM concentration reached a steady state and the SM-laden air was supplied to the adsorber. All adsorption experiments were duplicated and carried out at room temperature (21°C).

Table 4-2. Experimental parameters for adsorption of SM on BAC-606 in the fluidized bed (Kamravaei, 2015).

Changing parameter	Exp. no.	Apparent density, *AD* (kg m^{-3})	BAC feed rate, F_p (g min^{-1})	Gas flow rate, F_g (SLPM)	SM initial Conc, C_0 (ppm_v)
Adsorbent feed rate	1*	606	0.44	300	100
	2	606	1.40	300	100
	3	606	2.30	300	100
	4	606	3.30	300	100
Air flow rate	5	606	0.44	200	100
	6	606	0.44	250	100
	7	606	0.44	300	100
	8	606	0.44	350	100
Initial concentration	9	606	0.44	300	50
	10	606	0.44	300	100
	11	606	0.44	300	150
	12	606	0.44	300	200
	13	606	0.44	300	300
Apparent density	14	606	0.44	300	100
	15	707	1.40	300	100
	16	746	2.30	300	100
	17**	807	3.30	300	100

* Baseline case

** Measured in this study

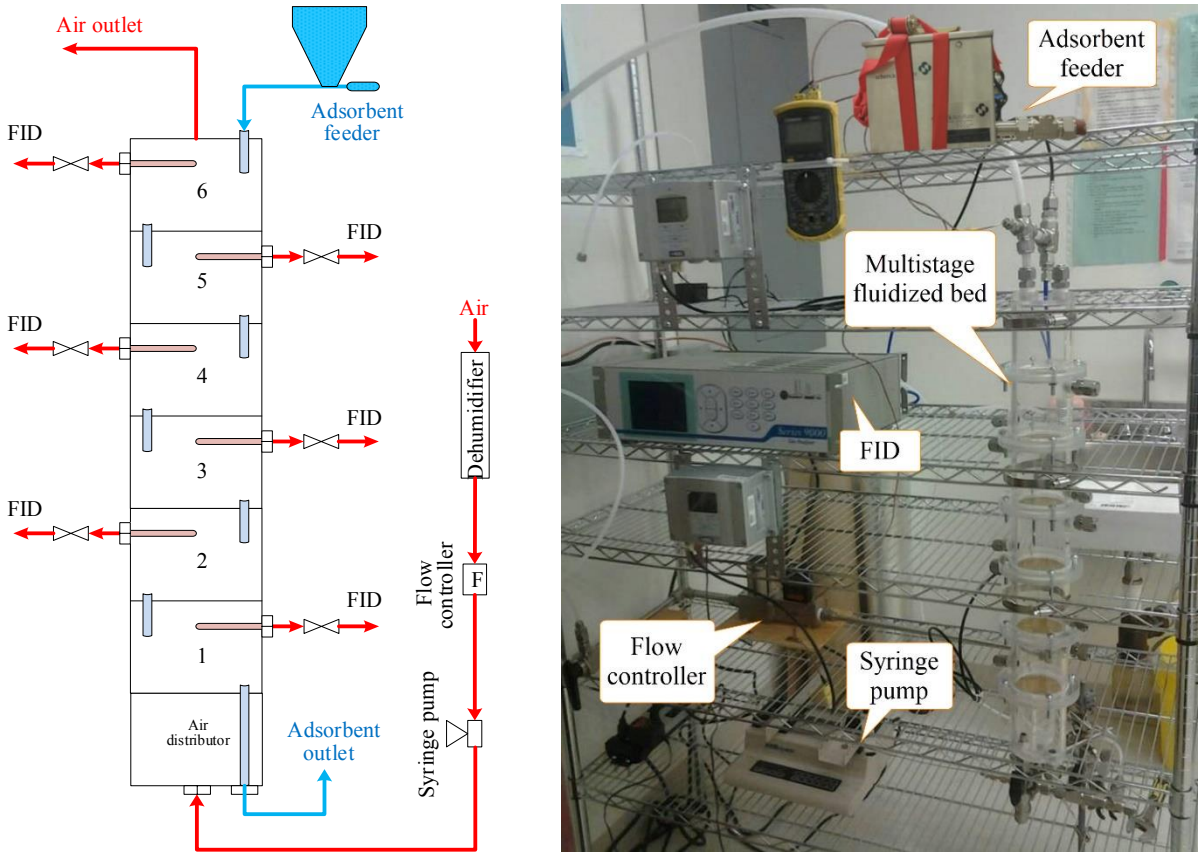

Figure 4-1. The fluidized bed setup.

4.5. Model development

4.5.1. Adsorption isotherm

The mixture of solvent is treated as a single adsorbate in this study. Therefore, the model predicts the total amount of VOCs adsorbed. The Langmuir equation demonstrated a good representation of the experimental data (Figure 4-2), and was selected to model the adsorption isotherms of SM on BAC samples with different service lives:

$$\frac{1}{q^*} = \frac{1}{q_m} + \frac{1}{bq_m C^*} \tag{4-1}$$

where q^* and C^* are equilibrium concentration of SM on BAC and in air, respectively; and q_m and b are Langmuir equation coefficients determined from fitting the model to the experimental data in Table S3 in Supplementary Information.

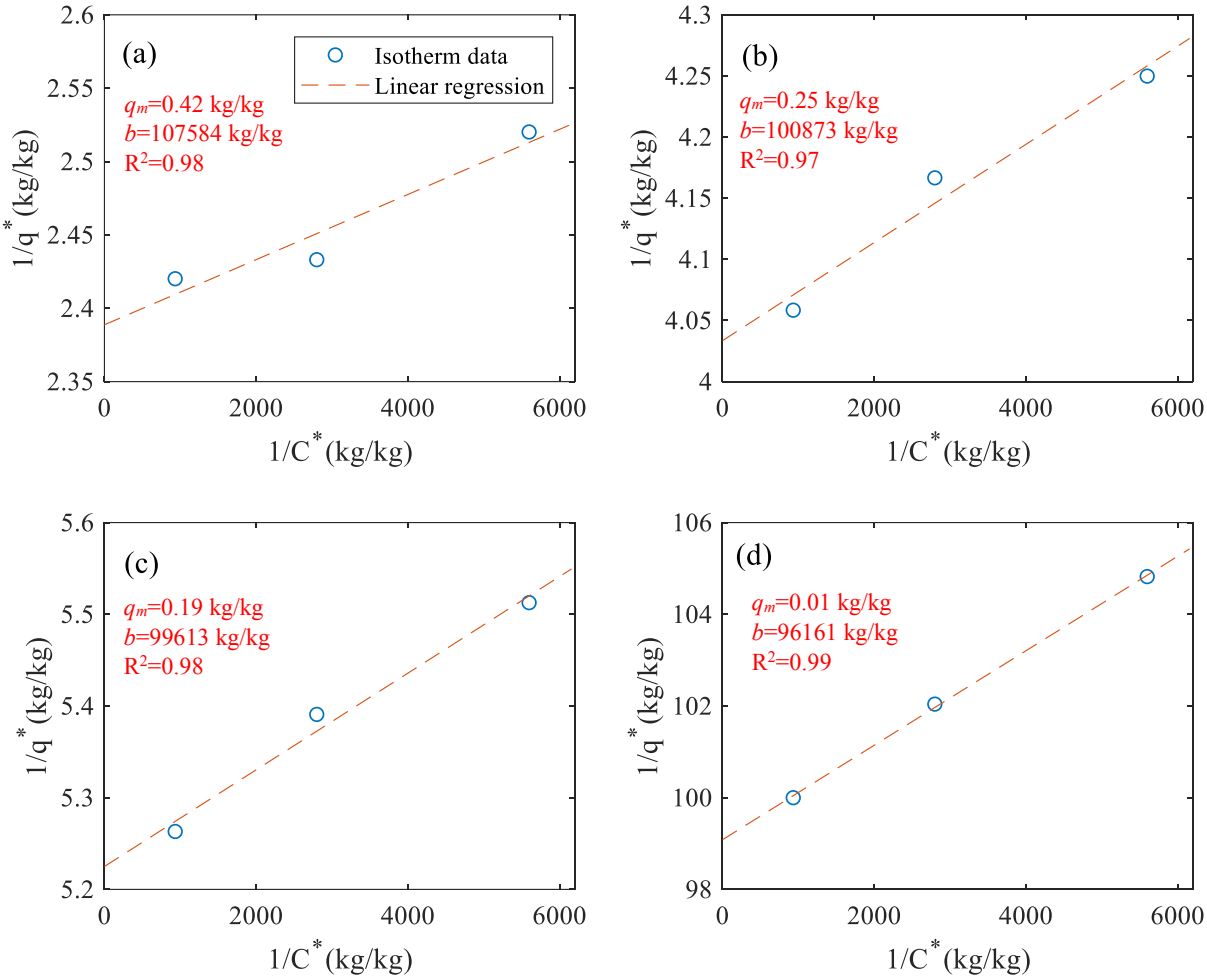

Figure 4-2. Langmuir isotherm for adsorption of SM on (a) BAC-606, (b) BAC-707, (c) BAC-746, (d) BAC-807.

To predict the isotherm of SM on BAC with different AD within the range of 606 to 807 kg/m^3, the Langmuir parameters (q_m and b) are represented as a function of apparent density and correlated with the AD using a second- and a first-degree polynomial equation, respectively (Figure 4-3).

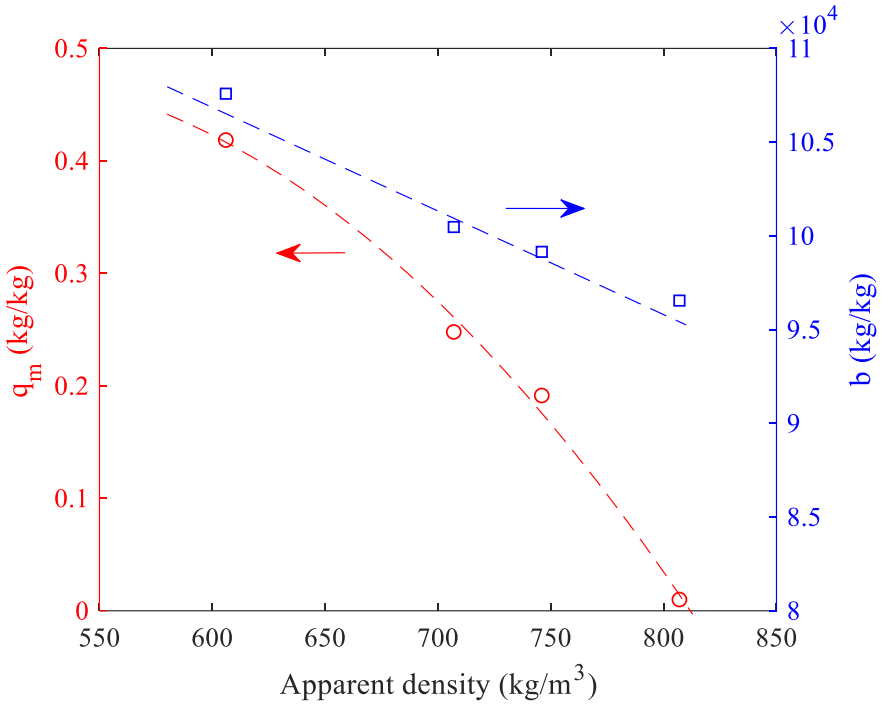

Figure 4-3. Langmuir isotherm parameters for SM on BAC as a function of BAC apparent density.

$$q_m(kg/kg) = -4.62\times10^{-6}\times AD^2 + 4.52\times10^{-3}\times AD - 0.63 \quad (4\text{-}2)$$

$$b(kg/kg) = -55.25\times AD + 1.40\times10^{5} \quad (4\text{-}3)$$

4.5.2. Governing equations in the two-phase model

According to the two-phase model, the fluidized bed consists of a bubble phase which contains no adsorbent particles and an emulsion (or particulate) phase comprised of the adsorbent particles and interstitial gas (Toomey and Johnstone, 1952, Davidson and Harrison, 1963, Kunii and Levenspiel, 1969). While the bubble phase is in plug flow, the gas in the emulsion phase could be considered either perfectly mixed (EGPM) or in plug flow (EGPF) (Mohanty et al., 2009, Mohanty and Meikap, 2011). These two model assumptions are presented in Figure 4-4.

At the bottom of each stage, the inlet stream with a concentration of C_{i-1} splits into two streams where the gas required for minimum fluidization (u_{mf}) enters the emulsion phase to keep the solids at minimum fluidization state, and the gas in excess of that (u-u_{mf}) rises through the bed as bubbles. The mass transfer in the stage is assumed to take place not only between the bubble and emulsion phases (Q) but also between gas and solids in the emulsion phase. At the top of each stage, the gas leaving the emulsion phase (C_{ei}) mixes with the gas from the bubble phase (C_{bi}), forming the outlet concentration of C_i.

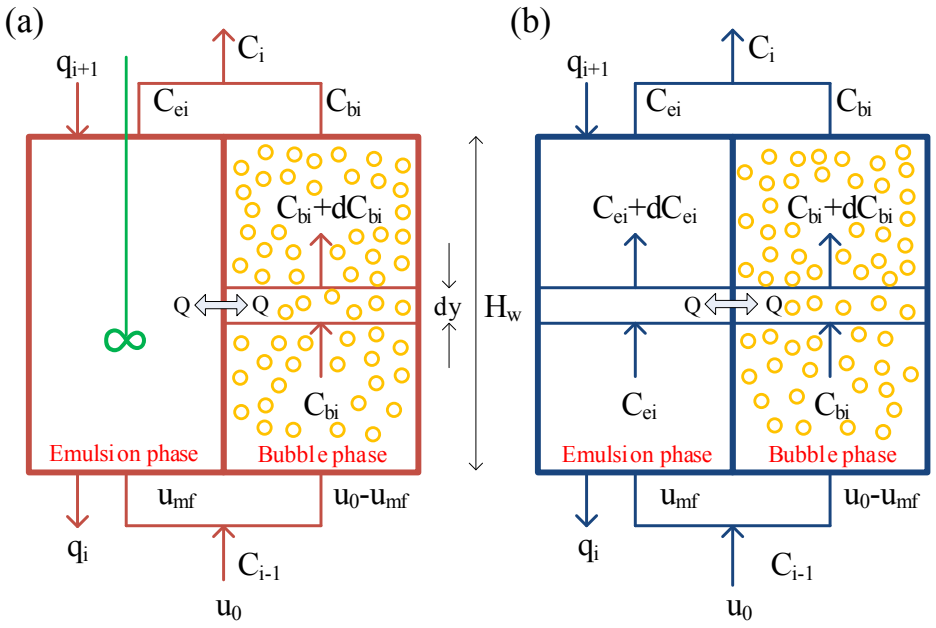

Figure 4-4. Schematic diagram of (a) EGPM and (b) EGPF (Hymore and Laguerie, 1984).

Writing a material balance at the top of a stage, the concentration of adsorbate leaving the i^{th} stage can be calculated by:

$$C_i = \beta C_{bi}\Big|_{y=H_w} + (1-\beta)C_{ei} \tag{4-4}$$

where,

$$\beta = 1 - \frac{u_{mf}}{u_0} \tag{4-5}$$

If a material balance is written on a single rising bubble and then integrated with respect to y knowing $C_{bi}=C_{i-1}$ at $y=0$, the following equation is obtained:

$$C_{bi}(y) = C_{ei} + \left(C_{i-1} - C_{ei}\right) exp\left(\frac{-Qy}{u_b V_b}\right) \tag{4-6}$$

where Q is the interphase mass transfer flow rate, u_b is bubble rise velocity, V_b is the total volume in a single bubble, and C_{ei} and C_{bi} are adsorbate concentrations in the emulsion and bubble phases, respectively.

The equation below can be obtained by writing a material balance in the emulsion phase when it is perfectly mixed:

$$N_b V_b u_b \left(C_{i-1} - C_{ei}\right)\left[1 - \exp\left(\frac{-QH_w}{u_b V_b}\right)\right] + u_{mf}\left(C_{i-1} - C_{ei}\right) = \left(\frac{Wm_i k_i}{A\rho_g}\right)\left(C_{ei} - \bar{C}_{ei}^{*}\right) \tag{4-7}$$

The first term refers to the adsorbate exchanged between the bubble and emulsion phases, where N_b is the number of bubbles per unit volume of bed. The second term shows the VOC that enters the bottom and leaves at the top. The term on the right accounts for the VOC consumed in the adsorption process, where W is the mass of solids on each stage, m is the slope of adsorption isotherm, k is adsorption rate constant, A is the cross-section area of the bed, and $\bar{C}_{ei}^{*}$ is the concentration of VOC in emulsion phase in equilibrium with solids with VOC content $\bar{q}_i$.

Solving Eq. (4-7) for C_{pi} results in the following equations:

$$C_{ei} = \bar{C}^*_{ei} + \left(C_{i-1} - \bar{C}^*_{ei}\right)\left(\frac{1-\beta\exp(-X)}{1-\beta\exp(-X)+k_i'}\right) \tag{4-8}$$

$$X = \frac{QH_w}{u_b V_b} \tag{4-9}$$

$$k_i' = \frac{Wm_i k_i}{A\rho_g u_0} \tag{4-10}$$

If the emulsion phase is considered to be in plug flow, a material balance is written on an infinitesimal height "*dy*":

$$(1-\beta)\frac{dC_{ei}}{dy} + \beta\frac{dC_{bi}}{dy} + \frac{k_i'}{H_w}\left(C_{ei} - \bar{C}^*_{ei}\right) = 0 \tag{4-11}$$

$$H_w^2(1-\beta)\frac{d^2C_{bi}}{dy^2} + H_w\left(X+k'\right)\frac{dC_{bi}}{dy} + k_i' X C_{bi} = k_i' X \bar{C}^*_{ei} \tag{4-12}$$

Solving Eq. (4-12) with boundary conditions $\frac{dc_b}{dy} = 0$ at $y = 0$ and $c_b = c_0$ at $y = 0$ results in:

$$C_{bi} = \frac{C_{i-1} - \bar{C}^*_{ei}}{m_{1i} - m_{2i}}\left(m_{1i}\exp\left(-m_{2i}y\right) - m_{2i}\exp\left(-m_{1i}y\right)\right) + \bar{C}^*_{ei} \tag{4-13}$$

$$C_{ei} = \frac{C_{i-1} - \bar{C}^*_{ei}}{m_{1i} - m_{2i}}\left[m_{1i}\left(1 - \frac{H_w}{X}m_{2i}\right)\exp\left(-m_{2i}H_w\right) - m_{2i}\left(1 - \frac{H_w}{X}m_{1i}\right)\exp\left(-m_{1i}H_w\right)\right] + \bar{C}^*_{ei} \tag{4-14}$$

$$m_{1i} = \frac{1}{2}\frac{X+k_i'}{H_w(1-\beta)} - \frac{1}{2}\left[\left(\frac{X+k_i'}{H_w(1-\beta)}\right)^2 - \left(\frac{4k_i'X}{H_w^2(1-\beta)}\right)\right]^{\frac{1}{2}} \tag{4-15}$$

$$m_{2i} = \frac{1}{2}\frac{X + k_i'}{H_w(1-\beta)} + \frac{1}{2}\left[\left(\frac{X + k_i'}{H_w(1-\beta)}\right)^2 - \left(\frac{4k_i'X}{H_w^2(1-\beta)}\right)\right]^{\frac{1}{2}} \tag{4-16}$$

Considering plug flow for gas in the emulsion phase, the concentration of VOC in that phase varies along the bed and therefore, an average concentration can be calculated according to Eq. (4-17):

$$\bar{C}_{ei} = \frac{1}{H_w}\int_0^{H_w} C_{ei}\,dy \tag{4-17}$$

The fraction of solids with residence times $t_1, t_2, \ldots, t_i$ on the first, second and i^{th} stage is given by the following equation:

$$E_i(t_1, t_2, \ldots, t_i) = \frac{1}{\tau}\exp\left(-\frac{1}{\tau}\sum_{j=1}^{i} t_j\right) \tag{4-18}$$

where

$$\tau = \frac{W}{F_p} \tag{4-19}$$

The rate of increase in VOC concentration for this fraction of particles is described by:

$$\frac{dq_i}{dt} = k_i\left(q_i^* - q_i\right) \tag{4-20}$$

After integrating Eq. (4-20), $\bar{q}_i$ can be given by the following formula (Hymore and Laguerie, 1984):

$$\bar{q}_i = q_0 \prod_{j=0}^{i} \alpha_j + \sum_{j=1}^{i} q_j^* \left(1-\alpha_j\right) \prod_{k=j+1}^{i} \alpha_k \tag{4-21}$$

$$\alpha_j = \frac{1}{1+k_j \tau} \tag{4-22}$$

Knowing $\bar{q}_i$, it is now possible to calculate $\bar{C}_{ei}^*$ using the adsorption isotherm.

4.5.3. Hydrodynamics

The gas velocity and the bed voidage are assumed to be equal to their values at the minimum fluidization condition, u_{mf} and ε_{mf}, respectively. The estimation of other parameters is summarized in Table 4-3. The minimum fluidization velocity ranged from 0.19 m s^{-1} for the virgin BAC (AD=606 kg/m^3) to 0.25 m s^{-1} for the fully-spent BAC (AD=807 kg/m^3). Also, the bubble diameter inside the lab- and industrial-scale adsorbers were in the ranges of 2.7-4.3 mm and 11.8-12.3 mm, respectively; depending on the adsorbent AD and operating conditions.

Table 4-3. Hydrodynamic correlations used in the calculations of two-phase models.

Parameter	Formula	Reference
Mean bubble diameter, d_b	$d_b = 1.6\rho_p d_p \left(\frac{u_0}{u_{mf}} - 1\right)^{0.63} \frac{H_w}{2}$	(Yasui and Johanson, 1958, Mori and Wen, 1975)
Bubble rise velocity, u_b	$u_b = u_0 - u_{mf} + 0.711\left(g d_b\right)^{\frac{1}{2}}$	(Kunii and Levenspiel, 1969)
Minimum fluidization velocity, u_{mf}	$\frac{1.75}{\phi \varepsilon_{mf}^3} \mathrm{Re}_{mf}^2 + \frac{150\left(1-\varepsilon_{mf}\right)}{\phi^2 \varepsilon_{mf}^3} \mathrm{Re}_{mf} - \mathrm{Ar} = 0$ $\mathrm{Re}_{mf} = \frac{\rho_g d_p u_{mf}}{\mu_g}$ $\mathrm{Ar} = \frac{\rho_g \left(\rho_p - \rho_g\right) g d_p^3}{\mu_g^2}$	(Abasaeed and Al-Zahrani, 1998)

Bed voidage at minimum fluidization, ε_{mf}	$\varepsilon_{mf} = \frac{1}{6}(6-\pi) = 0.472$	(Davidson and Harrison, 1963)
Mass of adsorbent on each stage, W	$W = \rho_p H_{mf} A(1-\varepsilon_{mf})$	(Hymore and Laguerie, 1984)
Bed height at minimum fluidization, H_{mf}	$H_{mf} = H_w\left(1-\frac{u_0-u_{mf}}{u_b}\right)$	(Hymore and Laguerie, 1984)
Total volume in a single bubble, V_b	$V_b = \frac{\pi d_b^3}{6}$	(Hymore and Laguerie, 1984)
Number of bubbles per unit bed volume, N_b	$N_b = \frac{u_0-u_{mf}}{u_b V_b}$	(Hymore and Laguerie, 1984)

4.5.4. Mass transfer

In the two-phase models, the mass transfer between bubble and emulsion phases can be described as follows (Davidson and Harrison, 1963, Kunii and Levenspiel, 1969, Hatzantonis et al., 2000):

$$Q = \left(\frac{3}{4}u_{mf} + 0.975 D_g^{\frac{1}{2}}\left(\frac{g}{d_b}\right)^{\frac{1}{4}}\right)\times \pi d_b^2 \tag{4-23}$$

The overall adsorption rate is described by the following equation:

$$\frac{dq_i}{dt} = k_i\left(q_i^* - q_i\right) = k_i m_i\left(C_i - C_i^*\right) \tag{4-24}$$

For an adsorption process, the following steps need to be considered:

- External diffusion
- Internal diffusion
- Surface diffusion

- Adsorption on the sites

In our case, external and surface diffusions are not rate-limiting steps (Hymore and Laguerie, 1984, Seader and Henley, 2006). Similarly, adsorption on the sites is essentially instantaneous in physisorption as it is only dependent on the collision frequency and adsorbate-site orientation (Seader and Henley, 2006). Thus, only internal diffusion needs to be considered.

When considering internal diffusion only, Seader and Henley (Seader and Henley, 2006) provided a relationship describing the adsorption rate constant:

$$k = \frac{60 D_e}{d_p^2 m} \tag{4-25}$$

where d_p is adsorbent diameter, and D_e is the internal mass transfer coefficient.

The internal mass transfer coefficient accounts for diffusion of adsorbate in air (D_g) as well as Knudsen diffusion (D_k):

$$\frac{1}{D_e} = \frac{\tau'}{\varepsilon_p}\left(\frac{1}{D_g} + \frac{1}{D_k}\right) \tag{4-26}$$

where τ' is tortuosity (Poulopoulos and Inglezakis, 2006) and ε_p is the adsorbent porosity.

$$\tau' = 1 - \frac{1}{2}\ln \varepsilon_p \tag{4-27}$$

$$D_k = 48.5 d_{pore}\left(\frac{T}{M}\right)^{0.5} \tag{4-28}$$

where, d_{pore} is the pore diameter of the adsorbent and M is the VOC molecular weight.

Similar to adsorption capacity, pore diameter and porosity are different for adsorbents of different service lives due to the heel buildup, as indicated by the different apparent densities. To

characterize the effect of heel build-up on overall removal efficiency, one approach is to derive correlations predicting the total pore volume and diameter as a function of apparent density.

For cylindrical pores, the average pore diameter can be calculated using the following formula (Khan, 2010):

$$d_{pore}(nm) = 6.1988 \frac{V_{ads}(cm^3/g)}{S_{BET}(m^2/g)} \tag{4-29}$$

where V_{ads} is the volume of nitrogen gas adsorbed at a relative pressure close to unity and S_{BET} is the BET surface area of the adsorbent. These two parameters are listed in Table 4-1 for the tested adsorbents and are plotted versus apparent density in Figure 4-5 (a). Applying linear regression, the following correlations can be used to predict V_{ads} and S_{BET}.

$$V_{ads}(cm^3/g) = -1.1336 \times AD(kg/m^3) + 1095.6 \tag{4-30}$$

$$S_{BET}(m^2/g) = -4.7782 \times AD(kg/m^3) + 4249.8 \tag{4-31}$$

The internal porosity of adsorbent, on the other hand, can be calculated by (Tefera et al., 2014):

$$\varepsilon_p = \rho_p V_{pore} \tag{4-32}$$

where ρ_p and V_{pore} are adsorbent particle density and total pore volume, respectively; the former may be calculated by (Tefera et al., 2014):

$$\rho_p = \frac{AD}{1-\varepsilon_b} \tag{4-33}$$

where ε_b is bulk bed porosity and can be estimated using the following formula for known values of bed diameter (D) and particle diameter (d_p) (Tefera et al., 2014):

$$\varepsilon_b = 0.379 + \frac{0.078}{\frac{D}{d_p} - 1.8} \tag{4-34}$$

A plot of the total pore volume as a function of apparent density (Figure 4-5 (b)) reveals a linear correlation between these two parameters, formulated as below:

$$V_{pore}(cm^3/g) = -0.0015608 \times AD(kg/m^3) + 1.5183 \tag{4-35}$$

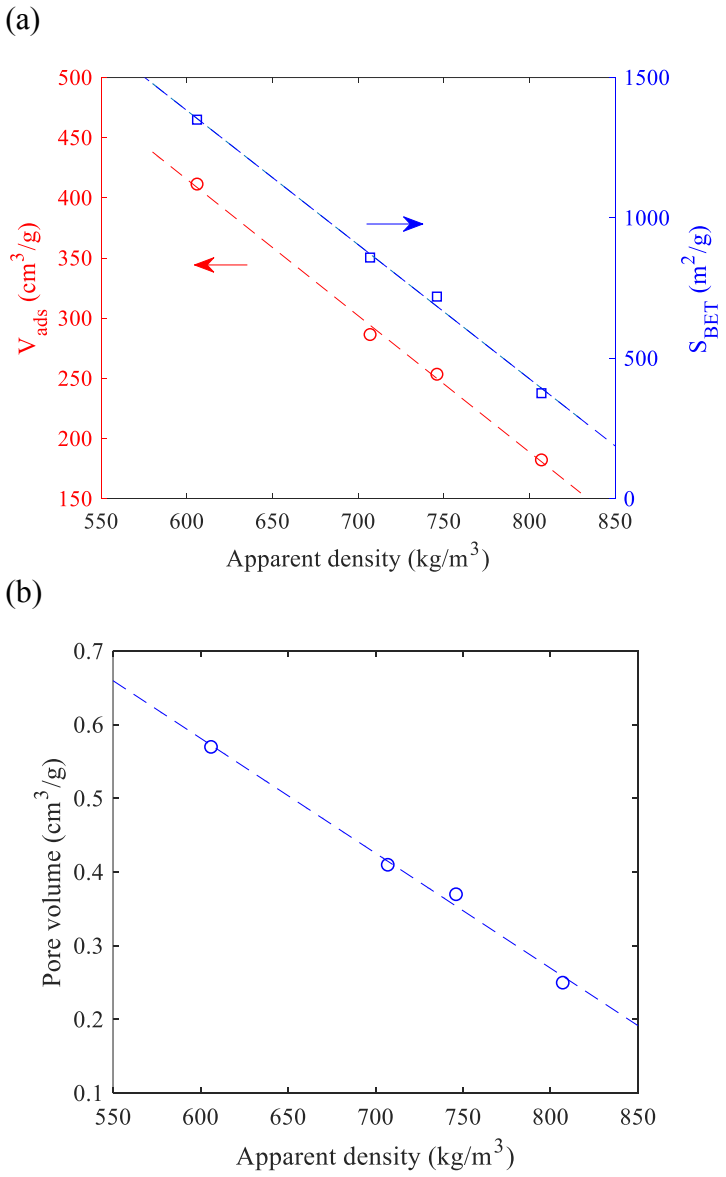

Figure 4-5. (a) V_{ads} and S_{BET}, and (b) total pore volume as a function of apparent density.

Finally, the removal efficiency (RE) in each stage is calculated using the following equation:

$$\mathrm{RE}\,(\%) = \frac{C_0 - C_i}{C_0} \times 100 \tag{4-36}$$

where C_0 and C_i are VOC concentration in the inlet gas stream and at the exit of stage i, respectively.

4.6. Results and discussion

A computer program was developed in Matlab R2018b to solve the above equations. Using this approach, the following results were obtained and compared with experiments.

4.6.1. Effect of operating parameters

Figure 4-6 demonstrates the effect of different operating conditions on the overall removal efficiency of the adsorption of SM on BAC. The removal efficiency increases slightly from 93% to 97% when the solid feed rate increased from 0.44 to 1.4 g min^{-1} and then plateaus after further increase (Figure 4-6 (a)). This trend is well captured by both EGPM and EGPF models. At removal efficiencies close to 100% (when the gas-phase SM concentrations are low), the adsorption process is primarily controlled by the kinetics of adsorption rather than the BAC adsorption capacity. Hence, increasing the solid feed rate at high removal efficiencies does not increase the removal efficiency.

The overall removal efficiency decreases with higher gas flow rates due to the reduced adsorbent-adsorbate contact time (Figure 4-6 (b)). Both EGPM and EGPF were able to accurately capture this downward trend except in experiment no. 8 when the highest air flow rate (350 SLPM) was used. At this flow rate, the assumption of the formation of only two phases (bubble phase and emulsion phase) is not valid anymore. In fact, when the operating velocity is higher than or close

to 8 times the minimum fluidization velocity, a third phase called the cloud or wake is formed around the bubble which has to be considered in the mass transfer resistance calculation (Missen et al., 1999, Mohanty et al., 2009, Mohanty and Meikap, 2011, Philippsen et al., 2015). The over-predicted overall removal efficiency at F_g=350 SLPM in both models could be attributed to the neglected mass transfer resistance associated with the cloud phase.

As the initial concentration increases, overall removal efficiency decreases, as shown in Figure 4-6 (c). While both EGPM and EGPF exhibit a general descending trend, the result from the EGPF model is closer to the measured value at C_0=150 ppm_v. As far as the calculations in the two-phase models are concerned, the shape of the isotherm is an important factor determining the adsorbate content of the adsorbent (q) and the slope of the isotherm (m) at each concentration (C). Because of this strong dependence, an uncertainty or an error in the shape of the isotherm (q or m) at a given concentration along the bed produces a potential error in calculated values. This error might be small in one stage but since the outlet concentration of one stage is the inlet of the next, the error can propagate to other stages or become amplified. Compared to EGPM, the EGPF model may be less susceptible to this type of error since the average concentration of adsorbate in the emulsion phase for each stage is used in calculations, which in turn, can dampen the error resulting from one (or a few) deviated value(s). Therefore, it can be said that apart from the physics of the system, e.g. the ratio of bed height to bed diameter (Kunii and Levenspiel, 1969, Lu et al., 2004) which might dictate the preference of one over the other, EGPF always dampens the error associated with isotherm measurements/predictions. Similarly, Mohanty et. al (Mohanty et al., 2009) stated that EGPF produced a better prediction of experimental data than EGPM.

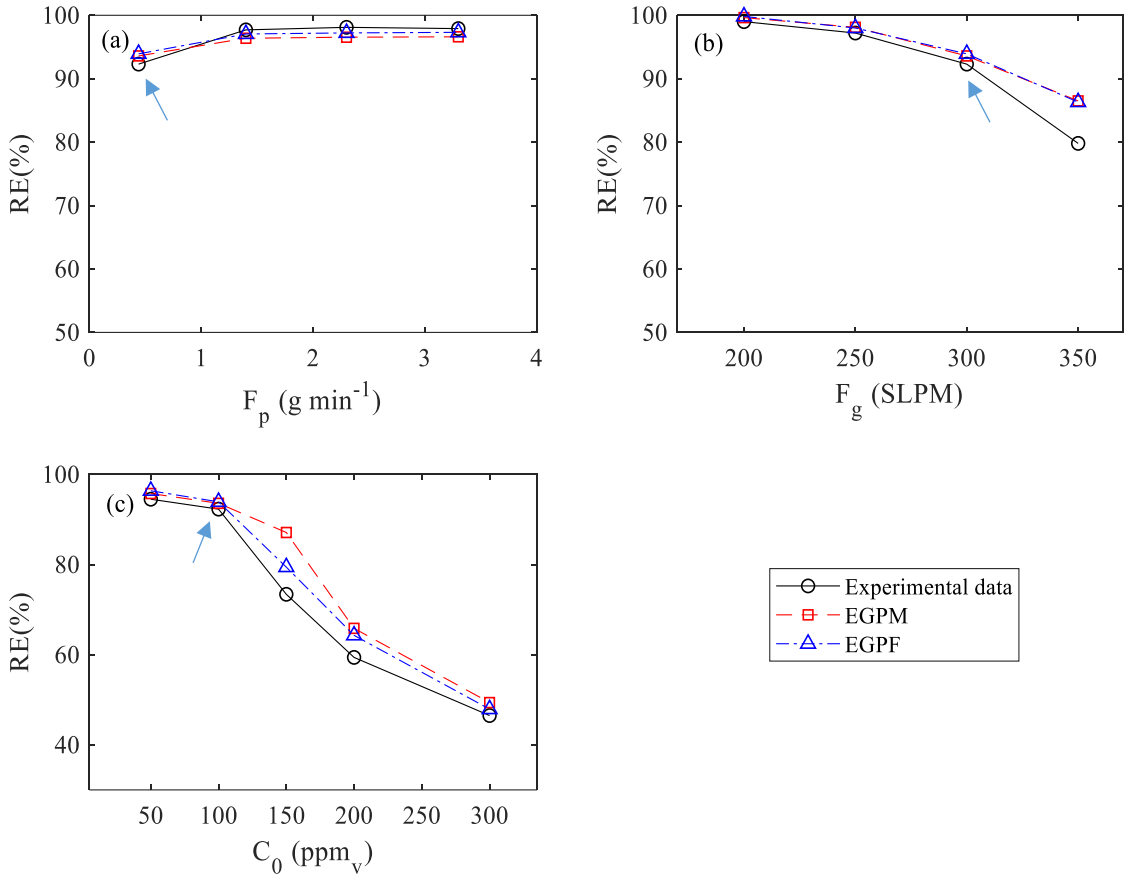

Figure 4-6. Experimental and predicted removal efficiencies as a function of (a) sorbent feed rate (exp. no. 1-4), (b) gas flow rate (exp. no. 5-8), and (c) initial concentration (exp. no. 9-13). The arrows in the figure show the baseline case.

Experimental and calculated stage-wise concentrations of SM along the bed for each set of the experiment are shown in Figure 4-7 with their associated data reported in Table S4 in Supplementary Information. Overall, there is a very good agreement between experimental and predicted data. The greatest difference occurred in experiment 11, in which the removal efficiency calculated by EGPM first deviated from experimental data at stage 2, and that deviation propagated to all subsequent stages because the adsorbate concentration in each stage is dependent on those in other stages. The coefficients of determination in the prediction of overall removal efficiency

for EGPM and EGPF are 0.91 and 0.96, respectively. Since EGPF could predict the experimental data better than EGPM, the subsequent discussion is only for the EGPF model.

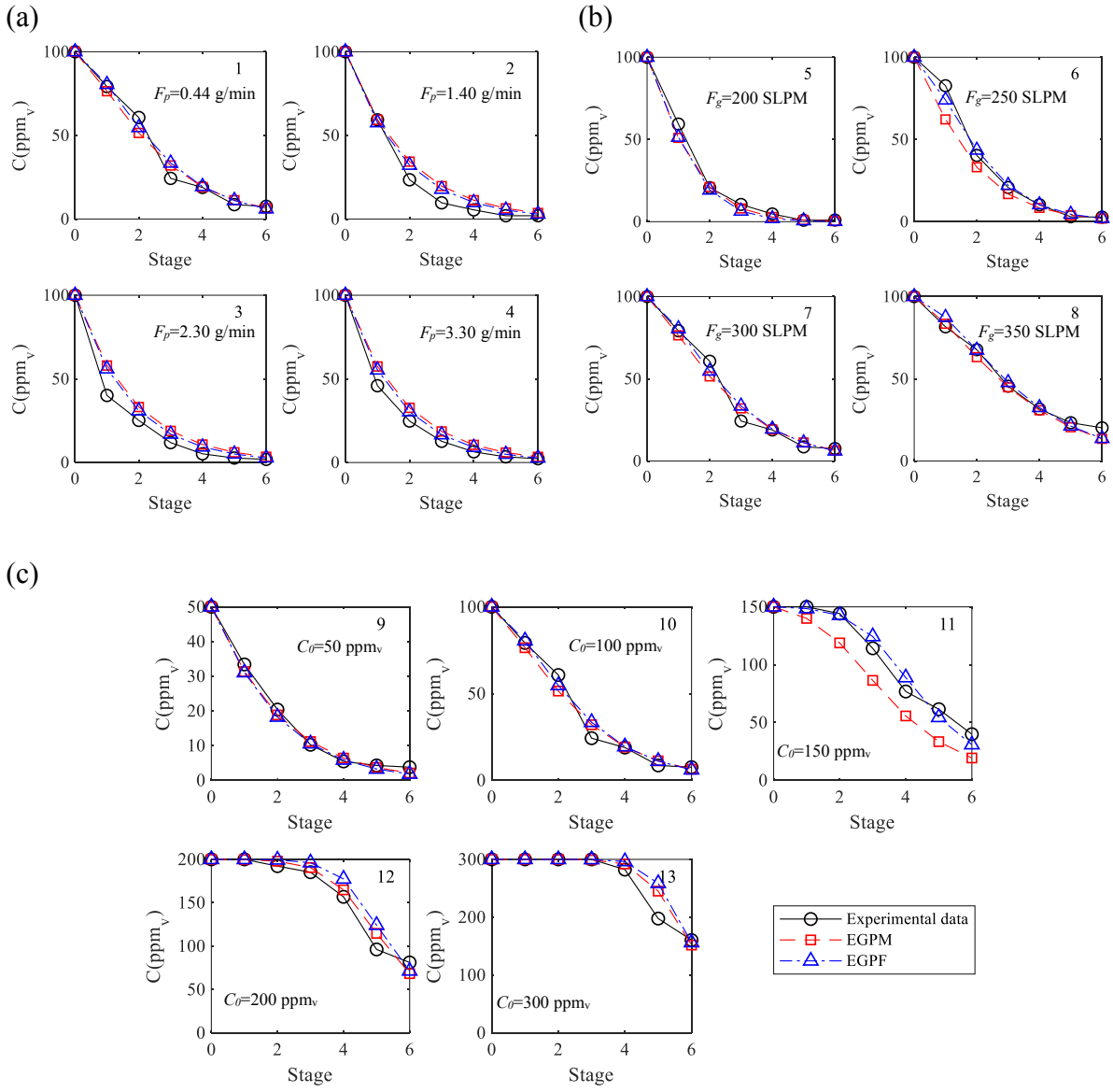

Figure 4-7. Stage-wise comparison of experimental vs. EGPM and EGPF prediction of gas-phase SM concentration in the fluidized bed in varying (a) adsorbent feed rate, (b) air flow rate, (c) initial concentration. The experiment number from Table 4-2 is shown on the top-right side of each diagram. Baseline case is F_p=0.44 g min^{-1}, F_g=300 SLPM, and C_0=100 ppm$_v$. Concentration at stage 0 denotes the inlet concentration.

4.6.2. Effect of heel build-up (apparent density)

When VOC emissions are controlled via cyclical adsorption/regeneration processes, it is important to account for the effect of heel formation. Heel build-up is described as the accumulation of species permanently and irreversibly adsorbed onto an adsorbent. Heel formation decreases the adsorbent capacity and lifetime, and thus increases the operation cost of emissions abatement system (Jahandar Lashaki et al., 2016, Fayaz et al., 2019, Mojtaba Hashemi et al., 2019). While heel can build up due to different mechanisms and factors (Jahandar Lashaki et al., 2016, Mojtaba Hashemi et al., 2019), a simple method to measure the extent of heel build-up is by monitoring the apparent density of the regenerated adsorbent; the higher heel-build up, the higher apparent density. To this end, the EGPF model was run and compared to experimental data for adsorbents with the apparent densities of 606, 707, 746, and 807 kg m^{-3}, consistent with adsorbents of different service lives (different levels of heel build-up).

Figure 4-8 depicts the overall removal efficiency as a function of apparent density when all operating conditions are set to those of the baseline case. The calculated removal efficiencies closely followed the experimental ones, indicating the ability of the model to predict the performance of adsorbents with a wide range of apparent densities in the lab-scale apparatus. However, more deviations from experimental results are expected when applying the model to the industrial-scale unit due to the difference in the designs and operation conditions discussed later.

Knowing the removal efficiencies for adsorbents with different ADs and taking into account the performance target and cost considerations (cost of adsorbents, reactivation process, etc.), the optimum service time of a batch of adsorbent can be estimated. At the baseline condition, the removal efficiency is always above 80% when the apparent density is kept lower than 700 kg m^{-3}.

Further increase in apparent density above 700 kg m^{-3} can result in a more rapid drop in removal efficiency.

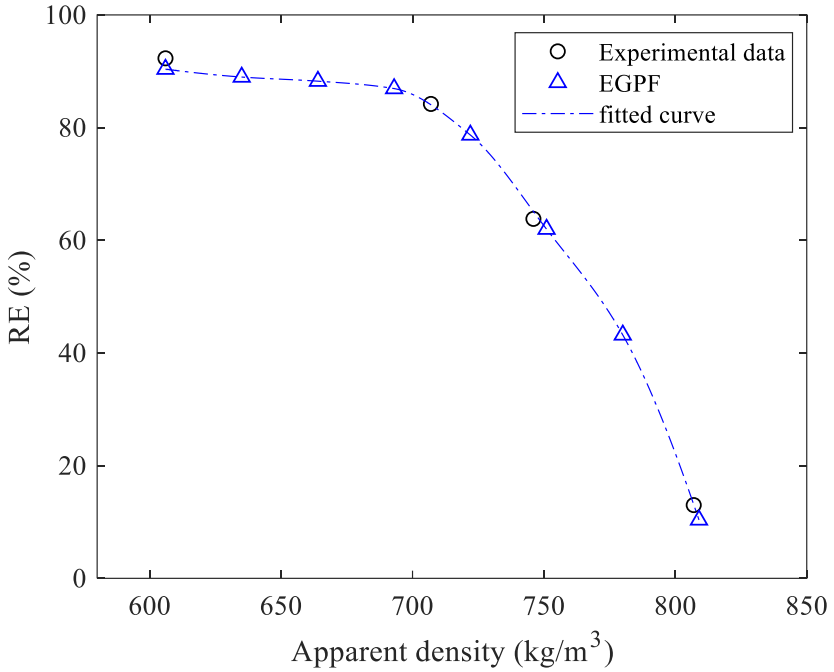

Figure 4-8. Comparison of experimental vs. EGPF model prediction of removal efficiency for the adsorption of SM on BAC with different apparent densities.

Stage-wise removal efficiency (Figure 4-9), on the other hand, shows some deviation from the experimental results especially in experiments no. 15 and 16 which could be attributed to two main factors: (i) model simplifying assumptions and (ii) experimental error. The constant bubble diameter along the bed, pseudo-first-order kinetics, and treating a mixture of solvents as a single compound (averaged values of physical/chemical properties and single-component adsorption instead of multi-component) are some examples of simplifying assumptions that might have led to such discrepancies. Minor experimental details might also introduce some experimental error. For instance, the ingress of fluidized particles into the inlet fitting of the sampling line connected to the FID might bias concentration measurement.

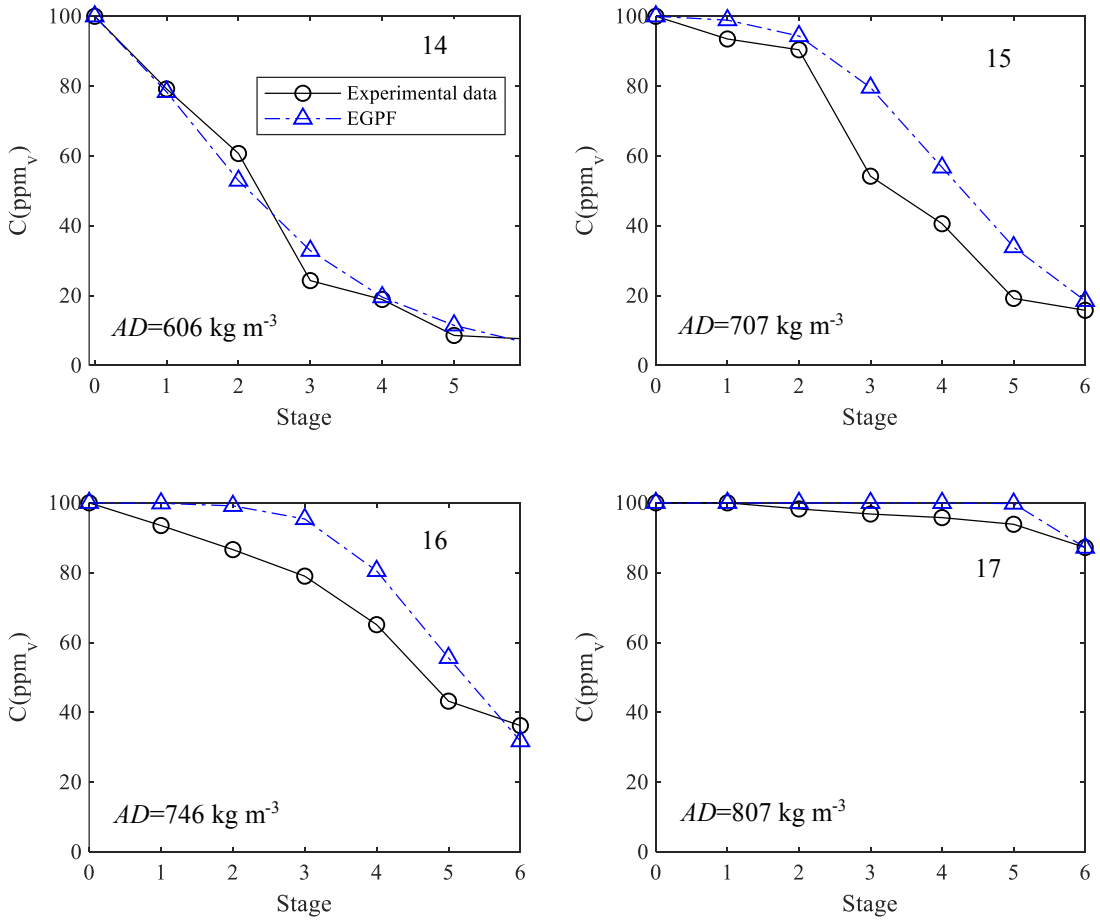

Figure 4-9. Stage-wise comparison of experimental vs. EGPF model prediction of gas-phase SM concentration in the fluidized bed operated at baseline scenario (F_p=0.44 g min^{-1}, F_g=300 SLPM, and C_0=100 ppm$_v$) with BAC with different ADs. The experiment number from Table 4-2 is shown on the top-right side of each diagram. Concentration at stage 0 denotes the inlet concentration.

To further assess the assumption of mole-weighted average values for molecular weight and air diffusivity, the sensitivity of EGPF model to these two parameters was evaluated for the experiments listed in Table 4-2. From the results demonstrated in Figure S4 in Supplementary Information, the model shows variations in the results in some cases after changing the value of molecular weight by ±10%. The deviation in the calculated removal efficiencies could be as big as 14% or as small as 0% depending on the operating condition. Therefore, even though assuming

a mole-weighted average value for the molecular weight of the solvent mixture is a common practice in adsorption calculations (Do, 1998), it might introduce some degree of error in the results in some cases.

The results, however, indicate that even doubling and halving the original value of the diffusion coefficient (3.2×10^{-6}-13×10^{-6} m^2/s) does not have a big influence on the model outcome. The selected range covers the diffusion coefficients for a wide range of organic chemicals as reported by Lugg (Lugg, 1968).

4.6.3. Adsorption in an industrial-scale fluidized adsorber

To verify the ability of the model to predict the performance of industrial-scale fluidized bed adsorbers, we used historical data from an industrial-scale fluidized bed system used for controlling emissions from an automotive painting booth. The industrial-scale fluidized bed adsorber comprises 6 rectangular stages with a cross-sectional area of 23.2 m^2. The weir height, the number of orifices on each stage, and the diameter of the orifices are 12.70 mm, 206,521, and 4 mm, respectively. Table 4-4 shows instantaneous snapshots of the operating conditions in the industrial-scale fluidized bed adsorber during the lifetimes of two BAC batches. The gas flow rate (F_g) and BAC feed rate (F_p) for all experiments were kept at 1.42×10^6 SLPM and 10.67 $ft^3\ hr^{-1}$, respectively. The latter translates into a range of 3,439 to 4,054 g min^{-1} depending on the AD.

Table 4-4. Experimental parameters and results for adsorption of SM in the industrial-scale fluidized bed adsorber.

Batch 1				Batch 2			
No.	Apparent density, *AD* (kg m^{-3})	Initial Conc. C_0 (ppm_v)	RE (%)	No.	Apparent density, *AD* (kg m^{-3})	Initial Conc. C_0 (ppm_v)	RE (%)
1	683	60.9	95.5	1	685	44.0	92.0
2	688	47.2	93.3	2	689	63.2	96.6
3	696	69.5	96.3	3	695	39.8	95.3
4	700	64.3	92.6	4	700	61.6	94.9
5	708	43.9	92.3	5	704	56.9	92.9
6	713	57.0	87.7	6	710	62.5	93.7
7	715	56.2	93.9	7	714	56.4	93.3
8	721	49.4	89.1	8	716	60.9	93.4
9	732	70.2	91.4	9	717	43.8	87.5
10	733	61.7	91.4	10	720	62.2	93.5
11	738	56.6	86.7	11	731	61.8	89.7
12	747	50.4	83.4	12	740	62.9	89.5
13	755	59.4	84.5	13	745	60.6	87.5
14	760	53.0	81.5	14	748	68.0	86.0
15	766	60.3	77.3	15	749	56.8	83.7
16	771	61.3	75.0	16	755	58.4	86.3
17	780	57.2	70.9	17	761	53.3	82.2
18	785	54.2	63.6	18	770	59.5	77.4
19	805	51.8	46.2	19	772	60.4	72.3

Figure 4-10 compares experimental and calculated removal efficiencies for the adsorption of SM on BAC with different ADs at different operating parameters in the industrial fluidized bed adsorber. This data along with that listed in Table 4-4 is demonstrated in Figure S5 in Supplementary Information bisected by the batch number.

It can be seen in Figure 4-10 that almost all (36 out of 38) predicted removal efficiencies were within absolute 10% of the experimental measurements with two points that showed absolute 11% and 12% deviation. The coefficients of determination for the 38 sets of experiments is 0.94. It should be noted that the difference between the circular cross section of the lab-scale adsorber and the rectangular cross section of the industrial-scale adsorber could be a source of error in calculations as the latter might create dead zones and cause edge effect. Another source of error lies in the difference in operating temperature as well as AD and concentration measurements which are more controlled in lab-scale operation compared to industrial-scale operation.

Incorporating relationships interpolating characteristics of the adsorbent (e. g. adsorption capacity, porosity, and pore width), the simulation of SM adsorption on BAC with different service lifetimes in a fluidized bed adsorber requires as inputs only the geometry of the bed, operating parameters, and apparent density of activated carbon. AD can be readily measured by weighing a fixed volume of the regenerated adsorbent samples and can be used as a surrogate for the degree of exhaustion of the adsorbent (ASTM International, 2014, Fayaz et al., 2019). Hence, the changes in AD after each adsorption/regeneration cycle can be incorporated with this model to predict the service time for a specific batch of adsorbents.

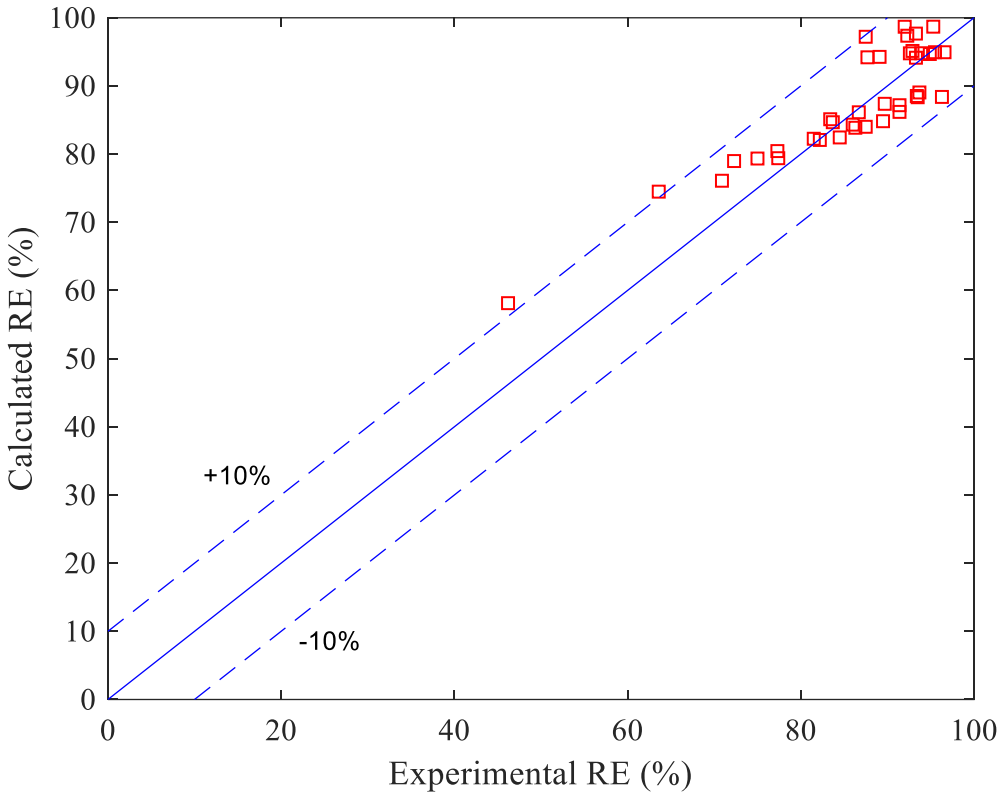

Figure 4-10. Experimental vs. calculated removal efficiencies for the adsorption of SM on BAC with different ADs at various operating conditions in an industrial fluidized bed.

4.7. Conclusion

A two-phase model was proposed to predict VOC adsorption in lab- and industrial-scale fluidized bed adsorbers. The model assumes the presence of a bubble phase free from adsorbent particles in plug flow, and an emulsion phase comprising the adsorbent particles and interstitial gas in perfectly mixed (EGPM) or plug flow (EGPF). The effect of operating conditions on the overall and stage-wise removal efficiency in two modes of EGPM and EGPF was investigated at different operating conditions (adsorbent feed rate, air flow rate, and initial concentration). EGPF produced slightly more accurate predictions (R^2=0.96 compared to 0.91) by diminishing the error as a result of employing the average VOC concentrations along the adsorbent layer in each stage. Important characteristics of the adsorbent (i.e. pore diameter, porosity, and adsorption capacity)

were correlated to its apparent density to allow the model to predict the performance of the fluidized bed running with adsorbents with different degrees of heel-build up (different service lives and apparent densities). The developed model was used to predict the performance of an industrial-scale fluidized bed adsorber with activated carbon of different levels of exhaustion. The calculated overall removal efficiencies were within absolute 10% of the measured ones in almost all (36 out of 38) test cases. The proposed model could help in overcoming the challenges of the scale-up, optimization, and operation of industrial fluidized bed adsorbers, leading to cost savings and performance improvements.

4.8. References

Abasaeed, A.E., Al-Zahrani, S.M., 1998. Modeling of Fluidized Bed Reactors for the Polymerization Reaction of Ethylene and Propylene. *Developments in Chemical Engineering and Mineral Processing*, **6**: 121-134.

ASTM International (2014). Standard Test Method for Apparent Density of Activated Carbon.

Cai, P., Schiavetti, M., De Michele, G., Grazzini, G.C., Miccio, M., 1994. Quantitative estimation of bubble size in PFBC. *Powder Technology*, **80**: 99-109.

Darton, R.C., Lanauze, R.D., Davidson, J.F., Harrison, D., 1977. Bubble Growth Due To Coalescence in Fluidized Beds. *Transactions of the Institution of Chemical Engineers*, **55**: 274-280.

Davidson, J.F., Harrison, D. (1963). Fluidized Particles. New York, Cambridge University Press.

Do, D.D. (1998). Adsorption Analysis: Equilibria And Kinetics. London, Imperial College Press.

Fayaz, M., Jahandar Lashaki, M., Abdolrazzaghi, M., Zarifi, M.H., Hashisho, Z., Daneshmand, M., Anderson, J.E., Nichols, M., 2019. Monitoring the residual capacity of activated carbon in an emission abatement system using a non-contact, high resolution microwave resonator sensor. *Sensors and Actuators B: Chemical*, **282**: 218-224.

Gallas, J.A.C., Herrmann, H.J., Sokołowski, S., 1992. Molecular dynamics simulation of powder fluidization in two dimensions. *Physica A: Statistical Mechanics and its Applications*, **189**: 437-446.

Garnavi, L., Kasiri, N., Hashemabadi, S.H., 2006. Mathematical modeling of a continuous fluidized bed dryer. *International Communications in Heat and Mass Transfer*, **33**: 666-675.

Hatzantonis, H., Yiannoulakis, H., Yiagopoulos, A., Kiparissides, C., 2000. Recent developments in modeling gas-phase catalyzed olefin polymerization fluidized-bed reactors: The effect of bubble size variation on the reactor's performance. *Chemical Engineering Science*, **55**: 3237-3259.

Hymore, K., Laguerie, C., 1984. Analysis and modelling of the operation of a counterflow multistage fluidized bed adsorber for drying moist air. *Chemical Engineering and Processing: Process Intensification*, **18**: 255-267.

Inglezakis, V.J., Poulopoulos, S.G. (2006). 6 - Reactors Scale-up. Adsorption, Ion Exchange and Catalysis. V. J. Inglezakis and S. G. Poulopoulos. Amsterdam, Elsevier**:** 523-550.

Jahandar Lashaki, M., Atkinson, J.D., Hashisho, Z., Phillips, J.H., Anderson, J.E., Nichols, M., 2016. The role of beaded activated carbon's pore size distribution on heel formation during cyclic adsorption/desorption of organic vapors. *Journal of Hazardous Materials*, **315**: 42-51.

Kamravaei, S., Shariaty, P. Jahandar Lashaki, M., Atkinson, J.D., Hashisho, Z., Phillips, J.H., Anderson, J.E., and Nichols, M. Crompton, D (2015). Effect of Operational Parameters on the Performance of a Multistage Fluidized Bed Adsorber. AIChE Annual Meeting. Salt lake City, UT, USA.

Keenan, J., Chao, J., Kaye, J., 1983. Gas Tables International Version-Thermodynamic Properties of Air, Products of Combustion and Component Gases. *Compressible Flow Functions*.

Khan, A.S.A. (2010). Installation and operation of autosorb-1-C-8 for BET surface area measurement of porous materials.

Khan, M.J.H., Hussain, M.A., Mansourpour, Z., Mostoufi, N., Ghasem, N.M., Abdullah, E.C., 2014. CFD simulation of fluidized bed reactors for polyolefin production – A review. *Journal of Industrial and Engineering Chemistry*, **20**: 3919-3946.

Kunii, D., Levenspiel, O. (1969). Fluidization engineering. New York, Wiley.

Loha, C., Chattopadhyay, H., Chatterjee, P.K., 2013. Euler-Euler CFD modeling of fluidized bed: Influence of specularity coefficient on hydrodynamic behavior. *Particuology*, **11**: 673-680.

Lu, W.-Z., Teng, L.-H., Xiao, W.-D., 2004. Simulation and experiment study of dimethyl ether synthesis from syngas in a fluidized-bed reactor. *Chemical Engineering Science*, **59**: 5455-5464.

Lugg, G.A., 1968. Diffusion coefficients of some organic and other vapors in air. *Analytical Chemistry*, **40**: 1072-1077.

McAuley, K.B., Talbot, J.P., Harris, T.J., 1994. A comparison of two-phase and well-mixed models for fluidized-bed polyethylene reactors. *Chemical Engineering Science*, **49**: 2035-2045.

Missen, R.W., Mims, C.A., Saville, B.A. (1999). Introduction to chemical reaction engineering and kinetics, Wiley New York.

Mohanty, C.R., Adapala, S., Meikap, B.C., 2009. Removal of hazardous gaseous pollutants from industrial flue gases by a novel multi-stage fluidized bed desulfurizer. *Journal of Hazardous Materials*, **165**: 427-434.

Mohanty, C.R., Malavia, G., Meikap, B.C., 2009. Development of a Countercurrent Multistage Fluidized-Bed Reactor and Mathematical Modeling for Prediction of Removal Efficiency of Sulfur Dioxide from Flue Gases. *Industrial & Engineering Chemistry Research*, **48**: 1629-1637.

Mohanty, C.R., Meikap, B.C., 2011. Modeling the operation of a three-stage fluidized bed reactor for removing CO2 from flue gases. *Journal of Hazardous Materials*, **187**: 113-121.

Mojtaba Hashemi, S., Jahandar Lashaki, M., Hashisho, Z., Phillips, J.H., Anderson, J.E., Nichols, M., 2019. Oxygen impurity in nitrogen desorption purge gas can increase heel buildup on activated carbon. *Separation and Purification Technology*, **210**: 497-503.

Mori, S., Wen, C.Y., 1975. Estimation of bubble diameter in gaseous fluidized beds. *AIChE Journal*, **21**: 109-115.

Na, K., Kim, Y.P., Moon, I., Moon, K.-C., 2004. Chemical composition of major VOC emission sources in the Seoul atmosphere. *Chemosphere*, **55**: 585-594.

Philippsen, C.G., Vilela, A.C.F., Zen, L.D., 2015. Fluidized bed modeling applied to the analysis of processes: review and state of the art. *Journal of Materials Research and Technology*, **4**: 208-216.

Poulopoulos, S.G., Inglezakis, V.J. (2006). Adsorption, ion exchange and catalysis: design of operations and environmental applications, Elsevier.

Roy, S., Mohanty, C.R., Meikap, B.C., 2009. Multistage Fluidized Bed Reactor Performance Characterization for Adsorption of Carbon Dioxide. *Industrial & Engineering Chemistry Research*, **48**: 10718-10727.

Seader, J.D., Henley, E.J. (2006). Separation process principles, John Wiley & Sons, Inc.

Tang, M., Cox, R., Kalberer, M., 2014. Compilation and evaluation of gas phase diffusion coefficients of reactive trace gases in the atmosphere: volume 1. Inorganic compounds. *Atmospheric Chemistry and Physics*, **14**: 9233-9247.

Tefera, D.T., Hashisho, Z., Philips, J.H., Anderson, J.E., Nichols, M., 2014. Modeling Competitive Adsorption of Mixtures of Volatile Organic Compounds in a Fixed-Bed of Beaded Activated Carbon. *Environmental Science & Technology*, **48**: 5108-5117.

Toomey, R.D., Johnstone, H.F., 1952. Gaseous Fluidization of Solid Particles. *Chemical Engineering Progress*, **48**: 220-226.

Werther, J., Hartge, E.-U., 2004. Modeling of Industrial Fluidized-Bed Reactors. *Industrial & Engineering Chemistry Research*, **43**: 5593-5604.

Yasui, G., Johanson, L.N., 1958. Characteristics of gas pockets in fluidized beds. *AIChE Journal*, **4**: 445-452.

Zhang, X., Gao, B., Creamer, A.E., Cao, C., Li, Y., 2017. Adsorption of VOCs onto engineered carbon materials: A review. *Journal of Hazardous Materials*, **338**: 102-123.

5. Chapter 5*: Modeling the Effect of Humidity and Temperature on VOC Removal Efficiency in a Multistage Fluidized Bed Adsorber

5.1. Abstract

The competitive adsorption of VOC and water vapor onto beaded activated carbon (BAC) in a fluidized bed adsorber was described by a two-phase model using the Manes method. The Manes method uses as input the single-component adsorption isotherms described by the Modified Dubinin-Radushkevich (MDR) model for adsorption of VOC and the Qi-Hay-Rood (QHR) model for adsorption of water vapor. The effect of temperature was accounted for later in the two-phase model using the Langmuir isotherm and the linear Van't Hoff relationship of its affinity coefficient. The simulation of the effect of relative humidity (RH) and temperature was validated using experimental data. Overall, very good agreement was observed between simulated and experimental results (e.g. R^2=0.97-0.98 when the overall removal efficiencies are compared). The results show that the effect of humidity on the adsorption of 1,2,4-trimethylbenzene (TMB) on BAC starts at 75% RH in the form of a reduction in overall removal efficiency as a result of a reduced number of available adsorption sites. The highest reduction in overall removal efficiency was 7.6% at RHs close to 100%. In dry condition, temperature variation had a small effect on removal efficiency, showing a reduction of 1.7% in overall removal efficiency when the adsorption temperature increased from 22 to 50 ˚C. On the other hand, at high RH values, temperature had a larger effect on removal efficiency due to RH change. Increasing the temperature by 5˚C increased

* This chapter is intended to be published as an original paper.

the removal efficiency by 6.9% for a stream of humid effluent (RH=95%). Taking into account the effect of humidity and temperature, the model can be used to optimize fluidized bed adsorbers operating at industrial conditions, leading to cost savings and performance improvements.

5.2. Nomenclature

Sym.	Description	Value /Formula	Units	Source
A	cross-section area of bed	4.56×10^{-3}	m^2	measured
a_p	external surface area per unit volume of particles	Table 5-2	m^{-1}	(Seader and Henley, 2006)
Ar	Archimedes number	Table 5-2	-	(Abasaeed and Al-Zahrani, 1998)
b	Langmuir coefficient	1.19×10^{5}	kg/kg	measured
C	VOC concentration	Eq. (5-1)	kg VOC/kg air	calculated
C^*	VOC concentration in air in equilibrium condition	Isotherms data	kg VOC/kg air	(Amdebrhan, 2018)
C_0	VOC concentration at bed entry	100 (ppm_v)	ppm_v, kg VOC/kg air	measured
C_b	VOC concentration in bubble phase	Eq. (5-3)	kg VOC/kg air	calculated
C_e	VOC concentration in emulsion phase	Eq. (5-4)	kg VOC/kg air	calculated
d_b	mean bubble diameter	Table 5-2	m	(Cai et al., 1994)
D_e	internal mass transfer coefficient	Table 5-2	$m^2\ s^{-1}$	(Seader and Henley, 2006)
D_g	VOC diffusivity in air	Table 5-1	$m^2\ s^{-1}$	(Tang et al., 2014)

D_k	Knudsen diffusion coefficient	Table 5-2	$m^2\ s^{-1}$	(Seader and Henley, 2006)
d_p	adsorbent mean diameter	Table 5-1	m	(Tefera et al., 2014)
d_{pore}	mean diameter of pores in adsorbent	Table 5-1	m	(Tefera et al., 2014)
F_g	air flow rate	300 (SLPM)	SLPM, $kg\ hr^{-1}$	measured
F_p	adsorbent feed rate	0.04 ($g\ min^{-1}$)	$g\ min^{-1}$, $kg\ hr^{-1}$	measured
g	standard gravity	9.8	$m\ s^{-2}$	(Abasaeed and Al-Zahrani, 1998)
H	weir height	0.004	m	measured
H_{mf}	height of bed on each stage at u_{mf}	Table 5-2	m	(Hymore and Laguerie, 1984)
IP	ionization potential	Table 5-1	eV	(Tefera et al., 2014)
K	MDR fitting parameter, a constant related to pore size distribution	Table 5-3	$mol^2\ J^{-2}$	calculated
k	adsorption rate constant	Table 5-2	s^{-1}	(Seader and Henley, 2006)
k'	coefficient	Eq. (5-6)	-	calculated
k_{QHR}	QHR fitting parameter	Table 5-3	-	calculated
m	slope of the isotherm	Table 5-2	kg air/kg BAC	calculated
M	VOC molecular weight	Table 5-1	$g\ mol^{-1}$	(Tefera et al., 2014)
N_b	number of bubbles per unit volume of bed	Table 5-2	m^{-3}	(Hymore and Laguerie, 1984)
P_{50}	QHR fitting parameter	Table 5-3	kPa	calculated
P_v^0	VOC vapor pressure in a single component system	N/A	kPa	N/A
P_v'	VOC vapor pressure in a mixture	N/A	kPa	N/A
P_{vS}	saturated VOC vapor pressure	Table 5-1	kPa	(Weast, 1981)

P_w^0	water vapor pressure in a single component system	N/A	kPa	N/A
P'_w	water vapor pressure in a mixture	N/A	kPa	N/A
P_{wS}	saturated water vapor pressure	Table 5-1	kPa	(Weast, 1981)
Q	mass transfer flow rate between a bubble and the particulate phase	Table 5-2	$m^3\ s^{-1}$	(Hatzantonis et al., 2000, Poulopoulos and Inglezakis, 2006)
q	VOC content of adsorbent	N/A	kg VOC/kg BAC	N/A
q^*	VOC equilibrium adsorption capacity for a single component system	Isotherms data	kg VOC/kg BAC	(Amdebrhan, 2018)
q_m	adsorbent maximum capacity in Langmuir equation	0.438	kg/kg	calculated
q_v	equilibrium adsorption capacity for VOC in a mixture	Eqs. (5-16) and (5-18)	kg/kg	calculated
q_w	equilibrium adsorption capacity for water vapor in a mixture	Eqs. (5-15) and (5-17)	kg/kg	calculated
RE	removal efficiency	Eq. (5-10)	-	(Hymore and Laguerie, 1984)
Re_{mf}	Reynolds number at u_{mf}	Table 5-2	-	(Abasaeed and Al-Zahrani, 1998)
R_g	gas constant	8.314×10^{-3}	kJ K^{-1} mol^{-1}	(Silberberg et al., 2016)
r_{mic}	adsorbent mean micropore width	Table 5-1	nm	(Tefera et al., 2014)
T	temperature	N/A	K	measured
u_0	superficial gas velocity	F_g/A	$m\ s^{-1}$	calculated
u_b	velocity of bubble rising through a bed	Table 5-2	$m\ s^{-1}$	(Kunii and Levenspiel, 1969)

u_{mf}	minimum fluidization velocity	Table 5-2	m s^{-1}	(Abasaeed and Al-Zahrani, 1998)
V_1	MDR fitting parameter, limiting adsorption volume for VOC in a single component system at low loadings	Table 5-2	cm^3 g^{-1}	calculated
V_b	bubble volume	Table 5-2	m^3	(Hymore and Laguerie, 1984)
v_v	molar volume of VOC adsorbed	M/ρ	cm^3 mol^{-1}	calculated
$V_{v,0}$	limiting adsorption volume for VOC in a single component system	Table 5-3	cm^3 g^{-1}	calculated
$V^0_{v,\max}$	adsorbed volume of VOC at its single-component relative pressure	Eq. (5-11)	cm^3 g^{-1}	(Kapoor et al., 1989)
$V_{v,\max}$	adsorbed volume of individual VOC at its mixture relative pressure	Eq. (5-13)	cm^3 g^{-1}	(Kapoor et al., 1989)
v_w	molar volume of water vapor adsorbed	M/ρ	cm^3 mol^{-1}	calculated
$V_{w,0}$	limiting adsorption volume for water vapor in a single component system	Table 5-3	cm^3 g^{-1}	calculated
$V^0_{w,\max}$	adsorbed volume of water vapor at single component relative pressure	Eq. (5-12)	cm^3 g^{-1}	(Qi et al., 1998)
$V_{w,\max}$	adsorbed volume of water vapor at its mixture relative pressure	Eq. (5-14)	cm^3 g^{-1}	(Qi et al., 1998)
W	mass of adsorbent on each stage	Table 5-2	kg	(Hymore and Laguerie, 1984)
X	coefficient	Eq. (5-5)	-	calculated
y	axis along the bed	N/A	m	N/A
Greek symbols				

α	coefficient	Eq. (5-8)	-	(Hymore and Laguerie, 1984)
α'	polarizability	Table 5-1	$\times 10^{-24}$ cm^3	(Tefera et al., 2014)
α''	MDR fitting parameter	Table 5-3	-	calculated
β	fraction of gas flowing as bubbles	Eq. (5-2)	-	(Hymore and Laguerie, 1984)
β'	affinity coefficient	Table 5-3	-	calculated
γ	surface tension	Table 5-1	mN m^{-1}	(Tefera et al., 2014)
ΔH_{ads}	heat of adsorption	Eq. (5-27)	kJ mol^{-1}	(Giraudet et al., 2006)
ΔH_{vap}	heat of vaporization	Table 5-1	kJ mol^{-1}	(Tefera et al., 2014)
ε_{mf}	void fraction at u_{mf}	Table 5-2	-	(Hymore and Laguerie, 1984)
ε_p	adsorbent internal porosity	Table 5-1	-	(Tefera et al., 2014)
ε_v'	adsorption potential of VOC in a mixture	Eq. (5-22)	J mol^{-1}	calculated
ε_v^0	adsorption potential of VOC in a single component system	Eq. (5-23)	J mol^{-1}	calculated
ε_w^0	adsorption potential of water vapor in a single component system	Eq. (5-24)	J mol^{-1}	calculated
μ_g	gas viscosity	Table 5-1	kg m^{-1} s^{-1}	(Keenan et al., 1983)
ρ_g	gas density	Table 5-1	kg m^{-3}	(Keenan et al., 1983)
ρ_p	adsorbent density	Table 5-1	kg m^{-3}	(Tefera et al., 2014)
τ	mean residence time of solids on each stage	Eq. (5-9)	s	(Hymore and Laguerie, 1984)
τ'	tortuosity	Table 5-2	-	(Poulopoulos and Inglezakis, 2006)
ϕ	adsorbent shape factor	Table 5-1	-	measured

5.3. Introduction

Volatile organic compounds (VOCs) are the main components in solvent-based paints, and can be found in the emissions from painting and coating operations such as automotive paint booths (Papasavva et al., 2001, Kim, 2011). VOCs are of environmental concerns due to their associated hazards for human health (Ramos et al., 2010, Kim, 2011) and their potential for contributing to urban air pollution (Kim, 2011). Adsorption in fluidized bed systems is an effective method for controlling VOC emissions from industries (Mohanty et al., 2009, Mohanty et al., 2009, Mohanty and Meikap, 2009, Mohanty and Meikap, 2011).

Models with various degrees of sophistication have been proposed in the literature for modeling the behavior of fluidized beds. While Computational Fluid Dynamics is still incapable of handling complicated processes in large geometries, either a two-phase model comprising bubble and emulsion phases or a three-phase model comprising an additional cloud phase can be used for describing the behavior of a fluidized bed (Philippsen et al., 2015). It is, however, reported that the latter employs more empirical equations which might make the calculations more time-consuming and less accurate, without having a significant advantage over the two-phase model in the practical range of operating parameters.

Cheng and Bi (Cheng and Bi, 2013) proposed a two-phase model for NOx adsorption in a fluidized bed. The model showed good agreement with experimental breakthrough curves and was used to study NOx concentration profiles along the bed. Hymore and Laguerie (Hymore and Laguerie, 1984) also derived a two-phase model that took into account the adsorption rate and residence time distribution of solids. Using the governing equations of this model, we previously proposed different simulations for the adsorption of 1,2,4-trimethylbenzene (TMB) (Davarpanah

et al., 2020) and a mixture of industrial solvents (Davarpanah et al., 2020) on beaded activated carbon (BAC).

In practical situations, however, industrial air streams might contain a certain amount of water vapor (up to 80-90 % relative humidity (RH) (Lodewyckx and Vansant, 1999)), depending on the type of process and/or the geographical location of the facility. For example, the water scrubber system designed to capture paint overspray in automotive painting booths can markedly increase the humidity of the VOC-laden air stream (Kim, 2011, Laskar et al., 2019). Similarly, a facility located in a humid environment might have high levels of humidity in its intake and effluent air streams. In these cases, humidity could interfere with VOC adsorption, leading to a reduction in the adsorption capacity of adsorbent towards VOCs. Depending on the extent of humidity interference, an additional treatment process might be necessary to avoid a reduction in removal efficiency (Laskar et al., 2019).

Changing the temperature of the effluent air stream may be considered as a way to improve the adsorption removal efficiency. Increasing the temperature would decrease the relative humidity which, in turn, could mitigate the interference of water vapor in the adsorption process. However, increasing the temperature is associated with a decrease in the maximum adsorption capacity in physical adsorption in the gas phase. In fact, an increase in temperature is expected to decrease the amount adsorbed on the surface of the adsorbent at a rate much faster than the increase in the surface diffusivity, leading to an overall reduction in removal efficiency whose extent depends on the thermodynamics of the adsorption process (Do, 1998). The conflicting effects of the temperature on the adsorption of VOCs from humid effluents suggest the importance of modeling the process.

Multicomponent adsorption of water vapor and VOCs in a fixed bed was studied by Laskar et al. (Laskar et al., 2019, Laskar et al., 2019) where single-component adsorption isotherms of adsorbates were used to predict the competitive adsorption process using Manes method. However, to the best of our knowledge, no research has investigated modeling multicomponent adsorption in a fluidized bed. This might be due to the complex dependence of the adsorption of different components to each other which is added to the intricacy of equations describing hydrodynamic and kinetic behavior of the bed.

The effect of temperature on adsorption removal efficiency in a fluidized bed was studied by Hymore and Laguerie (Hymore and Laguerie, 1984). In that study, however, the effect of temperature on adsorption capacity was not calculated through thermodynamic relations. The adsorption isotherms were first measured at three temperatures and then fitted with the Langmuir isotherm model. From the fitting, two equations were then derived to describe the Langmuir isotherm coefficients as a function of temperature (Hymore and Laguerie, 1984).

In this paper, competitive adsorption of VOC and water vapor is measured and modeled using a two-phase model incorporating the Manes method which only employs adsorption isotherms of single components in calculations. A thermodynamic approach is used to take into account the effect of temperature on the adsorption of VOC onto BAC without any further adsorption measurement. The results of this research could pave the way for a more realistic model that would be able to describe the behavior of FBs in real operating conditions with minimum input.

5.4. Experiments

5.4.1. Materials

Beaded activated carbon (BAC) and 1,2,4-trimethylbenzene (TMB) were used as the adsorbent and a VOC surrogate, respectively. The properties of adsorbent, adsorbates, and air are summarized in Table 5-1.

Table 5-1. The properties of adsorbent, adsorbates, and air.

Parameter	Value	Unit	Source
BAC mean diameter, d_p	7.5×10^{-4}	m	(Tefera et al., 2014)
BAC apparent density, ρ_p	601	kg m^{-3}	(Tefera et al., 2014)
BAC mean diameter of pores, d_{pore}	1.9×10^{-9}	m	measured
BAC internal porosity, ε_p	0.56	-	(Tefera et al., 2014)
BAC shape factor, ϕ	1	-	measured
BAC mean micropore width	1.02	nm	(Tefera et al., 2014)
TMB molecular weight, M	120.19	g mol^{-1}	(Tefera et al., 2014)
TMB diffusivity in air, D_g	6.45×10^{-6}	m^2 s^{-1}	(Tang et al., 2014)
TMB heat of vaporization	39.20	kJ mol^{-1}	(Tefera et al., 2014)
TMB polarizability	15.87	$\times10^{-24}$ cm^3	(Tefera et al., 2014)
TMB ionization potential	8.27	eV	(Tefera et al., 2014)
TMB surface tension	28.70	mN m^{-1}	(Tefera et al., 2014)
TMB saturated vapor pressure	0.30 (at 25 ˚C)	kPa	(Laskar et al., 2019)
Water vapor saturated pressure	3.17 (at 25 ˚C)	kPa	(Laskar et al., 2019)
Air density, ρ_g	1.20	kg m^{-3}	(Keenan et al., 1983)
Air viscosity, μ_g	1.82×10^{-5}	kg m^{-1} s^{-1}	(Keenan et al., 1983)

5.4.2. Experimental setup

Competitive adsorption of VOC and water vapor was conducted using a set up consisting of a lab-scale countercurrent fluidized bed adsorber, a humidity generation system, an adsorbate generation system, and an adsorbent feeder (Figure 5-1). More information about the fluidized bed apparatus including the trays and sampling tubes in the adsorber, the adsorbate generation system, the adsorbent feeder, etc. can be found elsewhere (Davarpanah et al., 2020, Davarpanah et al., 2020).

The fluidized bed was comprised of 6 Plexiglas cylindrical compartments (10.4 cm height and 7.6 cm ID) with a conical tube (a downcomer, 10-4 mm ID) on each stage which allowed for the transfer of adsorbent particles while maintaining an overflow height of 4 mm.

A Nafion™ gas humidifier (FC^{TM}, FC200-780-7MP) was used to humidify the air stream up to 93% RH. A water pump (Cole-Parmer, Masterflex®, 600 RPM) equipped with a speed controller circulated distilled water between the humidifier and a water container (3.4 L min^{-1}). The evaporation process inside the humidifier decreases the level and the temperature of the circulating distilled water inside the container. Make-up distilled water was occasionally added to the container to compensate for the consumed water, and the container was placed on a hot plate with a controlled temperature to counterbalance the temperature decrease. The humidity in the air stream was controlled by changing the temperature of distilled water and the air flow rate passing through the humidifier.

A baseline condition was defined as the air flow rate of 300 SLPM, the VOC initial concentration of 100 ppm$_v$, and the BAC feed rate of 0.44 g min^{-1}. All experiments for the effect of RH were conducted at the baseline condition, room temperature, and RH between 0 and 96%.

A heating tape (Omega®) connected to a variac (Staco Energy Products Co.) was used to control the temperature of the inlet VOC-laden stream. All experiments for the effect of temperature were conducted at the baseline condition, RH=0, and temperature between 22 and 50°C.

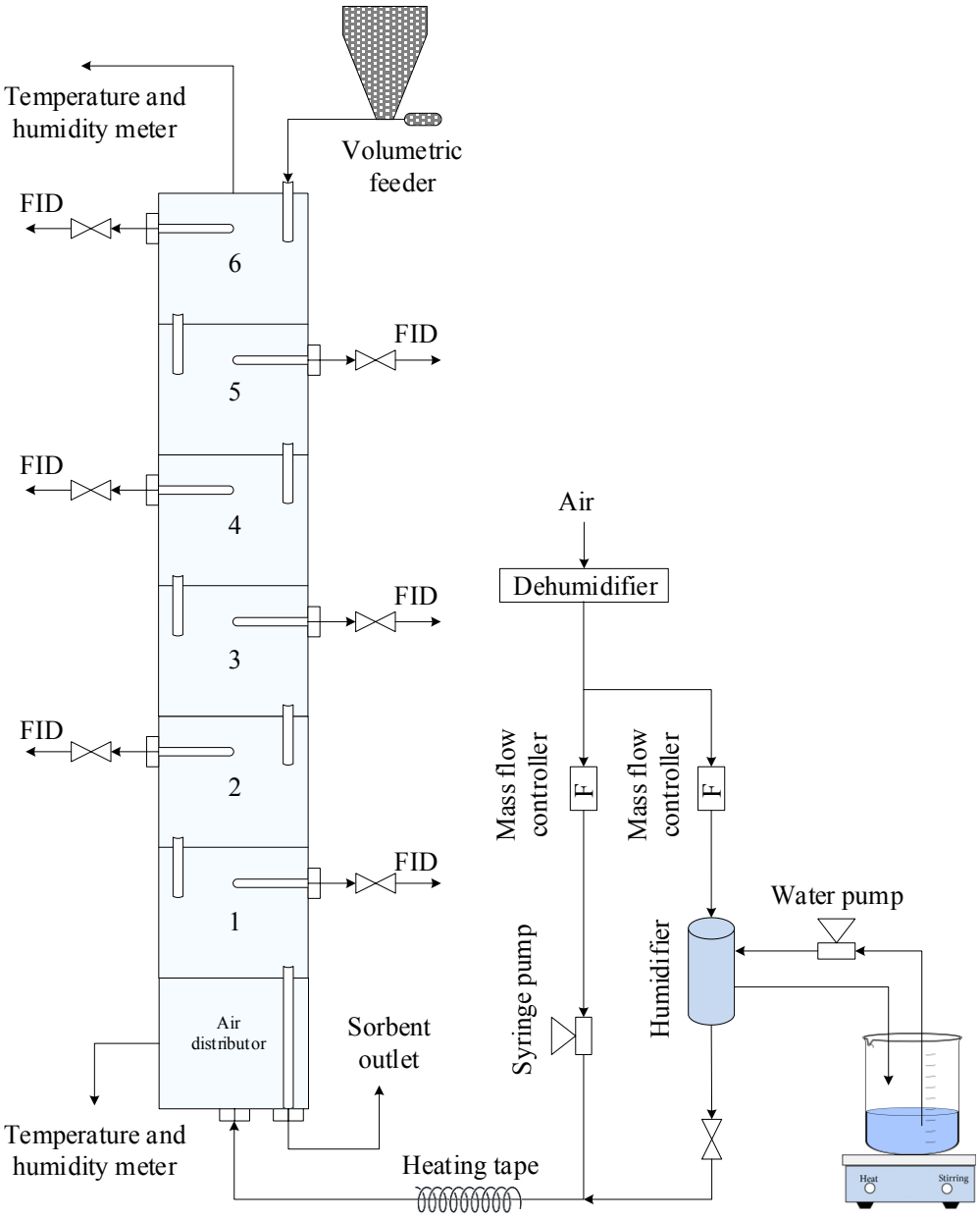

Figure 5-1. Schematic diagram of the fluidized bed apparatus.

5.5. Mathematical model

5.5.1. Two-phase model

A two-phase model was used to describe the adsorption of a VOC in the fluidized bed. According to the two-phase model, the fluidized bed is divided into two phases: an emulsion phase and a bubble phase. Depending on whether the emulsion gas is considered perfectly mixed or in plug flow, the model can be run in two modes of EGPM and EGPF, respectively. The governing equations for the two-phase model are derived with writing and solving the mass balance equations for gas in different phases at the top and bottom of a fluidized bed stage. The detailed assumptions and formulations for the two-phase model in EGPM and EGPF modes were explained elaborately in our previous studies (Davarpanah et al., 2020, Davarpanah et al., 2020). To simulate the adsorption of VOC in presence of water vapor, the concentration of water vapor along the bed is assumed constant. This assumption is valid at the conditions of this study as well as typical industrial emission control scenarios. Figure S6 (b) in Supplementary Information shows that the meaningful adsorption of water vapor on BAC (≥0.05 kg/kg) takes place at RH values in the range of 60-100%. In this range, the partial pressure of water vapor is between 1495.8 pa and 2493.2 pa (which is around 150-250 times the highest partial pressure of VOC along the bed at the condition of the experiments). Considering the equilibrium amount of VOC adsorbed at RHs>60% (Figure S6 (b)), the possible adsorption of water vapor on BAC is too slight to practically change the RH value along the bed. Consistently, humidity meters located at the top and bottom of the bed show no change in humidity along the bed.

We previously showed that both EGPM and EGPF provided similar accuracies when predicting the removal efficiency in the adsorption of TMB and a mixture of industrial solvents on BAC (Davarpanah et al., 2020, Davarpanah et al., 2020). However, in terms of calculations, EGPM

employs a simpler algorithm with a smaller number of trial and error loops which, in turn, makes it a better option for complex calculations than EGPF (Davarpanah et al., 2020). In this study, we are dealing with a multicomponent isotherm which is entangled, in many ways, in the calculations of the fluidized bed. Hence, to ensure convergence in the calculations and to reduce the computation time, the two-phase model is used in EGPM mode only.

According to the two-phase model, VOC concentration leaving the i^{th} stage of a multi-stage fluidized bed could be calculated using Eq. (5-1).

$$C_i = \beta C_{bi}\Big|_{y=H_w} + (1-\beta)C_{ei} \tag{5-1}$$

where,

$$\beta = 1 - \frac{u_{mf}}{u_0} \tag{5-2}$$

Writing a material balance on a single rising bubble, it can be shown that the concentration of VOC in the bubble phase is described by Eq. (5-3).

$$C_{bi}(y) = C_{ei} + \left(C_{i-1} - C_{ei}\right) exp\left(\frac{-Qy}{u_b V_b}\right) \tag{5-3}$$

where Q is the interphase mass transfer flow rate, u_b is bubble rise velocity, V_b is bubble volume, and C_{ei} and C_{bi} are TMB concentrations in the emulsion phase and bubble phase, respectively.

Writing a material balance on one stage of the fluidized bed with regard to VOC entering and exiting the stage, VOC exchanged between the particulate and bubble phases and VOC consumed in the adsorption process, it is shown that the concentration of VOC in the emulsion phase is described by the following correlations:

$$C_{ei} = \bar{C}^*_{ei} + \left(C_{i-1} - \bar{C}^*_{ei}\right)\left(\frac{1-\beta\exp(-X)}{1-\beta\exp(-X)+k_i'}\right) \tag{5-4}$$

$$X = \frac{QH_w}{u_b V_b} \tag{5-5}$$

$$k_i' = \frac{Wm_i k_i}{A\rho_g u_0} \tag{5-6}$$

If $\bar{q}_i$ is known, $\bar{C}^*_{ei}$ can be calculated using the adsorption isotherm.

$$\bar{q}_i = q_0 \prod_{j=0}^{i} \alpha_j + \sum_{j=1}^{i} q_j^* \left(1-\alpha_j\right) \prod_{k=j+1}^{i} \alpha_k \tag{5-7}$$

$$\alpha_j = \frac{1}{1+k_j\tau} \tag{5-8}$$

where τ can be calculated using the following equation:

$$\tau = \frac{W}{F_p} \tag{5-9}$$

Correlation of hydrodynamics and mass transfer incorporated in the two-phase model are listed in Table 5-2.

Table 5-2. Correlations used in the calculations of two-phase models.

Parameter	Formula	Reference
overall adsorption rate, k	$\frac{dq_i}{dt} = k_i\left(q_i^* - q_i\right) = k_i m_i\left(C_i - C_i^*\right)$ $k = \frac{60 D_e}{d_p^2 m}$ $D_e = \frac{\varepsilon_p}{\tau'}\left(\frac{1}{\frac{1}{D_g}+\frac{1}{D_k}}\right)$ $D_k = 48.5 d_{pore}\left(\frac{T}{M}\right)^{\frac{1}{2}}$	(Seader and Henley, 2006)
Mean bubble diameter, d_b	$d_b = 0.21\left(u_0 - u_{mf}\right)^{0.42} H^{0.8} \times \exp\left(-0.25\left(u_0 - u_{mf}\right)^2 - 0.1\left(u_0 - u_{mf}\right)\right)$	(Cai et al., 1994)
Bubble rise velocity, u_b	$u_b = u_0 - u_{mf} + 0.711\left(g d_b\right)^{\frac{1}{2}}$	(Kunii and Levenspiel, 1969)
Interphase mass transfer, Q	$Q = \left(\frac{1}{3}u_{mf} + \left(\frac{4\varepsilon_{mf} D_g u_b}{\pi d_b}\right)^{\frac{1}{2}}\right) \times \pi d_b^2$	(Hatzantonis et al., 2000, Poulopoulos and Inglezakis, 2006)
Minimum fluidization velocity, u_{mf}	$\frac{1.75}{\phi\varepsilon_{mf}^3}\mathrm{Re}_{mf}^2 + \frac{150\left(1-\varepsilon_{mf}\right)}{\phi^2\varepsilon_{mf}^3}\mathrm{Re}_{mf} - \mathrm{Ar} = 0$ $\mathrm{Re}_{mf} = \frac{\rho_g d_p u_{mf}}{\mu_g}$ $\mathrm{Ar} = \frac{\rho_g\left(\rho_p - \rho_g\right) g d_p^3}{\mu_g^2}$	(Abasaeed and Al-Zahrani, 1998)

Bed voidage at minimum fluidization, ε_{mf}	$\varepsilon_{mf} = \frac{1}{6}(6-\pi) = 0.472$	(Davidson and Harrison, 1963)
Mass of adsorbent on each stage, W	$W = \rho_p H_{mf} A\left(1-\varepsilon_{mf}\right)$	(Hymore and Laguerie, 1984)
Bed height at minimum fluidization, H_{mf}	$H_{mf} = H\left(1-\frac{u_0-u_{mf}}{u_b}\right)$	(Hymore and Laguerie, 1984)
Bubble volume, V_b	$V_b = \frac{\pi d_b^3}{6}$	(Hymore and Laguerie, 1984)
Number of bubbles per unit bed volume, N_b	$N_b = \frac{u_0-u_{mf}}{u_b V_b}$	(Hymore and Laguerie, 1984)
External specific surface area, a_p	$a_p = \frac{6}{d_p}$	(Seader and Henley, 2006)
Tortuosity, τ'	$\tau' = 1-\frac{1}{2}\ln\varepsilon_p$	(Poulopoulos and Inglezakis, 2006)

Finally, the removal efficiency (RE) is calculated using the following equation:

$$\mathrm{RE}(\%) = \frac{C_0 - C_6}{C_0} \times 100 \tag{5-10}$$

where C_0 and C_6 are VOC concentrations in the inlet gas stream and the top stage (stage #6), respectively.

5.5.2. Effect of humidity

A simplifying assumption in this study is that air properties (e.g. air density, air viscosity, and VOC diffusivity in air) are considered unchanged with the increase in humidity. Hence, the effect of humidity in the calculations of the fluidized bed is only reflected in the isotherms.

The competitive adsorption of water vapor and VOC in this study is described using a thermodynamically consistent approach developed by Manes (Manes, 1984). Manes method is

based on Polanyi model which assumes zero adsorption of water vapor wherever the adsorbed volume of organic adsorbate alone exceeds the adsorbed volume of water vapor alone. Manes method requires only the single-component adsorption isotherms of water vapor and VOC as inputs. Laskar et al. (Laskar et al., 2019, Laskar et al., 2019) used this method with slight modifications to calculate the competitive adsorption of water vapor and polar VOCs.

Modified Dubinin− Radushkevich (MDR) and Qi−Hay−Rood (QHR) equations are employed to describe the single-component adsorption isotherms of VOC and water vapor in the Manes method, respectively. They were chosen because they represent a good fit of the experimental data and because they were shown to be compatible with the Manes method (e.g. MDR and Manes are both based on Polanyi's Potential Theory) (Laskar et al., 2019, Laskar et al., 2019).

MDR isotherm for adsorption of VOC can be written as Eq. (5-11) (Kapoor et al., 1989):

$$V_{v,\max}^{0} = \left[1-\exp\left(-\alpha''\frac{P_v^0}{P_{vS}}\right)\right]V_{v,0}\exp\left[-\frac{K}{\beta'^2}\left(R_gT\right)^2\left(\ln\frac{P_{vS}}{P_v^0}\right)^2\right]+\exp\left(-\alpha''\frac{P_v^0}{P_{vS}}\right)V_1\frac{P_v^0}{P_{vS}} \tag{5-11}$$

where $V_{v,0}$, α, K/β^2, and V_1 are calculated by means of fitting the model to the experimental data.

QHR isotherm for adsorption of water vapor can be written as Eq. (5-12) (Qi et al., 1998):

$$V_{w,\max}^{0} = \frac{V_{w,0}}{1+\exp\left[k_{QHR}\left(\frac{P_{50}}{P_{wS}}-\frac{P_w^0}{P_{wS}}\right)\right]} \tag{5-12}$$

where, similar to MDR parameters, $V_{w,0}$, k_{QHR}, and P_{50}, are calculated by fitting.

Table 5-3 lists the parameters of MDR and QHR isotherms fitted to the equilibrium adsorption data of TMB and water vapor on BAC. A representation of isotherm graphs is shown in Figure S6 in Supplementary Information.

Table 5-3. The parameters of MDR and QHR isotherms for adsorption of TMB and water vapor on BAC at 298K.

Modified Dubinin− Radushkevich					
	$V_{v,0}$ (cm^3/g)	α'' (-)	$\beta'/K^{0.5}$(J/mol)	V_1 (cm^3/g)	R^2
TMB	0.44	130.03	32122.20	2.38	0.99
Qi−Hay−Rood					
	$V_{w,0}$ (cm^3/g)	k_{QHR} (-)	P_{50} (kPa)		R^2
Water vapor	0.49	26.45	2.13		0.98

The first step in Manes method is to calculate the adsorbed volume of the VOC by itself ($V_{v,\max}$) and the adsorbed volume of water vapor by itself ($V_{w,\max}$) at their corresponding relative vapor pressures in the mixture:

$$V_{v,\max} = \left[1-\exp\left(-\alpha''\frac{P_v'}{P_{vS}}\right)\right]V_{v,0}\exp\left[-\frac{K}{\beta'^2}\left(R_gT\right)^2\left(\ln\frac{P_{vS}}{P_v'}\right)^2\right] + \exp\left(-\alpha''\frac{P_v'}{P_{vS}}\right)V_1\frac{P_v'}{P_{vS}} \tag{5-13}$$

$$V_{w,\max} = \frac{V_{w,0}}{1+\exp\left[k_{QHR}\left(\frac{P_{50}}{P_{wS}}-\frac{P_w'}{P_{wS}}\right)\right]} \tag{5-14}$$

According to this method, the water vapor does not interfere with the adsorption of VOC when $V_{v,\max} > V_{w,\max}$ and therefore:

$$q_w = 0 \tag{5-15}$$

$$q_v = \rho_v V_{v,\max} \tag{5-16}$$

Competitive adsorption comes into play only when $V_{v,\max} < V_{w,\max}$. That is when the adsorption of VOC decreases as a result of its lower adsorption potential compared to water vapor.

$$q_w = \rho_w \left(V_{w,\max} - V_{v,\max}^0 \right) \tag{5-17}$$

$$q_v = \rho_v V_{v,\max}^0 \tag{5-18}$$

The volume of VOC adsorbed in this case is equal to the condensed water displaced:

$$V_{v,\max}^0 = V_{w,\max}^0 \tag{5-19}$$

Combining Eqs. (5-19) and (5-12) results in Eq. (5-20):

$$\frac{P_w^0}{P_{wS}} = \frac{P_{50}}{P_{wS}} - \frac{1}{k_{QHR}} \ln \left[\frac{V_{w,0}}{V_{v,\max}^0} - 1 \right] \tag{5-20}$$

Manes described the following equation based on the adsorption potential theory (Manes, 1984, Laskar et al., 2019):

$$\frac{\varepsilon_v'}{v_v} = \frac{\varepsilon_v^0}{v_v} - \frac{\varepsilon_w^0}{v_w} - \frac{R_g T}{v_w} \ln \frac{P_w'}{P_{wS}} \tag{5-21}$$

$$\varepsilon_v' = R_g T \ln \frac{P_{vS}}{P_v'} \tag{5-22}$$

$$\varepsilon_v^0 = R_g T \ln \frac{P_{vS}}{P_v^0} \tag{5-23}$$

$$\varepsilon_w^0 = R_g T \ln \frac{P_{wS}}{P_w^0} \tag{5-24}$$

The usage of potential theory makes the Manes method a good candidate for describing the competitive adsorption of water and immiscible VOCs such as TMB (TMB water solubility is 0.006 %w/w). More information about the Manes method including a flowchart describing the

numerical solution procedure is reported elsewhere (Laskar et al., 2019). In order to couple equations of Manes method (vapor pressures based) with those of the two-phase model (concentration based), the ideal gas law was used, along with appropriate conversion coefficients.

5.5.3. Effect of temperature

We previously discussed that the MDR isotherm is a good candidate for calculations of the Manes method since they are both based on Polanyi's Potential Theory, and therefore, thermodynamically consistent (Manes, 1984, Kapoor et al., 1989, Laskar et al., 2019). However, it was shown in other studies (Amdebrhan, 2018, Davarpanah et al., 2020) that the isotherms of TMB on BAC is well represented by Langmuir isotherm. In order to describe the effect of temperature here, the Langmuir isotherm is used which is simpler than MDR with fewer fitting parameters:

$$q^* = \frac{q_m b C^*}{1 + bC^*} \tag{5-25}$$

where q^* and C^* are the adsorption capacity and VOC concentration in equilibrium condition, and q_m and b are the maximum adsorption capacity and the Langmuir affinity coefficient, respectively. Parameters q_m and b were calculated to be 0.438 kg/kg and 1.19×10^{-5} kg/kg for adsorption of TMB on BAC, respectively (Davarpanah et al., 2020). A representation of Langmuir isotherm describing the adsorption of TMB on BAC is shown in Figure S7 in Supplementary Information.

The effect of temperature is taken into account by correlation below describing Langmuir affinity coefficient, b:

$$b = b_0 \exp\left(\frac{-\Delta H_{ads}}{RT}\right) \quad (5\text{-}26)$$

where b_0 is the pre-exponential constant in Langmuir isotherm, ΔH_{ads} is the heat of adsorption, and R and T are gas constant and temperature, respectively.

The heat of adsorption, ΔH_{ads} can be calculated using the model previously developed for adsorption of VOC onto activated carbon (Giraudet et al., 2006):

$$-\Delta H_{ads} = 103.2 + 1.16\alpha' + 0.76\Delta H_{vap} - 3.87IP - 0.7\gamma - 26.19r_{mic} \quad (5\text{-}27)$$

where α' is polarizability, ΔH_{vap} is the heat of vaporization, γ is surface tension, IP is the ionization potential, and r_{mic} is adsorbent mean micropore width (nm), all listed in Table 5-1.

5.6. Results and discussion

5.6.1. Effect of humidity

Figure 5-2 compares the experimental and modeled removal efficiencies as a function of RH for competitive adsorption of TMB and water vapor at room temperature. The removal efficiency was steady and unchanged up to a certain RH when a drop in removal efficiency is seen, followed by another plateau between RH 90% and 100%.

The modeled results show good agreement with the experimental data (R^2=0.98). According to the model, the effect of water vapor on the adsorption of TMB onto BAC is negligible below RH=75% due to the low affinity of water vapor molecules towards BAC in that range of RH. This is in agreement with previous studies reporting the effect of humidity on adsorption of VOCs onto activated carbon (Huggahalli and Fair, 1996, Qi et al., 2000, Laskar et al., 2019). At RH above 75%, however, the water vapor interferes with TMB adsorption, leading to a reduction in the

amount of TMB adsorbed which is consistent with the sharp increase in water vapor uptake in its single adsorption isotherm (see the water vapor isotherm on BAC in Figure S6 in Supplementary Information). The maximum reduction in TMB removal efficiency is 7.6%, at RH~100%. This relatively small reduction could be explained by the high adsorption affinity of TMB towards BAC which ensues from its non-polar characteristic. It was previously reported that the adsorption of water-miscible/polar VOCs (e.g. acetone and 2-propanol) is significantly impacted by humidity due to their low adsorption affinities towards BAC and their tendency for forming hydrogen bonds with water molecules during competitive adsorption (Laskar et al., 2019).

The experimental and modeled concentrations of TMB along the bed are presented in Figure 5-3 with their data listed in Table S5 in Supplementary Information. The model correctly predicted the experimental stage-wise concentrations of TMB over the range of 0-93% RH ($0.98<R^2<0.99$).

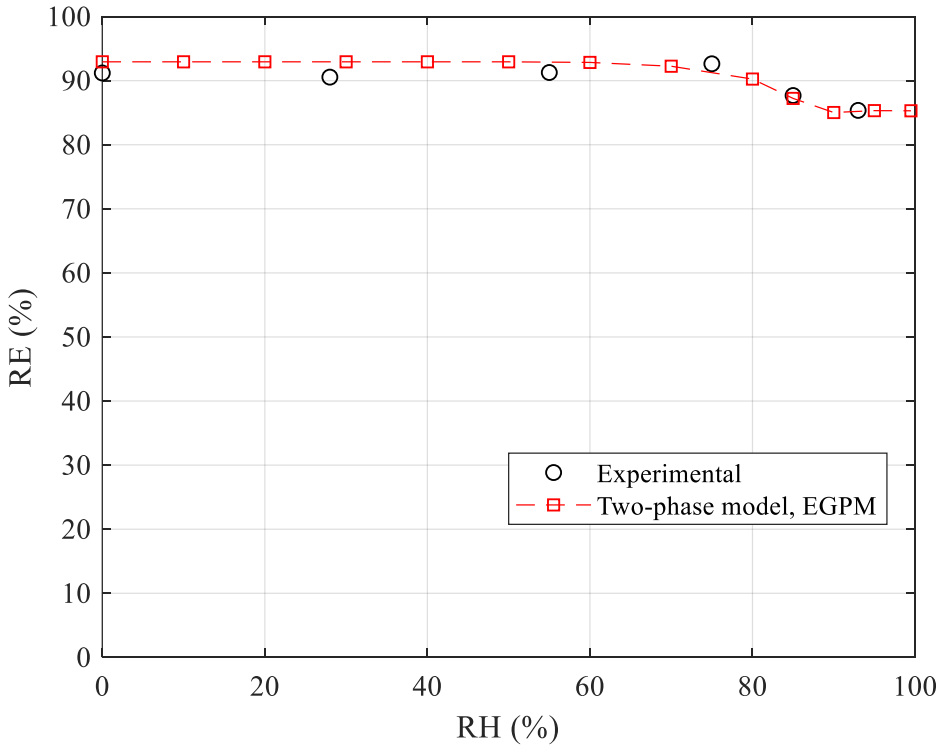

Figure 5-2.The effect of RH on the overall removal efficiency in the adsorption of TMB on BAC at baseline condition.

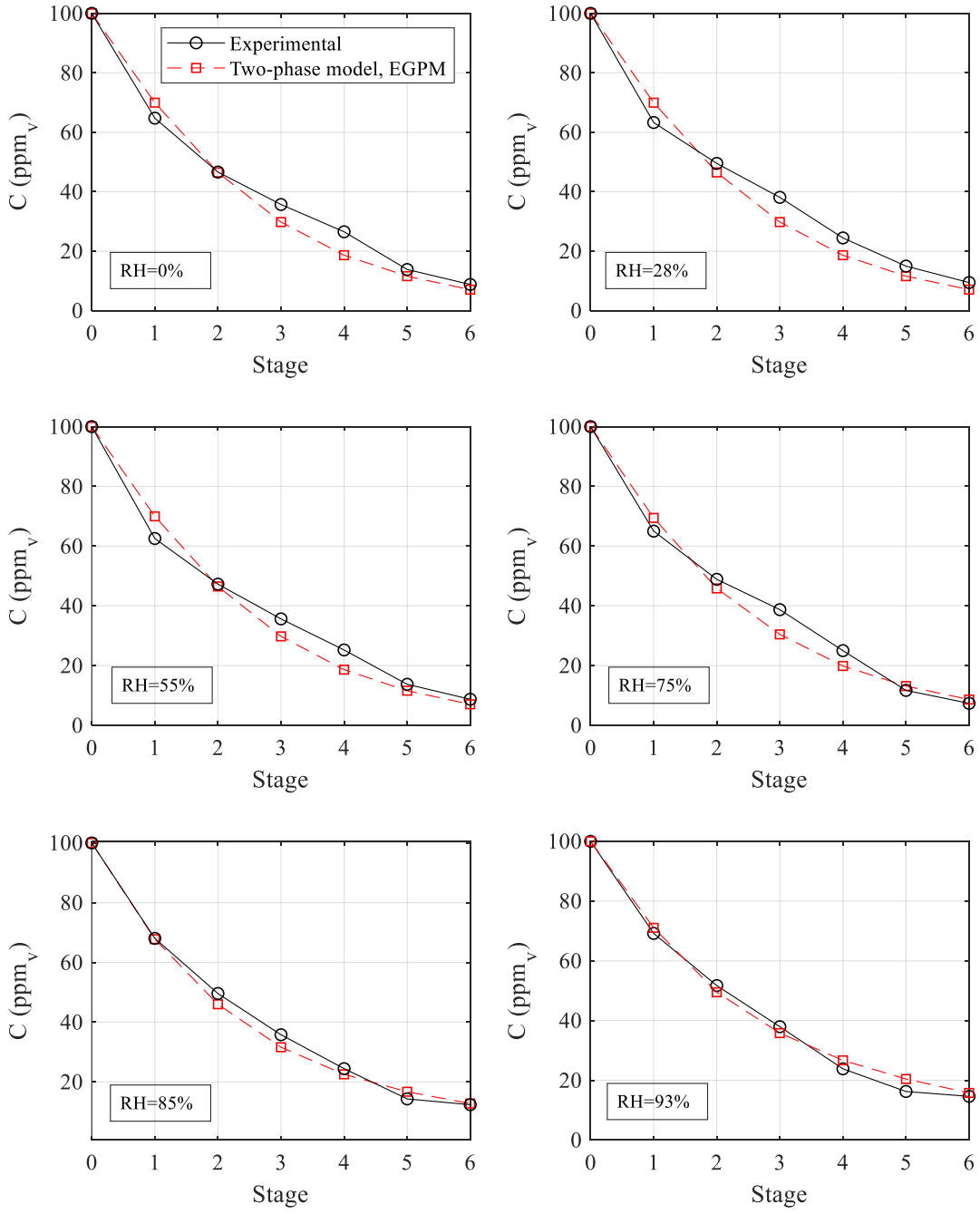

Figure 5-3. Stage-wise concentration of BAC along the bed at baseline condition and different RHs.

5.6.2. Effect of temperature

The overall removal efficiency in the adsorption of TMB on BAC at three different temperatures in the range of 22-50 °C is shown in Figure 5-4. In general, a downward trend is

observed for the overall removal efficiency. This can be explained by the negative value of enthalpy which indicates an exothermic reaction. According to Le Chatelier's principle, the addition of heat to a reaction (or increasing the temperature) works in favor of the endothermic direction of the reaction to reduce the amount of heat in the system (Silberberg et al., 2016). This trend is totally captured by the model (R^2=0.97). Some discrepancies between experimental and calculated results might be due to the simplifying assumptions used in the models (e.g. neglecting radial concentration gradients and considering constant bubble diameter along the bed) or error in experimental measurements. The latter is more explained later when the results of stage-wise concentration are discussed.

At low RH, increasing the temperature from 22 °C to 50 °C reduces the removal efficiency by 1.7% through changing the equilibrium adsorption capacity of TMB on BAC according to eq. (5-26). The extent of the reduction in removal efficiency, however, is specific to the operating conditions, as well as the adsorbent and adsorbate used in this study. It was previously shown that the impact of adsorption capacity on the overall removal efficiency in a fluidized bed varies at different operating conditions (Davarpanah et al., 2020). It is also expected that the effect of temperature on VOC removal efficiency is larger when the adsorption capacity is a limiting factor in the adsorption process.

The change to the isotherm, however, is not the only effect of temperature change. Increasing the temperature would also reduce the RH value by increasing the equilibrium vapor pressure of water. Since water vapor adsorption on activated carbon follows a type V isotherm, increasing the temperature can be used as a good strategy for keeping the RH value below the threshold of humidity influence, hence, recovering the removal efficiency. For example, for 100 ppm_v TMB at 95% RH and 25°C, increasing the temperature of the air stream by only 5 °C upstream of the

fluidized bed reduces the RH to 71%, where the competing effect of water vapor on TMB adsorption is negligible. The reduction of the removal efficiency by increasing the temperature is also expected to be negligible as depicted in Figure 5-4. Thus, the overall removal efficiency would increase by around 6.9%.

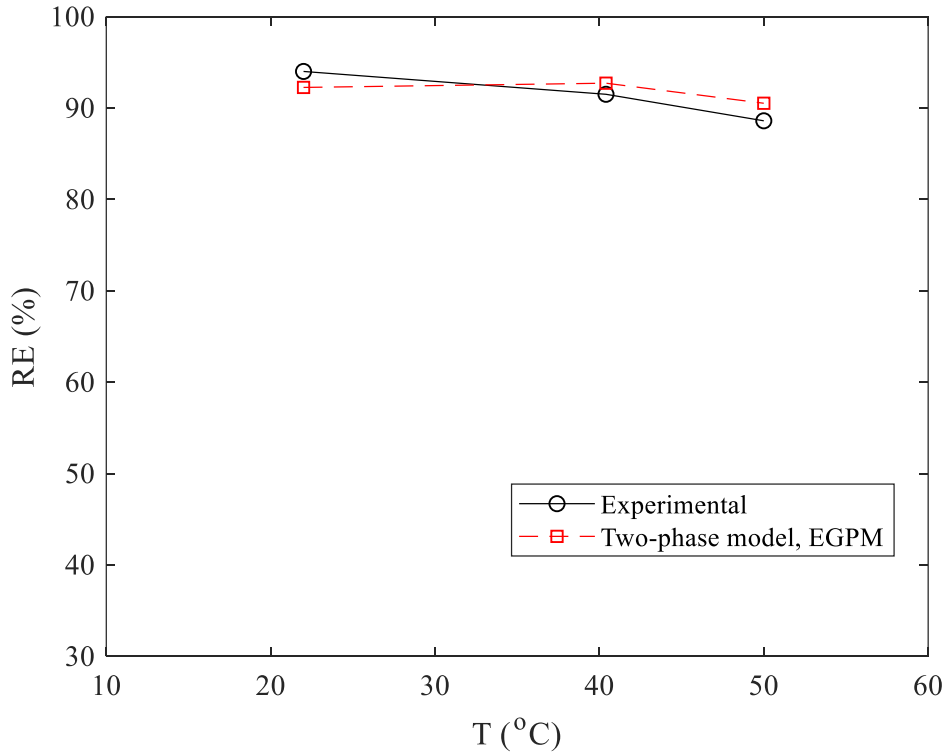

Figure 5-4. Experimental and predicted removal efficiencies as a function of temperature for adsorption of TMB on BAC.

Figure 5-5 shows the stage-wise concentration of TMB throughout the bed; with its corresponding data summarized in Table S6 in Supplementary Information. Overall, there is good agreement between experimental and predicted stage-wise concentrations at all three temperatures. At temperatures above 22°C, an unexpected peak is observed in TMB concentration in stage 2 which is most likely attributed to experimental error. For example, the formation of TMB droplets at the tip of the syringe needle in the adsorbate generation system is expected due to the high viscosity of TMB (2.011 cp at 20 °C). The droplet formation challenges the smooth injection of

VOC inside the pipe and creates fluctuations in the FID measurement, which in turn, would introduce some degrees of error to the stage-wise concentration. In order to minimize this error, glass wood was placed in the pipe to create a buffer for TMB and FID measurements were analyzed for outliers and averaged over the range of operation carefully.

Moreover, adsorbent particles might enter the gas sampling tubes due to the high agitation inside the fluidized bed and bias the measured concentrations. A mesh was placed at the inlet fitting of the sampling line but even a single adsorbent particle stuck on the mesh can be a source of error in concentration measurements.

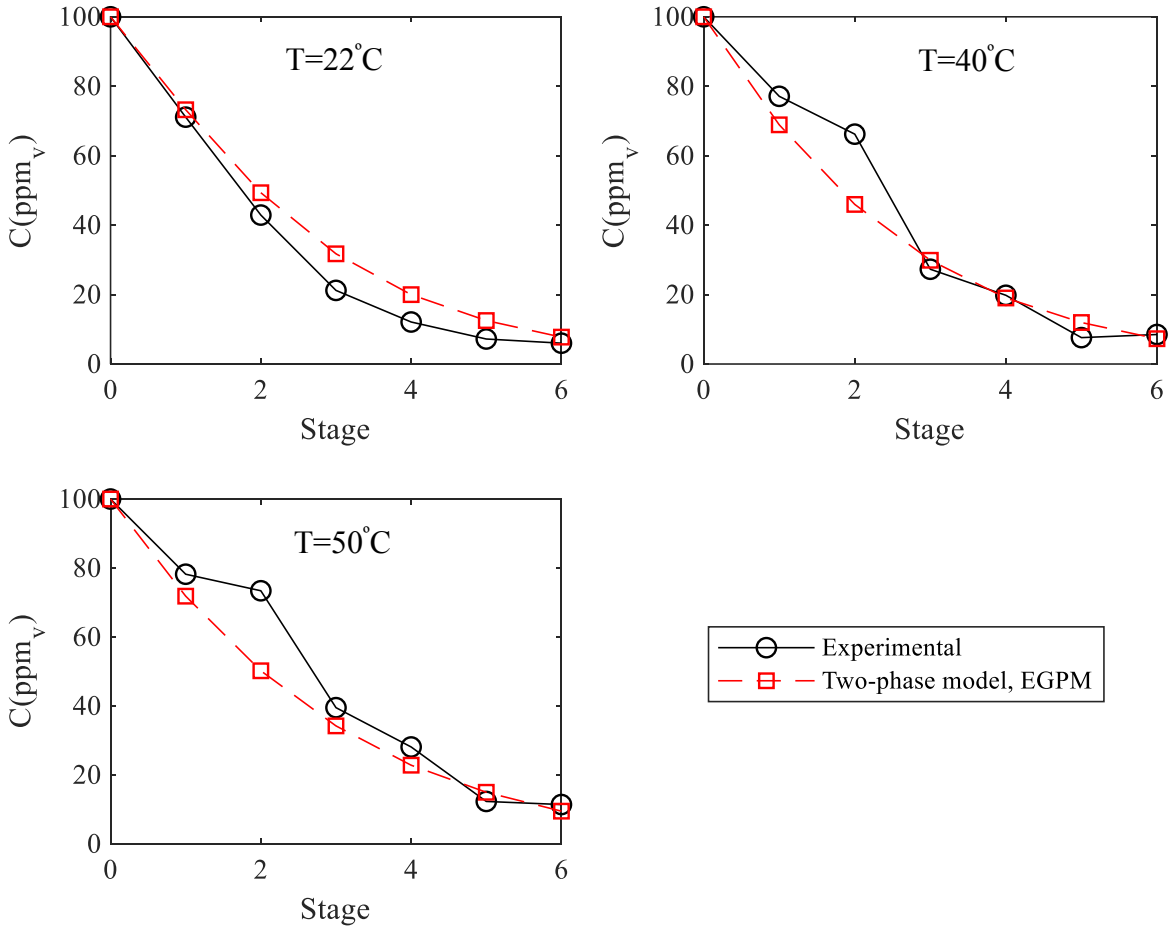

Figure 5-5. Stage-wise comparison of experimental vs. EGPM prediction of TMB concentration along the fluidized bed at different temperatures.

5.7. Conclusion

The effects of humidity and temperature on the adsorption of a VOC onto BAC were modeled using a two-phase model. Results showed that the impact of humidity on VOC removal efficiency was negligible below 75% RH. At higher values of RH, however, a drop in the removal efficiency was observed which eventually plateaued at RH close to 100% after decreasing the overall removal efficiency by 7.6 %. In dry condition, temperature had a small effect on removal efficiency. For instance, increasing the temperature from 22 to 50˚C resulted in a 1.7% reduction in the overall removal efficiency. However, at high RH values, increasing the temperature reduces the RH, which improves the removal efficiency. For instance, at 95% RH, a 5˚C increase in temperature can reduce the RH by 24%, which improves the removal efficiency by 6.9%. Although the magnitude of the effects of humidity and temperature reported in this study depends on the adsorbate, adsorbent, and the operating conditions, the model presented can still be used to maximize the performance of a fluidized bed adsorber operating at various industrial conditions including different values of RH and temperature.

5.8. References

Abasaeed, A.E., Al-Zahrani, S.M., 1998. Modeling of Fluidized Bed Reactors for the Polymerization Reaction of Ethylene and Propylene. *Developments in Chemical Engineering and Mineral Processing*, **6**: 121-134.

Amdebrhan, B.T. (2018). Evaluating the Performance of Activated Carbon, Polymeric, and Zeolite Adsorbents for Volatile Organic Compounds Control. Department of Civil and Environmental Engineering, University of Alberta. **Master of Science**.

Cai, P., Schiavetti, M., De Michele, G., Grazzini, G.C., Miccio, M., 1994. Quantitative estimation of bubble size in PFBC. *Powder Technology*, **80**: 99-109.

Cheng, X., Bi, X.T., 2013. Modeling and simulation of nitrogen oxides adsorption in fluidized bed reactors. *Chemical Engineering Science*, **96**: 42-54.

Davarpanah, M., Hashisho, Z., Crompton, D., Anderson, J.E., Nichols, M., 2020. Modeling VOC adsorption in lab- and industrial-scale fluidized bed adsorbers: Effect of operating parameters and heel build-up. *Journal of Hazardous Materials*, **400**: 123129.

Davarpanah, M., Hashisho, Z., Phillips, J.H., Crompton, D., Anderson, J.E., Nichols, M., 2020. Modeling VOC adsorption in a multistage countercurrent fluidized bed adsorber. *Chemical Engineering Journal*, **394**: 124963.

Davidson, J.F., Harrison, D. (1963). Fluidized Particles. New York, Cambridge University Press.

Do, D.D. (1998). Adsorption Analysis: Equilibria And Kinetics. London, Imperial College Press.

Giraudet, S., Pré, P., Tezel, H., Le Cloirec, P., 2006. Estimation of adsorption energies using the physical characteristics of activated carbons and the molecular properties of volatile organic compounds. *Carbon*, **44**: 2413-2421.

Hatzantonis, H., Yiannoulakis, H., Yiagopoulos, A., Kiparissides, C., 2000. Recent developments in modeling gas-phase catalyzed olefin polymerization fluidized-bed reactors: The effect of bubble size variation on the reactor's performance. *Chemical Engineering Science*, **55**: 3237-3259.

Huggahalli, M., Fair, J.R., 1996. Prediction of Equilibrium Adsorption of Water onto Activated Carbon. *Industrial & Engineering Chemistry Research*, **35**: 2071-2074.

Hymore, K., Laguerie, C., 1984. Analysis and modelling of the operation of a counterflow multistage fluidized bed adsorber for drying moist air. *Chemical Engineering and Processing: Process Intensification*, **18**: 255-267.

Kapoor, A., Ritter, J.A., Yang, R.T., 1989. On the Dubinin-Radushkevich equation for adsorption in microporous solids in the Henry's law region. *Langmuir*, **5**: 1118-1121.

Keenan, J., Chao, J., Kaye, J., 1983. Gas Tables International Version-Thermodynamic Properties of Air, Products of Combustion and Component Gases. *Compressible Flow Functions*.

Kim, B.R., 2011. VOC Emissions from Automotive Painting and Their Control: A Review. *Environmental Engineering Research*, **16**: 1-9.

Kunii, D., Levenspiel, O. (1969). Fluidization engineering. New York, Wiley.

Laskar, I.I., Hashisho, Z., Phillips, J.H., Anderson, J.E., Nichols, M., 2019. Competitive adsorption equilibrium modeling of volatile organic compound (VOC) and water vapor onto activated carbon. *Separation and Purification Technology*, **212**: 632-640.

Laskar, I.I., Hashisho, Z., Phillips, J.H., Anderson, J.E., Nichols, M., 2019. Modeling the Effect of Relative Humidity on Adsorption Dynamics of Volatile Organic Compound onto Activated Carbon. *Environmental Science & Technology*, **53**: 2647-2659.

Lodewyckx, P., Vansant, E.F., 1999. Influence of Humidity on Adsorption Capacity from the Wheeler-Jonas Model for Prediction of Breakthrough Times of Water Immiscible Organic Vapors on Activated Carbon Beds. *American Industrial Hygiene Association Journal*, **60**: 612-617.

Manes, M. (1984). Estimation of the effects of humidity on the adsorption onto activated carbon of the vapors of water-immiscible organic liquids. Engineering Foundation Conference. Bavaria, West Ger, Fundamentals of Adsorption**:** 335-344.

Mohanty, C.R., Adapala, S., Meikap, B.C., 2009. Removal of hazardous gaseous pollutants from industrial flue gases by a novel multi-stage fluidized bed desulfurizer. *Journal of Hazardous Materials*, **165**: 427-434.

Mohanty, C.R., Malavia, G., Meikap, B.C., 2009. Development of a Countercurrent Multistage Fluidized-Bed Reactor and Mathematical Modeling for Prediction of Removal Efficiency of Sulfur Dioxide from Flue Gases. *Industrial & Engineering Chemistry Research*, **48**: 1629-1637.

Mohanty, C.R., Meikap, B.C., 2009. Pressure drop characteristics of a multi-stage counter-current fluidized bed reactor for control of gaseous pollutants. *Chemical Engineering and Processing: Process Intensification*, **48**: 209-216.

Mohanty, C.R., Meikap, B.C., 2011. Modeling the operation of a three-stage fluidized bed reactor for removing CO2 from flue gases. *Journal of Hazardous Materials*, **187**: 113-121.

Papasavva, S., Kia, S., Claya, J., Gunther, R., 2001. Characterization of automotive paints: an environmental impact analysis. *Progress in Organic Coatings*, **43**: 193-206.

Philippsen, C.G., Vilela, A.C.F., Zen, L.D., 2015. Fluidized bed modeling applied to the analysis of processes: review and state of the art. *Journal of Materials Research and Technology*, **4**: 208-216.

Poulopoulos, S.G., Inglezakis, V.J. (2006). Adsorption, ion exchange and catalysis: design of operations and environmental applications, Elsevier.

Qi, S., Hay, K.J., Rood, M.J., 1998. Isotherm equation for water vapor adsorption onto activated carbon. *Journal of Environmental Engineering*, **124**: 1130-1134.

Qi, S., Hay, K.J., Rood, M.J., Cal, M.P., 2000. Equilibrium and heat of adsorption for water vapor and activated carbon. *Journal of Environmental Engineering*, **126**: 267-271.

Ramos, M.E., Bonelli, P.R., Cukierman, A.L., Ribeiro Carrott, M.M.L., Carrott, P.J.M., 2010. Adsorption of volatile organic compounds onto activated carbon cloths derived from a novel regenerated cellulosic precursor. *Journal of Hazardous Materials*, **177**: 175-182.

Seader, J.D., Henley, E.J. (2006). Separation process principles, John Wiley & Sons, Inc.

Silberberg, M.S., Venkateswaran, R., Amateis, P., Lavieri, S. (2016). Chemistry, McGraw-Hill Education.

Tang, M., Cox, R., Kalberer, M., 2014. Compilation and evaluation of gas phase diffusion coefficients of reactive trace gases in the atmosphere: volume 1. Inorganic compounds. *Atmospheric Chemistry and Physics*, **14**: 9233-9247.

Tefera, D.T., Hashisho, Z., Philips, J.H., Anderson, J.E., Nichols, M., 2014. Modeling Competitive Adsorption of Mixtures of Volatile Organic Compounds in a Fixed-Bed of Beaded Activated Carbon. *Environmental Science & Technology*, **48**: 5108-5117.

Weast, R.C. (1981). CRC Handbook of chemistry and physics : a ready-reference book of chemical and physical data. Boca Raton, Fla, CRC Press.

6. Chapter 6*: Process intensification in binary adsorption of VOC-water vapor on zeolite in a countercurrent fluidized bed adsorber

6.1. Abstract

In this study, the fast ideal adsorbed solution theory was coupled with a two-phase bubbling bed approach to describe the adsorption of volatile organic compounds (VOCs) on zeolite in the presence of water vapor in a multistage fluidized bed adsorber. The binary adsorption of VOC-water vapor was predicted using their single-component adsorption isotherms. The model was verified by experimental data obtained at a wide range of operating conditions before being used for studying the process intensification. Validation tests revealed that the model could accurately predict the experimental removal efficiencies (R^2=0.94), as well as VOC concentration profiles inside the bed (R^2=0.98). The intensification simulations showed that increasing the adsorbent feed rate is effective when there is a need for more adsorption sites (e.g. at high inlet concentrations), and is quite ineffective when the adsorption process is limited by low solid-gas contact time (e.g. high air flow rates). Increasing the adsorbent feed rate can also diminish the interference of water vapor in adsorption of VOC (even at RH as high as 75%). Reducing air flow rate at constant VOC load is always effective especially when there are enough adsorption sites available (e.g. high adsorbent feed rate, and low VOC loads and RHs). Similarly, increasing the number of stages can effectively improve the fluidized bed performance at high adsorbent feed rates and low VOC inlet concentrations and RHs. Using 3 adsorbers of 2 stages instead of 1 adsorber of 6 stages can improve the removal efficiency up to 34.5% in the range of operating conditions simulated. While

* This chapter is intended to be published as an original paper.

having the same high weir height along the bed yields better performance than having the same low weir height, an optimized arrangement of weir heights in a descending order from the top to the bottom of the bed would maximize the removal efficiency.

6.2. Introduction

Volatile Organic Compounds (VOCs) contribute to urban air pollution by forming photochemical smog (Yamamoto et al., 2010). It is estimated that approximately 1.9 million tonnes of VOCs were released in Canada in 2018, with the oil and gas industry being the largest contributor at 35% (674 kt) of the total emissions, followed by paints and solvents accounting for 22% (412 kt) of the national total (Government of Canada, 2020).

Treating dilute industrial VOCs emissions (<10,000 ppm_v) typically includes an adsorption process, either alone or as a pre-concentration step before a secondary treatment such as catalytic oxidation (Sullivan et al., 2004, Zheng et al., 2020). While various adsorption systems with different applications and performances have been introduced (Ghoshal and Manjare, 2002), fluidized bed adsorbers have attracted considerable attention due to their high efficiency, low pressure drops, continuous process, and good operational control (Hymore and Laguerie, 1984, Mohanty et al., 2009, Roy et al., 2009, Kamravaei et al., 2017).

Despite the widespread application of fluidized bed adsorbers in industries, their optimization and intensification can be challenging due to the complex processes involved (Hymore and Laguerie, 1984, Werther and Hartge, 2004). Understanding the operation of a fluidized bed requires good insights into the mass, momentum, and heat transfer inside the bed. The interconnected impacts of variables in a countercurrent fluidized bed could make the calculations so complicated that understanding the intricate effects of different parameters on the behavior of

the system is only possible through sophisticated modeling and simulation tools (Davarpanah et al., 2020). For example, a simple change in adsorbent diameter can influence the particle fluid dynamics and the solid-gas mass transfer in many ways, thereby altering the overall removal efficiency of the adsorber (Davarpanah et al., 2020).

Another challenge to modeling the fluidized bed in real life is the common presence of water vapor in industrial gas emissions (Laskar et al., 2019, Laskar et al., 2019). Depending on the type of process and the climate condition, emissions from industries might contain humidity which could interfere with VOC adsorption and reduce the performance of the adsorber. For example, emissions from a combustion process, an automotive painting booth running a water scrubber system, and any industries with humid air intake are likely to contain a considerable level of moisture (Lodewyckx and Vansant, 1999, Laskar et al., 2019). Even though the calculations of the competitive adsorption would significantly add to the complexity of fluidized bed modeling, taking into account the effect of humidity is critical to the development of a holistic model for simulating fluidized bed operation.

The effect of various operating parameters including adsorbent feed rate, initial concentration, gas flow rate, weir height, and the number of stages on the adsorption of VOCs was thoroughly investigated in our previous studies (Davarpanah et al., 2020, Davarpanah et al., 2020). There are also a few other studies on the same topic (Hymore and Laguerie, 1984, Mohanty et al., 2009, Mohanty and Meikap, 2011). The consensus in the literature is that decreasing the initial concentration and increasing the adsorbent feed rate, weir height and the number of stages would enhance the overall removal efficiency (Mohanty et al., 2009, Mohanty and Meikap, 2011, Davarpanah et al., 2020). However, there is a need for understanding the process intensification in fluidized bed operation. To the best of our knowledge, no research has ever reported on practical

plans for process improvement in a fluidized bed adsorber; and many questions concerning the best configuration of beds, the best arrangement of weir heights, and the optimum number of stages are all left unanswered.

On the other hand, studies on mathematical modeling of VOC-water vapor competitive adsorption in a fluidized bed are scarce. Lashkar et al. (Laskar et al., 2019) used the Manes method to describe multi-component adsorption of VOC and water vapor onto activated carbon in a fixed bed adsorber. However, there are fundamental differences (e.g. adsorption mechanisms and isotherms shapes) between the adsorption of water vapor on activated carbon and on zeolite which, in turn, requires different approaches for modeling (Halasz et al., 2002, Laskar et al., 2019). Moreover, compared to a fixed bed adsorber, the behavior of a fluidized bed adsorber is much more difficult to predict due to the formation of bubbles and the presence of two phases (gas and solid) in fluidized bed operation (Davidson and Harrison, 1963).

In this study, a modeling approach is presented to describe the adsorption of VOC on zeolite in the presence of water vapor in a multistage countercurrent fluidized bed adsorber. The model is then verified for common operational changes before being used for investigating the intensification of the adsorption system. The intensification approaches reported in this study can be effectively used for optimizing the design and operation of adsorbers for efficient VOC emissions control.

6.3. Model development and verification

The model parameters and variables are defined in Table 6-1.

Table 6-1. Model parameters and variables.

Sym.	Description	Value /Formula	Units	Source
A	cross-section area of bed	4.56×10^{-3}	m^2	measured
A'	adsorbent surface area	Table 6-3	$m^2\ g^{-1}$	measured
Ar	Archimedes number	Table 6-2	-	(Abasaeed and Al-Zahrani, 1998)
a_p	external surface area per unit volume of particles	Table 6-2	m^{-1}	(Seader and Henley, 2006)
b	parameter in O'Brien and Myers equation	Figure S8	pa^{-1}	calculated
C	TMB concentration	Eq. (6-1)	kg TMB/kg air	calculated
C^*	TMB concentration in air in equilibrium condition	Table S7	kg TMB/kg air	(Amdebrhan, 2018)
C_0	TMB concentration at bed entry	Table 6-4	ppm_v, kg TMB/kg air	variable
C_b	TMB concentration in bubble phase	Eq. (6-3)	kg TMB/kg air	calculated
C_e	TMB concentration in particulate phase	Eq. (6-4)	kg TMB/kg air	calculated
C_μ	adsorbed phase concentration	Eq. (6-13)	mol g^{-1}, g/g	calculated
$C_{\mu s}$	maximum adsorbed concentration	Figure S8	mol g^{-1}, g/g	calculated
$C_{\mu T}$	total amount adsorbed	Eq. (6-15)	mol g^{-1}, g/g	calculated
C_μ^0	adsorbed amount of pure component at the hypothetical pressure P^0	Eq. (6-15)	mol g^{-1}, g/g	calculated
d_b	mean bubble diameter	Table 6-2	m	(Cai et al., 1994)
D_e	internal mass transfer coefficient	Table 6-2	$m^2\ s^{-1}$	(Seader and Henley, 2006)
D_g	TMB diffusivity in air	Table 6-3	$m^2\ s^{-1}$	(Tang et al., 2014)

D_k	Knudsen diffusion coefficient	Table 6-2	$m^2\ s^{-1}$	(Seader and Henley, 2006)
d_p	adsorbent mean diameter	Table 6-3	m	measured
d_{pore}	mean diameter of pores in adsorbent	Table 6-3	m	measured
F_g	air flow rate	Table 6-4	SLPM, kg hr^{-1}	variable
F_p	adsorbent feed rate	Table 6-4	g min^{-1}, kg hr^{-1}	variable
g	standard gravity	9.8	m/s^2	-
H	weir height	4×10^{-3}	m	variable
H_{mf}	height of bed on each stage at u_{mf}	Table 6-2	m	(Hymore and Laguerie, 1984)
i	index of the stage number	-	-	-
k	adsorption rate constant	Table 6-2	s^{-1}	(Seader and Henley, 2006)
k'	coefficient	Eq. (6-6)	-	calculated
m	slope of the isotherm	Table 6-2	kg air/kg zeolite	calculated
M	TMB molecular weight	Table 6-3	g mol^{-1}	-
n	Index of the component number	-	-	-
N	total number of components	-	-	-
N_b	number of bubbles per unit volume of bed	Table 6-2	m^{-3}	(Hymore and Laguerie, 1984)
P	total pressure	Eq. (6-11)	pa	calculated
P^0	hypothetical pressure of the pure component that gives the same spreading pressure (π) on the surface	Eq. (6-11)	pa	calculated
Q	mass transfer flow rate between a bubble and the particulate phase	Table 6-2	$m^3\ s^{-1}$	(Hatzantonis et al., 2000, Poulopoulos and Inglezakis, 2006)

q	TMB content of adsorbent	-	kg TMB/kg zeolite	calculated
q^*	TMB content of adsorbent in equilibrium condition	Table S7	kg TMB/kg zeolite	(Amdebrhan, 2018)
R	gas constant	8.314×10^{-3}	kJ K^{-1} mol^{-1}	-
RE	removal efficiency	Eq. (6-10)	-	(Hymore and Laguerie, 1984)
Re_{mf}	Reynolds number at u_{mf}	Table 6-2	-	(Abasaeed and Al-Zahrani, 1998)
T	temperature	298	K	measured
u_0	superficial gas velocity	F_g/A	m s^{-1}	calculated
u_b	velocity of bubble rising through a bed	Table 6-2	m s^{-1}	(Kunii and Levenspiel, 1969)
u_{mf}	minimum fluidization velocity	Table 6-2	m s^{-1}	(Abasaeed and Al-Zahrani, 1998)
V_b	bubble volume	Table 6-2	m^3	(Hymore and Laguerie, 1984)
W	mass of adsorbent on each stage	Table 6-2	kg	(Hymore and Laguerie, 1984)
x	mole fraction in the adsorbed phase	-	-	-
X	coefficient	Eq. (6-5)	-	calculated
y	mole fraction in the gas phase	-	-	-
z	axis along the bed	-	m	-
z'	parameter	Eq. (6-13)	mol g^{-1}, g/g	(Do, 1998)
α	coefficient	Eq. (6-8)	-	(Hymore and Laguerie, 1984)
β	fraction of gas flowing as bubbles	Eq. (6-2)	-	(Hymore and Laguerie, 1984)
ε_{mf}	void fraction at u_{mf}	Table 6-2	-	(Hymore and Laguerie, 1984)
ε_p	adsorbent internal porosity	Table 6-3	-	measured
η	parameter	Eq. (6-18)	-	calculated

μ_g	gas viscosity	Table 6-3	kg m^{-1} s^{-1}	(Keenan et al., 1983)
π	spreading pressure	Eq. (6-13)	pa	(Do, 1998)
ρ_g	gas density	Table 6-3	kg m^{-3}	(Keenan et al., 1983)
ρ_p	adsorbent density	Table 6-3	kg m^{-3}	measured
σ^2	parameter in O'Brien and Myers equation	Figure S8	-	measured
τ	mean residence time of solids on each stage	Eq. (6-9)	s	(Hymore and Laguerie, 1984)
τ'	tortuosity	Table 6-2	-	(Poulopoulos and Inglezakis, 2006)
ϕ	adsorbent shape factor	Table 6-3	-	measured

6.3.1. Two-phase model

The two-phase model was thoroughly explained and expanded upon in our previous studies (Davarpanah et al., 2020, Davarpanah et al., 2020). According to the two-phase model, the fluidized bed is divided into two phases: an emulsion phase and a bubble phase, the latter is assumed to be free of solids. The gas in the emulsion phase could be considered perfectly mixed or in plug flow, resulting in two distinct modes of EGPM and EGPF, respectively. It was previously explained that both modes would produce results with similar accuracies while EGPM employs a simpler algorithm with a smaller number of trial and error loops which, in turn, makes it a better option for complex calculations where convergence is a challenging issue (Davarpanah et al., 2020).

In this study, the two-phase model is employed in EGPM mode to simulate the competitive adsorption of VOC-water vapor in a fluidized bed. It should be noted that this section presents only the formulas used in the simulation, while additional information including assumptions and

derivation of formulas can be found elsewhere (Hymore and Laguerie, 1984, Davarpanah et al., 2020).

Based on the two-phase model, VOC concentration leaving i^{th} stage of a multistage fluidized bed could be calculated using Eq. (6-1).

$$C_i = \beta C_{bi}\big|_{z=H} + (1-\beta)C_{ei} \tag{6-1}$$

where z is the axis along the bed, H is the weir height, C_{bi} and C_{ei} are VOC concentrations in bubble phase and emulsion phase, respectively; and:

$$\beta = 1 - \frac{u_{mf}}{u_0} \tag{6-2}$$

where u_{mf} and u_0 are minimum fluidization velocity and superficial gas velocity, respectively.

The concentration of VOC in the bubble phase is described by Eq. (6-3).

$$C_{bi}(z) = C_{ei} + (C_{i-1} - C_{ei})exp\left(\frac{-Qz}{u_b V_b}\right) \tag{6-3}$$

where Q is the interphase mass transfer flow rate, u_b is bubble rise velocity, and V_b is bubble volume.

The concentration of VOC in the emulsion phase is described by the following correlations:

$$C_{ei} = \bar{C}^*_{ei} + \left(C_{i-1} - \bar{C}^*_{ei}\right)\left(\frac{1-\beta\exp(-X)}{1-\beta\exp(-X)+k_i'}\right) \tag{6-4}$$

$$X = \frac{QH}{u_b V_b} \tag{6-5}$$

$$k_i' = \frac{Wm_i k_i}{A\rho_g u_0} \tag{6-6}$$

where H is the weir height, m is the slope of the isotherm, k is adsorption rate constant, A is the cross-section area of the bed, ρ_g is the air density, u_0 is the superficial air velocity, and $\bar{C}_{ei}^*$ is the concentration of TMB in equilibrium with $\bar{q}_i$ (eq. (6-7)).

$$\bar{q}_i = q_0 \prod_{j=0}^{i} \alpha_j + \sum_{j=1}^{i} q_j^* \left(1-\alpha_j\right) \prod_{k=j+1}^{i} \alpha_k \tag{6-7}$$

$$\alpha_j = \frac{1}{1+k_j\tau} \tag{6-8}$$

where k is the adsorption rate constant and τ can be calculated using the following equation:

$$\tau = \frac{W}{F_p} \tag{6-9}$$

where W is the mass of adsorbent on each stage and F_p is the adsorbent feed rate.

The hydrodynamic and mass transfer correlations incorporated in the two-phase model are listed in Table 6-2.

Table 6-2. Correlations used in the calculations of the two-phase model.

Parameter	Formula	Reference
Overall adsorption rate, k	$\frac{dq_i}{dt} = k_i\left(q_i^* - q_i\right) = k_i m_i\left(C_i - C_i^*\right)$ $k = \frac{60 D_e}{d_p^2 m}$ $D_e = \frac{\varepsilon_p}{\tau'}\left(\frac{1}{\frac{1}{D_g}+\frac{1}{D_k}}\right)$ $D_k = 48.5 d_{pore}\left(\frac{T}{M}\right)^{\frac{1}{2}}$	(Seader and Henley, 2006)
Mean bubble diameter, d_b	$d_b = 0.21\left(u_0 - u_{mf}\right)^{0.42} H^{0.8} \times \exp\left(-0.25\left(u_0 - u_{mf}\right)^2 - 0.1\left(u_0 - u_{mf}\right)\right)$	(Cai et al., 1994)
Bubble rise velocity, u_b	$u_b = u_0 - u_{mf} + 0.711\left(g d_b\right)^{\frac{1}{2}}$	(Kunii and Levenspiel, 1969)
Interphase mass transfer, Q	$Q = \left(\frac{1}{3}u_{mf} + \left(\frac{4\varepsilon_{mf} D_g u_b}{\pi d_b}\right)^{\frac{1}{2}}\right) \times \pi d_b^2$	(Hatzantonis et al., 2000, Poulopoulos and Inglezakis, 2006)
Minimum fluidization velocity, u_{mf}	$\frac{1.75}{\phi\varepsilon_{mf}^3}\mathrm{Re}_{mf}^2 + \frac{150\left(1-\varepsilon_{mf}\right)}{\phi^2\varepsilon_{mf}^3}\mathrm{Re}_{mf} - \mathrm{Ar} = 0$ $\mathrm{Re}_{mf} = \frac{\rho_g d_p u_{mf}}{\mu_g}$ $\mathrm{Ar} = \frac{\rho_g\left(\rho_p - \rho_g\right) g d_p^3}{\mu_g^2}$	(Abasaeed and Al-Zahrani, 1998)

Bed voidage at minimum fluidization, ε_{mf}	$\varepsilon_{mf} = \frac{1}{6}(6-\pi) = 0.472$	(Davidson and Harrison, 1963)
Mass of adsorbent on each stage, W	$W = \rho_p H_{mf} A(1-\varepsilon_{mf})$	(Hymore and Laguerie, 1984)
Bed height at minimum fluidization, H_{mf}	$H_{mf} = H\left(1-\frac{u_0-u_{mf}}{u_b}\right)$	(Hymore and Laguerie, 1984)
Bubble volume, V_b	$V_b = \frac{\pi d_b^3}{6}$	(Hymore and Laguerie, 1984)
Number of bubbles per unit bed volume, N_b	$N_b = \frac{u_0-u_{mf}}{u_b V_b}$	(Hymore and Laguerie, 1984)
External specific surface area, a_p	$a_p = \frac{6}{d_p}$	(Seader and Henley, 2006)
Tortuosity, τ'	$\tau' = 1-\frac{1}{2}\ln\varepsilon_p$	(Poulopoulos and Inglezakis, 2006)

Finally, the removal efficiency (RE) is calculated using the following equation:

$$\mathrm{RE}(\%) = \frac{C_0 - C_6}{C_0} \times 100 \tag{6-10}$$

where C_0 and C_6 are VOC concentration in the inlet gas stream and the uppermost stage, respectively.

6.3.2. Fast ideal adsorbed solution theory

Fast Ideal Adsorbed Theory (Fast-IAST) was used in this study to describe the binary adsorption of TMB and water vapor. IAST was first proposed by Myers and Prausnitz (Myers and Prausnitz, 1965) based on the analog Raoult's Law:

$$Py_n = x_n P_n^0(\pi) \tag{6-11}$$

for n=1, 2, 3, …, N; where P is the total pressure, y is the mole fraction in the gas phase, x is the mole fraction in the adsorbed phase, P^0 is the hypothetical pressure of the pure component that gives the same spreading pressure (π) on the surface, and N is the total number of components.

Eq. (6-11) is constrained by:

$$\sum_{n=1}^{N} x_n = 1 \tag{6-12}$$

Based on the Gibbs equation, P^0 can be calculated by defining the parameter of reduced spreading pressure as:

$$z'_n = \frac{\pi A'}{RT} = \int_0^{P_n^0} \frac{C_{\mu n}}{P} dP \tag{6-13}$$

where π is spreading pressure, A' is the adsorbent specific area, R is the universal gas constant, T is absolute temperature, C_μ is adsorbed phase concentration.

At equilibrium condition, all components have the same spreading pressure:

$$z'_1 = z'_2 = ... = z'_N \tag{6-14}$$

Eqs. (6-11)-(6-14) provides 2N+1 equations which are to be solved to obtain 2N+1 unknows (Do, 1998):

- Mole fractions in the adsorbed phase, x_n, (N+1 values)
- Spreading pressure, π (one value)
- Hypothetical pressures of pure components which give the same spreading pressures as that of the mixture, P_n^0, (N+1 values)

After finding the unknowns and assuming ideal mixing at constant π and T, the total amount adsorbed on the adsorbent is:

$$\frac{1}{C_{\mu T}} = \sum_{n=1}^{N} \frac{x_n}{C_{\mu n}^{0}} \tag{6-15}$$

where $C_{\mu T}$ is the total amount adsorbed and C_{μ}^{0} is the adsorbed amount of pure component at the hypothetical pressure P^0.

Knowing the total amount adsorbed, the concentration of component *n* on the adsorbent surface is calculated by the following equation:

$$C_{\mu n} = x_n C_{\mu T} \tag{6-16}$$

IAST is a versatile thermodynamic model that predicts multicomponent adsorption isotherms using a set of pure-component adsorption isotherms (Do, 1998). The choice of pure-component adsorption isotherms is arbitrary and any isotherms that fit the experimental data best can be used in this model (Do, 1998).

Despite all the advantages, the numerical calculation of the integration equation (Eq. (6-13)) for reduced spreading pressure is challenging as it usually imposes a high calculation load and reduces the convergence rate (Do, 1998). Langmuir equation is an exception because it gives an analytical solution for the integration equation. However, the Langmuir equation is not diverse enough to describe the experimental data of many practical systems as it contains only two fitting parameters (Do, 1998).

To tackle this issue, O'Brien and Myers (O'Brien and Myers, 1985, O'Brien and Myers, 1988) proposed the Fast-IAST method. They also introduced a three-parameter isotherm which is capable of describing many adsorption systems (Do, 1998). The O'Brien-Myers isotherm is obtained from two terms of a series expansion of the adsorption integral equation in terms of the central moments of the adsorption energy distribution (Do, 1998):

$$C_{\mu} = C_{\mu s}\left[\frac{\eta}{1+\eta} + \frac{\sigma^2\eta(1-\eta)}{2(1+\eta)^3}\right] \tag{6-17}$$

where,

$$\eta = bP^{0} \tag{6-18}$$

$C_{\mu s}$ is the maximum adsorbed concentration, and b and σ^2 are O'Brien and Myers isotherm parameters. The parameters $C_{\mu s}$, b, and σ^2 were determined by fitting the experimentally measured isotherm data (Table S7 in Supplementary Information) (Amdebrhan, 2018) using O'Brien and Myers isotherm model (Figure S8 in Supplementary Information).

Combining Eq. (6-17) and Eq. (6-13):

$$z' = C_{\mu s}\left[\ln(1+\eta) + \frac{\sigma^2\eta}{2(1+\eta)^2}\right] \tag{6-19}$$

Eqs. (6-19), (6-14) and (6-11), after some modifications, can be written into N equations:

$$z'_n(\eta_n) - z'_{n+1}(\eta_{n+1}) = 0 \tag{6-20}$$

for n=1, 2, 3, …, N-1; and:

$$\sum_{n=1}^{N}\frac{b_n P_n}{\eta_n} - 1 = 0 \tag{6-21}$$

The Newton-Raphson method was used to solve the Fast-IAST equations. The analytical derivative of the $z'(\eta)$ used in the Newton-Raphson method is:

$$\frac{dz'}{d\eta} = C_{\mu s}\left[\frac{1}{1+\eta} + \frac{\sigma^2(1-\eta)}{2(1+\eta)^3}\right] \tag{6-22}$$

A graphical representation of the solution to Fast-IAST for competitive adsorption of TMB and water vapor in the range of their measured isotherms is shown in Figure 6-1.

(a)

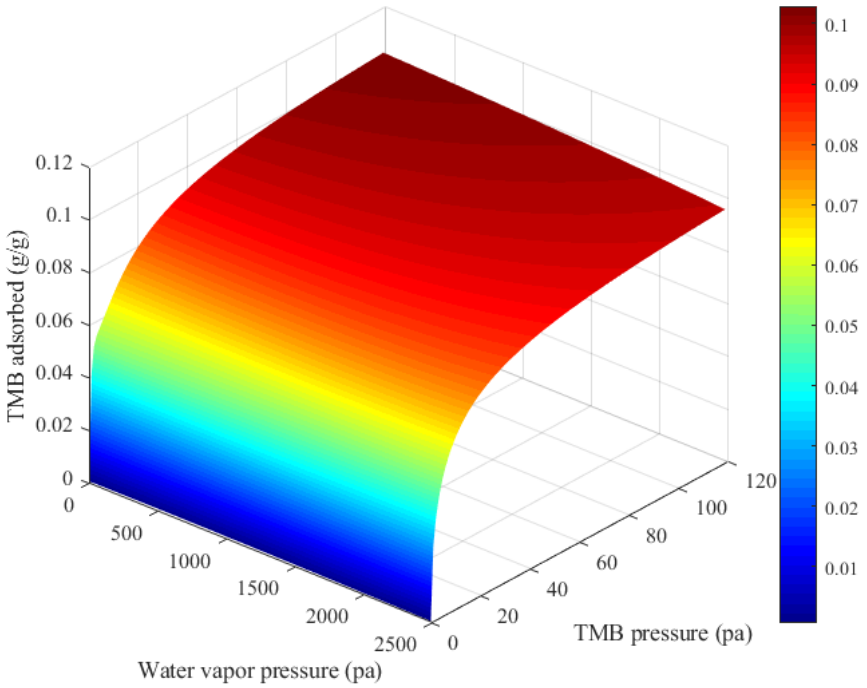

(b)

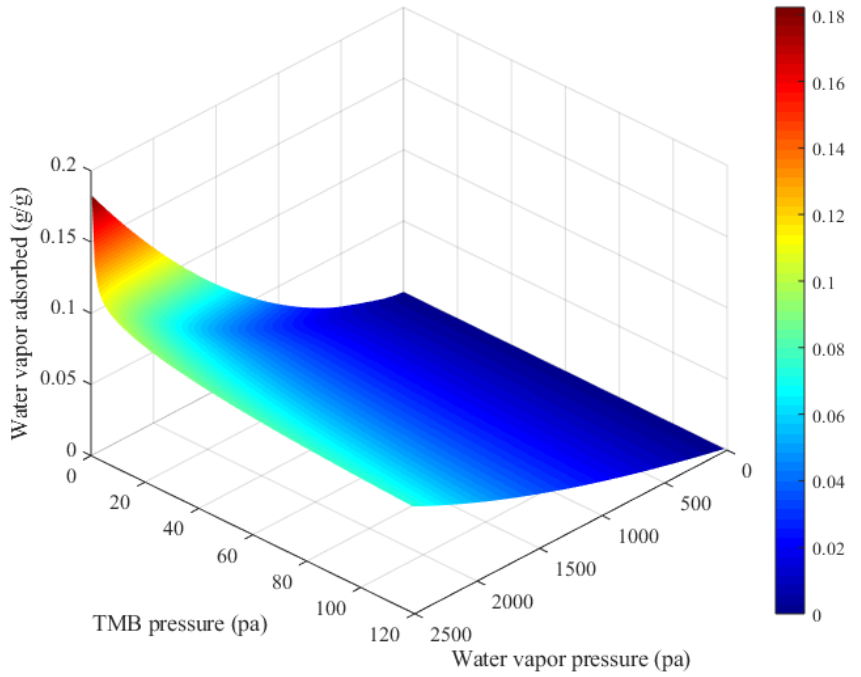

Figure 6-1. (a) TMB and (b) water vapor adsorbed in binary adsorption of TMB-water vapor on zeolite.

6.3.3. Model verification

1,2,4-Trimethylbenzene (TMB) was chosen as the VOC surrogate in this study. TMB is one of the major chemicals present in automotive painting booth air (Kim, 2011, Mojtaba Hashemi et al., 2019). Zeolite adsorbent used in this study was ZEOCAT F603 (ZEOCHEM®), consisting of USY and ZSM-5 (50:50 wt. %). The properties of adsorbent, adsorbates and air are summarized in Table 6-3.

Table 6-3. The properties of adsorbent, adsorbates and air.

Parameter	Value	Unit	Source
Zeolite mean diameter, d_p	5×10^{-4}	m	measured
Zeolite surface area, A'	380	$m^2\ g^{-1}$	measured
Zeolite apparent density, ρ_p	660	$kg\ m^{-3}$	measured
Zeolite mean diameter of pores, d_{pore}	4.16×10^{-9}	m	measured
Zeolite internal porosity, ε_p	0.23	-	measured
Zeolite shape factor, ϕ	1	-	measured
TMB molecular weight, M	120.19	$g\ mol^{-1}$	-
TMB diffusivity in air, D_g	6.45×10^{-6}	$m^2\ s^{-1}$	(Tang et al., 2014)
TMB saturated vapor pressure	0.30 (at 25 °C)	kPa	(Laskar et al., 2019)
Water vapor saturated pressure	3.17 (at 25 °C)	kPa	(Laskar et al., 2019)
Air density, ρ_g	1.20	$kg\ m^{-3}$	(Keenan et al., 1983)
Air viscosity, μ_g	1.82×10^{-5}	$kg\ m^{-1}\ s^{-1}$	(Keenan et al., 1983)

The lab-scale adsorber simulated consists of 6 Plexiglas cylindrical compartments (10.4 cm height and 7.6 cm ID) separated via perforated plates. There is a protruding conical downcomer

(10-4 mm ID) on each stage, which allows for particles transfer to the stage below. The protruding downcomer creates a weir height of 4 mm on each stage. More information about the fluidized bed apparatus including the adsorbent screw conveyor, adsorbate generation system, and VOC concentration measurement system is given elsewhere (Davarpanah et al., 2020, Davarpanah et al., 2020).

The experimental conditions used to verify the models are summarized in Table 6-4. Experiment no. 3 was chosen as a reference condition for additional investigation of intensification plans where need be. The experiments had been mostly conducted at the relative humidity of 30% to reduce electrostatic effects during operation. In experiments involving water vapor, a separate stream of air had been humidified up to 55-95% RH and then mixed with the VOC stream before being introduced into the adsorber.

Table 6-4. Experimental conditions for fluidized bed operation in adsorption of TMB on zeolite.

No.	Adsorbent feed rate, F_p, (g/min)	TMB Conc, C_0, (ppm_v)	Air flow rate, F_g, (SLPM)	TMB load, L_{TMB}, (μL/min)	Relative humidity (%)	Removal efficiency (%)
1	**1**	100	300	168	30	27.7
2	**1.7**	100	300	168	30	44.6
3*	**2.3**	100	300	168	30	51.5
4	**3.5**	100	300	168	30	64.0
5	2.3	**25**	300	**42**	30	85.2
6	2.3	**50**	300	**84**	30	67.4
7	2.3	**100**	300	**168**	30	51.5
8	2.3	**150**	300	**252**	30	38.2

9	2.3	100	**150**	**84**	30	92.8
10	2.3	100	**200**	**112**	30	83.2
11	2.3	100	**300**	**168**	30	51.5
12	2.3	100	300	168	**0**	67.2
13	2.3	100	300	168	**10**	57.5
14	2.3	100	300	168	**30**	51.5
15	2.3	100	300	168	**50**	47.5
16	2.3	100	300	168	**75**	35.4

* Reference condition

6.4. Results and discussion

6.4.1. Model verification

6.4.1.1. Effect of operating parameters on overall removal efficiency

The effect of different operating conditions on the overall removal efficiency in the adsorption of TMB on zeolite is shown in Figure 6-2. Overall, there is a good agreement between experimental data and predicted results. In fact, predicted removal efficiencies are within absolute 10% of the experimental measurements with R^2=0.94 (see Figure S9 in Supplementary Information).

According to the predicted results, the overall removal efficiency follows a continuously rising trend from 24.6 to 71.4% when the solid feed rate increases from 1 to 3.2 g min^{-1}. This is different from the adsorption of TMB on beaded activated carbon when an initial increase was observed with increasing the solid feed rate, followed by a plateau at higher solid feed rates (Davarpanah et al., 2020). The source of this discrepancy lies in the difference between the adsorption capacity of activated carbon and zeolite, with the former having 5 times the maximum adsorption capacity towards TMB than the latter (Davarpanah et al., 2020). The controlling factor in adsorption of

TMB on zeolite is primarily the adsorption capacity while that in adsorption on activated carbon is the adsorption kinetics. Hence, increasing the solid feed rate could increase the removal efficiency in adsorption of TMB on zeolite but has a negligible effect on the adsorption of TMB on activated carbon (Davarpanah et al., 2020).

From the modeled results plotted in Figure 6-2 (b), the overall removal efficiency decreases almost linearly from 78% to 39% when TMB initial concentration increases from 25 to 150 ppm_v. A similar descending trend is observed in removal efficiency with increasing the gas flow rate as a result of reduced adsorbent-adsorbate contact time (Figure 6-2 (c)). Both effects are consistent with those reported in the literature (Mohanty et al., 2009, Mohanty and Meikap, 2011, Davarpanah et al., 2020).

The effect of water vapor on the adsorption of TMB onto activated carbon is also captured by the model (Figure 6-2 (d)). Contrary to the adsorption of TMB on activated carbon in which the impact of water vapor does not appear until RH~60% (Laskar et al., 2019), the detrimental effect of water vapor on adsorption of TMB on zeolite starts at very low RHs. This is due to the major difference between the isotherm type of water vapor on activated carbon and zeolite. Water vapor adsorption on activated carbon typically follows type V isotherm due to the insignificant formation of water clusters bonded to surface functional groups at low pressures and the capillary condensation of water vapor inside the pores at high pressures (Laskar et al., 2019, Laskar et al., 2019). Water vapor adsorption on hydrophobic zeolite, in contrast, follows type III isotherm because the pore size distribution of the adsorbent allows for the adsorption of water molecules even at low pressures but the forces between water and zeolite surface are smaller than those between water molecules (Do, 1998, Halasz et al., 2002).

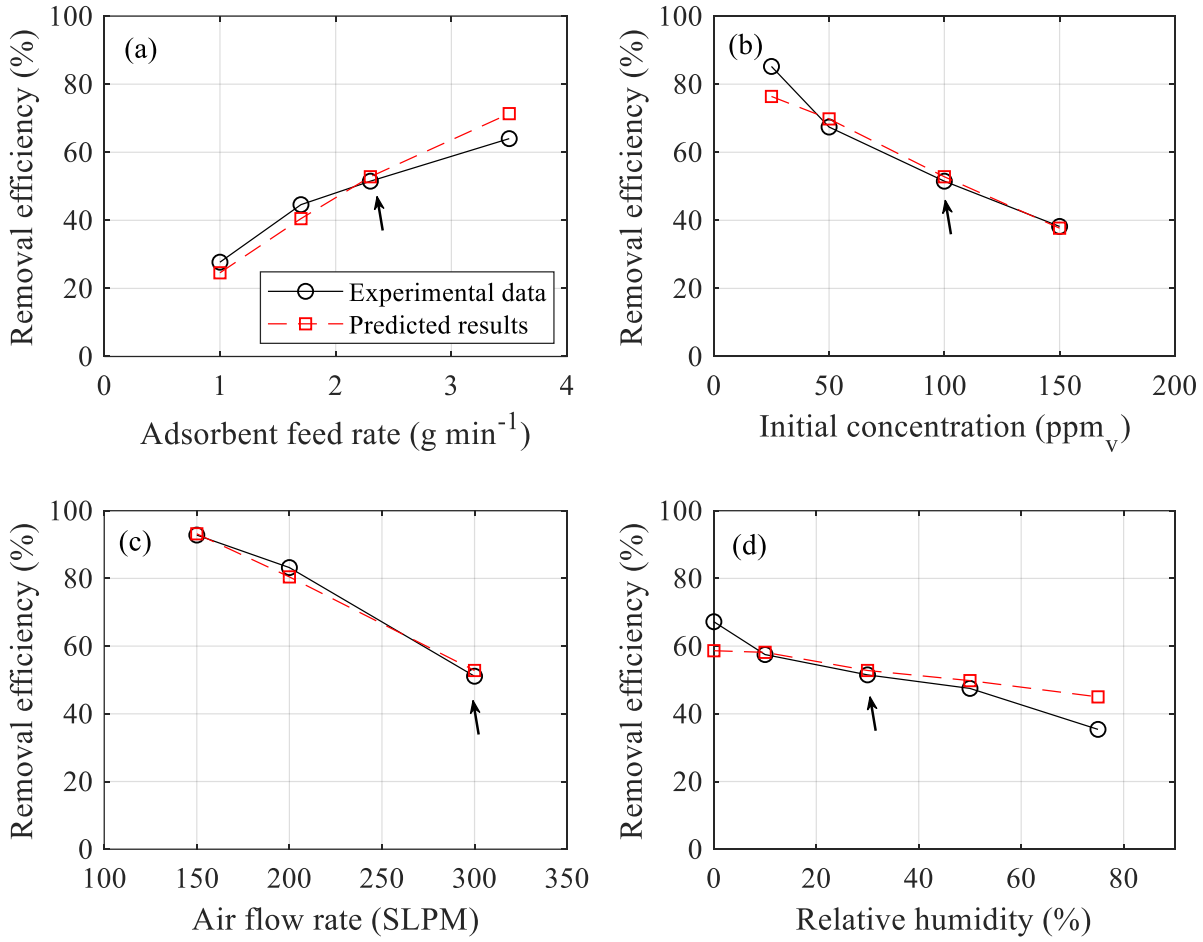

Figure 6-2. Experimental and predicted removal efficiencies as a function of (a) adsorbent feed rate (exp. no. 1-4), (b) initial concentration (exp. no. 5-8), (c) gas flow rate (exp. no. 9-11), and (d) relative humidity (exp. no. 12-16). Arrows in the figure indicate the reference case.

6.4.1.2. Effect of operating parameters on stage-wise concentration

The experimental and modeled stage-wise concentrations of TMB inside the bed are compared in Figure 6-3. The model results are also listed in Table S8 in Supplementary Information. In general, the model correctly predicts the experimental concentration of VOC along the bed (R^2=0.98). In some cases, such as experiments no. 2, 4, 5, 6, 12, and 16, small discrepancies between the experimental and modeled results are observed which might be related to model error and/or experimental error.

Model error is mainly due to the simplifying assumptions in both governing equations and empirical parameters which were elaborated in our previous studies (Davarpanah et al., 2020, Davarpanah et al., 2020). In experiments no. 5 and 6, however, the general overprediction of TMB concentration may ensue from the slight underprediction of TMB adsorption equilibrium data by O'Brien-Myers isotherm at low concentrations (see Figure S8 in the Supplementary Information).

Experiment no. 12 was conducted at RH=0%. In dry condition, adsorbent particles tended to adhere to the fluidized bed wall due to the electrostatic effect. More adsorbent on stages means lower experimental concentration compared to the model prediction. Another source of experimental error that might have affected experiments no. 2 is the ingress of the fluidized zeolite particles into the inlet fitting of the gas sampling line. Although a mesh was placed at the inlet fitting, a single zeolite particle being stuck on the mesh might bias the concentration measurement.

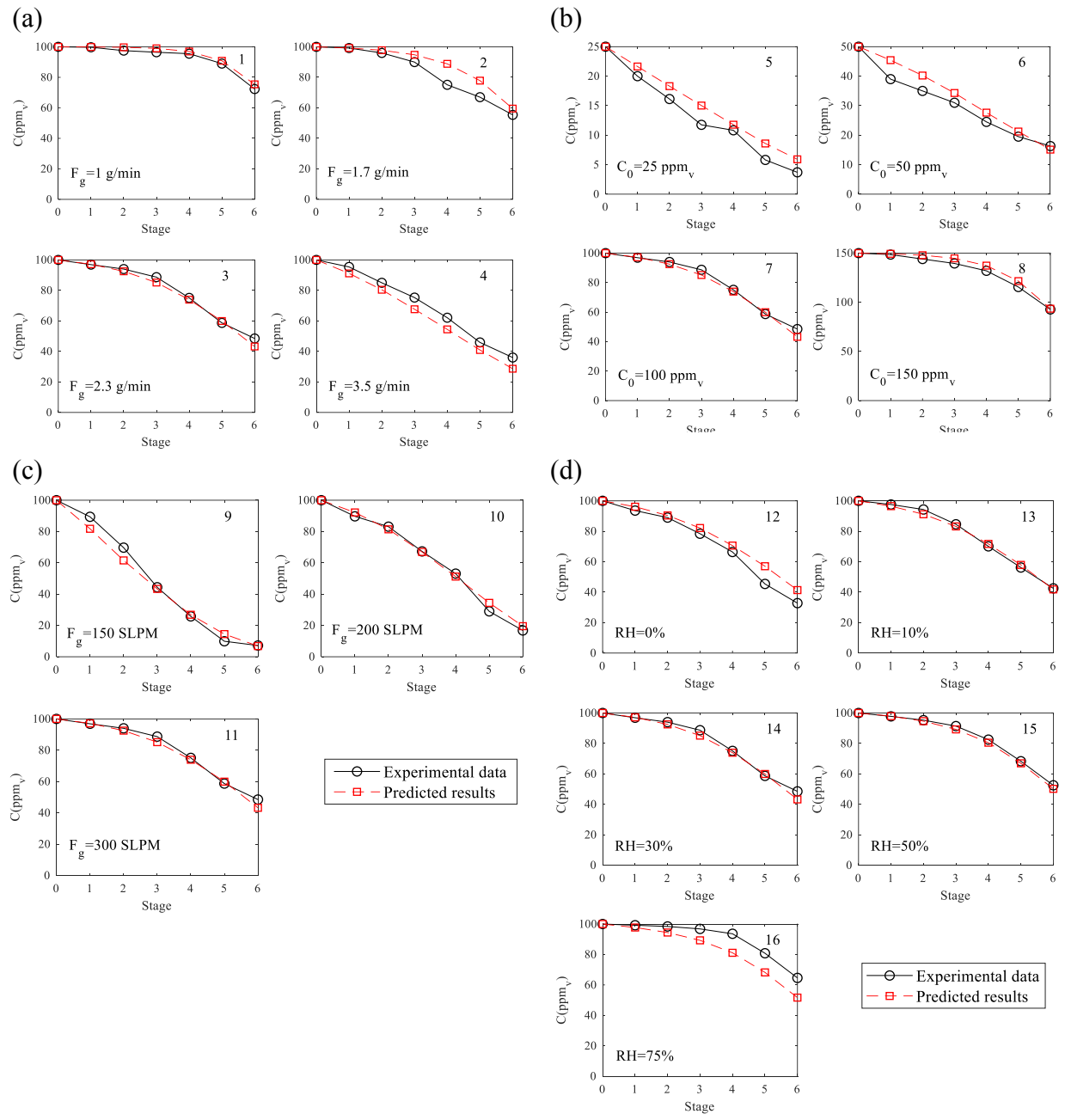

Figure 6-3. Stage-wise comparison of experimental vs. predicted results of TMB concentration in the fluidized bed in varying (a) adsorbent feed rate, (b) initial concentration, (c) air flow rate, and (d) relative humidity. Experiment numbers from Table 6-4 are shown on the top-right side of diagrams. The reference case is shown in diagram no. 3, 7, 11, and 14. Concentration at stage 0 denotes the inlet concentration.

6.4.2. Process intensification

Process intensification in a fluidized bed is a challenging task. Offering a generic intensification plan is often not possible without considering the specificity of operating conditions, associated cost, and regulatory policies. For example, introducing more adsorbent into the bed would increase the removal efficiency. As the adsorbent feed rate increases and the removal efficiency improves, the adsorption limiting factor shifts from adsorption sites available to adsorption kinetics, thereby diminishing the effectiveness of increasing the adsorbent feed rate. This situation requires a tradeoff between slight improvement in removal efficiency and the adsorbent (and its associated post-treatment) cost.

In many other cases, the process is constrained by some design and operating factors. For example, from the results in Figure 6-2 (b), the removal efficiency is higher when the VOC concentration is lower. However, the amount of VOC produced is dictated by the process (not the treatment operation) and is likely to be within a specific range. There might also be some constraints regarding space and equipment availability.

In this section, different possible intensification plans are discussed in two levels of operation and design. Since the experimental conditions listed in Table 6-4 cover a wide range of operating parameters, they are used in intensification simulations to ensure a more comprehensive outcome. Whenever a more in-depth analysis is needed, the reference condition (also indicated in Table 6-4) is used.

6.4.2.1. Intensification at the operation level

Changing the operating parameters is probably the first step in the intensification process of existing systems since it requires minimum system upgrade and adjustment. Increasing the

adsorbent feed rate, and reducing the air flow rate at constant VOC load are two important intensification schemes at the operation level studied in this section.

6.4.2.1.1. Increasing the adsorbent feed rate

It can be seen in Figure 6-2 (a) that increasing the adsorbent feed rate enhances the overall removal efficiency. However, depending on the operating condition, increasing the adsorbent feed rate might not always be an effective strategy (Davarpanah et al., 2020).

Figure 6-4 displays the effect of increasing the adsorbent feed rate on the removal efficiency at different operating conditions. At first glance, it can be noticed that increasing the adsorbent feed rate improves the removal efficiency, although the extent of improvement is different in various cases.

In general, the adsorption process is influenced by the availability of adsorption sites as well as the adsorption kinetics. Increasing the adsorbent feed rate increases the adsorption sites available while it does not impact the adsorption kinetics. Therefore, it can be used as a good strategy when the availability of adsorption sites is the bottleneck of the adsorption process e.g. when inlet concentration is high or the adsorbent has low adsorption capacity. Figure 6-4 (a) shows that the removal efficiency for a stream of VOC with the concentration of 150 ppm_v can reach close to that of 25 ppm_v, if enough adsorbent is introduced into the adsorber.

When the adsorption process is controlled by the adsorption kinetics, however, the removal efficiency cannot reach higher than a certain level, no matter how high the adsorbent feed rate is. This trend is well captured in Figure 6-4 (b) when the removal efficiency plateaus at 89% with increasing the adsorbent feed rate at a high air flow rate of 300 SLPM. At lower air flow rates (150 and 200 SLPM), however, the removal efficiency can easily approach 100% due to the availability of adsorption sites at high adsorbent feed rates and improved solid-gas contact time at low air flow

rates. Finding the threshold when adding more adsorbent to the bed loses its enhancement effect is a key for process intensification which is possible by means of simulation and modeling.

Figure 6-4 (c) shows that the interference of water vapor in TMB adsorption only occurs at low adsorbent feed rates. There are abundant adsorption sites available at high absorbent feed rates which provide enough adsorption capacity for both water vapor and TMB molecules. The weakened effect of RH at high adsorbent feed rates, as well as the leveled trend of removal efficiency below 100% confirm that the adsorption capacity has improved but the removal efficiency is still limited by the adsorption kinetics.

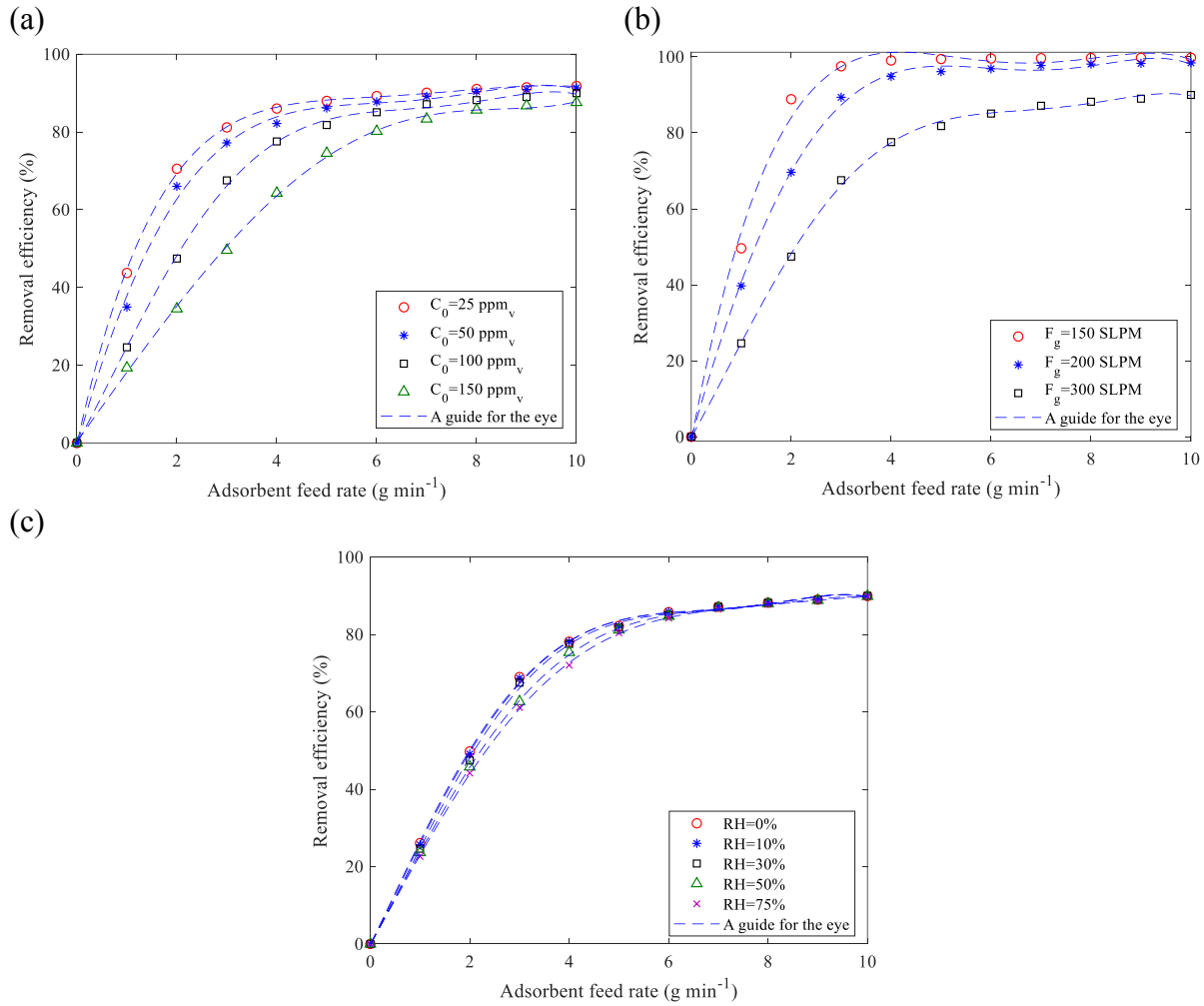

Figure 6-4. Effect of adsorbent feed rate on removal efficiency: (a) experiment no. 5-8, (b) experiment no. 9-11, and (c) experiment no. 12-16.

6.4.2.1.2. Reducing the air flow rate at constant VOC load

As discussed before, reducing the air flow rate is a good strategy to improve the adsorption kinetics and removal efficiency. The VOC load, nevertheless, is determined by the process; hence, reducing the air flow rate at constant concentration is not possible unless one or more additional fluidized bed adsorbers are added. However, depending on the process, it might be feasible to decrease the air flow rate at a constant VOC load, which in turn, increases the inlet concentration. In this situation, the diminishing effect of increased concentration (Figure 6-2 (b)) might counteract the improvement due to decreased air flow rate (Figure 6-2 (c)), and the utility of this strategy requires close inspection.

Figure 6-5 depicts the effect of air flow rate on the removal efficiency at constant TMB load. Overall, reducing the air flow rate at a constant TMB load can increase the removal efficiency. This increase is lower when the adsorbent feed rate is low (Figure 6-5 (a)) or when the TMB load is high (Figure 6-5 (b) and (c)). This is because reducing air flow rate only improves the adsorption kinetics while the lack of adsorption sites remains an issue at low adsorbent feed rates and at high TMB loads.

It can be seen in Figure 6-5 (d) that the gap between removal efficiencies obtained at different RHs becomes wider when the air flow rate decreases which is due to the fact that the improved solid-gas contact time facilitates the adsorption of both TMB and water vapor on zeolite. Hence, while there are improvements in the removal efficiency with reducing the air flow rate at all RHs, the interference of water vapor in TMB adsorption is greater at lower values of air flow rate.

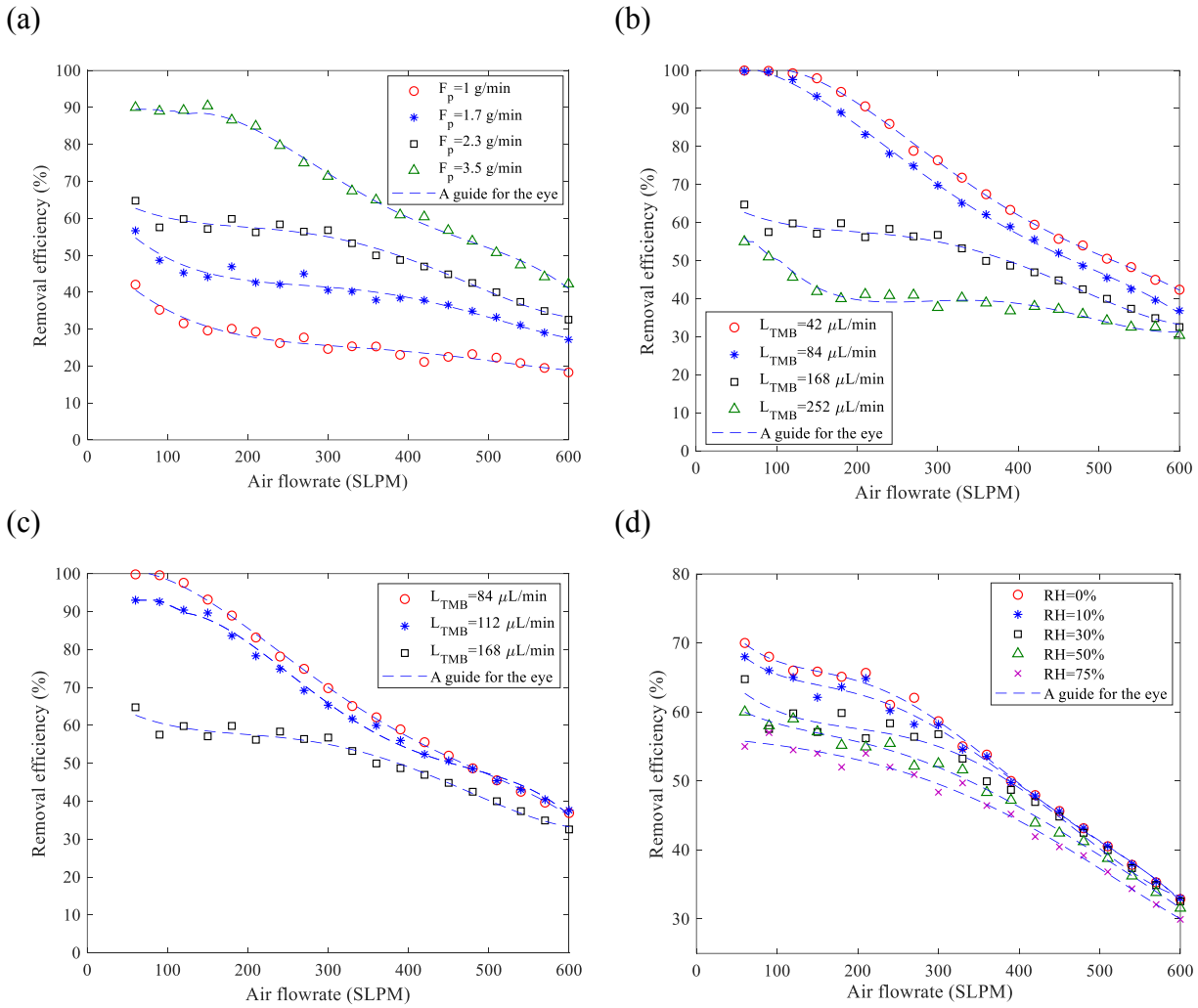

Figure 6-5. Effect of air flow rate on removal efficiency at constant TMB load and different experimental conditions: (a) experiment no. 1-4, (b) experiment no. 5-8, (c) experiment no. 9-11, and (d) experiment no. 12-16.

6.4.2.2. Intensification at the design level

While changing the operating parameters is a good strategy for after-design intensification of the adsorption process in a fluidized bed, there are many intensification schemes that could be considered at the design level. In this section, increasing the number of stages, changing the adsorber configurations, and increasing the weir height are investigated as intensification plans, followed by a study on optimizing the weir height configuration.

6.4.2.2.1. Increasing the number of stages

Determining the number of stages is a critical step in designing a multistage fluidized bed. The effect of the number of stages in a fluidized adsorber on the overall removal efficiency is displayed in Figure 6-6 for various cases listed in Table 6-4.

Adding more stages can easily improve the removal efficiency when the adsorbent feed rate is high (e.g. Figure 6-6 (a) when F_p=3.2 g min^{-1}), or the inlet concentration is low (e.g. Figure 6-6 (b) when C_0=25-50 ppm_v). In general, when there are enough adsorption sites available, increasing the number of stages can enhance the adsorbent retention time inside the bed and improve the removal efficiency. However, at low adsorbent feed rates (e.g. Figure 6-6 (a) when F_p=1-1.7 g min^{-1}) and at high inlet concentrations (e.g. Figure 6-6 (b) when C_0=150 ppm_v), an equilibrium condition occurs between VOC in the adsorbent and that in the gas phase at early stages when the availability of adsorption sites becomes a limiting factor; hence, adding more stages becomes ineffective. These results are consistent with those presented in Figure 6-3 where some experiments at low adsorbent feed rates and high inlet concentrations (e.g. exp. no. 1-2 and 8) do not exhibit a reduction in TMB concentrations from the inlet levels in the lower adsorber stages.

According to Figure 6-6 (c), removal efficiency is improved as the number of stages increases at different air flow rates and constant adsorbent feed rate and inlet concentration, due to improved adsorbent retention time.

The effect of the number of stages on the removal efficiency at various RHs (Figure 6-6 (d)) shows that adding more stages in a fluidized bed adsorber would not eliminate the competing effect of water vapor on TMB adsorption. As discussed in Figure 6-4 (c), the interference of water vapor in TMB adsorption is contingent on the availability of adsorption sites, which is not impacted by increasing the number of stages.

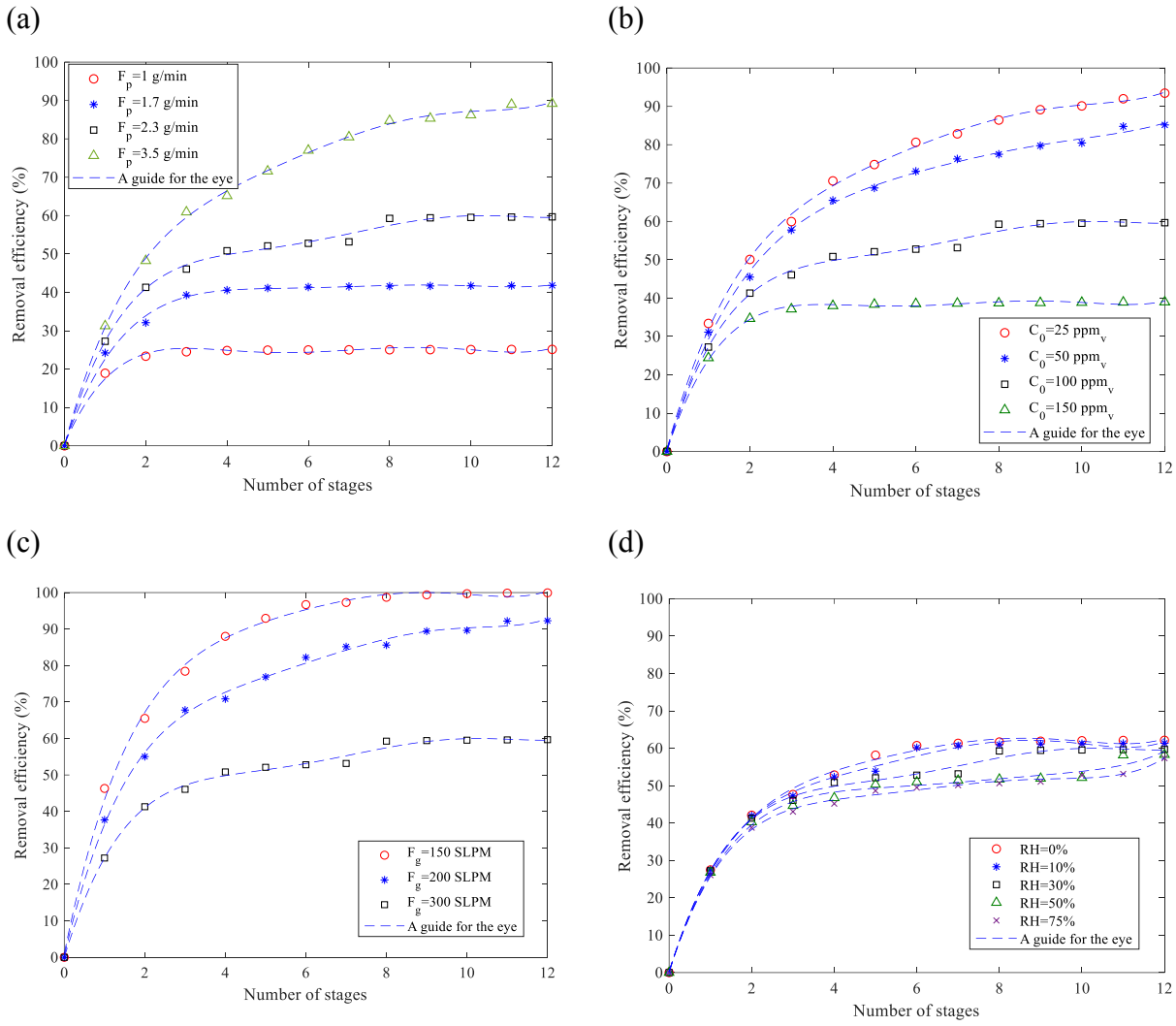

Figure 6-6. Effect of the number of stages on removal efficiency at different experimental conditions: (a) experiment no. 1-4, (b) experiment no. 5-8, (c) experiment no. 9-11, and (d) experiment no. 12-16.

6.4.2.2.2. Adsorber configurations

Choosing the right adsorber configuration is essential for the efficient operation of fluidized bed adsorbers. Different configurations that can be obtained using 6 stages are schematically shown in Figure 6-7. Configuration (a) depicts the 6-stage fluidized bed adsorber which was operated to obtain the experimental data and simulated to obtain the modeled results in this study.

In configurations (b)-(d), the air and adsorbent streams are equally split into the number of adsorbers.

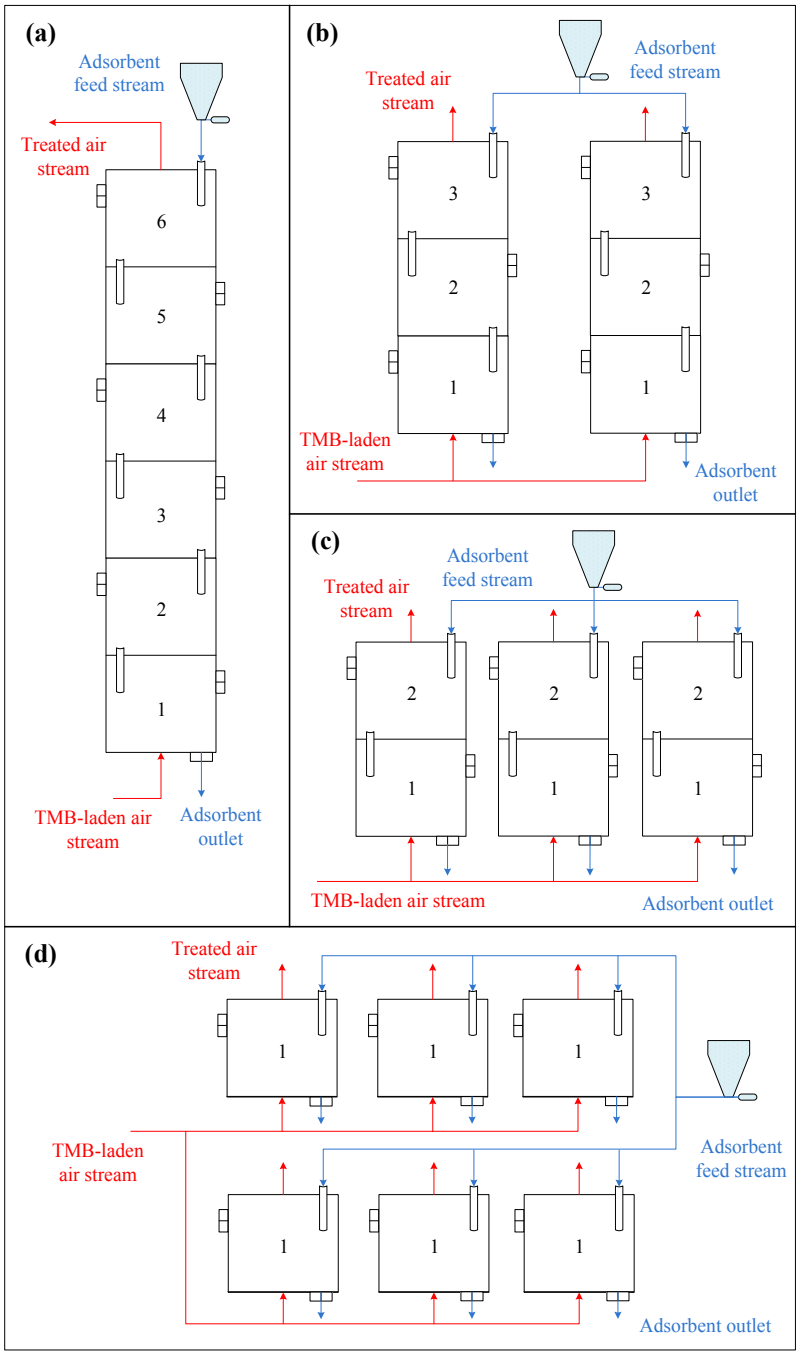

Figure 6-7. Schematic diagrams of fluidized bed adsorbers with various configurations: (a) 1 adsorber of 6 stages, (b) 2 adsorbers of 3 stages, (c) 3 adsorbers of 2 stages, and 6 adsorbers of 1 stage.

The effect of adsorber configuration on the removal efficiency at various operating conditions is plotted in Figure 6-8 with its data reported in Table S9 in Supplementary Information. One of the criteria for choosing the right configuration is its ability to provide the minimum fluidization flow rate at the lowest air flow rate expected in the process. In experiment no. 9 where the configuration of 6 adsorbers is concerned, the gas flow rate for each adsorber (~25 SLPM) falls below that required for minimum fluidization in the bed (~30 SLPM). Hence, that case is neither simulated nor reported in Figure 6-8.

It can be noticed with a cursory look that the removal efficiency can be noticeably improved by choosing the right configuration. For example, using 2 adsorbers of 3 stages instead of 1 adsorber of 6 stages, can increase the removal efficiency by 28.4% for the reference condition (exp. no. 3) while this improvement can be as large as 34.5% for experiment no. 8.

In general, going from 1 adsorber of 6 stages to 6 adsorbers of 1 stage, the advantages of having more stages (increased adsorbent retention time) and higher adsorbent feed rate (ample available adsorption sites) are replaced by the advantages of reducing the air flow rate (increased solid-gas contact). This tradeoff suggests an optimum point somewhere in between two extreme sides of abundant adsorption sites for 1 adsorber of 6 stages and improved kinetics for 6 adsorbers of 1 stage.

While both configurations of 3 adsorbers of 2 stages and 2 adsorbers of 3 stages take advantage of ample adsorption sites and improved adsorption kinetics, in all experiments, except exp. no. 9 and 10, the configuration of 2 adsorbers of 3 stages yields better removal efficiencies. The reason lies in the fact that most experiments were conducted at the high air flow rate of 300 SLPM and the advantages of reducing the air flow rate overcome the advantages of more stages and higher adsorbent feed rates. In experiments no. 9 and 10, however, the air flow rate is already low (150

and 200 SLPM, respectively) and reducing the air flow rate is the second priority after increasing the number of stages as well as the adsorbent feed rate. For the same reason, 6 adsorbers of 1 stage always yield better removal efficiencies than 1 adsorber of 6 stages, except in experiment no. 10 when the air flow rate is relatively low.

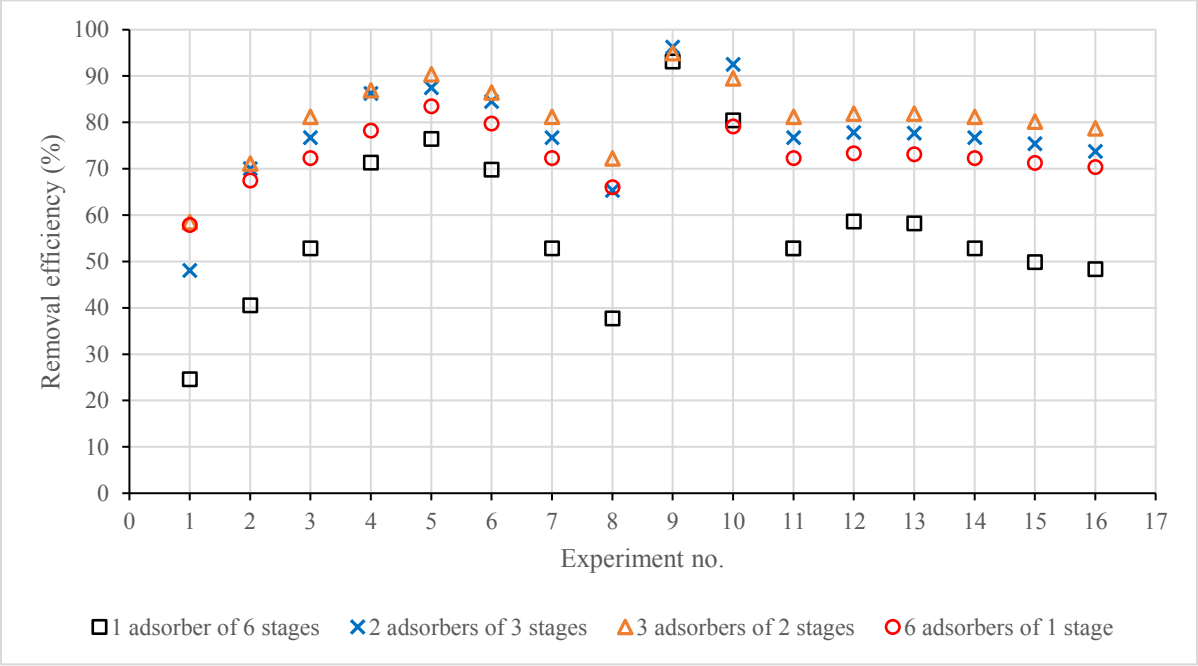

Figure 6-8. Effect of adsorber configuration on the removal efficiency at various experimental conditions.

6.4.2.2.3. Increasing the weir height

Figure 6-9 demonstrates the effect of weir height on the removal efficiency of the 6-stage fluidized bed adsorber for different experiments listed in Table 6-4. The model results are also listed in Table S10 in Supplementary Information. Similar to increasing the number of stages, increasing the weir height would improve the removal efficiency by enhancing the adsorbent retention time inside the bed. This improvement is larger when the adsorbent feed rate is high (exp. no. 4), or the inlet concentration is low (exp. no. 5 and 6) due to the availability of adsorption sites and nonequilibrium state between VOC in adsorbent and in the gas phase. When the adsorbent

feed rate is low or the inlet concentration is high (exp. no. 1-3 and 8), the adsorption process is controlled by the lack of available adsorption sites, and changing the weir height (and the adsorbent retention time) would marginally impact the removal efficiency.

While increasing the weir height from 2 to 20 mm noticeably improves the removal efficiency, a further increase in weir height from 20 to 40 mm results in negligible improvement. It should be noted that for high weir heights, more adsorbent is needed to fill up the stages, which in turn, requires a larger desorber for cyclic adsorption/desorption operations. To have a better understanding of the effect of the weir height increase on the removal efficiency, the simulation was run for the reference condition with its results demonstrated in Figure 6-10. From the results, the removal efficiency is improved by 3.5% when the weir height is increased from 2 to 22 mm. After 22 mm the curve practically plateaus and increasing the weir height up to 40 mm improves the removal efficiency only by 0.1%.

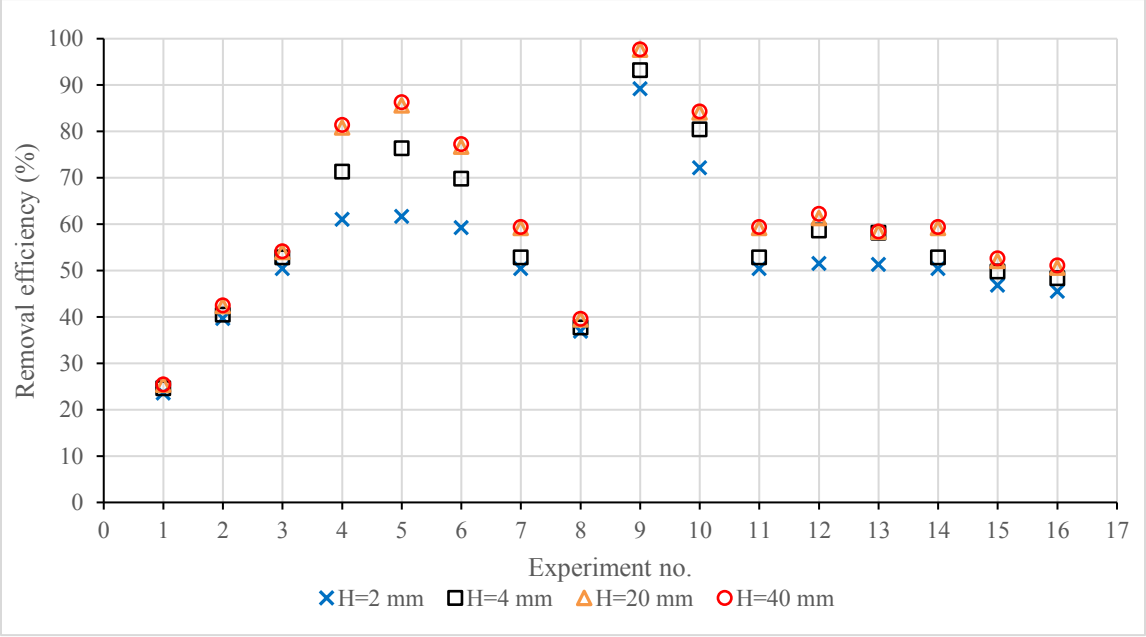

Figure 6-9. Effect of weir height on the removal efficiency at different experimental conditions.

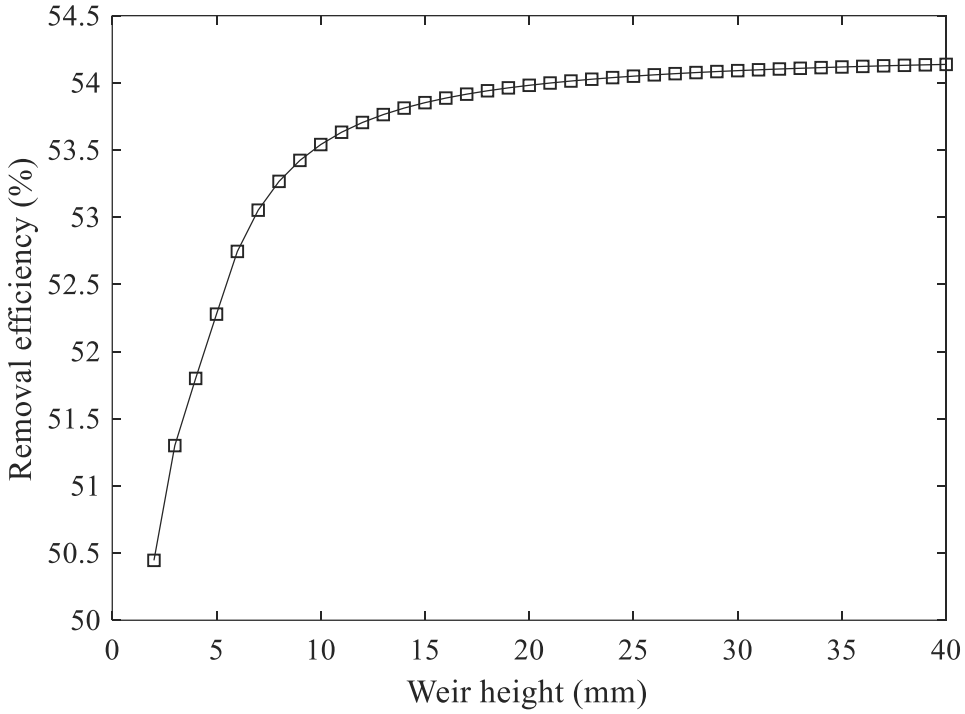

Figure 6-10. Effect of weir height (same height on all stages) on the removal efficiency for the reference condition.

6.4.2.2.4. Optimizing the weir height configuration

It was discussed in the previous section that the improvement in removal efficiency with increasing weir height greatly depends on the operating conditions and could be as small as 0.9% (for exp. no. 1) or as large as 21.7% (for exp. no. 5) in the range of simulated cases. In a countercurrent multistage fluidized bed, the mass transfer driving force between gas and solid phases (hence, their proximity to the equilibrium state) is different on each stage. The virgin adsorbent particles are fed at the top of the adsorber where they come in contact with the gas stream with low VOC content. As the adsorbents pass through the downcomers into the stages below, they are loaded with VOC. The VOC concentration decreases as the gas stream travels from the bottom to the top of the bed. In the bottom stage, loaded adsorbents are in contact with inlet high VOC concentration.

To investigate the optimum arrangement of weir heights, the reference condition was simulated with varying weir height on each stage in the range of 2 to 22 mm, in increments of 2 mm (e.g. 2, 4, 6, …, 22 mm). The results of the simulation are summarized in Table 6-5, separated by the maximum weir height allowed in the bed.

In general, the optimum weir height arrangements suggest a decreasing order for the weir heights from the top stage to the bottom stage. The reason can be explained by inspecting the adsorption sites available and kinetics at the top and bottom of the bed. At the top of the bed, the gas stream with relatively low TMB content is in contact with virgin adsorbents. While the presence of virgin adsorbent at the top stage ensures abundant available adsorption sites, the adsorption kinetics is substantially influenced by the low concentration of TMB. Increasing the weir height can improve the solid-gas contact time (by increasing the adsorbent retention time) on the top stage where it is needed the most.

At the bottom stage, the TMB concentration is high and the adsorbent is partially loaded. High TMB concentration means facilitated adsorption kinetics and partially loaded adsorbent suggests a lack of available adsorption sites. Therefore, increasing the weir height would not be effective since the adsorption process is possibly limited by insufficient available adsorption sites (not short solid-gas contact time).

With a closer look at the results in Table 6-5 and comparing them with those presented in Figure 6-9 and in Table S10 in Supplementary Information, it can be noticed that optimizing the weir height for each stage can considerably improve the removal efficiency compared to having the same (and the maximum) weir height on all stages. For example, when the maximum weir height allowed in the bed is 4 mm, the optimum arrangement of weir height yields 58.8% removal efficiency, while an adsorber with a weir height of 4 mm on all stages achieves only 52.8% removal

efficiency. When the maximum weir height allowed in the bed is 20 mm, the removal efficiencies achieved are 65.5% and 54% for the optimum arrangement of weir height and the same weir height on all stages, respectively. The reason for the poor performance of an adsorber with the same weir height on all stages compared to one with an optimized arrangement of weir heights might be the fact that having high weir height on bottom stages where modified gas-solid contact time is not needed would reduce the particle fluidization and hinder the mass transfer between the gas phase and the adsorbent particles.

It is also worth mentioning that maximum removal efficiency obtained using the optimum configuration of weir heights initially increases when the maximum weir height allowed in the bed increases, and then plateaus at maximum weir height of 20 mm. Thus, even when the maximum weir height allowed in the bed is 22 mm, the best arrangement of weir heights suggests a weir height of 20 mm in the top stage.

Table 6-5.The best weir height configuration for a fluidized bed working in the reference condition as a function of maximum weir height allowed in the bed.

	Maximum weir height allowed in the bed (mm)	2	4	6	8	10	12	14	16	18	20	22
Optimum weir height (mm)	Stage no. 6	2	4	6	8	10	12	14	16	18	20	20
	Stage no. 5	2	4	6	6	6	8	8	8	8	8	8
	Stage no. 4	2	4	4	4	4	4	4	4	4	4	4
	Stage no. 3	2	2	2	2	2	2	2	2	2	2	2
	Stage no. 2	2	2	2	2	2	2	2	2	2	2	2
	Stage no. 1	2	2	2	2	2	2	2	2	2	2	2
	RE (%)	50.4	58.8	61.8	63.2	64.0	64.6	65.0	65.2	65.4	65.6	65.6

6.5. Conclusion

A modeling approach incorporating fast ideal adsorbed solution theory integrated with a two-phase model was introduced to predict the adsorption of TMB on zeolite in the presence of humidity in a multistage countercurrent fluidized bed. The model uses the pure component adsorption isotherm of TMB and water vapor for calculations of binary adsorption. A comparison of experimental data and predicted results showed that the model was responsive to typical changes in operating conditions. The model was then used to investigate the intensification process in fluidized bed operation. The following conclusions can be drawn from the intensification results:

- Increasing the adsorbent feed rate can effectively improve the removal efficiency when there is a need for more adsorption sites (e.g. at high inlet concentrations). It becomes quite ineffective when the adsorption process is limited by low solid-gas contact time (e.g. high air flow rates).
- Increasing the adsorbent feed rate can also reduce the interference of water vapor in adsorption of VOC by making abundant adsorption sites available for adsorption of both VOC and water molecules.
- Provided that the minimum fluidization is maintained, reducing air flow rate at constant VOC load enhances the removal efficiency especially when there are enough adsorption sites available (e.g. high adsorbent feed rate, and low VOC loads and RHs).
- Increasing the number of stages can effectively improve the fluidized bed removal efficiency when the availability of adsorption sites is not an issue (e.g. at high adsorbent feed rates and low VOC inlet concentrations and RHs). This improvement becomes less effective as the number of stages increases and the bottleneck of the adsorption process shifts from the adsorbent retention time to the adsorption sites availability.
- 3 adsorbers of 2 stages and 2 adsorbers of 3 stages were the best configurations in the range of operating conditions simulated, with the later producing better removal efficiencies when the air flow rate was low (e.g. 150 and 200 SLPM). Switching from 1 adsorber of 6

stages to 3 adsorbers of 2 stages could improve the removal efficiency up to 34.5% for the cases simulated.

- Having the same high weir height along the bed yields better removal efficiencies than using the same low weir height. However, an optimized arrangement of weir heights in descending order from the top to the bottom of the bed can maximize the removal efficiency.

The modeling approach and intensification plans presented in this study can be effectively used to optimize the design and operation of fluidized bed adsorbers, leading to cost savings and performance improvements.

6.6. References

Abasaeed, A.E., Al-Zahrani, S.M., 1998. Modeling of Fluidized Bed Reactors for the Polymerization Reaction of Ethylene and Propylene. *Developments in Chemical Engineering and Mineral Processing*, **6**: 121-134.

Amdebrhan, B.T. (2018). Evaluating the Performance of Activated Carbon, Polymeric, and Zeolite Adsorbents for Volatile Organic Compounds Control. Department of Civil and Environmental Engineering, University of Alberta. **Master of Science**.

Cai, P., Schiavetti, M., De Michele, G., Grazzini, G.C., Miccio, M., 1994. Quantitative estimation of bubble size in PFBC. *Powder Technology*, **80**: 99-109.

Davarpanah, M., Hashisho, Z., Crompton, D., Anderson, J.E., Nichols, M., 2020. Modeling VOC adsorption in lab- and industrial-scale fluidized bed adsorbers: Effect of operating parameters and heel build-up. *Journal of Hazardous Materials*, **400**: 123129.

Davarpanah, M., Hashisho, Z., Phillips, J.H., Crompton, D., Anderson, J.E., Nichols, M., 2020. Modeling VOC adsorption in a multistage countercurrent fluidized bed adsorber. *Chemical Engineering Journal*, **394**: 124963.

Davidson, J.F., Harrison, D. (1963). Fluidized Particles. New York, Cambridge University Press.

Do, D.D. (1998). Adsorption Analysis: Equilibria And Kinetics. London, Imperial College Press.

Ghoshal, A.K., Manjare, S.D., 2002. Selection of appropriate adsorption technique for recovery of VOCs: an analysis. *Journal of Loss Prevention in the Process Industries*, **15**: 413-421.

Government of Canada (2020). Canada's Air Pollutant Emissions Inventory Report 2020.

Halasz, I., Kim, S., Marcus, B., 2002. Hydrophilic and hydrophobic adsorption on Y zeolites. *Molecular Physics*, **100**: 3123-3132.

Hatzantonis, H., Yiannoulakis, H., Yiagopoulos, A., Kiparissides, C., 2000. Recent developments in modeling gas-phase catalyzed olefin polymerization fluidized-bed reactors: The effect of bubble size variation on the reactor's performance. *Chemical Engineering Science*, **55**: 3237-3259.

Hymore, K., Laguerie, C., 1984. Analysis and modelling of the operation of a counterflow multistage fluidized bed adsorber for drying moist air. *Chemical Engineering and Processing: Process Intensification*, **18**: 255-267.

Kamravaei, S., Shariaty, P., Jahandar Lashaki, M., Atkinson, J.D., Hashisho, Z., Phillips, J.H., Anderson, J.E., Nichols, M., 2017. Effect of Beaded Activated Carbon Fluidization on Adsorption of Volatile Organic Compounds. *Industrial & Engineering Chemistry Research*, **56**: 1297-1305.

Keenan, J., Chao, J., Kaye, J., 1983. Gas Tables International Version-Thermodynamic Properties of Air, Products of Combustion and Component Gases. *Compressible Flow Functions*.

Kim, B.R., 2011. VOC Emissions from Automotive Painting and Their Control: A Review. *Environmental Engineering Research*, **16**: 1-9.

Kunii, D., Levenspiel, O. (1969). Fluidization engineering. New York, Wiley.

Laskar, I.I., Hashisho, Z., Phillips, J.H., Anderson, J.E., Nichols, M., 2019. Competitive adsorption equilibrium modeling of volatile organic compound (VOC) and water vapor onto activated carbon. *Separation and Purification Technology*, **212**: 632-640.

Laskar, I.I., Hashisho, Z., Phillips, J.H., Anderson, J.E., Nichols, M., 2019. Modeling the Effect of Relative Humidity on Adsorption Dynamics of Volatile Organic Compound onto Activated Carbon. *Environmental Science & Technology*, **53**: 2647-2659.

Lodewyckx, P., Vansant, E.F., 1999. Influence of Humidity on Adsorption Capacity from the Wheeler-Jonas Model for Prediction of Breakthrough Times of Water Immiscible Organic Vapors on Activated Carbon Beds. *American Industrial Hygiene Association Journal*, **60**: 612-617.

Mohanty, C.R., Adapala, S., Meikap, B.C., 2009. Removal of hazardous gaseous pollutants from industrial flue gases by a novel multi-stage fluidized bed desulfurizer. *Journal of Hazardous Materials*, **165**: 427-434.

Mohanty, C.R., Malavia, G., Meikap, B.C., 2009. Development of a Countercurrent Multistage Fluidized-Bed Reactor and Mathematical Modeling for Prediction of Removal Efficiency of Sulfur Dioxide from Flue Gases. *Industrial & Engineering Chemistry Research*, **48**: 1629-1637.

Mohanty, C.R., Meikap, B.C., 2011. Modeling the operation of a three-stage fluidized bed reactor for removing CO2 from flue gases. *Journal of Hazardous Materials*, **187**: 113-121.

Mojtaba Hashemi, S., Jahandar Lashaki, M., Hashisho, Z., Phillips, J.H., Anderson, J.E., Nichols, M., 2019. Oxygen impurity in nitrogen desorption purge gas can increase heel buildup on activated carbon. *Separation and Purification Technology*, **210**: 497-503.

Myers, A.L., Prausnitz, J.M., 1965. Thermodynamics of mixed-gas adsorption. *AIChE Journal*, **11**: 121-127.

O'Brien, J.A., Myers, A.L., 1985. Rapid calculations of multicomponent adsorption equilibria from pure isotherm data. *Industrial & Engineering Chemistry Process Design and Development*, **24**: 1188-1191.

O'Brien, J.A., Myers, A.L., 1988. A comprehensive technique for equilibrium calculations in adsorbed mixtures: the generalized FastIAS method. *Industrial & Engineering Chemistry Research*, **27**: 2085-2092.

Poulopoulos, S.G., Inglezakis, V.J. (2006). Adsorption, ion exchange and catalysis: design of operations and environmental applications, Elsevier.

Roy, S., Mohanty, C.R., Meikap, B.C., 2009. Multistage Fluidized Bed Reactor Performance Characterization for Adsorption of Carbon Dioxide. *Industrial & Engineering Chemistry Research*, **48**: 10718-10727.

Seader, J.D., Henley, E.J. (2006). Separation process principles, John Wiley & Sons, Inc.

Sullivan, P.D., Rood, M.J., Dombrowski, K.D., Hay, K.J., 2004. Capture of Organic Vapors Using Adsorption and Electrothermal Regeneration. *Journal of Environmental Engineering*, **130**: 258-267.

Tang, M., Cox, R., Kalberer, M., 2014. Compilation and evaluation of gas phase diffusion coefficients of reactive trace gases in the atmosphere: volume 1. Inorganic compounds. *Atmospheric Chemistry and Physics*, **14**: 9233-9247.

Werther, J., Hartge, E.-U., 2004. Modeling of Industrial Fluidized-Bed Reactors. *Industrial & Engineering Chemistry Research*, **43**: 5593-5604.

Yamamoto, T., Kataoka, S., Ohmori, T., 2010. Characterization of carbon cryogel microspheres as adsorbents for VOC. *Journal of Hazardous Materials*, **177**: 331-335.

Zheng, J., Song, W., Du, L., Wang, L., Li, S., 2020. Desorption of VOCs from polymer adsorbent in Multistage Fluidized bed. *Chinese Journal of Chemical Engineering*.

7. Chapter 7*: The effect of (semi)empirical formulas on the two-phase modeling of fluidized bed adsorbers

7.1. Abstract

Choosing proper empirical/semi-empirical formulas for estimating different variables is imperative when modeling a fluidized bed using the two-phase theory. In this study, a two-phase model was used in two modes of emulsion gas in perfectly mixed flow (EGPM) and in plug flow (EGPF), to predict the adsorption of volatile organic compounds (VOC) in a multistage fluidized bed adsorber. The impact of different formulas for estimating bubble size, bed porosity at minimum fluidization velocity, adsorption and interphase mass transfer coefficients, as well as tortuosity on the performance of the model was determined by comparing the model outcomes with experimental data. Finally, using a large dataset of fluidized bed adsorption obtained from systems with different adsorbents, adsorbates, bed sizes, and operating conditions, a generic set of formulas was suggested which could be used to describe the behavior of different countercurrent fluidized bed adsorbers. From the results, the two-phase model could successfully predict the experimental data, with EGPF mode showing better performance than EGPM with average relative error (ARE) values of 6.3% and 9.8%, respectively. It was also found that while choosing proper formulas to describe the hydrodynamic and adsorptive behavior of the bed is always important, choosing the right formulas for bed voidage and interphase mass transfer coefficient plays a specifically crucial role in determining the accuracy of the two-phase model. The generic set of formulas proposed showed good agreement with a large dataset of fluidized bed adsorption experiments with ARE=6.3%.

* This chapter is intended to be published as an original paper.

7.2. Nomenclature

Sym.	Description	Value /Formula	Units	Source
A	cross-section area of bed	4.56×10^{-3}	m^2	measured
Ar	Archimedes number	Table 7-3	–	(Abasaeed and Al-Zahrani, 1998)
a_p	external surface area per unit volume of particles	Table 7-6	m^{-1}	(Seader and Henley, 2006)
C	VOC concentration	Eq. (7-2)	kg/kg	calculated
C^*	VOC concentration in air in equilibrium condition	Figure S10	kg/kg	measured
C_0	VOC concentration at bed entry	Table 7-2	ppm, kg/kg	measured
C_b	VOC concentration in bubble phase	Eqs. (7-4) and (7-8)	kg/kg	calculated
C_p	VOC concentration in particulate phase	Eqs. (7-5) and (7-9)	kg/kg	calculated
d_b	mean bubble diameter	Table 7-4	m	calculated
d_{b0}	initial bubbles diameter	Table 7-4	m	calculated
d_{bm}	maximum bubble diameter	Table 7-4	m	calculated
D	bed diameter	7.6×10^{-2}	m	measured
D_e	internal mass transfer coefficient	Table 7-6	$m^2\ s^{-1}$	calculated
D_g	VOC diffusivity in air	6.45×10^{-6}	$m^2\ s^{-1}$	(Tang et al., 2014)
D_k	Knudsen diffusion coefficient	Table 7-6	$m^2\ s^{-1}$	(Seader and Henley, 2006)
d_p	adsorbent mean diameter	Table 7-1	m	(Amdebrhan, 2018)
d_{pore}	mean diameter of pores in adsorbent	Table 7-1	m	(Amdebrhan, 2018)

F_g	air flow rate	Table 7-2	SLPM, kg hr^{-1}	measured
F_p	adsorbent feed rate	Table 7-2	g min^{-1}, kg hr^{-1}	measured
g	standard gravity	9.8	m/s^2	(Abasaeed and Al-Zahrani, 1998)
h	height in the bed	N/A	N/A	N/A
H	weir height	4×10^{-3}	m	measured
H_{mf}	height of bed on each stage at u_{mf}	Table 7-3	m	(Hymore and Laguerie, 1984)
k	adsorption rate constant	Table 7-6	s^{-1}	calculated
k'	coefficient	Eq. (7-7)	–	calculated
K_{bc}	bubble to cloud mass transfer coefficient	Table 7-8	s^{-1}	calculated
K_{be}	bubble to emulsion mass transfer coefficient	Table 7-8	s^{-1}	calculated
K_{ce}	cloud to emulsion mass transfer coefficient	Table 7-8	s^{-1}	calculated
K_f	Freundlich constant	1.869	kg/kg	calculated
m	slope of the isotherm	Eq. (7-16)	kg/kg	calculated
M	TMB molecular weight	120.19	g mol^{-1}	(Tefera et al., 2014)
m_1	coefficient	Eq. (7-10)	–	calculated
m_2	coefficient	Eq. (7-11)	–	calculated
n	Freundlich constant	0.2115	–	calculated
n_0	number of orifices	4823	–	measured
N_b	number of bubbles per unit volume of bed	Table 7-3	m^{-3}	(Hymore and Laguerie, 1984)
Q	mass transfer flow rate between a bubble and the particulate phase	Table 7-8	m^3 s^{-1}	calculated
q	VOC content of adsorbent	N/A	kg/kg	N/A

q^*	VOC content of adsorbent in equilibrium condition	Figure S10	kg/kg	measured
RE	removal efficiency	Eq. (7-17)	–	(Hymore and Laguerie, 1984)
Re_{mf}	Reynolds number at u_{mf}	Table 7-3	–	(Abasaeed and Al-Zahrani, 1998)
S_b	bubble surface area	Table 7-3	m^2	(Hymore and Laguerie, 1984)
T	Temperature	294	K	measured
u_0	superficial gas velocity	F_g/A	m s^{-1}	calculated
u_b	velocity of bubble rising through a bed	Table 7-3	m s^{-1}	(Kunii and Levenspiel, 1969)
u_{mf}	minimum fluidization velocity	Table 7-3	m s^{-1}	(Abasaeed and Al-Zahrani, 1998)
V_b	bubble volume	Table 7-3	m^3	(Hymore and Laguerie, 1984)
W	mass of adsorbent on each stage	Table 7-3	kg	(Hymore and Laguerie, 1984)
X	coefficient	Eq. (7-6)	–	calculated
y	axis along the bed	–	m	–
α	coefficient	Eq. (7-14)	–	(Hymore and Laguerie, 1984)
β	fraction of gas flowing as bubbles	Eq. (7-3)	–	(Hymore and Laguerie, 1984)
ε_{mf}	void fraction at u_{mf}	Table 7-5	–	calculated
ε_p	adsorbent internal porosity	Table 7-1	–	(Amdebrhan, 2018)
μ_g	gas viscosity	1.82×10^{-5}	kg m^{-1} s^{-1}	(Keenan et al., 1983)
ρ_g	gas density	1.20	kg m^{-3}	(Keenan et al., 1983)
ρ_p	adsorbent density	Table 7-1	kg m^{-3}	(Amdebrhan, 2018)

τ	mean residence time of solids on each stage	Eq. (7-15)	s	(Hymore and Laguerie, 1984)
τ'	tortuosity	Table 7-7	–	(Do, 1998)
ϕ	adsorbent shape factor	Table 7-1	–	measured
ζ	coefficient	Table 7-6	–	calculated

7.3. Introduction

The fluidization technology is an effective method for contacting solids and fluids. A fluidized bed (FB) has several advantages including continuous process, low pressure drops, uniform temperature, and narrow residence time distribution which makes it a good candidate for a number of operations such as adsorption (Kamravaei et al., 2017), calcinations/sulfation (Scala et al., 2000, Scala et al., 2004), and combustion (Schulzke et al., 2018). However, the prevalence of FBs in industrial applications, similar to many other technological systems, is contingent on the knowledge development in that area.

Understanding the operation of a countercurrent FB requires good insights on transfer phenomena inside the bed. While experimental measurements can shed some light on the FB operation, advanced modeling and simulation tools can be used to fully comprehend the intricate effects of different parameters on the behavior of the system. Over the past few decades, several models have been introduced for simulation of FBs, among which the fundamental two-phase theory of Toomey and Johnstone (Toomey and Johnstone, 1952) has attracted a lot of attention as the first model that takes into account heat and mass transfers.

The two-phase theory is based on two major assumptions. First, a FB consists of two phases: a particulate phase comprising solid particles and interstitial gas, and a bubble phase comprising rising bubbles free from particles. Second, all gas in excess of that required for minimum

fluidization flows through the bed as bubbles while the particulate phase remains stagnant at minimum fluidizing condition (Toomey and Johnstone, 1952, Davidson and Harrison, 1963, Kunii and Levenspiel, 1969). More sophisticated versions of the two-phase model were later developed by Davidson and Harrison (Davidson and Harrison, 1963), Kunii and Levenspiel (Kunii and Levenspiel, 1969), and Hymore and Languerie (Hymore and Laguerie, 1984). Many other authors used similar models to study FBs behavior (Grace, 1986, McAuley et al., 1994, Lu et al., 2004, Mohanty et al., 2009). While all these models utilize the same governing equations, they use different formulas to describe hydrodynamics (e.g. bubble motion) and mass transfer (e.g. kinetics and mass transfer coefficients).

There are several mathematical formulas in the literature describing different processes inside FBs (Hatzantonis et al., 2000). These formulas, however, vary as adsorbent, adsorbate, or the FB scale change. For instance, bubble size which was found to be an important parameter affecting many other variables (such as bubble volume, bubble rising velocity, and interphase mass transfer flow rate) (Davarpanah et al., 2020) could be calculated using several formulas which, in turn, may change the final results to a large extent (Yasui and Johanson, 1958, Kato and Wen, 1969, Geldart, 1970, Mori and Wen, 1975, Darton et al., 1977). The combined effect of formulas might add to the complexity of calculations when there are more variables that could be predicted by more than one formula; and this is the reason that models with universal applicability are scares.

The objectives of this work are (i) to develop a two-phase model to predict the adsorption of volatile organic compounds (VOC) in a multistage fluidized bed adsorber, (ii) to study the performance of the model using different formulas for calculation of bubble diameter, interphase mass transfer flow rate, bed porosity at minimum fluidization, mass transfer coefficient, and

tortuosity of adsorbent, and (iii) to propose a generic set of formulas which could maximize the accuracy of prediction for a large adsorption dataset.

The adsorption dataset was compiled from experiments conducted using three different adsorbates (1,2,4-Trimethylbenzene (TMB), a solvent mixture (SM) representing the emissions from automotive painting booths, and water vapor) on three different adsorbents (activated carbon, polymeric adsorbent, and alumina) at a range of operating conditions (adsorbent feed rate, gas flow rate, initial concentration, weir height and the number of stages) in FBs of different scales (lab–, bench–, and industrial–scale). Using a diverse range of data for finding the optimum set of formulas would improve its ability to predict the adsorption performance of different FB systems.

7.4. Experimental setup

The setup for FB experiments was presented and described in detail in our previous studies (Davarpanah et al., 2020, Davarpanah et al., 2020). In summary, the FB adsorber consists of 6 individual compartments each of which has 10.4 cm height and 7.6 cm diameter. Each stage has a conical downcomer (10–4 mm in diameter), allowing adsorbent particles flow from one stage to another while maintaining an overflow height of 4 mm. There is a perforated distributor with around 4823 apertures (0.4 mm in diameter each) at the bottom of each stage which gives an open surface area of 13.3% for gas to rise in the bed.

A flame–ionization detector (Baseline Mocon, Series 9000) measured the concentration of TMB at the center of each compartment. The gas flow rate and concentration were adjusted using a mass flow controller (Alicat Scientific) and a syringe pump (Chemyx Inc, Nexus 6000), respectively. A volumetric feeder (Schenck AccuRate) at the top of the FB was used to feed the polymeric adsorbent of DOWEX OPTIPORE® V–503 (hereinafter referred to as DOWEX) into

the adsorber. DOWEX Properties are listed in Table 7-1. The density and viscosity of inlet gas were considered approximately equal to those of air. All adsorption experiments were duplicated and carried out at room temperature (21°C).

Table 7-1. DOWEX properties (Amdebrhan, 2018).

Parameter	Value	Unit
Mean diameter, d_p	1×10^{-3}	m
Apparent density, ρ_p	340	kg m^{-3}
Mean diameter of pores, d_{pore}	3.4×10^{-9}	m
Internal porosity, χ	0.32	–
Shape factor, ϕ	1	–

The models were validated using experimental data reported by Kamravaei et al. (Kamravaei et al., 2016) (Table 7-2).

Table 7-2. Experimental parameters for adsorption of TMB on DOWEX in the FB.

Changing parameter	Exp. no.	F_p (g min^{-1})	F_g (SLPM)	C_0 (ppm_v)	Injection rate (µL min^{-1})
Adsorbent feed rate	1	0.3	300	100	168.32
	2	0.9	300	100	168.32
	3	1.6	300	100	168.32
	4	2.4	300	100	168.32
Initial concentration	5	0.3	300	50	84.13
	6	0.3	300	100	168.32
	7	0.3	300	150	252.78
	8	0.3	300	200	336.64

Initial concentration	9	1.6	300	50	84.13
	10	1.6	300	100	168.32
	11	1.6	300	150	252.78
	12	1.6	300	200	336.64
Air flow rate	13	0.3	200	100	112.21
	14	0.3	250	100	140.27
	15	0.3	300	100	168.32
	16	0.3	350	100	196.37
Air flow rate	17	1.6	200	100	112.21
	18	1.6	250	100	140.27
	19	1.6	300	100	168.32
	20	1.6	350	100	196.37

7.5. Theory

7.5.1. Adsorption isotherm

The adsorption isotherm of TMB on DOWEX previously reported in (Amdebrhan, 2018) was fitted using the Freundlich model:

$$\ln\left(q^*\right) = \ln\left(K_f\right) + \frac{1}{n}\ln\left(C^*\right) \tag{7-1}$$

where K_f and n are Freundlich constants with the latter indicating surface heterogeneity. K_f and n were calculated 1.869 kg/kg and 0.2115, respectively (see Figure S10 in Supplementary Information).

7.5.2. Two-phase model

In this section, only the main equations of the two-phase model are presented. More information about the two-phase model including assumptions and the derivation of formulas could be found in our previous publications (Davarpanah et al., 2020, Davarpanah et al., 2020), as well as other references (Davidson and Harrison, 1963, Hymore and Laguerie, 1984).

Briefly, in the two-phase model, the bed is assumed to consist of two phases: an emulsion phase and a bubble phase. While the gas in the bubble phase is in plug flow, the gas in the emulsion phase is considered either in plug flow (EGPF) or perfectly mixed (EGPM). Figure 7-1 illustrates a schematic of EGPF and EGPM models.

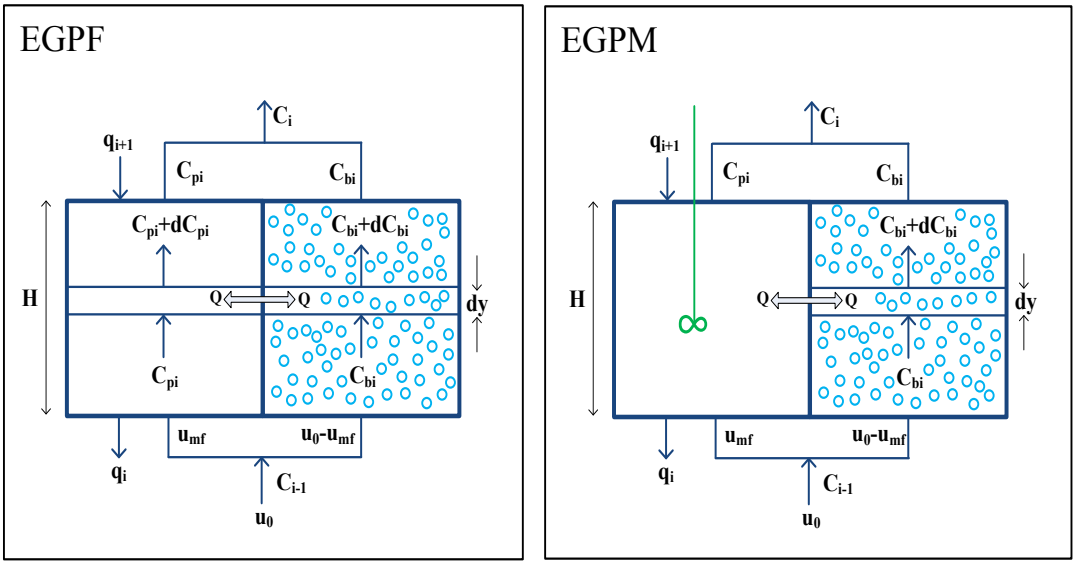

Figure 7-1. Schematic diagram of EGPF and EGPM (Hymore and Laguerie, 1984).

According to Figure 7-1, VOC concentration leaving i^{th} stage could be calculated using Eq. (7-2).

$$C_i = \beta C_{bi}\Big|_{y=H} + (1-\beta)C_{pi} \tag{7-2}$$

where,

$$\beta = 1 - \frac{u_{mf}}{u_0} \tag{7-3}$$

Using a material balance on a rising bubble and integrating it with respect to the height of the bed, it can be shown that the concentration of VOC in the bubble phase is defined as a function of height (y) as:

$$C_{bi}(y) = C_{pi} + \left(C_{i-1} - C_{pi}\right) exp\left(\frac{-Qy}{u_b V_b}\right) \tag{7-4}$$

where Q is the interphase mass transfer flow rate, u_b is bubble rise velocity, V_b is bubble volume, and C_{pi} and C_{bi} are VOC concentrations in particulate phase and bubble phase, respectively.

Assuming the particulate phase to be perfectly mixed, the concentration of VOC could be calculated using the following equations:

$$C_{pi} = \bar{C}^*_{pi} + \left(C_{i-1} - \bar{C}^*_{pi}\right)\left(\frac{1 - \beta \exp(-X)}{1 - \beta \exp(-X) + k_i'}\right) \tag{7-5}$$

where

$$X = \frac{QH}{u_b V_b} \tag{7-6}$$

$$k_i' = \frac{W m_i k_i}{A \rho_g u_0} \tag{7-7}$$

On the other hand, if the particulate phase is assumed to be in plug flow, solving a material balance written for infinitesimal height "*dy*" could result in the following equations:

$$C_{bi} = \frac{C_{i-1} - \bar{C}^*_{pi}}{m_{1i} - m_{2i}} \left(m_{1i} \exp\left(-m_{2i} y\right) - m_{2i} \exp\left(-m_{1i} y\right) \right) + \bar{C}^*_{pi} \tag{7-8}$$

$$C_{pi} = \frac{C_{i-1} - \bar{C}^*_{pi}}{m_{1i} - m_{2i}} \left[m_{1i} \left(1 - \frac{H}{X} m_{2i} \right) \exp\left(-m_{2i} H\right) - m_{2i} \left(1 - \frac{H}{X} m_{1i} \right) \exp\left(-m_{1i} H\right) \right] + \bar{C}^*_{pi} \tag{7-9}$$

$$m_{1i} = \frac{1}{2} \frac{X + k'_i}{H\left(1-\beta\right)} - \frac{1}{2} \left[\left(\frac{X + k'_i}{H\left(1-\beta\right)} \right)^2 - \left(\frac{4 k'_i X}{H^2 \left(1-\beta\right)} \right) \right]^{\frac{1}{2}} \tag{7-10}$$

$$m_{2i} = \frac{1}{2} \frac{X + k'_i}{H\left(1-\beta\right)} + \frac{1}{2} \left[\left(\frac{X + k'_i}{H\left(1-\beta\right)} \right)^2 - \left(\frac{4 k'_i X}{H^2 \left(1-\beta\right)} \right) \right]^{\frac{1}{2}} \tag{7-11}$$

Considering plug flow for gas in the particulate phase, the concentration of VOC in the particulate phase varies along the bed and therefore, an average concentration could be calculated according to Eq. (7-12):

$$\bar{C}_{pi} = \frac{1}{H} \int_0^H C_{pi} dy \tag{7-12}$$

$\bar{q}_i$ can be given by the following formula (Hymore and Laguerie, 1984):

$$\bar{q}_i = q_0 \prod_{j=0}^{i} \alpha_j + \sum_{j=1}^{i} q^*_j \left(1 - \alpha_j\right) \prod_{k=j+1}^{i} \alpha_k \tag{7-13}$$

where,

$$\alpha_j = \frac{1}{1+k_j\tau} \tag{7-14}$$

$$\tau = \frac{W}{F_p} \tag{7-15}$$

Knowing $\bar{q}_i$, $\bar{C}^*_{pi}$ is calculated using Freundlich isotherm.

7.5.3. Hydrodynamics

General hydrodynamic formulas used in this research are listed in Table 7-3.

Table 7-3. General hydrodynamic formulas used in the calculations of two-phase models.

Parameter	Formula	Reference
Bubble rise velocity, u_b	$u_b = u_0 - u_{mf} + 0.711(gd_b)^{\frac{1}{2}}$	(Kunii and Levenspiel, 1969)
Minimum fluidization velocity, u_{mf}	$\frac{1.75}{\phi\varepsilon_{mf}^3}\mathrm{Re}_{mf}^2 + \frac{150(1-\varepsilon_{mf})}{\phi^2\varepsilon_{mf}^3}\mathrm{Re}_{mf} - \mathrm{Ar} = 0$ $\mathrm{Re}_{mf} = \frac{\rho_g d_p u_{mf}}{\mu_g}$ $\mathrm{Ar} = \frac{\rho_g(\rho_p - \rho_g)gd_p^3}{\mu_g^2}$	(Abasaeed and Al-Zahrani, 1998)
Mass of adsorbent on each stage, W	$W = \rho_p H_{mf} A(1-\varepsilon_{mf})$	(Hymore and Laguerie, 1984)
Bed height at minimum fluidization, H_{mf}	$H_{mf} = H\left(1 - \frac{u_0 - u_{mf}}{u_b}\right)$	(Hymore and Laguerie, 1984)
Bubble volume, V_b	$V_b = \frac{\pi d_b^3}{6}$	(Hymore and Laguerie, 1984)
Bubble surface, S_b	$S_b = \pi d_b^2$	(Hymore and Laguerie, 1984)

Number of bubbles per unit bed volume, N_b	$N_b = \frac{u_0 - u_{mf}}{u_b V_b}$	(Hymore and Laguerie, 1984)

Other hydrodynamic parameters such as bubble diameter and bed void fraction at minimum fluidization could be calculated using various formulas presented in the following tables. The ranges of values in this study are also given in the tables to make the comparison of formulas easier. It should be noted that those formulas which could not satisfy the condition of our system are not reported. As an example, equations derived for predicting the bubble diameter for conditions such as when bubble diameter is identical to tube diameter or when bubbles are rising in a large volume of liquid are excluded.

The most common formulas used for the estimation of bubble diameter are listed in Table 7-4. Bubble diameter could be a function of the height along the adsorbent layer on each stage, the number of orifices per unit surface area of distributer, adsorbent properties, air velocity, and minimum fluidization velocity. It is worth mentioning that some references provide the formulas for calculating bubble diameter as a function of height, while others report formulas for calculating mean bubble diameter. In former cases, the mean bubble diameter could be approximated considering $y=H/2$ (Poulopoulos and Inglezakis, 2006).

Table 7-4. Common formulas for estimating bubble diameter, d_b.

No.	Formula	Value (mm)	Ref.
1	$d_{b0} = 0.821\left(\frac{A\left(u_0 - u_{mf}\right)}{n_0}\right)^{0.4}$, $d_b = d_{b0} + 1.4\rho_p d_p\left(\frac{u_0}{u_{mf}}\right)y$	6–10	(Kato and Wen, 1969)
2	$d_{b0} = 0.347\left(\frac{A\left(u_0 - u_{mf}\right)}{n_0}\right)^{\frac{2}{5}}$, $d_b = \left(u_0 - u_{mf}\right)^{\frac{1}{2}}\left(y + d_{b0}\right)^{\frac{3}{4}} g^{-\frac{1}{4}}$	5.4–8.3	(Rowe, 1976, Hatzantonis et al., 2000)
3	$d_b = 0.54\left(u_0 - u_{mf}\right)^{0.4}\left(y + 4\sqrt{\frac{A}{n_0}}\right)^{0.8} g^{-0.2}$	4.4–5.8	(Darton et al., 1977, Grosso and Chiovetta, 2005, Poulopoulos and Inglezakis, 2006)
4	$d_{b0} = 0.821\left(\frac{A\left(u_0 - u_{mf}\right)}{n_0}\right)^{0.4}$, $d_b = d_{b0} + 0.027\left(u_0 - u_{mf}\right)^{0.94} y$	2.8–3.8	(Geldart, 1970, Mori and Wen, 1975)
5	$d_b = 1.6\rho_p d_p\left(\frac{u_0}{u_{mf}} - 1\right)^{0.63} y$	2–3	(Yasui and Johanson, 1958, Mori and Wen, 1975)
6	$d_{b0} = 0.347\left(\frac{A\left(u_0 - u_{mf}\right)}{n_0}\right)^{\frac{2}{5}}$, $d_{bm} = 0.652\left(A\left(u_0 - u_{mf}\right)\right)^{\frac{2}{5}}$, $d_b = d_{bm} - \left(d_{bm} - d_{b0}\right)exp\left(\frac{-0.3y}{D}\right)$	1.5–2	(Mori and Wen, 1975, Hatzantonis et al., 2000, Lu et al., 2004, Poulopoulos and Inglezakis, 2006)

7	$\bar{d}_b = 0.21\left(u_0 - u_{mf}\right)^{0.42} H^{0.8} \times \exp\left(-0.25\left(u_0 - u_{mf}\right)^2 - 0.1\left(u_0 - u_{mf}\right)\right)$	1.7–1.8	(Cai et al., 1994)

Table 7-5 lists four well–known formulas employed for the prediction of bed void fraction at minimum fluidization, some with more parameters than the others.

Table 7-5. Common formulas for estimating ε_{mf} .

No.	Formula	Value	Ref.
1	$\varepsilon_{mf} = \frac{1}{6}(6 - \pi)$	0.476	(Davidson and Harrison, 1963)
2	$\varepsilon_{mf} = \left(\frac{0.071}{\phi}\right)^{\frac{1}{3}}$	0.414	(Poulopoulos and Inglezakis, 2006)
3	$\varepsilon_{mf} = 0.586\phi^{-0.72}\mathrm{Ar}^{-0.029}\left(\frac{\rho_g}{\rho_p}\right)^{0.021}$	0.392	(Davidson and Harrison, 1963, Poulopoulos and Inglezakis, 2006)
4	$\varepsilon_{mf} = \left(\frac{0.091\left(1 - \varepsilon_{mf}\right)}{\phi^2}\right)^{\frac{1}{3}}$	0.386	(Poulopoulos and Inglezakis, 2006)

7.5.4. Mass transfer

The overall adsorption rate is presented by the following equation:

$$\frac{dq}{dt} = k\left(q^* - q\right) = km\left(C - C^*\right) \tag{7-16}$$

The rate of adsorption depends on (i) external diffusion, (ii) internal diffusion, (iii) surface diffusion, and (iv) adsorption on the sites. In FBs, steps external and surface diffusion are fast and their contribution to the overall mass transfer resistance is negligible. Adsorption on the sites does

create a significant resistance in physical adsorption of VOC on DOWEX either. Therefore, the only step which has to be considered is internal diffusion (Davarpanah et al., 2020, Davarpanah et al., 2020). Two main formulas for calculating the mass transfer coefficient based on the internal diffusion are listed in Table 7-6.

Table 7-6. Common formulas for calculating mass transfer coefficient, *k*.

No.	Formula	Value (s^{-1})	Ref.
1	$D_e = \frac{\varepsilon_p}{\tau'}\left(\frac{1}{\frac{1}{D_g}+\frac{1}{D_k}}\right)$, $D_k = 4850 d_{pore}\left(\frac{T}{M}\right)^{\frac{1}{2}}$, where d_{pore} is in cm and $km = \frac{60 D_e}{d_p^2}$	4.70×10^{-3}–8.51×10^{-3}	(Seader and Henley, 2006)
2	$\xi = \frac{q_0^* - 1}{q_{0.5}^*}$, $D_e = \frac{D_g \varepsilon_p}{2}\left[1-\exp\left(-\frac{d_{pore}\bar{u}}{3D_g}\right)\right]$, $\bar{u} = \left(\frac{8RT}{\pi M}\right)^{0.5}$ $k = 7.75\frac{\rho_g C_{in} a_p D_e}{\left(1-0.225\xi^{0.4}\right) q_0^* d_p}$, $a_p = \frac{6}{d_p}$ where $q_{0.5}^*$ is the VOC content of adsorbent which is in equilibrium with VOC with concentration $C_0/2$.	5.64×10^{-3}–1.37×10^{-2}	(Hymore and Laguerie, 1984)

Do (Do, 1998) indicated that tortuosity in formula no. 1 in Table 7-6 could be described by formulas in Table 7-7.

Table 7-7. Common formulas for calculating tortuosity, τ'.

No.	Formula	Value	Ref.
1	$\tau' = 1 + \frac{1}{2}\left(1 - \varepsilon_p\right)$	1.34	(Do, 1998)
2	$\tau' = 1 - \frac{1}{2}\ln \varepsilon_p$	1.57	(Do, 1998)
3	$\tau' = \frac{1}{\sqrt{\varepsilon_p}}$	1.77	(Do, 1998)

Based on the two-phase theory, other than adsorption on solids, there is a mass transfer between the bubble phase and the particulate phase which could be calculated using formulas listed in Table 7-8.

Table 7-8. Common formulas for calculating interphase mass transfer, Q.

No.	Formula	Value (m^3/s)	Ref.
1	$K_{bc} = \frac{3}{4}u_{mf} + 0.975 D_g^{\frac{1}{2}}\left(\frac{g}{d_b}\right)^{\frac{1}{4}}$, $K_{bc} \simeq K_{be}$ $Q = K_{bc} \times S_b$	9.54×10^{-6}–1.65×10^{-5}	(Davidson and Harrison, 1963, Kunii and Levenspiel, 1969, Hatzantonis et al., 2000)
2	$K_{bc} = \frac{1}{3}u_{mf} + \left(\frac{4\varepsilon_{mf} D_g u_b}{\pi d_b}\right)^{\frac{1}{2}}$, $K_{bc} \simeq K_{be}$ $Q = K_{bc} \times S_b$	5.29×10^{-6}–9.68×10^{-6}	(Sit and Grace, 1981, Hatzantonis et al., 2000, Poulopoulos and Inglezakis, 2006)

3	$K_{bc} = 2\frac{u_{mf}}{d_b}$, $K_{ce} = 6.78\left(\frac{\varepsilon_{mf} D_g u_b}{d_b^{\,3}}\right)^{\frac{1}{2}}$ $\frac{1}{K_{be}} = \frac{1}{K_{bc}} + \frac{1}{K_{ce}}$ $Q = K_{be} \times S_b$	1.08×10^{-6}– 2.11×10^{-6}	(Peters et al., 1982, Hatzantonis et al., 2000)
4	$K_{bc} = \frac{3}{4}u_{mf} + 0.75 D_g^{\frac{1}{2}}\left(\frac{g}{d_b}\right)^{\frac{1}{4}}$, $K_{ce} = 1.13\left(\frac{\varepsilon_{mf} D_g u_b}{d_b}\right)^{\frac{1}{2}}$ $\frac{1}{K_{be}} = \frac{1}{K_{bc}} + \frac{1}{K_{ce}}$ $Q = K_{be} \times S_b$	1.30×10^{-6}– 2.61×10^{-6}	(Kunii and Levenspiel, 1969, Hatzantonis et al., 2000, Poulopoulos and Inglezakis, 2006)

Eqs (7-2), (7-4), and (7-5) for EGPM mode and Eqs (7-2), (7-8), and (7-9) for EGPF mode should be solved to determine VOC concentration leaving stage *i*. Calculating the concentration of VOC in each stage, the removal efficiency (RE) for each stage is calculated using the following formula:

$$\mathrm{RE}(\%) = \frac{C_0 - C_i}{C_0} \times 100 \tag{7-17}$$

where C_0 and C_i are VOC concentrations in the inlet gas stream and at the exit of stage *i*, respectively.

The average relative error (ARE) was calculated using the following equation (Foo and Hameed, 2010):

$$\text{ARE}\ (\%) = \frac{100}{n}\sum_{i=1}^{n}\left|\frac{\exp_i - \text{cal}_i}{\exp_i}\right| \tag{7-18}$$

where $\exp_i$ and cal_i are the experimental and calculated results, respectively.

The computer program used to solve the equations was developed in Matlab R2018b.

7.6. Results and discussion

7.6.1. Effect of operating conditions on adsorption of TMB on DOWEX

The results presented in this section (section 4.1) were all obtained from a simulation that used formula no. 1 in Tables 4–8. It will be shown after discussing the combined effect of formulas in section 4.2.6 that using formula no. 1 in Tables 4–8 in calculations of two-phase model would yield the best accuracy (i.e. lowest ARE) when modeling the adsorption of TMB on DOWEX in a FB.

7.6.1.1. Overall removal efficiency

Figure 7-2 compares the overall removal efficiencies calculated using the two-phase model in EGPM and EGPF modes with experimental measurements at different adsorbent feed rates, air flow rates, and initial concentrations. The two-phase model, in both modes, is able to accurately predict the removal efficiency as a function of adsorbent feed rate, initial concentration, and gas flow rate (Figure 7-2). Comparing the two modes, EGPF shows better performance than EGPM with an ARE=6.3% compared to 9.8%. These results agree with those of Mohanty et al. (Mohanty et al., 2009, Mohanty and Meikap, 2011).

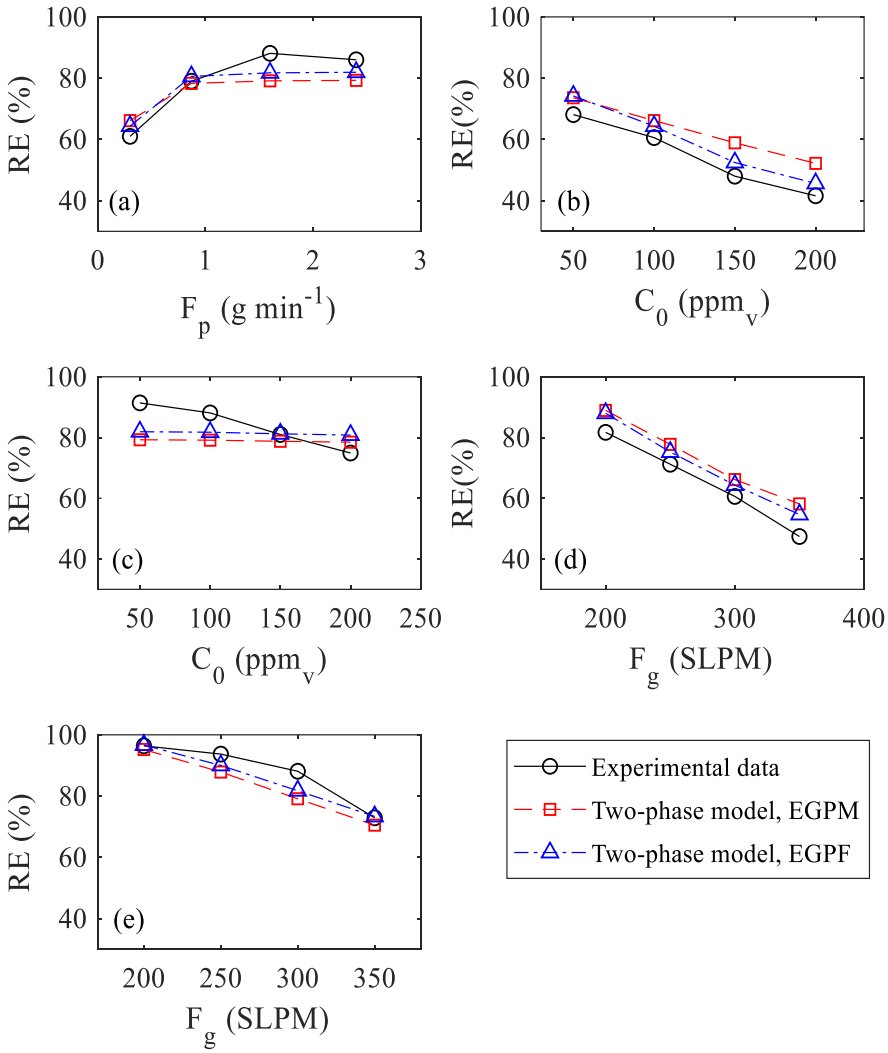

Figure 7-2. Experimental and predicted removal efficiencies as a function of (a) adsorbent feed rate (exp. no. 1–4), (b) initial concentration when F_p=0.3 g/min (exp. no. 5–8), (c) initial concentration when F_p=1.6 g/min (exp. no. 9–12), (d) gas flow rate when F_p=0.3 g/min (exp. no. 13–16), and (e) gas flow rate when F_p=1.6 g/min (exp. no. 17–20).

There is no clear explanation of the effect of the gas mixing pattern in the emulsion phase on the performance of the two-phase model. It is reported that EGPF might produce better results than EGPM when the ratio of bed height to bed diameter in a bubbling bed is relatively high (Kunii and Levenspiel, 1969, Lu et al., 2004). A high ratio of air velocity to minimum fluidization velocity, on the other hand, could lead to the preference of EGPM over EGPF (Kunii and Levenspiel, 1969, Lu et al., 2004). Some researchers adopted an intermediary approach to describe the mixing of the

gas in the emulsion phase. For instance, Shiau and Lin (Shiau and Lin, 1993) introduced a model in which the emulsion phase is divided into a series of well-mixed tanks, each of which exchanges the emulsion gas between neighboring stages. In some other cases, the model outcomes were reported to be relatively insensitive to the gas–mixing pattern in the emulsion phase (Grace, 1986). Therefore, a specific flow pattern for describing the gas mixing in the emulsion phase is not always guaranteed when modeling FBs.

Since EGPF showed better performance than EGPM in this study, the simulation of the stage-wise concentration of TMB, as well as the effect of different hydrodynamic and mass transfer formulas on the performance of the two-phase model is reported only for EGPF model.

7.6.1.2. Stage-wise concentrations

The stage–wise comparison of TMB concentration predicted using EGPF is compared to experimental data in Figure 7-3. The results of stage-wise simulation for both EGPF and EGPM are listed in Table S11 in Supplementary Information. As can be seen in Figure 7-3, EGPF predictions are in close agreement with experimental results. In experiments no. 7 and 8, the concentration of TMB has been leveled at stage 1, suggesting an equilibrium condition.

In some cases such as experiments no. 5, 12, and 16, small deviations from experimental results are seen, which could be attributed to both model error and experimental error. Model error is mainly due to the simplifying assumptions in both empirical parameters and governing equations such as uniform bed temperature, pseudo-first-order kinetics, and linear adsorption isotherm in the range of C_P^* and $\bar{C}_P$. Some degrees of experimental error should also be considered, especially when working with polymeric adsorbents which tend to develop static charges. A single bead of DOWEX stuck on the mesh in the inlet of the sampling tube might cause an error in VOC concentration measured.

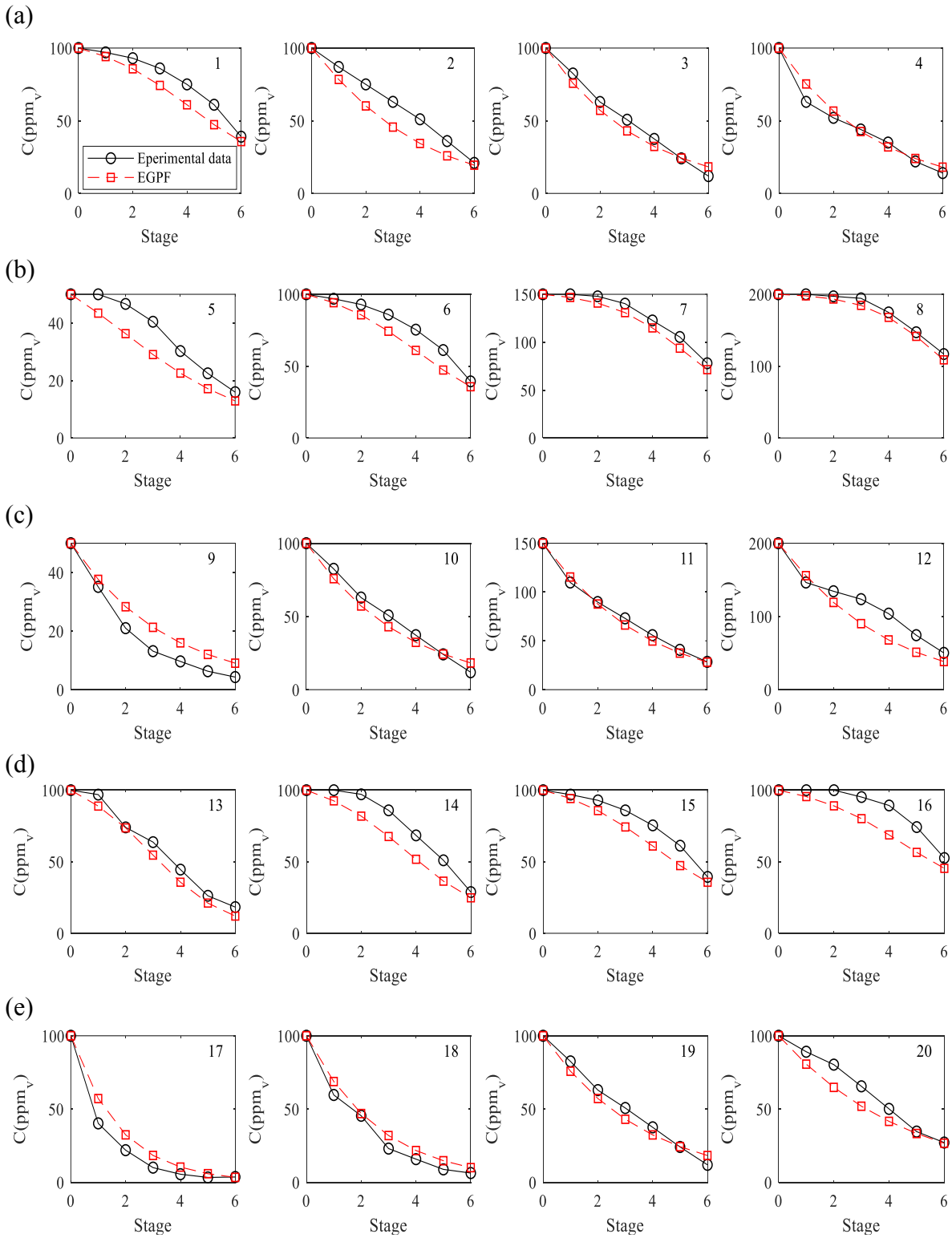

Figure 7-3. Stage–wise comparison of experimental vs. EGPF prediction of TMB concentration in the fluidized bed in varying (a) adsorbent feed rate (exp. no. 1–4), (b) initial concentration when F_p=0.3 g/min (exp. no. 5–8), (c) initial concentration when F_p=1.6 g/min (exp. no. 9–12),

(d) gas flow rate when F_p=0.3 g/min (exp. no. 13–16), and (e) gas flow rate when F_p=1.6 g/min (exp. no. 17–20). Experiment number from Table 7-2 is shown on the top–right side of each diagram. Concentration at stage 0 denotes the inlet concentration.

7.6.2. Effect of different formulas on the performance of EGPF model

As mentioned in section 3, different empirical and semi-empirical formulas have been reported in the literature to predict bubble diameter, bed void fraction at minimum fluidization, mass transfer coefficient, and tortuosity, all summarized in Tables 4–8. In this section, the effect of those formulas on the performance of the two-phase model in EGPF mode is put to the test. To this end, the simulation of TMB on DOWEX incorporating the best set of formulas (formula no.1 in Tables 4–8) was utilized, and the impact of each formula on the accuracy of model predictions was examined by changing that particular formula.

7.6.2.1. Bubble diameter

The measurement of bubble size has been conducted by different methods including local probe detection (Sellakumar and Zakkay, 1988, Almstedt and Zakkay, 1990, Olowson and Almstedt, 1990), X-ray photography (King and Harrison, 1980, Barreto et al., 1983, Hoffmann and Yates, 1986) and photographing the erupting bed surface (Kawabata et al., 1981, Chitester et al., 1984). Many formulas have been proposed for predicting the bubble diameter. Some formulas are based on theoretical approaches, whereas some are purely empirical and give no insight into the reasons that make bubbles grow to a particular size. Figure 7-4 depicts the performance of different formulas for the prediction of bubble diameter. The ARE ranged from 6.3% to 12.6% depending on the formula used for calculating bubble size.

Formula no. 1, suggested by Kato and Wen (Kato and Wen, 1969), incorporates the approximations of Kobayashi et al. (Kobayashi et al., 1965) for bubble diameter and Davidson and

Harrison (Davidson and Harrison, 1963) for initial bubble diameter. The validity of this correlation was tested using the experimental data of Cooke et al. (Cooke et al., 1968). Formula no. 2 was suggested based on fitting previously published data on bubble size where it is unrestricted by the bed walls. This semi-empirical formula incorporated only one adjustable parameter which was found using the method of least squares (Rowe, 1976).

Formula no. 3 assumes that bubbles rise in preferred paths and travel a specific distance before coalescing with neighboring bubbles. The distance traveled is proportional to bubbles lateral separation (Darton et al., 1977). Having been tested with experimental data, the formula was found to be inaccurate when bubble growth is limited by the presence of fine particles in the bed (d_p < 100 μm) or when there is slug flow which typically happens if the following conditions are met (Darton et al., 1977):

$$\frac{u-u_{mf}}{0.35\sqrt{gD}} > 0.2$$

$$\frac{h}{D} > 0.35\left(1-\frac{1}{\sqrt{n_0}}\right)$$

Formula no. 4 was suggested by Geldart (Geldart, 1970) using experimental data obtained in two- and three-dimensional fluidized beds in various air velocities and different solid properties. It should be noted that no practical bed can be completely 2D and the term refers to a bed with a rectangular cross-section whose length is 10-100 times bigger than its width (the width and length of the rectangular cross-section of the 2D bed used by Geldart (Geldart, 1970) were 1.27 cm and 68 cm, respectively). Formula no. 5 was obtained based on experiments conducted by Yasui and Johnson (Yasui and Johanson, 1958). They measured bubble diameter and the rate of the bubble

rising in FBs using a light probe technique. Two different FB setups with diameters of 10.2 and 15.2 cm were used and the experiments were conducted using a wide range of different solids.

Formula no. 6 was established by Mori and Wen (Mori and Wen, 1975) with the assumption that bubbles generated in a bubbling FB with diameter d_{b0} continuously grow till they reach the maximum bubble size of d_{bm} and then break up into smaller bubbles as they grow further. This formula takes into account the effect of bed diameter on the bubble diameter and is reported to be valid in the range of $0.5 \leq u_{mf} \leq 20$ cm/s, $0.006 \leq d_p \leq 0.045$ cm, $u_0 - u_{mf} \leq 48$ cm/s, and $D \leq 130$ cm. However, when validating the model using the experimental data, there were cases with more than 50% absolute error (Mori and Wen, 1975).

Cai et al. (Cai et al., 1994) introduced formula no. 7 after analyzing the experimental data reported in previous studies conducted at different pressures and gas velocities. Considering 5 variables in the formula, which were obtained by fitting the experimental data, the authors successfully reduced the average error of the fitting to ±11.8%. Even though the average error reported is relatively low, the comparison of the calculated and experimental data in their study shows data points that are quite spread out from the average, raising questions about the versatility of the formula.

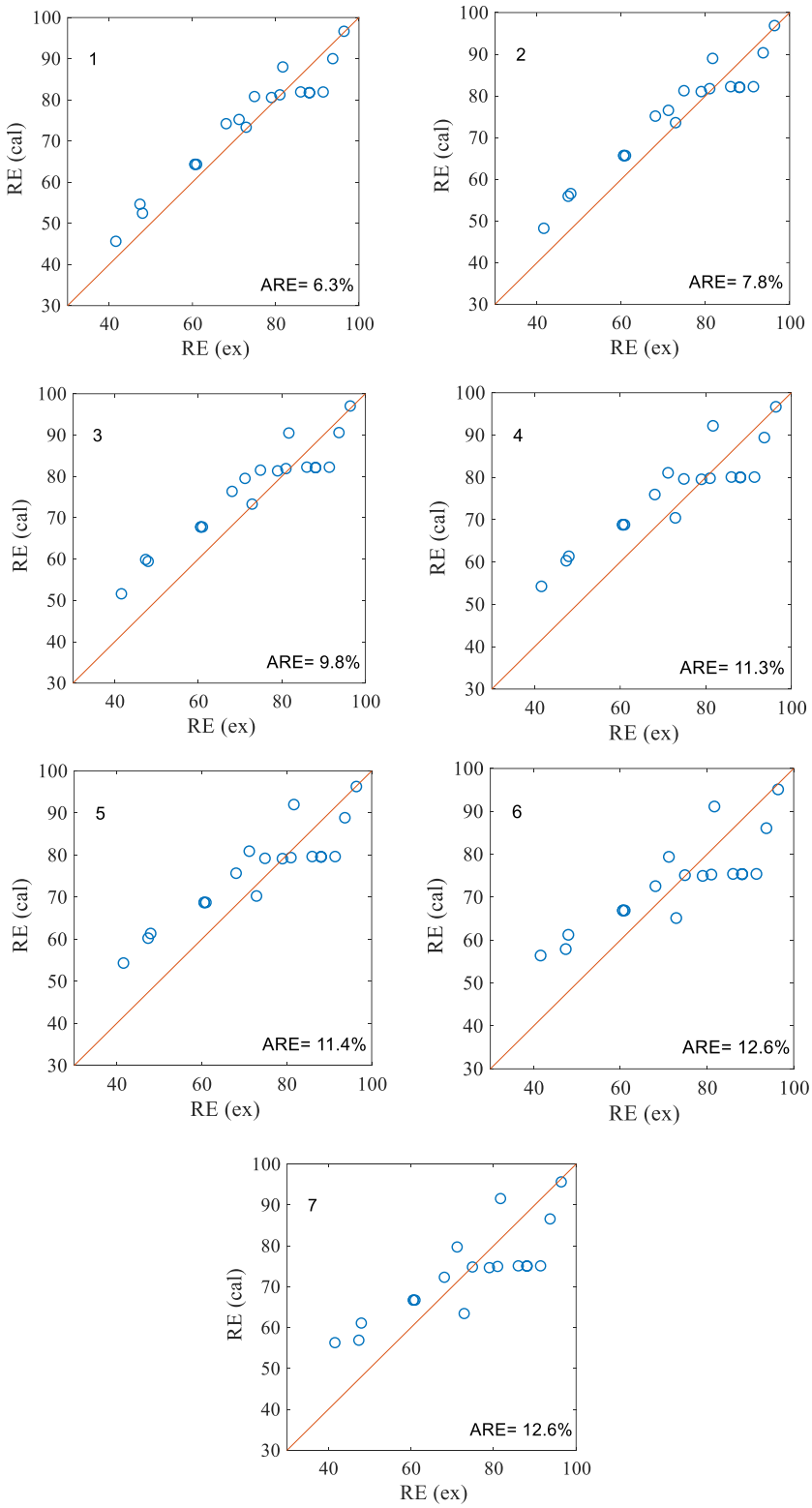

Figure 7-4. Experimental versus calculated removal efficiencies using EGPF model and different formulas for the estimation of bubble diameter (d_b) listed in Table 7-4. The numbers at the top left of the figures represent the formula number in Table 7-4.

7.6.2.2. Bed voidage

Figure 7-5 shows the deviation of calculated results from experimental removal efficiencies while using different formulas for predicting bed porosity at minimum fluidization velocity (ε_{mf}). It can be seen from the results that ε_{mf} is one of the most important parameters influencing the outcome of the simulation to a great extent.

Solids in formula no. 1 are assumed to be uniform and spherical with the cubic mode of packing (Davidson and Harrison, 1963). The calculation is rather simple and the result is within an acceptable range. The bed voidage at incipient fluidization can also be evaluated using the approximations of Wen and Yu (Wen and Yu, 1966) (formulas no 2 and 4 in Table 7-5) which take into account the sphericity factor, or that of Broadhurst and Becker (Broadhurst and Becker, 1975) (formula no. 3 in Table 7-5) which allows for the effect of not only sphericity but also solid and gas properties.

In the case of spherical solids (ϕ=1), the value of bed porosity at u=u_{mf} calculated using formulas no. 2–4 is 0.414, 0.392, and 0.386, respectively. These values are very close to the typical voidage of a fixed bed containing spherical particles (0.39–0.40). However, we know that, unless solids in the bed are large, the value of voidage at incipient fluidization in a FB should be greater than that of a fixed bed. Poulopoulos and Inglezakis (Poulopoulos and Inglezakis, 2006) clearly stated that "if a value below 0.4 is predicted, it should be considered suspicious. Values around 0.5 are typical". Consistently, formulas no. 2–4 yielded poor predictions of the experimental results.

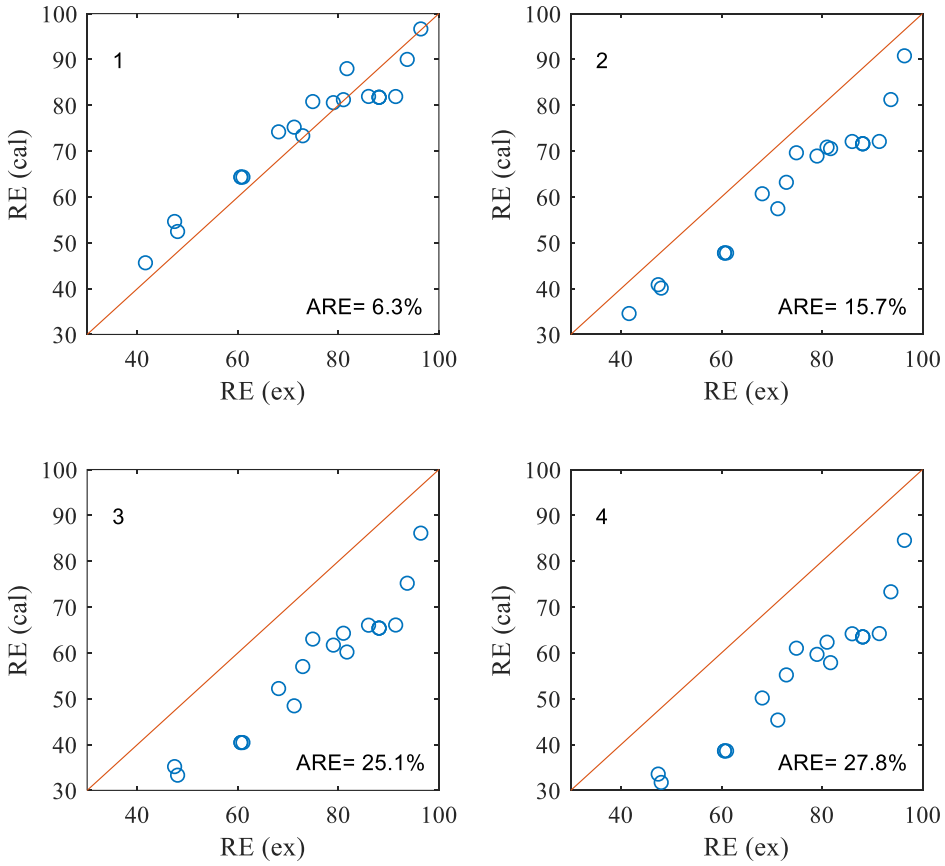

Figure 7-5. Experimental versus calculated removal efficiencies using EGPF model and different formulas for the estimation of bed porosity at u=u_{mf} (ε_{mf}) listed in Table 7-5. The numbers at the top left of the figures represent the formula number in Table 7-5.

7.6.2.3. Adsorption rate constant

Two formulas were employed in EGPF to predict the adsorption rate constant and the results are compared in Figure 7-6. The first formula was established based on Fick's first law for molecular diffusion through a fluid in a pore (Seader and Henley, 2006). The second formula, developed by Hall et al. (Hall et al., 1966), was derived from an exact numerical solution of pore–diffusion equations and was used for the prediction of water vapor adsorption on alumina particles (Hymore and Laguerie, 1984). The range of mass transfer coefficient values calculated by both

formulas (Table 7-6) are very close, and while both formulas accomplish quite reasonable results, the first one shows better performance in the simulation of FB.

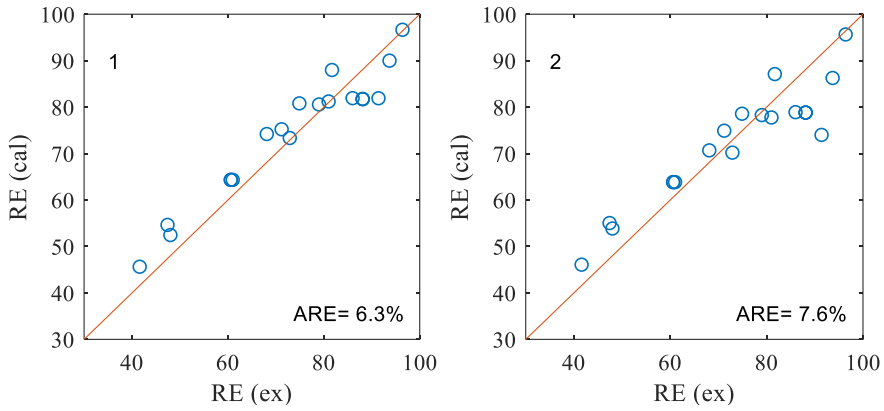

Figure 7-6. Experimental versus calculated removal efficiencies using EGPF model and different formulas for the estimation of mass transfer rate (k) listed in Table 7-6. The numbers at the top left of the figures represent the formula number in Table 7-6.

7.6.2.4. Tortuosity

The tortuosity in adsorption rate formula no.1 in Table 7-6 could be calculated by different formulas listed in Table 7-7. The first formula was obtained by Akanni et al. (Akanni et al., 1987) using a Monte–Carlo simulation for a dilute suspension of spheres in which the diffusion occurs on a length scale shorter than the heterogeneity of the solids, whereas formula no. 2 was obtained by applying the variational method to a bed of overlapping spheres (Do, 1998). Formula no.3 is also a simple and well–known formula for calculating tortuosity (Do, 1998).

Table 7-7 displays the performance of EGPF using different formulas for calculating tortuosity. It can be seen that the first formula leads to the best prediction and as the value of tortuosity increases, the results diverge more from the diagonal line in the ex–cal removal efficiency figure. Tortuosity values calculated as a function of porosity using different formulas are shown in Figure 7-8. The obtained values are close to each other only when the porosity is above 0.5; however, at

lower porosity values the formulas outcomes diverge, and choosing the proper formula to estimate tortuosity becomes more important. The surge of tortuosity in low porosities in formulas no. 2 and 3 could cause a large unrealistic reduction in adsorption rate constant (see formula no.1 in Table 7-6).

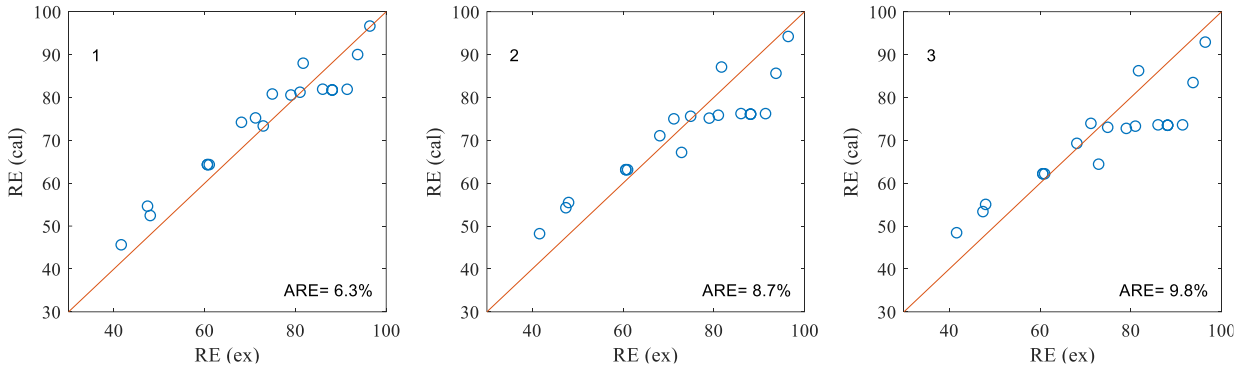

Figure 7-7. Experimental versus calculated removal efficiencies using EGPF model and different formulas for the estimation of tortuosity (τ') listed in Table 7-7. The numbers at the top left of the figures represent the formula number in Table 7-7.

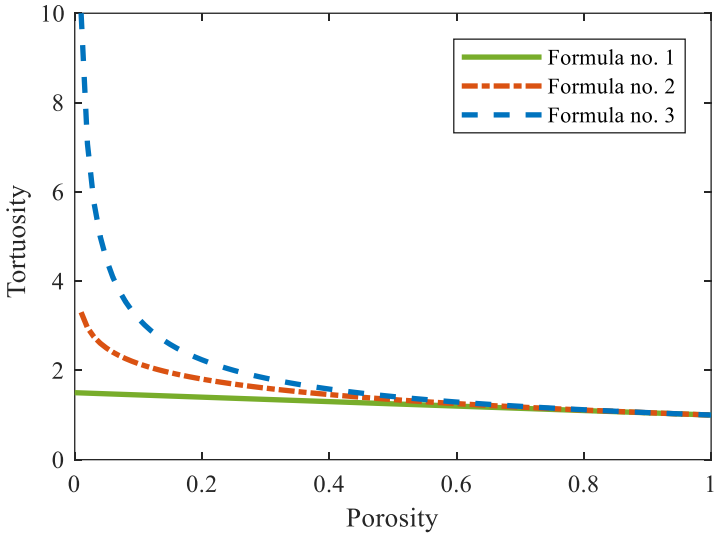

Figure 7-8. Variation of tortuosity as a function of porosity.

7.6.2.5. Interphase mass transfer

Four different formulas were used to estimate bubble–solid interphase mass transfer needed for the prediction of the removal efficiencies (Table 7-8). The first formula was derived theoretically by completing a mass balance on an infinitesimal element around a bubble and solving the equations in a spherical coordinate system. The full derivation of this well–known formula is described elsewhere (Davidson and Harrison, 1963). This theoretical formula was verified experimentally by Baird and Davidson (Baird and Davidson, 1962) in a liquid system with D_g replaced by the liquid–phase diffusing coefficient. Formula no. 2 was obtained from experimental results where a non–interfering technique was used to measure the concentration of ozone in bubbles injected into a bed of inactive 390 μm glass beads fluidized by ozone-free air (Sit and Grace, 1981).

Formula no. 3 takes into consideration a third phase (in addition to the emulsion and bubble phases) called the cloud phase (Peters et al., 1982). This formula showed favorable results when describing the transient and steady-state behavior of a bubbling fluidized bed at various conditions including the extent of flow reversal of gas, rate constant, reaction order, and superficial gas velocity (Peters et al., 1982). Formula no. 4 was theoretically proven using the Davidson bubble model for calculating bubble–cloud mass transfer and Higbie penetration model for calculating cloud–emulsion mass transfer (Kunii and Levenspiel, 1969).

Figure 7-9 shows that the first two formulas lead to more accurate predictions than the last two. Formulas no. 1 and 2 were developed to consider the interphase mass transfer between two phases: an emulsion phase and a bubble phase; whereas formulas no. 3 and 4 consider a third phase (cloud and wake phase) in their calculations. It has been reported that the cloud/wake region is generated at high air velocities (above 8 times the minimum fluidization velocity) as a result of bubbles

carrying a considerable amount of solids behind them (Mohanty et al., 2009, Mohanty and Meikap, 2011). The highest air velocity examined in this study, however, results in u/u_{mf}=6.8. In other words, there are only two phases under the operating conditions in this study, and adding an extra mass–transfer resistance to the calculations of interphase mass transfer coefficient in formulas no. 3 and 4 yields underpredicted REs.

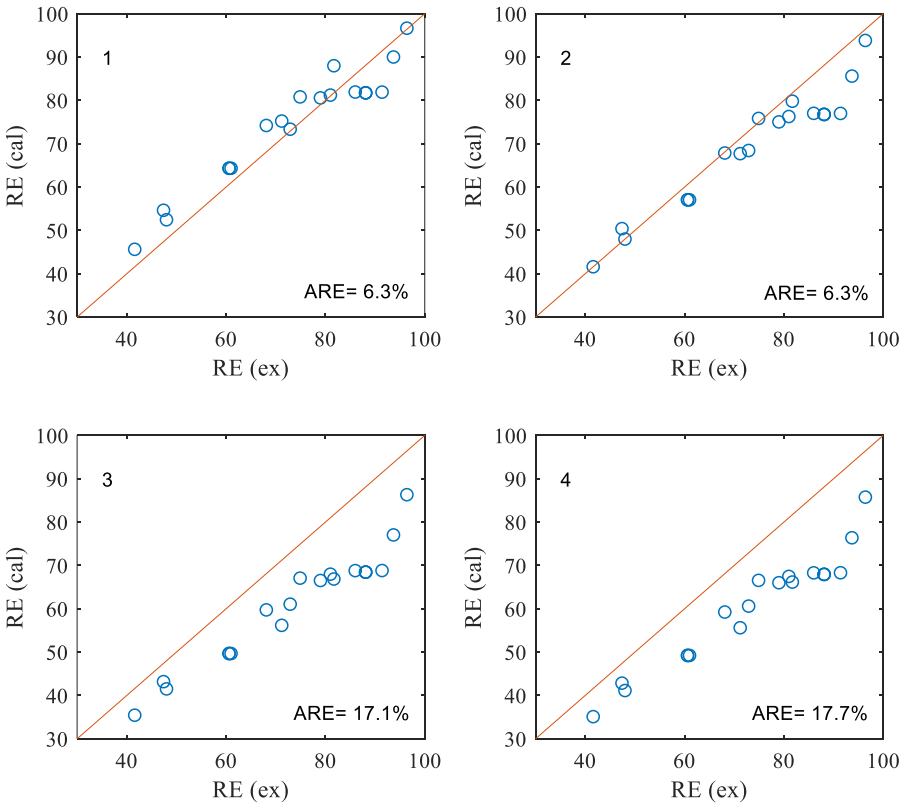

Figure 7-9. Experimental versus calculated removal efficiencies using EGPF model and different formulas for the estimation of interphase mass transfer flow rate (Q) listed in Table 7-8. The numbers at the top left of the figures represent the formula number in Table 7-8.

7.6.2.6. The combined effect of formulas

The effect of each formula on the performance of the two-phase model in EGPF mode was discussed by changing one formula at a time while keeping the rest of them fixed. However, as far

as the outcome of the model is concerned, the combined effect of formulas should not be overlooked. Table 7-9 lists the top 20 sets of formulas that show the best performances in predicting the overall removal efficiency in adsorption of TMB on DOWEX.

It was previously discussed that some formulas were less likely to generate accurate results in the range of our operating parameters. Those formulas, however, cannot be totally disregarded since they were used and verified by many researchers. For example, even though the estimation of ε_{mf} is more realistic when using formula no. 1 (ε_{mf}=0.48~0.5) in Table 7-5, formula no. 2 (ε_{mf}=0.41) might also produce satisfactory results when used along with other formulas describing hydrodynamics and mass transfer inside the bed. Hence, there are still many choices for formulas used in the two-phase model. This emphasizes the importance of introducing a generic set of formulas verified by a large dataset.

Table 7-9. Top 20 sets of formulas for prediction of overall removal efficiency in adsorption of TMB on DOWEX using EGPF. The table lists the formula numbers in their associated tables.

no.	d_b	ε_{mf}	k	τ'	Q	ARE (%)
1	1	1	1	1	1	6.3
2	1	1	1	1	2	6.3
3	2	1	1	1	2	6.4
4	3	2	1	1	1	7.0
5	1	1	2	-	1	7.6
6	5	4	1	1	1	7.7
7	2	1	1	1	1	7.8
8	3	1	1	1	2	7.8
9	5	3	1	1	1	7.8
10	3	3	1	1	1	8.0
11	2	2	1	1	1	8.2
12	1	1	1	2	1	8.7

13	2	1	2	-	1	8.7
14	5	2	1	1	2	8.8
15	1	1	2	-	2	8.9
16	2	1	2	-	2	8.9
17	5	2	1	1	1	8.9
18	4	4	1	1	1	9.1
19	3	4	1	1	1	9.1
20	4	3	1	1	1	9.3

7.6.3. A generic formula for the simulation of FBs

In the previous section, it was discussed that using different formulas could noticeably influence the performance of the two-phase model when simulating FB operation. In this section, all possible combinations of formulas listed in Table 7-4 –Table 7-8 were tested in the simulation of a large dataset of FB experiments conducted at different adsorbent feed rates, gas flow rates, initial concentrations, weir heights, and numbers of stages. The data was acquired from different setups (lab-scale, bench-scale and industrial-scale adsorbers) using three adsorbates (TMB, a solvent mixture (SM), and water vapor) on three types of adsorbents: activated carbon (with a wide range of apparent densities), DOWEX, and alumina particles (Table S12 in Supplementary Information). The simulation was also run in two different modes of EGPM and EGPF.

The results show that the experimental data is best predicted when the formulas listed in Table 7-10 are used, resulting in the AREs of 6.3% and 7.3% for EGPM and EGPF modes, respectively. The numbers in Table 7-10 refer to the formulas' number in the corresponding tables (Table 7-4–Table 7-8).

Figure 7-10 illustrates the deviation of calculated results from experimental data when the optimized sets of formulas were used in EGPM and EGPF modes. With a cursory look, the

calculated results seem to be fairly in agreement with the experiments. Using EGPM mode (which produced the highest precision), for example, 98% of calculated results were within absolute 15% of the experimental measurements, 87% within absolute 10%, and 66% within absolute 5%. The optimized set of formulas suggested in Table 7-10 were produced based on data from a variety of design and operating conditions; hence, could be considered general enough to be used for simulation of various fluidized bed adsorbers with different choices of adsorbent, adsorbate, size and operating condition.

Table 7-10. The best set of formulas for simulating the adsorption process in a multistage fluidized bed. The table lists the formula numbers in their associated tables.

Mode	d_b	ε_{mf}	k	τ'	Q	ARE (%)
EGPM	4	2	1	1	1	6.3
EGPF	3	1	1	2	1	7.3

(a)

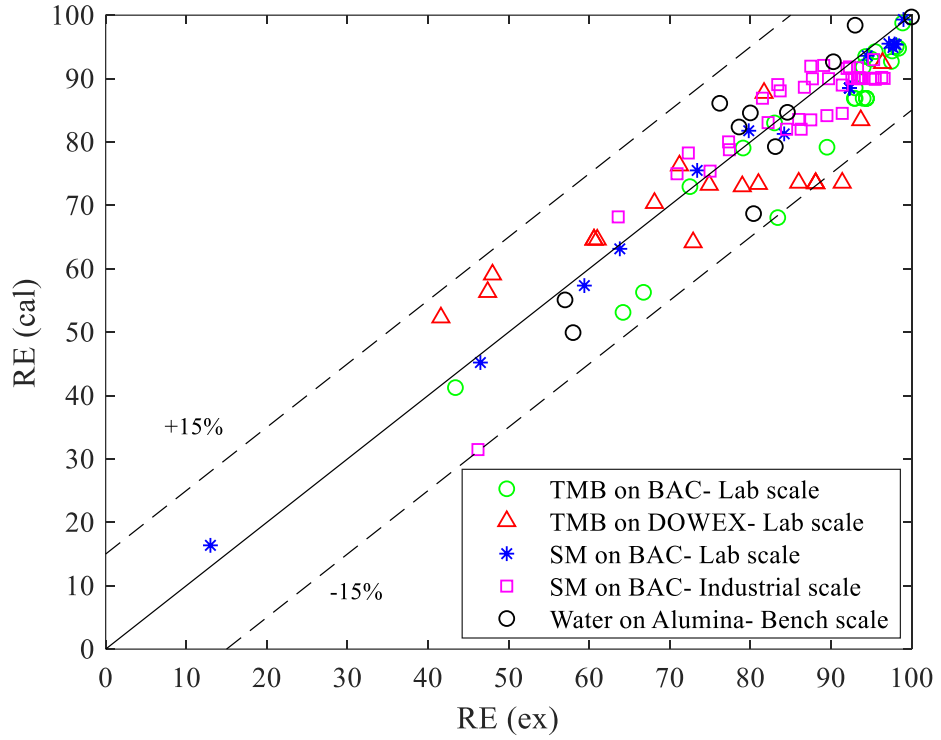

(b)

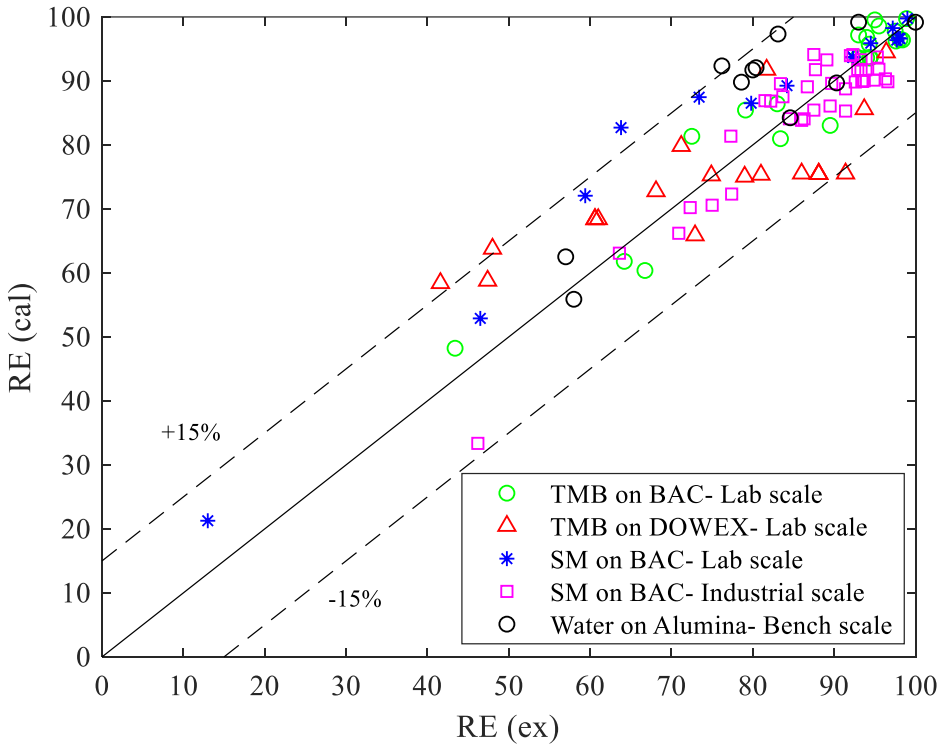

Figure 7-10. The performance of (a) EGPM and (b) EGPF models in prediction of experimental data using the optimized set of formula listed in Table 7-10.

7.7. Conclusions

A two-phase model was developed in two modes of EGPM and EGPF to predict the adsorption of a VOC in a multistage fluidized bed. The verification of calculated results against experimental data showed that the two-phase model could successfully predict the results of the adsorption process in different operation conditions (ARE= 6.3% and 9.8% for EGPF and EGPF, respectively). The effect of different formulas on the performance of the two-phase model was studied and discussed. It was shown that proper choices of empirical and semi-empirical formulas in the calculations of the two-phase model is imperative especially when the estimations of bed voidage and interphase mass transfer coefficient are concerned. The top 20 sets of formulas that yielded the best performance of the two-phase model were presented for the adsorption of TMB on DOWEX. Finally, a generic set of formulas was proposed which could maximize the prediction accuracy (lowest ARE) for a large dataset of fluidized bed adsorption experiments. Using FB adsorption data with a variety of design and operating conditions improve the predictability of the suggested set of formulas for describing various fluidized bed systems with different characteristics.

7.8. References

Abasaeed, A.E., Al-Zahrani, S.M., 1998. Modeling of Fluidized Bed Reactors for the Polymerization Reaction of Ethylene and Propylene. *Developments in Chemical Engineering and Mineral Processing*, **6**: 121-134.

Akanni, K.A., Evans, J.W., Abramson, I.S., 1987. Effective transport coefficients in heterogeneous media. *Chemical Engineering Science*, **42**: 1945-1954.

Almstedt, A.E., Zakkay, V., 1990. An investigation of fluidized-bed scaling-capacitance probe measurements in a pressurized fluidized-bed combustor and a cold model bed. *Chemical Engineering Science*, **45**: 1071-1078.

Amdebrhan, B.T. (2018). Evaluating the Performance of Activated Carbon, Polymeric, and Zeolite Adsorbents for Volatile Organic Compounds Control. Department of Civil and Environmental Engineering, University of Alberta. **Master of Science**.

Baird, M.H.I., Davidson, J.F., 1962. Gas absorption by large rising bubbles. *Chemical Engineering Science*, **17**: 87-93.

Barreto, G.F., Yates, J.G., Rowe, P.N., 1983. The effect of pressure on the flow of gas in fluidized beds of fine particles. *Chemical Engineering Science*, **38**: 1935-1945.

Broadhurst, T.E., Becker, H.A., 1975. Onset of fluidization and slugging in beds of uniform particles. *AIChE Journal*, **21**: 238-247.

Cai, P., Schiavetti, M., De Michele, G., Grazzini, G.C., Miccio, M., 1994. Quantitative estimation of bubble size in PFBC. *Powder Technology*, **80**: 99-109.

Chitester, D.C., Kornosky, R.M., Fan, L.S., Danko, J.P., 1984. Characteristics of fluidization at high pressure. *Chemical Engineering Science*, **39**: 253-261.

Cooke, M., Haris, W., Highley, J., Williams, O., 1968. *Tripartite Chem. Engng Conf. Symp. on Fluidisation I*: 14-20.

Darton, R.C., Lanauze, R.D., Davidson, J.F., Harrison, D., 1977. Bubble Growth Due To Coalescence in Fluidized Beds. *Transactions of the Institution of Chemical Engineers*, **55**: 274-280.

Davarpanah, M., Hashisho, Z., Crompton, D., Anderson, J.E., Nichols, M., 2020. Modeling VOC adsorption in lab- and industrial-scale fluidized bed adsorbers: Effect of operating parameters and heel build-up. *Journal of Hazardous Materials*, **400**: 123129.

Davarpanah, M., Hashisho, Z., Phillips, J.H., Crompton, D., Anderson, J.E., Nichols, M., 2020. Modeling VOC adsorption in a multistage countercurrent fluidized bed adsorber. *Chemical Engineering Journal*, **394**: 124963.

Davidson, J.F., Harrison, D. (1963). Fluidized Particles. New York, Cambridge University Press.

Do, D.D. (1998). Adsorption Analysis: Equilibria And Kinetics. London, Imperial College Press.

Foo, K.Y., Hameed, B.H., 2010. Insights into the modeling of adsorption isotherm systems. *Chemical Engineering Journal*, **156**: 2-10.

Geldart, D., 1970. The size and frequency of bubbles in two- and three-dimensional gas-fluidised beds. *Powder Technology*, **4**: 41-55.

Grace, J.R. (1986). Modelling and Simulation of Two-Phase Fluidized Bed Reactors. Chemical Reactor Design and Technology: Overview of the New Developments of Energy and Petrochemical Reactor Technologies. Projections for the 90's. H. I. de Lasa. Dordrecht, Springer Netherlands**:** 245-289.

Grosso, W., Chiovetta, M., 2005. Modeling a fluidized-bed reactor for the catalytic polimerization of ethylene: particle size distribution effects. *Latin American applied research*, **35**: 67-76.

Hall, K.R., Eagleton, L.C., Acrivos, A., Vermeulen, T., 1966. Pore- and Solid-Diffusion Kinetics in Fixed-Bed Adsorption under Constant-Pattern Conditions. *Industrial & Engineering Chemistry Fundamentals*, **5**: 212-223.

Hatzantonis, H., Yiannoulakis, H., Yiagopoulos, A., Kiparissides, C., 2000. Recent developments in modeling gas-phase catalyzed olefin polymerization fluidized-bed reactors: The effect of bubble size variation on the reactor's performance. *Chemical Engineering Science*, **55**: 3237-3259.

Hoffmann, A.C., Yates, J.G., 1986. Experimental Observations of Fluidized Beds at Elevated Pressures. *Chemical Engineering Communications*, **41**: 133-149.

Hymore, K., Laguerie, C., 1984. Analysis and modelling of the operation of a counterflow multistage fluidized bed adsorber for drying moist air. *Chemical Engineering and Processing: Process Intensification*, **18**: 255-267.

Kamravaei, S., Shariaty, P., Hashisho, Z., Phillips, J.H., Anderson, J.E., Nichols, M., Crompton, D. (2016). Performance of a Multistage Fluidized Bed Adsorber Using Polymeric Adsorbent to Capture Volatile Organic Compounds. AIChE Annual Meeting. San Francisco, CA, USA.

Kamravaei, S., Shariaty, P., Jahandar Lashaki, M., Atkinson, J.D., Hashisho, Z., Phillips, J.H., Anderson, J.E., Nichols, M., 2017. Effect of Beaded Activated Carbon Fluidization on Adsorption of Volatile Organic Compounds. *Industrial & Engineering Chemistry Research*, **56**: 1297-1305.

Kato, K., Wen, C.Y., 1969. Bubble assemblage model for fluidized bed catalytic reactors. *Chemical Engineering Science*, **24**: 1351-1369.

Kawabata, J.I., Yumiyama, M., Tazaki, Y., Honma, S., Chiba, T., Sumiya, T., Endo, K., 1981. Characteristics of gas-fluidised beds under pressure. *JOURNAL OF CHEMICAL ENGINEERING OF JAPAN*, **14**: 85-89.

Keenan, J., Chao, J., Kaye, J., 1983. Gas Tables International Version-Thermodynamic Properties of Air, Products of Combustion and Component Gases. *Compressible Flow Functions*.

King, D.F., Harrison, D., 1980. The bubble phase in high-pressure fluidized beds. *Fluidization*: 101-108.

Kobayashi, H., Arai, F., Chiba, T., 1965. Behavior of Bubbles in Gas Solid Fluidized Bed. *Chemical engineering*, **29**.

Kunii, D., Levenspiel, O. (1969). Fluidization engineering. New York, Wiley.

Lu, W.-Z., Teng, L.-H., Xiao, W.-D., 2004. Simulation and experiment study of dimethyl ether synthesis from syngas in a fluidized-bed reactor. *Chemical Engineering Science*, **59**: 5455-5464.

McAuley, K.B., Talbot, J.P., Harris, T.J., 1994. A comparison of two-phase and well-mixed models for fluidized-bed polyethylene reactors. *Chemical Engineering Science*, **49**: 2035-2045.

Mohanty, C.R., Malavia, G., Meikap, B.C., 2009. Development of a Countercurrent Multistage Fluidized-Bed Reactor and Mathematical Modeling for Prediction of Removal Efficiency of Sulfur Dioxide from Flue Gases. *Industrial & Engineering Chemistry Research*, **48**: 1629-1637.

Mohanty, C.R., Meikap, B.C., 2011. Modeling the operation of a three-stage fluidized bed reactor for removing CO2 from flue gases. *Journal of Hazardous Materials*, **187**: 113-121.

Mori, S., Wen, C.Y., 1975. Estimation of bubble diameter in gaseous fluidized beds. *AIChE Journal*, **21**: 109-115.

Olowson, P.A., Almstedt, A.E., 1990. Influence of pressure and fluidization velocity on the bubble behaviour and gas flow distribution in a fluidized bed. *Chemical Engineering Science*, **45**: 1733-1741.

Peters, M.H., Fan, L.-S., Sweeney, T.L., 1982. Reactant dynamics in catalytic fluidized bed reactors with flow reversal of gas in the emulsion phaset. *Chemical Engineering Science*, **37**: 553-565.

Poulopoulos, S.G., Inglezakis, V.J. (2006). Adsorption, ion exchange and catalysis: design of operations and environmental applications, Elsevier.

Rowe, P.N., 1976. Prediction of bubble size in a gas fluidised bed. *Chemical Engineering Science*, **31**: 285-288.

Scala, F., Cammarota, A., Chirone, R., Salatino, P., 2004. Comminution of limestone during batch fluidized-bed calcination and sulfation. *AIChE Journal*, **43**: 363-373.

Scala, F., Salatino, P., Boerefijn, R., Ghadiri, M., 2000. Attrition of sorbents during fluidized bed calcination and sulphation. *Powder Technology*, **107**: 153-167.

Schulzke, T., Westermeyer, J., Giani, H., Hornsby, C., 2018. Combustion of Refined Renewable Biomass Fuel (RRBF) in a bubbling fluidized bed. *Renewable Energy*, **124**: 84-94.

Seader, J.D., Henley, E.J. (2006). Separation process principles, John Wiley & Sons, Inc.

Sellakumar, K.M., Zakkay, V., 1988. Bubble Characterization in Pressurized Fluidized-Bed Combustors with Bed Internals. *Combustion Science and Technology*, **60**: 359-374.

Shiau, C.-Y., Lin, C.-J., 1993. An improved bubble assemblage model for fluidized-bed catalytic reactors. *Chemical Engineering Science*, **48**: 1299-1308.

Sit, S.P., Grace, J.R., 1981. Effect of bubble interaction on interphase mass transfer in gas fluidized beds. *Chemical Engineering Science*, **36**: 327-335.

Tang, M., Cox, R., Kalberer, M., 2014. Compilation and evaluation of gas phase diffusion coefficients of reactive trace gases in the atmosphere: volume 1. Inorganic compounds. *Atmospheric Chemistry and Physics*, **14**: 9233-9247.

Tefera, D.T., Hashisho, Z., Philips, J.H., Anderson, J.E., Nichols, M., 2014. Modeling Competitive Adsorption of Mixtures of Volatile Organic Compounds in a Fixed-Bed of Beaded Activated Carbon. *Environmental Science & Technology*, **48**: 5108-5117.

Toomey, R.D., Johnstone, H.F., 1952. Gaseous Fluidization of Solid Particles. *Chemical Engineering Progress*, **48**: 220-226.

Wen, C.Y., Yu, Y.H., 1966. A generalized method for predicting the minimum fluidization velocity. *AIChE Journal*, **12**: 610-612.

Yasui, G., Johanson, L.N., 1958. Characteristics of gas pockets in fluidized beds. *AIChE Journal*, **4**: 445-452.

8. Chapter 8*: Verification of (semi)empirical relations for predicting fluidization in a fluidized bed using CFD

8.1. Abstract

The main objective of this study is to verify different (semi)empirical formulas used to predict hydrodynamic parameters of a fluidized bed against CFD simulations. The hydrodynamic parameters investigated include minimum fluidization velocity, bed voidage at minimum fluidization condition, bubble diameter, and bubble velocity. All simulations were completed using 3D Euler-Euler-based model available in ANSYS Fluent 19.2. The study of solid volume-averaged velocity inside the bed revealed a minimum fluidization velocity of 0.194 m/s, which was in agreement with the result obtained when the pressure drop in a fluidized bed was set equal to that in a fixed bed. The time-averaged solid volume fraction showed that the constant value of 0.476 (with the assumption of the uniform cubic mode of packing) was a good estimation for bed voidage at minimum fluidization condition. The study of air turbulent viscosity demonstrated high air turbulence above the bed and inside large bubbles within the bed. Higher mean bed heights and higher levels of air circulation were observed at higher air flow rates. The analysis of different formulas predicting bubble diameter and bubble velocity at different bed heights and air flow rates showed that Yasui-Johnson's formula for estimating the bubble diameter could produce results in good agreement with CFD simulations.

* This chapter is intended to be published as an original paper.

8.2. Nomenclature

Symbol	Description	Value	Units
A	cross-section area of bed	4.56×10^{-3}	m^2
Ar	Archimedes number	variable	-
D	adsorber diameter	7.6×10^{-2}	m
d_b	mean bubble diameter	variable	mm, m
d_p	adsorbent mean diameter	7.5×10^{-4}	m
F_g	air flow rate	Table 8-2	SLPM
g	standard gravity	9.8	$m\ s^{-2}$
H	bed height	variable	mm, m
n_0	number of orifices on distributer	4823	-
Re_{mf}	Reynolds number at u_{mf}	variable	-
t	flow time	variable	s
u_0	superficial gas velocity	Table 8-2	$m\ s^{-1}$
u_b	velocity of bubble rising through a bed	variable	$m\ s^{-1}$
u_s	velocity of solid phase	variable	$m\ s^{-1}$
U_s	volume-averaged velocity of solid phase	variable	$m\ s^{-1}$
u_{mf}	minimum fluidization velocity	variable	$m\ s^{-1}$
V_{fb}	fluidized bed volume	4.61×10^{-4}	m^3
y	axis along the bed	-	m
ε_{mf}	bed voidage at u_{mf}	variable	-
μ_g	gas viscosity	1.82×10^{-5}	$kg\ m^{-1}\ s^{-1}$
ρ_g	gas density	1.20	$kg\ m^{-3}$
ρ_p	adsorbent apparent density	601	$kg\ m^{-3}$
ϕ	adsorbent shape factor	1	-

8.3. Introduction

Fluidized bed systems are widely used in various industrial processes (e. g. adsorption, granulation, combustion, and gasification) owing to their favorable heat and mass transfer characteristics resulting from excellent gas-solid contact (Davidson and Harrison, 1963, Kunii and Levenspiel, 1969). Evaluating the performance of a fluidized bed entails a good understanding of the hydrodynamic behavior of the gas-solid flows, which is challenging and still unrevealed in many applications due to the complexity of interactions between phases (Almohammed et al., 2014, Stroh et al., 2016).

In that regard, many researchers have developed (semi)empirical approaches for calculating hydrodynamic parameters (e.g. minimum fluidization velocity and bubble formation), based on experimental lab-scale data (Kobayashi et al., 1965, Kunii and Levenspiel, 1969, Darton et al., 1977, Sit and Grace, 1981, Adánez and Abanades, 1991, Cai et al., 1994, Samuelsberg and Hjertager, 1996, Mathiesen et al., 2000). Although such approaches can provide remarkable insights into the hydrodynamic behavior of fluidized beds, their validity is restricted by the conditions of the experimental data incorporated. Hence, the verification of (semi)empirical approaches for different applications is imperative for developing fluidized bed models.

In recent years, together with the rapid advancements of computing power and numerical algorithms, computational fluid dynamics (CFD) has emerged as a viable tool to span the gaps between experiments and theoretical solutions. Generally, two modeling approaches are widely used for CFD simulation of gas-particle flows (i) Euler-Lagrange method, also quoted in the literature as Discrete Particle Model (DPM), and (ii) Euler-Euler method, also known as Two-Fluid Model (TFM) (Almohammed et al., 2014, Stroh et al., 2016). Both Euler-Lagrange and

Euler-Euler methods consider the gas phase as a continuum, and the main difference is how to deal with the solid phase (Almohammed et al., 2014, Stroh et al., 2016).

In the Euler-Lagrange method, the motion of each individual element is computed based on Newton's law of motion and Navier-Stokes equations (Shi et al., 2019). This approach allows the simulation of different particle types with various sizes, shapes, and densities; and gives more detailed information such as bubble positions, size distribution, and age distribution compared to the Eulerian-Eulerian model (Stroh et al., 2016, Xue et al., 2017). However, calculating trajectories for each individual particle/parcel (depending on deterministic/stochastic particle collision model used) makes the Euler-Lagrange method computationally expensive for large systems (Stroh et al., 2016).

In the Euler-Euler method, the solid phase is treated as a continuum, and coupling between phases is achieved through a shared pressure and interphase forces including the drag force, lift force, and virtual mass force (Almohammed et al., 2014, Azimi et al., 2015, Stroh et al., 2016, Shi et al., 2019). The biggest advantage of this model is the balance it offers between computational costs and the level of details (Stroh et al., 2016, Shi et al., 2019).

There are several factors in the Euler-Euler simulation of a fluidized bed which play important roles in determining the hydrodynamics of a gas-solid system. These factors include the gas-solid drag model, the specularity and restitution coefficients, and the frictional viscosity (Loha et al., 2012, Loha et al., 2013, Almohammed et al., 2014, Loha et al., 2014, Shi et al., 2019).

The impact of the aforementioned hydrodynamically-important factors on the performance of the CFD simulations was extensively studied in the literature (Du et al., 2006, Loha et al., 2012, Loha et al., 2013, Almohammed et al., 2014, Loha et al., 2014, Zhou et al., 2017, Shi et al., 2019). Du et al. (Du et al., 2006) compared the effect of different drag models on the numerical predictions

of velocity profiles and solid flow patterns in a spouted bed and showed that the Gidaspow model predicted the experimental data very well. Goldschmidt et al. (Goldschmidt et al., 2001) studied the effect of the coefficient of restitution and showed that the hydrodynamics of dense gas fluidized beds strongly depend on the energy dissipated in particle-particle collisions. Huilin et al. (Huilin et al., 2003) later confirmed this result and showed that considering the effect of particle-particle interactions was essential for obtaining realistic simulations using a fundamental hydrodynamics model. Taghipour et al. (Taghipour et al., 2005) studied the hydrodynamics of a two-dimensional gas-solid fluidized bed reactor at different restitution coefficients. They found that the sensitivity of the model to the restitution coefficient was higher at gas velocities below that required for minimum fluidization.

In a more comprehensive study, Shi et al. (Shi et al., 2019) evaluated the effect of model dimensionality, the flow regimes, specularity coefficient, restitution coefficient, and drag sub-models in the simulation of a fluidized bed using the Euler-Euler approach. They stated that a certain combination of hydrodynamic variables and models in 2D simulations might produce results in agreement with experiments. However, taking into account the 3rd dimension was found to be essential to producing physically realistic results (Shi et al., 2019). The results of 3D simulations were also reported to be less sensitive to the choice of numerical parameters compared to 2D simulations. They also found that the application of κ-ε model to describe the turbulence inside the bed provides slightly better agreement with experimental data compared to the laminar model (Shi et al., 2019). According to their results, the optimum values for the specularity coefficient and the restitution coefficient were 0.1 and 0.9, respectively; and the simulation produced more accurate results when the frictional viscosity was taken into calculations (Shi et al., 2019).

In this study, the findings of Shi et al. (Shi et al., 2019) have been employed to simulate one stage of a fluidized bed adsorber using the 3D Euler-Euler model. This study aims to compare the CFD simulation results and the results of empirical/semi-empirical formulas describing minimum fluidization velocity, bed voidage at minimum fluidization velocity, bubble diameter, and bubble velocity inside the fluidized bed. Along with that purpose, hydrodynamic variables such as solid volume fraction and air turbulent viscosity at different time instances, time-averaged solid volume fraction, and volume-averaged solid velocity are presented and discussed.

8.4. Numerical simulation

8.4.1. Model setup

One compartment of a cylindrical multistage fluidized bed adsorber was simulated for all analyses. The height and the diameter of the compartment were 101.6 mm and 76.2 mm, respectively. Beaded activated carbon (BAC) particles with the diameter of 0.75 mm and the true density of 1000 kg/m^3 were fluidized with air uniformly distributed at the bottom of the compartment at ambient conditions. The static bed heights were 4, 8, and 12 mm with a solids volume fraction of 0.6.

8.4.2. Computational model

The models, schemes, and conditions applied to the numerical simulations in this study are summarized in Table 8-1. The Euler-Euler two-fluid approach, which considers the gas and solid phases as an interpenetrating continuum, was used to describe the hydrodynamics of gas-solid flow. The hydrodynamic model incorporates the conservation equations of mass and momentum solved for each phase separately. The momentum equation for the gas and solid phases included additional source terms to describe the inter-phase momentum transfer.

The flow properties of the gas phase were described using the standard k-ε turbulence model (with standard wall functions), and the particle motion in the solid phase was modeled using the kinetic theory of granular flows (KTGF). KTGF, based on the theory of non-uniform dense gases (Chapman et al., 1990), describes the kinetic energy associated with the particle velocity fluctuations as a function of granular temperature which is a measure of particles random oscillations. Using KTGF, the pressure and viscosity of the solid phase can be determined through empirical equations which consider the energy dissipation during particle-particle and particle–wall collisions, represented by restitution coefficient and specularity coefficient, respectively. The closure equations used in this study to describe granular, bulk, and frictional viscosities, as well as granular temperature, solids pressure, and radial distribution are listed in Table 8-1.

The Syamlal-O'Brien (Syamlal and O'Brien, 1989) drag function which is based on the measurement of the terminal particle velocities in fluidized beds was used. Both turbulence interaction and turbulent dispersion between the gas phase and the solid phase were estimated by Simonin's functions (Simonin and Viollet, 1990). All constitutive equations used in this study are summarized in Table S13 in Supplementary Information with their parameters explained in Table S14 in Supplementary information.

The coefficient of restitution was set to 0.9. The same optimum value has been reported in the literature investigating the effect of restitution coefficient (Taghipour et al., 2005, Shi et al., 2019). The specularity coefficient of 0.1 was used to quantify the nature of particle-wall collisions. Although no experimental value of the specularity coefficient has been reported in the literature, some researchers reported that using K=0.1 would yield results within an acceptable range of experiments (Shi et al., 2019). The inlet boundary condition specified a superficial gas velocity

ranging from 0.146 to 1.096 m/s (translated into 40-300 standard liter per minute (SLPM) gas flow rate) in different simulations.

The computational geometry (1:1 scale) was discretized with three block-structured grids using a finite volume method with 72,800 cells (Figure 8-1). The grid cell size in each direction was always larger than twice the particle diameter. This condition is important for the validity of the drag closure equation used in this study (Shi et al., 2019).

The coupled algorithm was applied for pressure–velocity coupling. This algorithm is suitable for transient simulations with relatively large time steps (Ansys, Release 19.2). The least-squares cell-based method which has been reported to be accurate and computationally inexpensive was used for gradient evaluation (Ansys, Release 19.2). The pressure staggering option (PRESTO!) scheme was applied for pressure discretization. This scheme uses the discrete continuity balance for a staggered control volume about the face to compute the staggered pressure (Ansys, Release 19.2).

Quadratic upwind interpolation for convection kinematics (QUICK) scheme (Leonard, 1979) was selected to discretize the convective terms in the momentum equations. The modified high-resolution interface capturing (HRIC) scheme (Muzaferija et al., 1998) was activated to estimate the volume fractions of gas and solid. Including a non-linear blend of upwind and downwind differencing schemes, the modified HRIC scheme offers better accuracy compared to the QUICK and the first-order upwind schemes (Muzaferija et al., 1998). Second-order upwind schemes were used to discretize the convective terms in the k-ε model. A time step of 1×10^{-3} s was used with 50 inner iterations per time step. The numbers of time steps and iterations were adequate to achieve convergence in all cases simulated.

Table 8-1. List of simulation models/schemes/conditions.

Parameter/variable/name	**Model/scheme/value**
Models	
Multiphase model	Eulerian-Eulerian
Volume fraction parameters	Implicit Scheme
BAC density	1000 kg/m^3
BAC particle diameter	0.75 mm
Granular viscosity	Syamlal-O'Brien
Granular Bulk viscosity	Lun et al.
Frictional Viscosity	Schaeffer
Frictional pressure	Based-ktgf
Friction packing limit	0.61
Granular temperature	Algebraic
Solid pressure	Syamlal-O'Brien
Radial distribution	Syamlal-O'Brien
Packing limit	0.63
Viscous model	RANS k-ε model (dispersed)
Phase interaction	
Drag model	Syamlal-O'Brien
Turbulent dispersion	Simonin
Turbulent interaction	Simonin et al.
Restitution coefficient	0.9
Boundary conditions	
Inlet air velocity	0.146-1.096 m/s
Wall shear condition for solid	Specularity coefficient=0.1
Solution	
Pressure-velocity coupling	Coupled Scheme
Spatial discretization-gradient	Least Squares Cell Based
Spatial discretization-Pressure	PRESTO!

Spatial discretization-momentum	QUICK
Spatial discretization-volume fraction	Modified HRIC
Spatial discretization-turbulent kinetic energy	Second order Upwind
Spatial discretization-turbulent dissipation rate	Second order Upwind
Transient formulation	First order implicit
Initial (static) BAC height in bed	4, 8, 12 mm
Time step	1e-3 s
Max iterations per time step	50
Model precision	Double

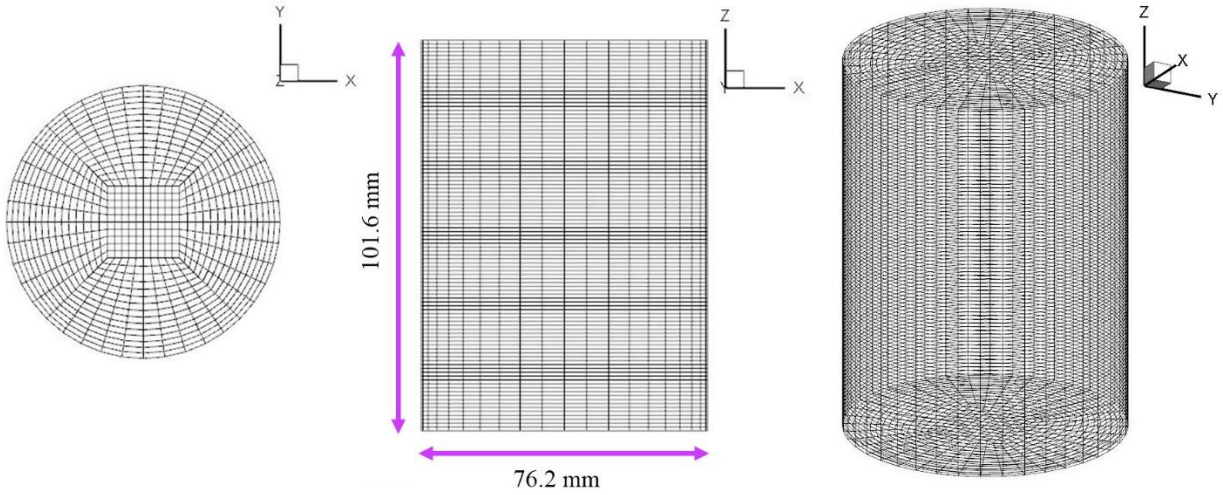

Figure 8-1. 3D bed geometry and mesh grid.

The simulations were carried out in various initial (static) bed heights and air velocities using the commercial CFD package ANSYS® FLUENT™ 19.2 running on a computer equipped with Intel Core i7-8700 (3.20 GHz) processor with 6 physical cores (12 logical cores). The time span simulated (known as simulation time or flow time) was 5 seconds when determining minimum fluidization velocity (u_{mf}) and bed voidage at u_{mf}, and 10 seconds when studying the bubble properties. The simulation conditions are all summarized in Table 8-2. The computation time was typically 3 days for 5 seconds of simulation time, and 5 days for 10 seconds of simulation time.

Table 8-2. Simulation conditions.

Simulation no.	Particles height (mm)	Inlet air flow rate (SLPM)	Inlet air velocity (m/s)	Simulation time (s)
Minimum fluidization velocity (u_{mf}) and bed voidage at u_{mf}				
1	4	40	0.146	5
2	4	50	0.183	5
3	4	53	0.194	5
4	4	55	0.201	5
5	4	60	0.219	5
Bubble diameter and bubble velocity				
6	4	300	1.096	10
7	8	300	1.096	10
8	12	300	1.096	10
9	12	250	0.822	10
10	12	200	0.548	10

8.5. Results and discussion

8.5.1. CFD model validation

To validate the suitability of the models for the present simulations, a comparison was carried out between the experimental data reported by Taghipour et al. (Taghipour et al., 2005) and the simulated results obtained for a 3D fluidized bed reactor. According to the experimental setup, the reactor (1.5 m in height, 0.28 m in length, and 0.025 m in width) was filled with spherical glass particles. The diameter and the density of the particles were 250-300 μm and 2,500 kg/m^3, respectively. The height of the initial packed bed was 0.4 m with a solid volume fraction of 0.6. In the simulation, the particles were fluidized by air flow (0.46 m/s).

Figure 8-2 shows the comparison of measured and predicted time-averaged gas volume fraction at the height of 0.2 m. As can be seen in the figure, the higher gas volume fraction is distributed in

the central region, while the lower gas volume fraction is observed close to the wall. The accumulation of solid particles close to the wall is due to the intensive particle-wall friction. The good agreement between the simulated and experimental values of time-averaged gas volume fraction suggests that the present numerical models are capable of simulating the gas-solid flow in a fluidized bed reactor.

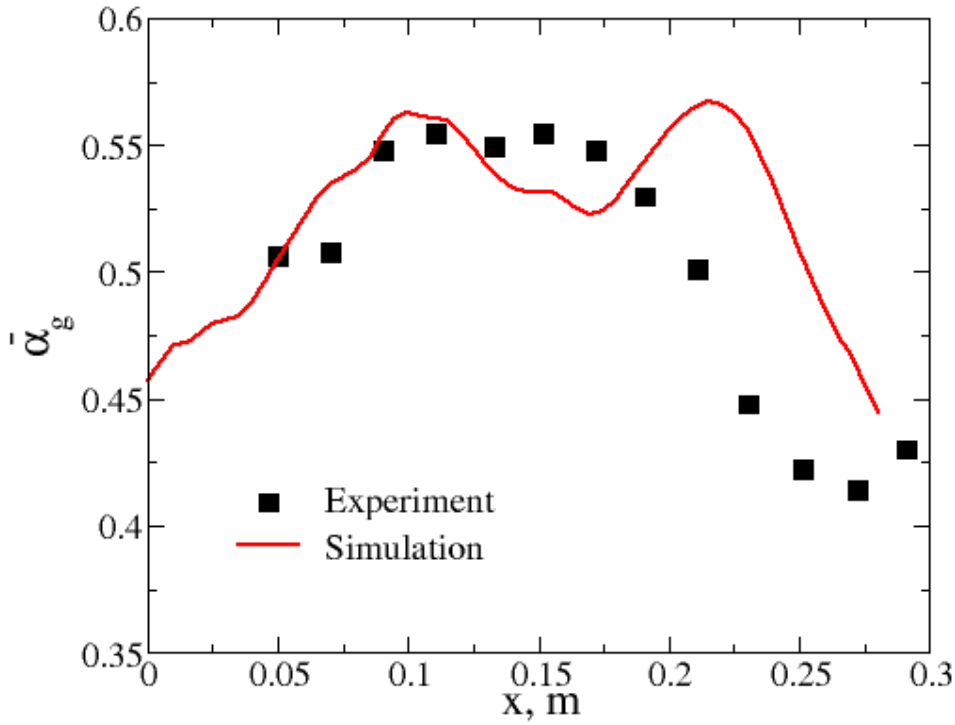

Figure 8-2. Time-averaged gas volume fraction profile along x-coordinate at the inlet gas velocity of 0.46 m/s and the height of 0.2 m. Experimental data are taken from Taghipour et al. (Taghipour et al., 2005)

8.5.2. Minimum fluidization velocity

Minimum fluidization velocity is defined as the lowest gas velocity possible which can fluidize a bed of solid particles. Determining the starting point of the fluidization for the purpose of designing and operating a fluidized bed is the most obvious reason for calculating the minimum fluidization velocity (de Lasa, 2012). In practice, however, the gas velocity in an industrial

fluidized bed is usually 3-6 times higher than that required for minimum fluidization due to several reasons (McAuley et al., 1994, Davarpanah et al., 2020, Davarpanah et al., 2020).

The main reason for operating industrial fluidized beds at gas velocities higher than that required for minimum fluidization is the economic justification of enhancing the treatment rate in processes such as drying and adsorption. Moreover, the minimum fluidization velocity might vary during the operation as a result of changes in the particle size distribution of solid particles which occurs due to particle attrition, agglomeration, and elutriation (de Lasa, 2012). Hence, operating at velocities higher than minimum fluidization velocity would always be necessary to prevent channeling, the formation of non-fluidized zones, and the leakage of bed solids into the inlet air stream. This is especially important when gas distributors in a fluidized bed are less ideal (de Lasa, 2012).

Since industrial fluidized beds are less likely to work at minimum fluidization velocity, an accurate determination of that variable has limited practical values. Nevertheless, the minimum fluidization velocity is a convenient parameter to characterize the interactions between gas and solid particles. Therefore, it is widely used in empirical and semi-empirical formulas to predict bed expansion, mass transfer coefficients, bubble properties in fluidized bed contactors (Kunii and Levenspiel, 1969, de Lasa, 2012). Most of these formulas also use the bed voidage at minimum fluidization velocity in their calculations.

Figure 8-3 shows the volume-averaged velocity (also known as global velocity) of the solid phase over the simulated time span. The volume-averaged velocity which is an indication of the spin-up and start-up time for the volume-force driven flows can be calculated by (Nikrityuk et al., 2005, Shi et al., 2019):

$$U_s = \frac{1}{V_{fb}} \int_0^x \int_0^y \int_0^H \left(\sqrt{u_{s,x}^2 + u_{s,y}^2 + u_{s,z}^2} \right) dxdydz \tag{8-1}$$

where V_{fb} is the volume of the fluidized bed reactor and u_s is the velocity of the solid phase.

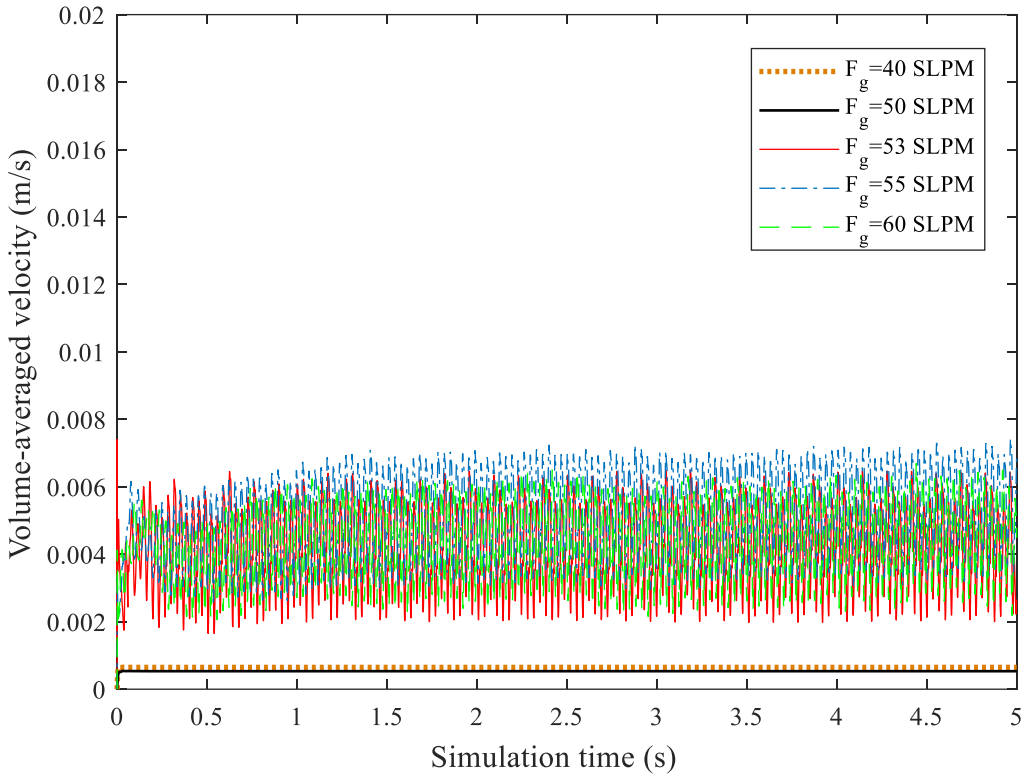

Figure 8-3. Time history of the volume-averaged solid velocity for simulations no 1-5.

At flow rates 40 and 50 SLPM, corresponding to the inlet velocities of 0.146 and 0.183 m/s, respectively, there is no change in the volume-averaged velocity, suggesting no fluidization at those flow rates. At flow rates below that required for minimum fluidization, gas percolates upward through the void spaces between stationary particles without agitating the solid phase. At higher flow rates and starting from 53 SLPM, fluctuations in the volume-averaged velocity are observed which are attributed to the small vibration of particles in restricted regions (Kunii and Levenspiel, 1969). At minimum fluidization flow rate, which was found to be 53 SLPM, the gas-

particles drag force starts to counterbalance the particles' gravitational force. As a result, the vertical component of the compressive force on adjacent particles is withdrawn and particles are suspended by the rising gas (Kunii and Levenspiel, 1969). Common formulas used in the literature to estimate minimum fluidization velocity, along with their outcomes are listed in Table 8-3.

Table 8-3. Well-known formulas for estimating minimum fluidization velocity (u_{mf}) and their outcomes.

No.	Formula/method	F_{mf} (SLPM)	u_{mf} (m/s)	Ref.
1	CFD	53.0	0.194	-
2	$\frac{1.75}{\phi\varepsilon_{mf}^3}\mathrm{Re}_{mf}^2+\frac{150(1-\varepsilon_{mf})}{\phi^2\varepsilon_{mf}^3}\mathrm{Re}_{mf}-\mathrm{Ar}=0$ $\mathrm{Re}_{mf}=\frac{\rho_g d_p u_{mf}}{\mu_g}$ $\mathrm{Ar}=\frac{\rho_g(\rho_p-\rho_g)gd_p^3}{\mu_g^2}$	53.5	0.195	(Abasaeed and Al-Zahrani, 1998)
3	$u_{mf}=\frac{7.169\times10^{-4}d_p^{1.82}(\rho_p-\rho_g)^{0.94}g}{\rho_g^{0.06}\mu_g^{0.88}}$	49.2	0.180	(Leva, 1959, Thonglimp et al., 1984)
4	$\mathrm{Re}_{mf}=(1136+0.0408\mathrm{Ar})^{0.5}-33.7$ $\mathrm{Re}_{mf}=\frac{\rho_g d_p u_{mf}}{\mu_g}$ $\mathrm{Ar}=\frac{\rho_g(\rho_p-\rho_g)gd_p^3}{\mu_g^2}$	27.3	0.100	(Wen and Yu, 1966)

Formula #2 is derived from the Ergun equation (which describes the pressure drop in a fixed bed) and is primarily based upon the fact that the pressure drop in a fluidized bed at minimum fluidization condition is equal to that in a fixed bed (Ergun, 1952). A fluidized bed is perceived as

a fixed bed at air velocities below that required for minimum fluidization. As the gas velocity increases in a fluidized bed, the pressure drop increases linearly until it balances with the weight of the particles. This equilibrium point at which the pressure drop in a fluidized bed starts to deviate from that in a fixed bed is the minimum fluidization velocity (Hockman, 1981). A trial-and-error is needed to solve formula #2 for u_{mf}.

Formulas #2 was reworked with the aim of eliminating the variables ε_{mf} and ϕ to obtain formulas #3 and #4. Formula #3 proposed by Leva (Leva, 1959) is the most commonly used formula to estimate the minimum fluidization velocity directly and without a trial-and-error procedure (Thonglimp et al., 1984, de Lasa, 2012). The data in support of this formula was obtained from a wide range of experiments with different solids and gas properties. Formula #4 was proposed by Wen and Yu (Wen and Yu, 1966), in an attempt to simplify the terms in the Ergun equation. This formula incorporates the following assumptions (Wen and Yu, 1966):

$$\frac{1}{\phi\varepsilon_{mf}^3} \cong 14\,,\ \frac{\left(1-\varepsilon_{mf}\right)}{\phi^2\varepsilon_{mf}^3} \cong 11$$

Comparing the values of minimum fluidization velocity in Table 8-3, the prediction of formula #2 seems to be in close agreement with that of CFD (0.195 vs. 0.194 m/s, respectively). It is hardly surprising given that formula #2 is the definition of u_{mf} from the pressure drop perspective and the fact that no simplifying assumption is used in the derivation of this formula. Formula #2 was successfully used in various studies to simulate the adsorption process inside fluidized beds (Abasaeed and Al-Zahrani, 1998, Davarpanah et al., 2020, Davarpanah et al., 2020). The solution method which usually involves a trial-and-error procedure is the biggest downside of this formula.

Formula #3 is the next best formula for the prediction of u_{mf}. The reason for good prediction of this formula might be the exploitation of many experimental measurements obtained at different

conditions including various solid material (activated carbon, sand, coal, silica, iron powder, etc.), solid shape (spherical, sharp, irregular, etc.), solid diameter (0.01-0.1 mm), and fluidizing gases (air, H_2, CO_2, N_2, etc.). Formula #4, on the other hand, fails to predict an accurate value for minimum fluidization velocity. This is due to the unrealistic predictions of the terms containing the bed voidage at minimum fluidization velocity in the Ergun equation (Poulopoulos and Inglezakis, 2006). It will be shown later that the formulas suggested by Wen and Yu (Wen and Yu, 1966) for prediction of bed voidage at u_{mf} would lead to erroneous values as well.

8.5.3. Bed voidage at minimum fluidization velocity

The bed voidage at minimum fluidization condition is defined as the averaged bed volume fraction occupied by gas at minimum fluidization velocity (de Lasa, 2012). Similar to minimum fluidization velocity, bed voidage at minimum fluidization velocity is an important parameter in fluidized bed modeling. For example, bed voidage at minimum fluidization velocity is directly used in the calculations of minimum fluidization velocity, interphase mass transfer coefficient, and the mass of adsorbent on each stage, and indirectly impacts many other parameters such as bubble properties, adsorption rate, and gas concentration in different phases. Hence, an accurate estimation of this parameter is essential to ensure accurate outcomes of fluidized bed simulations.

Figure 8-4 compares the initial solid volume fraction with the time-averaged solid volume fraction at minimum fluidization velocity. The figure contains the snapshots of the middle slice of the 3D domain which has been magnified at the bottom area to make the comparison easier. At minimum fluidization velocity, the bed height increases due to the gas-particles drag force, resulting in an increase in the bed voidage. It can be seen in Figure 8-4 (b) that the solid volume fraction decreases over the layer of adsorbent from the bottom to the top. After averaging the solid phase volume fraction over the bed height, the averaged bed voidage at minimum fluidization

velocity was calculated 0.471. The same value for the bed voidage at minimum fluidization velocity is obtained if the bed height is compared at the initial state and minimum fluidization velocity, considering the conservation of mass and a solid volume fraction of 0.6 at initialization.

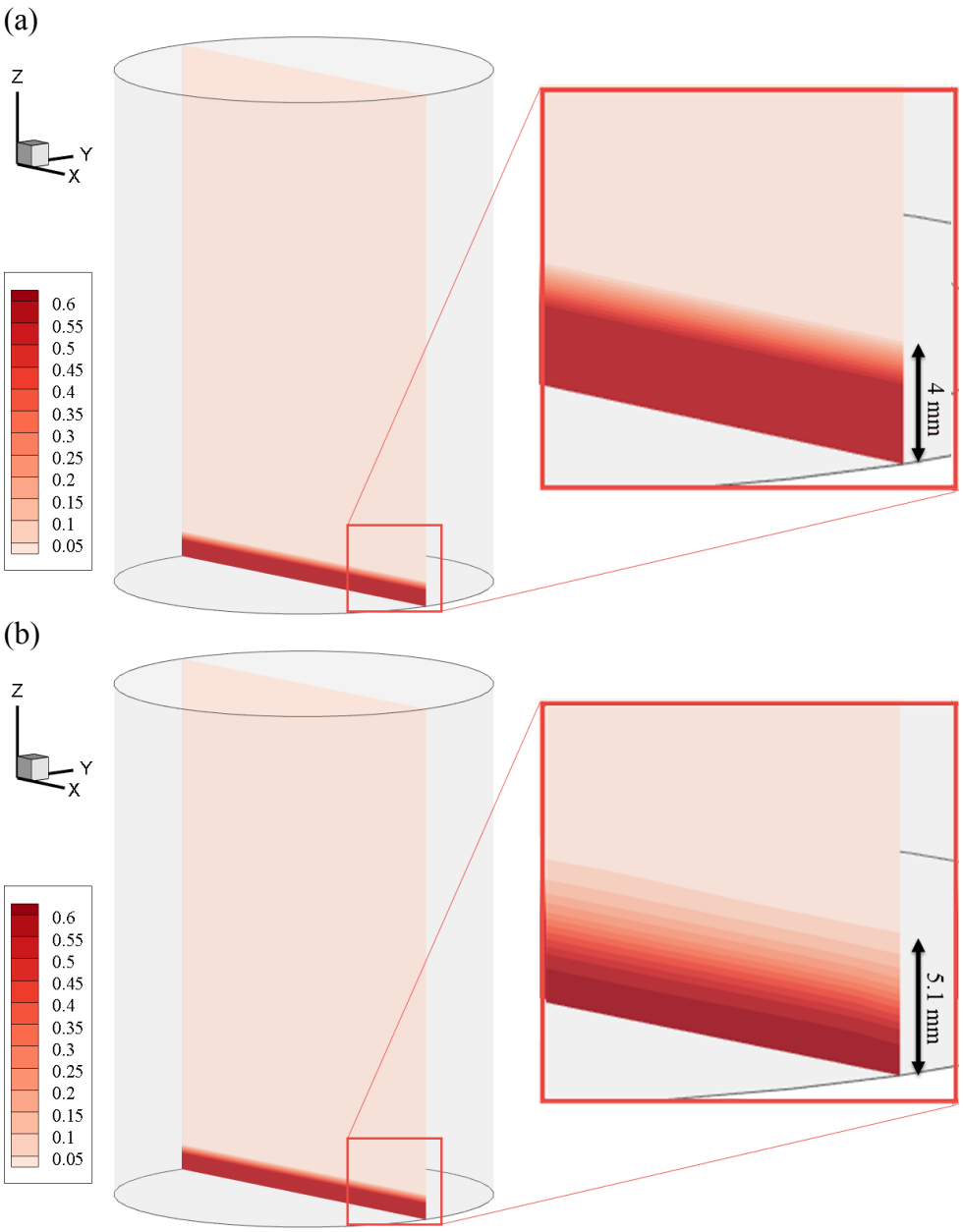

Figure 8-4. (a) Initial solid volume fraction vs (b) time-averaged solid volume fraction at minimum fluidization velocity (simulation no. 3).

Common formulas for estimating the bed voidage at minimum fluidization velocity, along with their outcomes are listed in Table 8-4. A good agreement is seen between the CFD result and the value estimated by formula #3. Formula #3 is a simple formula that assumes solids to be uniform and spherical with the cubic mode of packing (Davidson and Harrison, 1963). This formula calculates a bed voidage of 0.476 at minimum fluidization velocity, regardless of solid and gas properties. The suggested value is totally within the expected range of bed voidage at minimum fluidization velocity. Likewise, Zenz (Zenz, 1982) reported that the assumption of the bed voidage at minimum fluidization conditions not being impacted by changes in the gas properties would produce better results than a correlation obtained from a limited dataset. The same value for bed voidage at minimum fluidization velocity was successfully used in several research studies (Hymore and Laguerie, 1984, Davarpanah et al., 2020, Davarpanah et al., 2020). We previously showed in Chapter 7 that formula #3 had the best performance in modeling the adsorption process inside a fluidized bed using two-phase theory.

Formula #2 proposed by Broadhurst and Becker (Broadhurst and Becker, 1975) overpredicts the CFD results. Bed voidage at minimum fluidization velocity in this formula is influenced by adsorbent sphericity, size, and density, as well as, gas density and viscosity. It has been reported that formula #2 is valid only when $Re_{fm}<10$ and produces more accurate results for relatively small particles (<0.4 mm) (Poulopoulos and Inglezakis, 2006). Moreover, when the prediction of the Broadhurst–Becker equation is smaller than 0.37, this formula should not be used (Poulopoulos and Inglezakis, 2006). Since formula #2 is based on experimental findings, its application is limited to the experimental conditions used to establish this correlation and that could be the reason for the deviation of its prediction form the CFD result in this study (Broadhurst and Becker, 1975, Poulopoulos and Inglezakis, 2006).

The bed voidage at minimum fluidization can also be evaluated using the approximations of Wen and Yu (Wen and Yu, 1966) (formulas no 4 and 5 in Table 8-4) which take into account the sphericity factor. In the case of spherical solids (ϕ=1), the value of bed porosity at $u=u_{mf}$ calculated using formulas no. 4 and 5 are 0.414, and 0.386, respectively. These values are very close to the typical voidage of a fixed bed containing spherical particles (0.39–0.40) (Poulopoulos and Inglezakis, 2006). However, unless solids in the bed are large, the value of voidage at minimum fluidization in a fluidized bed should be greater than that of a fixed bed. Poulopoulos and Inglezakis (Poulopoulos and Inglezakis, 2006) reported that the value of bed voidage at minimum fluidization should be around 0.5, and values below 0.4 are to be considered suspicious. Formulas no. 4 and 5 yielded poor predictions of bed voidage at minimum fluidization when compared to the CFD results. Consistently, it was discussed in the previous section that the estimations of ε_{mf} by Wen-Yu did not produce accurate results for minimum fluidization velocity either.

Table 8-4. Well-known formulas for estimating bed voidage at minimum fluidization velocity, ε_{mf} and their outcomes.

No.	Formula/method	ε_{mf} (-)	Ref.
1	CFD	0.471	-
2	$\varepsilon_{mf} = 0.586\phi^{-0.72}\mathrm{Ar}^{-0.029}\left(\frac{\rho_g}{\rho_p}\right)^{0.021}$ $\mathrm{Ar} = \frac{\rho_g\left(\rho_p-\rho_g\right)gd_p^3}{\mu_g^2}$	0.542	(Davidson and Harrison, 1963, Poulopoulos and Inglezakis, 2006)
3	$\varepsilon_{mf} = \frac{1}{6}(6-\pi)$	0.476	(Davidson and Harrison, 1963)
4	$\varepsilon_{mf} = \left(\frac{0.071}{\phi}\right)^{\frac{1}{3}}$	0.414	(Poulopoulos and Inglezakis, 2006)

5	$\varepsilon_{mf} = \left(\frac{0.091\left(1-\varepsilon_{mf}\right)}{\phi^2} \right)^{\frac{1}{3}}$	0.386	(Poulopoulos and Inglezakis, 2006)

8.5.4. Bubble diameter and bubble velocity

Gas bubbles are formed either directly at the distributor or from the break-up of the distributor jets (de Lasa, 2012). As bubbles rise through the bed, their sizes change (can increase by coalescing into adjacent bubbles or decrease by break up resulting from solid particles penetrations) until they eventually burst at the surface of the bed (de Lasa, 2012, Shi et al., 2019). The bubble growth is limited by the column size or bubble stability; and the bubble rising velocity depends on the bubble size and is normally higher for larger bubbles (de Lasa, 2012). Since bubbles are not perfectly spherical, the bubble diameter always refers to the equivalent bubble diameter defined as the diameter of a sphere which has a volume equal to the bubble volume.

Time histories of the volume-averaged velocity for simulations no. 6-10 are depicted in Figure 8-5. Noticeable narrow peaks captured within the first second of the volume-averaged velocity profiles in all cases are attributed to the start-up time when the gas flows through the packed particle bed and instigates the solid fluidization (Shi et al., 2019). The fluidization process reaches a dynamic steady state within the first second, and thereafter, steady fluctuations of solid volume fraction are explained by continuous formation, rise, coalescence, and the break-up of bubbles (Shi et al., 2019).

An increase in solid volume-averaged velocity is observed (and expected according to eq. (8-1)) when the bed height increases from 4 to 12 mm at the constant flow rate of 300 SLPM (simulation no. 1-3) due to the presence of more solid particles inside the constant volume of the contactor. The increase in the volume-averaged solid velocity after increasing the gas flow rate from 200 to

300 SLPM at constant bed height (simulation no. 3-5) is due to the higher gas flow rate which means higher agitation, and therefore, higher solid velocity.

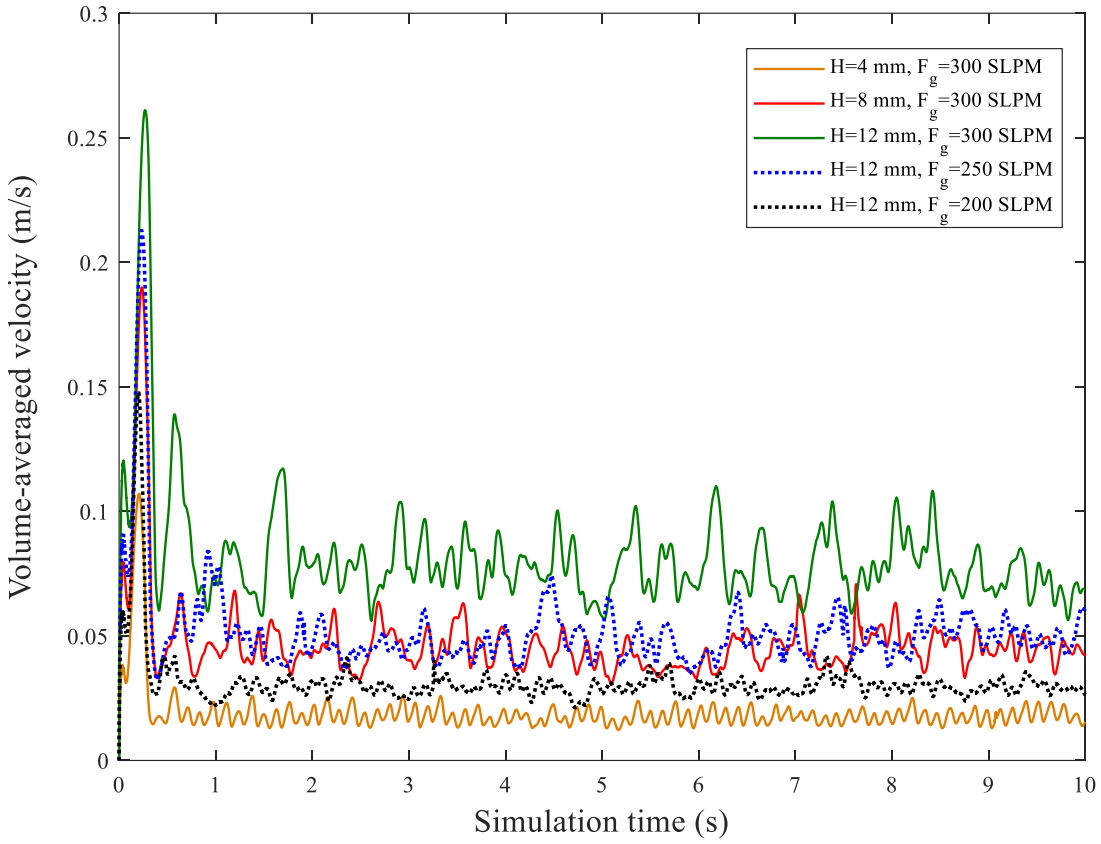

Figure 8-5. Time history of the volume-averaged solid velocity for simulations no. 6-10.

Figure 8-6 illustrates the snapshots of the slice of a 3D contour plot of the solid volume fraction for simulations no. 6-8. Consistent with the results of the volume-averaged velocity, the sudden jump in solid particles at t=0.18 s is attributed to the startup time. Gas bubbles are observed in several snapshots at different time instances, and the burst of the bubbles at the surface of the bed layer is captured in some cases (especially those with higher bed heights, (b) and (c)).

The snapshots of the slice of a 3D contour plot of the gas turbulent viscosity ratio are shown in Figure 8-7 for simulations no. 6-8. The turbulent viscosity ratio, defined as the ratio of turbulent

viscosity (μ_t) to molecular viscosity (μ_0), is an indication of the turbulence level within the simulation domain (Shi et al., 2019). The red color in plots represents the maximum turbulent viscosity ratio, whereas the blue color denotes the minimum value of zero. Comparing the maximum turbulent viscosity ratio in figures obtained for different bed heights, it can be noticed that the maximum turbulent viscosity ratio increases from 50 to 75 as the bed height increases from 4 to 12 mm. This is due to the fact that a thick layer of solid particles agitated inside the bed would establish a larger resistance for the uniform stream of air compared to a thin layer. Hence the turbulence is expected to be higher when the height of the bed layer is higher.

Comparing Figure 8-6 and Figure 8-7, the distribution of turbulence seems to be consistent with the solid volume fraction patterns. There is a relatively high turbulent viscosity ratio (μ_t/μ_0>30) close to the surface inside the big bubble space at the start-up (t=0.18 s) which is better captured at higher bed heights (cases (b) and (c)). The prevailing pattern after reaching the dynamic steady state is weak turbulent viscosity ratios within the expanded bed layer; although, relatively high turbulent viscosity ratios are occasionally seen inside large bubbles (compare section (c) at t=1.8 s in Figure 8-6 and Figure 8-7). Above the bed surface, however, there is strong turbulence indicating that only a small amount of gas is trapped inside the bed (as bubbles) and the gas primarily fills the space above the bed surface (Shi et al., 2019).

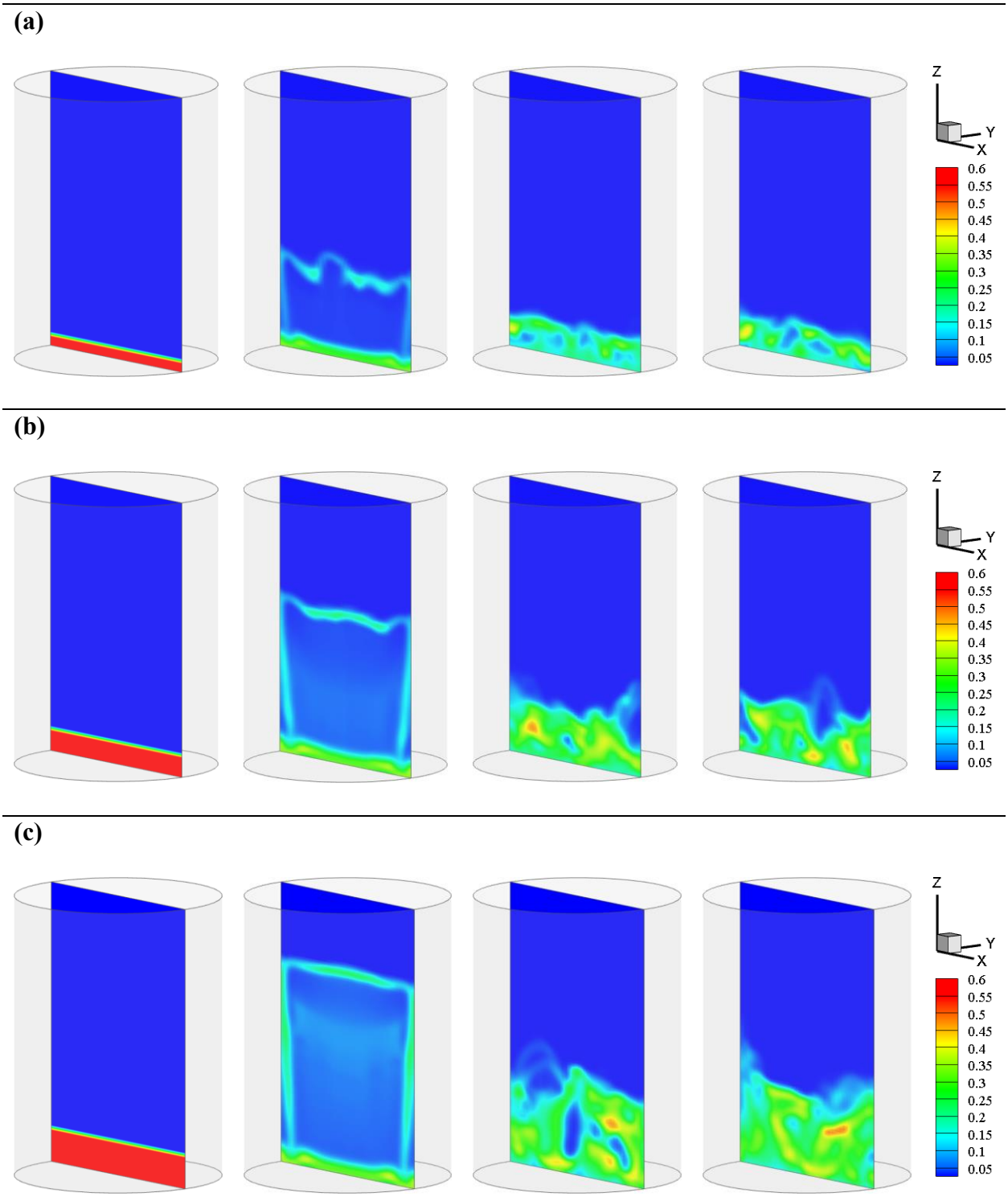

Figure 8-6. Snapshots of solid volume fraction at different time instances. (a) sim. #6: H=4 mm, F_g=300 SLPM, (b) sim. #7: H=8 mm, F_g=300 SLPM, (c) sim. #8. H=12 mm, F_g=300 SLPM.

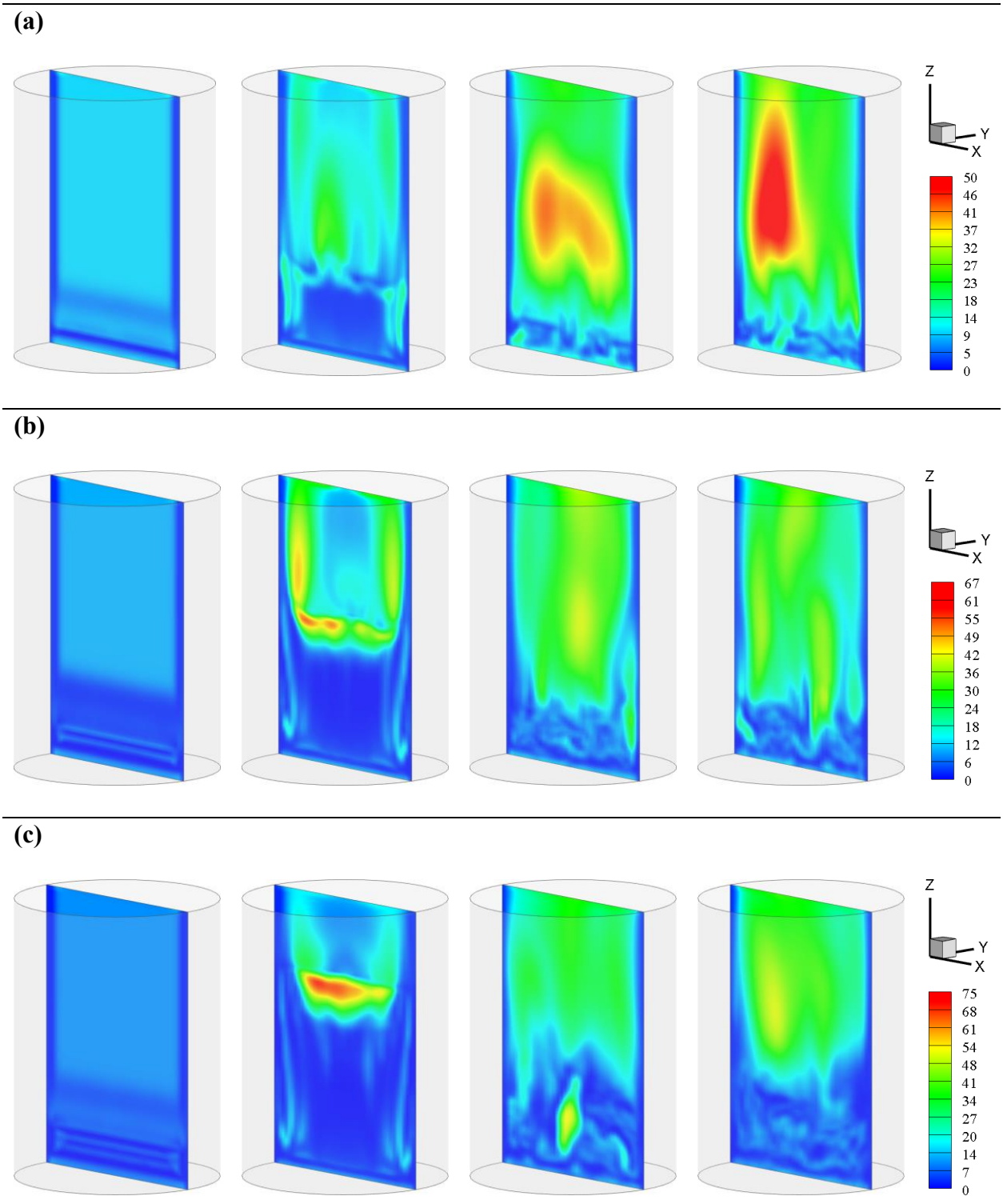

Figure 8-7. Snapshots of air turbulent viscosity ratio at different time instances. (a) sim. #6: H=4 mm, F_g=300 SLPM, (b) sim. #7: H=8 mm, F_g=300 SLPM, (c) sim. #8. H=12 mm, F_g=300 SLPM.

Figure 8-8 presents a time-averaged solid volume fraction of the middle slice of the 3D domain for simulations no. 8-10. As air flow rate decreases from 300 SLPM in simulation no. 8 to 200 SLPM in simulation no. 10, both bed height and bed voidage decrease. Mean bed voidage for experiments no. 8-10 were calculated 0.761, 0.729, and 0.686, respectively.

The solid volume fraction in the central area of the bed is somewhat similar to that close to the walls. This is quite different than tall bubbling beds which show higher solid volume fraction in the regions close to the wall (Shi et al., 2019). In practice, bubbles formed at the bottom of the bed rise to the bed surface while changing shape and size due to the intensive breakage and coalescence. The burst of large bubbles at the bed surface forces the solid particles towards the walls along which they fall to the gravitational force; and this is the reason that higher solid volume fractions are observed close to the walls in tall bubbling beds (Shi et al., 2019). In our case, however, relatively low bed height and high flow rates would make intense agitations inside the bed which prevent the observation of a distinct pattern for solids falling along the walls.

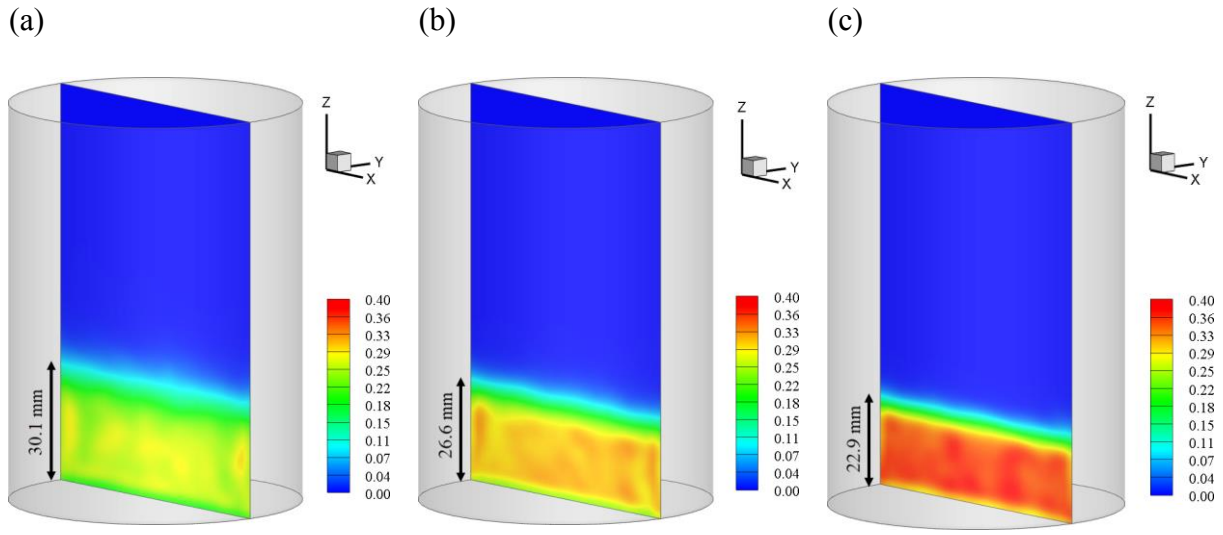

Figure 8-8. Time-averaged solid volume fraction. (a) sim. #8: H=12 mm, F_g=300 SLPM, (b) sim. #9: H=12 mm, F_g=250 SLPM, (c) sim. #10. H=12 mm, F_g=200 SLPM.

The time-averaged gas velocity vector plots of the middle slice of the 3D domain for simulations no. 8-10 are shown in Figure 8-9. The distribution of gas velocity shows a circulating pattern for the fluidizing gas which starts slightly above the bottom of the bed. This pattern is generally high in the center of the bed and gradually disappears above the bed surface. The level of circulation, which appears as vortices, is higher at higher gas flow rates. These vortices play an important role in heat and mass transfer inside the bed. Shi et al. (Shi et al., 2019) stated that the formation of vortices occurs when the falling gas inside the bed encounters the rising inlet gas. Harrison et al. (Harrison et al., 1961) reported that the shear force exerted by the solid particles on the bubbles rising through a fluidized bed can induce circulation of gas inside the bubbles as well.

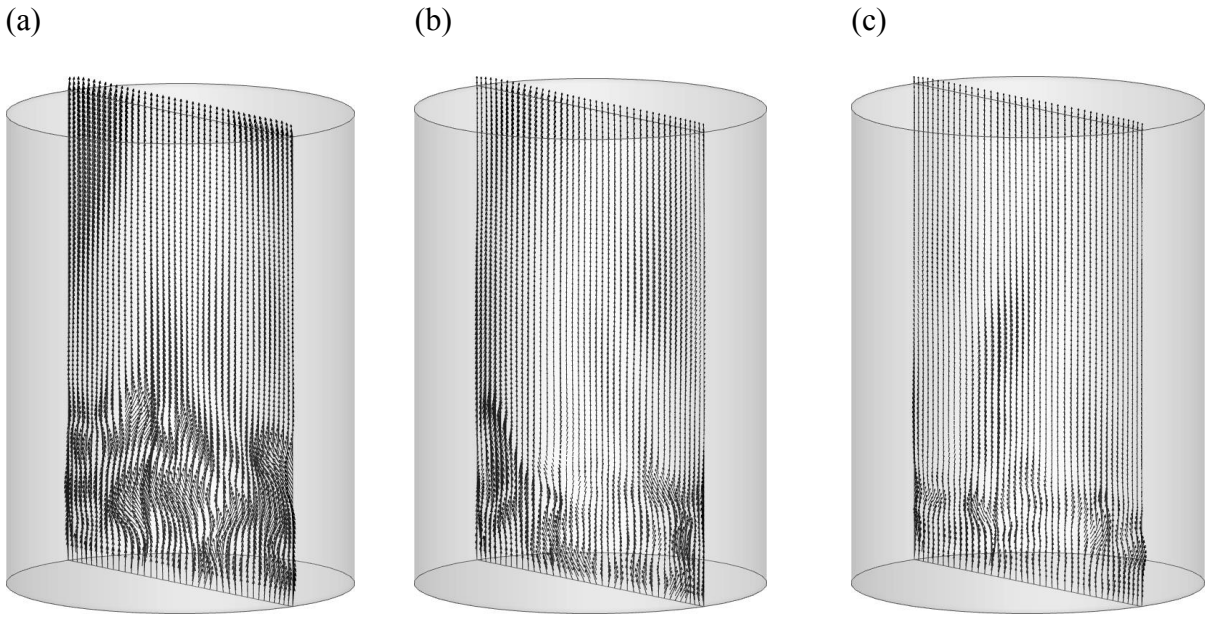

Figure 8-9. Time-averaged gas velocity vector. (a) sim. #8: H=12 mm, F_g=300 SLPM, (b) sim. #9: H=12 mm, F_g=250 SLPM, (c) sim. #10. H=12 mm, F_g=200 SLPM.

Several formulas are proposed for estimating bubble diameter in the literature (Mori and Wen, 1975, Thonglimp et al., 1984). Some formulas are based on theoretical approaches, whereas some others are purely empirical, based on experimental measurements. The experimental measurements of bubble size are conducted using different methods including local probe

detection (Sellakumar and Zakkay, 1988, Almstedt and Zakkay, 1990, Olowson and Almstedt, 1990), X-ray photography (King and Harrison, 1980, Barreto et al., 1983, Hoffmann and Yates, 1986) and photographing the erupting bed surface (Kawabata et al., 1981, Chitester et al., 1984). Unlike bubble diameter which can be calculated using various formulas, there is only one main formula, proposed by Wen (Wen, 1984, Poulopoulos and Inglezakis, 2006), for estimating bubble velocity in a fluidized bed. This formula, however, is a function of bubble diameter and minimum fluidization velocity which, in turn, can be calculated by several formulas.

The most frequently used formulas for estimating bubble diameter and bubble velocity, along with their outcomes are listed in Table 8-5. Depending on the formula, bubble diameter could be calculated as a function of gas velocity, minimum fluidization velocity, bed height, adsorbent properties, and the number of orifices per unit surface area of distributer. Some formulas calculate bubble diameter at specific bed height, whereas others calculate mean bubble diameter over the bed height. In the case of the former, the mean bubble diameter could be approximated assuming $y=H/2$ (Poulopoulos and Inglezakis, 2006). Bubble velocity is a function of gas velocity, minimum fluidization velocity, and bubble diameter. The bubble velocity is also affected by the density and viscosity of the gas, as well as the size and density of the solid indirectly since all these parameters impact the minimum fluidization velocity.

Formula no. 2 which was first proposed by Kato and Wen (Kato and Wen, 1969), combines the approximation of Kobayashi et al. (Kobayashi et al., 1965) for bubble diameter and the estimation of Davidson and Harrison (Davidson and Harrison, 1963) for initial bubble diameter. This formula was validated against experimental data reported by Cooke et al. (Cooke et al., 1968). Formula no. 3 was suggested after fitting a collection of data on bubble diameter when the bubble growth is not restricted by the walls. One adjustable parameter in this formula was found using the method of

least squares (Rowe, 1976). Formula no. 4 was suggested by Geldart (Geldart, 1970) after analyzing the experimental data obtained in two- and three-dimensional fluidized beds in several air velocities and solid properties. It should be noted that a two-dimensional bed has a rectangular cross-section with its length 10-100 times its width (in this case 1.27 vs. 68 cm).

Yasui and Johnson (Yasui and Johanson, 1958) suggested formula no. 5 based on experiments conducted in two different fluidized bed setups with diameters of 10.2 and 15.2 cm, using a wide range of different solids. Bubble diameter and bubble rising velocity were measured inside fluidized beds using a light probe technique. Formula no. 6 assumes that a bubble travels a specific distance before coalescing with neighboring bubbles. The distance traveled is proportional to the bubble lateral separation (Darton et al., 1977). Compared to experimental measurements, the formula was found to produce inaccurate estimations of bubble diameter when bubble growth is limited by the presence of fine particles in the bed (d_p<100 μm) or when there is slug flow which typically happens if (Darton et al., 1977):

$$\frac{u_0 - u_{mf}}{0.35\sqrt{gD}} > 0.2, \frac{H}{D} > 0.35\left(1 - \frac{1}{\sqrt{n_0}}\right)$$

Formula no. 7 was proposed by Cai et al. (Cai et al., 1994) after a comprehensive analysis of previously-published data. Incorporating 5 variables in the formula obtained by fitting the experimental data, the average error of the fitting for a large dataset was as little as ±11.8% which, in turn, makes it possible to use this formula for different flow regimes at different pressures and gas velocities. Formula no. 8 was introduced by Mori and Wen (Mori and Wen, 1975) with the assumption that bubbles that are generated with the diameter d_{b0} continuously grow till they reach the maximum bubble size of d_{bm} and then break up into smaller bubbles as they grow further. Although this formula was reported to be valid in the range of $0.5 \leq u_{mf} \leq 20$ cm/s, $0.006 \leq d_p \leq 0.045$

cm, u_0-u_{mf}≤48 cm/s, and D≤130 cm; the model validation against experimental measurements reveals cases with more than 50% absolute error (Mori and Wen, 1975).

Comparing the mean bubble velocities in Table 8-5, a small difference is observed between the values calculated using the formulas and those obtained from the CFD simulations. The highest absolute errors for simulation no. 6-10 are 0.09, 0.12, 0.18, 0.18, and 0.14 m/s which belong to formula no. 1, 8, 8, 1, and 8, respectively. The difference between the values of bubble velocity calculated by the formulas and by the CFD simulations is slight due to the fact that u_{mf}, which plays a more significant role in determining bubble velocity than bubble diameter, is constant in all cases and estimated by formula no. 2 in Table 8-3.

However, the difference between the values of bubble diameter calculated by the formulas and predicted by the CFD simulations is large. Figure 8-10 demonstrates the absolute difference (absolute error) between the results of formulas and CFD. Overall, formula no. 5 shows a good prediction of bubble diameter compared to values obtained from CFD simulations, in a variety of conditions. However, since empirical formulas are developed based on experimental data, their accuracy is greatly contingent on the experimental conditions. Therefore, some formulas might show a better prediction of the results at specific conditions than others. For example, although formula no. 5 has overall good prediction, formula no. 6 shows better prediction at the conditions of simulation #10 and similar prediction at the conditions of simulation #7. At the conditions of simulation #6, formula no. 5 and after that formula no. 7 yielded the best predictions of the CFD results. Similarly, those formulas produced accurate results when used to simulate the adsorption of VOCs onto activated carbon in a fluidized bed adsorber operating at the same conditions (Davarpanah et al., 2020, Davarpanah et al., 2020).

In Chapter 7, it was discussed that formula no. 2 (which has the worst prediction of CFD results in adsorption of VOC onto activated carbon) could accurately predict the results of VOC adsorption onto polymeric adsorbent of DOWEX OPTIPORE® V–503 in a fluidized bed adsorber operating at the same conditions. This suggests that, in addition to the simulation conditions, the adsorbent/adsorbate system is an important factor in determining the best formula for the prediction of bubble diameter. In an attempt to find a generic set of formulas capable of predicting a variety of adsorption systems in different fluidized bed adsorbers, formula no. 4 (whose results in Figure 8-10 lie between formula no. 5 and formula no. 2) was suggested in Chapter 7 for predicting the bubble diameter.

Table 8-5. Well-known formulas for estimating bubble diameter (d_b), and bubble velocity, (u_b), and their outcomes.

No.	Formula/method	bubble diameter (mm)/ bubble velocity (m/s)					Ref.
		Sim. #6	Sim. #7	Sim. #8	Sim. #9	Sim. #10	
1	CFD- mean bubble diameter	3.0	7.2	10.3	9.2	7.2	-
	CFD- mean bubble velocity	1.03	1.13	1.20	0.77	0.56	-
2	$d_{b0} = 0.821\left(\frac{A\left(u_0 - u_{mf}\right)}{n_0}\right)^{0.4}$, $d_b = d_{b0} + 1.4\rho_p d_p \left(\frac{u_0}{u_{mf}}\right) y$	10.1	17.2	24.3	20.5	16.6	(Kato and Wen, 1969)
	$u_b = u_0 - u_{mf} + 0.711\left(g d_b\right)^{\frac{1}{2}}$	1.12	1.19	1.25	0.95	0.64	
3	$d_{b0} = 0.347\left(\frac{A\left(u_0 - u_{mf}\right)}{n_0}\right)^{\frac{2}{5}}$, $d_b = \left(u_0 - u_{mf}\right)^{\frac{1}{2}} \left(y + d_{b0}\right)^{\frac{3}{4}} g^{-\frac{1}{4}}$	7.3	10.5	13.4	11.8	10.0	(Rowe, 1976, Hatzantonis et al., 2000)
	$u_b = u_0 - u_{mf} + 0.711\left(g d_b\right)^{\frac{1}{2}}$	1.09	1.13	1.16	0.87	0.58	

4	$d_{b0}=0.821\left(\frac{A\left(u_0-u_{mf}\right)}{n_0}\right)^{0.4}$, $d_b=d_{b0}+0.027\left(u_0-u_{mf}\right)^{0.94}y$	6.8	10.5	14.2	11.8	9.3	(Geldart, 1970, Mori and Wen, 1975)
	$u_b=u_0-u_{mf}+0.711\left(gd_b\right)^{\frac{1}{2}}$	1.08	1.13	1.16	0.87	0.57	
5	$d_b=1.6\rho_p d_p\left(\frac{u_0}{u_{mf}}-1\right)^{0.63}y$	3.8	7.6	11.3	9.8	8.2	(Yasui and Johanson, 1958, Mori and Wen, 1975)
	$u_b=u_0-u_{mf}+0.711\left(gd_b\right)^{\frac{1}{2}}$	1.04	1.10	1.14	0.85	0.55	
6	$d_b=0.54\left(u_0-u_{mf}\right)^{0.4}\times\left(y+4\sqrt{\frac{A}{n_0}}\right)^{0.8}g^{-0.2}$	5.4	6.8	8.2	7.5	6.6	(Darton et al., 1977, Grosso and Chiovetta, 2005, Poulopoulos and Inglezakis, 2006)
	$u_b=u_0-u_{mf}+0.711\left(gd_b\right)^{\frac{1}{2}}$	1.06	1.08	1.10	0.82	0.53	
7	$d_b=0.21\left(u_0-u_{mf}\right)^{0.42}H^{0.8}\times\exp\left(-0.25\left(u_0-u_{mf}\right)^2-0.1\left(u_0-u_{mf}\right)\right)$	1.8	3.1	4.4	4.3	4.1	(Cai et al., 1994)
	$u_b=u_0-u_{mf}+0.711\left(gd_b\right)^{\frac{1}{2}}$	1.00	1.02	1.05	0.77	0.50	
8	$d_{b0}=0.347\left(\frac{A\left(u_0-u_{mf}\right)}{n_0}\right)^{\frac{2}{5}}$, $d_{bm}=0.652\left(A\left(u_0-u_{mf}\right)\right)^{\frac{2}{5}}$, $d_b=d_{bm}-\left(d_{bm}-d_{b0}\right)exp\left(\frac{-0.3y}{D}\right)$	1.9	2.4	2.9	2.7	2.4	(Mori and Wen, 1975, Hatzantonis et al., 2000, Lu et al., 2004, Poulopoulos and Inglezakis, 2006)
	$u_b=u_0-u_{mf}+0.711\left(gd_b\right)^{\frac{1}{2}}$	1.00	1.01	1.02	0.74	0.46	

In calculations of u_b, u_{mf} was obtained from formula no. 2 in Table 8-3.

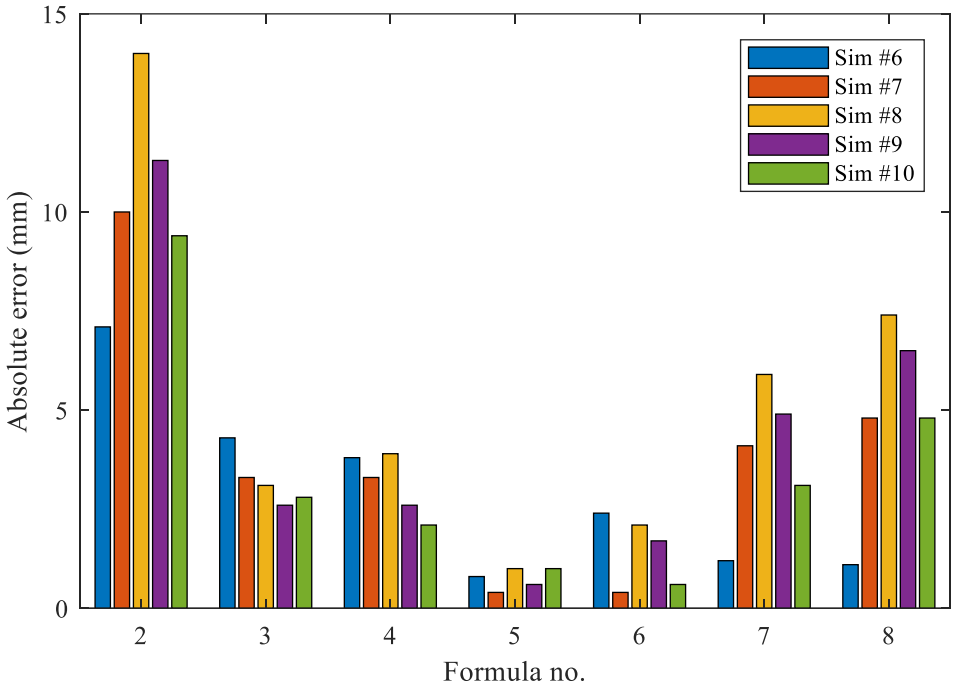

Figure 8-10. Absolute error, relative to CFD results, for different formulas estimating bubble diameter at various simulation conditions.

8.6. Conclusion

One stage of a lab-scale fluidized bed adsorber was stimulated in 3D using a commercial CFD software package (ANSYS® FLUENT™). Models and approaches suggested by Shi et al. (Shi et al., 2019) were used in CFD simulations. Hydrodynamically-important variables such as solid volume fraction and air turbulent viscosity at different time instances, time-averaged solid volume fraction, and volume-averaged solid velocity were analyzed. The results of different (semi)empirical formulas describing minimum fluidization velocity, bed voidage at minimum fluidization velocity, bubble diameter, and bubble velocity were compared to those obtained by CFD. According to the CFD results, minimum fluidization velocity inside the bed was 0.194 m/s which was best estimated when the pressure drop in a fluidized bed is set equal to that in a fixed bed. A constant value of 0.476 was found to be a good estimation of bed voidage at minimum

fluidization velocity, consistent with the value obtained from CFD simulations (0.471). High air turbulence was found mostly above the bed and inside the large bubbles within the bed. Higher mean bed heights and higher levels of air circulation were observed at higher air flow rates. Analyzing the formulas for predicting bubble diameter and bubble velocity at different bed heights and air flow rates, Yasui-Johnson's formula for estimating the bubble diameter was found to produce results in good agreement with CFD simulations.

8.7. References

Abasaeed, A.E., Al-Zahrani, S.M., 1998. Modeling of Fluidized Bed Reactors for the Polymerization Reaction of Ethylene and Propylene. *Developments in Chemical Engineering and Mineral Processing*, **6**: 121-134.

Adánez, J., Abanades, J.C., 1991. Minimum fluidization velocities of fluidized-bed coal-combustion solids. *Powder Technology*, **67**: 113-119.

Almohammed, N., Alobaid, F., Breuer, M., Epple, B., 2014. A comparative study on the influence of the gas flow rate on the hydrodynamics of a gas–solid spouted fluidized bed using Euler–Euler and Euler–Lagrange/DEM models. *Powder Technology*, **264**: 343-364.

Almstedt, A.E., Zakkay, V., 1990. An investigation of fluidized-bed scaling-capacitance probe measurements in a pressurized fluidized-bed combustor and a cold model bed. *Chemical Engineering Science*, **45**: 1071-1078.

Ansys (Release 19.2). Ansys fluent theory guide. USA, ANSYS Inc.

Azimi, E., Karimipour, S., Nikrityuk, P., Szymanski, J., Gupta, R., 2015. Numerical simulation of 3-phase fluidized bed particle segregation. *Fuel*, **150**: 347-359.

Barreto, G.F., Yates, J.G., Rowe, P.N., 1983. The effect of pressure on the flow of gas in fluidized beds of fine particles. *Chemical Engineering Science*, **38**: 1935-1945.

Broadhurst, T.E., Becker, H.A., 1975. Onset of fluidization and slugging in beds of uniform particles. *AIChE Journal*, **21**: 238-247.

Cai, P., Schiavetti, M., De Michele, G., Grazzini, G.C., Miccio, M., 1994. Quantitative estimation of bubble size in PFBC. *Powder Technology*, **80**: 99-109.

Chapman, S., Cowling, T.G., Burnett, D. (1990). The mathematical theory of non-uniform gases: an account of the kinetic theory of viscosity, thermal conduction and diffusion in gases, Cambridge university press.

Chitester, D.C., Kornosky, R.M., Fan, L.S., Danko, J.P., 1984. Characteristics of fluidization at high pressure. *Chemical Engineering Science*, **39**: 253-261.

Cooke, M., Haris, W., Highley, J., Williams, O., 1968. *Tripartite Chem. Engng Conf. Symp. on Fluidisation I*: 14-20.

Darton, R.C., Lanauze, R.D., Davidson, J.F., Harrison, D., 1977. Bubble Growth Due To Coalescence in Fluidized Beds. *Transactions of the Institution of Chemical Engineers*, **55**: 274-280.

Davarpanah, M., Hashisho, Z., Crompton, D., Anderson, J.E., Nichols, M., 2020. Modeling VOC adsorption in lab- and industrial-scale fluidized bed adsorbers: Effect of operating parameters and heel build-up. *Journal of Hazardous Materials*, **400**: 123129.

Davarpanah, M., Hashisho, Z., Phillips, J.H., Crompton, D., Anderson, J.E., Nichols, M., 2020. Modeling VOC adsorption in a multistage countercurrent fluidized bed adsorber. *Chemical Engineering Journal*, **394**: 124963.

Davidson, J.F., Harrison, D. (1963). Fluidized Particles. New York, Cambridge University Press.

de Lasa, H. (2012). Chemical Reactor Design and Technology: Overview of the New Developments of Energy and Petrochemical Reactor Technologies. Projections for the 90's, Springer Science & Business Media.

Du, W., Bao, X., Xu, J., Wei, W., 2006. Computational fluid dynamics (CFD) modeling of spouted bed: Assessment of drag coefficient correlations. *Chemical Engineering Science*, **61**: 1401-1420.

Ergun, S., 1952. Fluid flow through packed columns. *Chem. Eng. Prog.*, **48**: 89-94.

Geldart, D., 1970. The size and frequency of bubbles in two- and three-dimensional gas-fluidised beds. *Powder Technology*, **4**: 41-55.

Goldschmidt, M.J.V., Kuipers, J.A.M., van Swaaij, W.P.M., 2001. Hydrodynamic modelling of dense gas-fluidised beds using the kinetic theory of granular flow: effect of coefficient of restitution on bed dynamics. *Chemical Engineering Science*, **56**: 571-578.

Grosso, W., Chiovetta, M., 2005. Modeling a fluidized-bed reactor for the catalytic polimerization of ethylene: particle size distribution effects. *Latin American applied research*, **35**: 67-76.

Harrison, D., Davidson, J.F., de Kock, J.W., 1961. On the nature of aggregative and particulate fluidization. *Transactions of the Institution of Chemical Engineers*, **39**: 202-211.

Hatzantonis, H., Yiannoulakis, H., Yiagopoulos, A., Kiparissides, C., 2000. Recent developments in modeling gas-phase catalyzed olefin polymerization fluidized-bed reactors: The effect of bubble size variation on the reactor's performance. *Chemical Engineering Science*, **55**: 3237-3259.

Hockman, J.N. (1981). A Study of Bubble Size in a Large Particle Fluidized Bed at Elevated Temperatures. Mechanical Engineering, Oregon State University. **Master of Science**.

Hoffmann, A.C., Yates, J.G., 1986. Experimental Observations of Fluidized Beds at Elevated Pressures. *Chemical Engineering Communications*, **41**: 133-149.

Huilin, L., Yurong, H., Gidaspow, D., 2003. Hydrodynamic modelling of binary mixture in a gas bubbling fluidized bed using the kinetic theory of granular flow. *Chemical Engineering Science*, **58**: 1197-1205.

Hymore, K., Laguerie, C., 1984. Analysis and modelling of the operation of a counterflow multistage fluidized bed adsorber for drying moist air. *Chemical Engineering and Processing: Process Intensification*, **18**: 255-267.

Kato, K., Wen, C.Y., 1969. Bubble assemblage model for fluidized bed catalytic reactors. *Chemical Engineering Science*, **24**: 1351-1369.

Kawabata, J.I., Yumiyama, M., Tazaki, Y., Honma, S., Chiba, T., Sumiya, T., Endo, K., 1981. Characteristics of gas-fluidised beds under pressure. *JOURNAL OF CHEMICAL ENGINEERING OF JAPAN*, **14**: 85-89.

King, D.F., Harrison, D., 1980. The bubble phase in high-pressure fluidized beds. *Fluidization*: 101-108.

Kobayashi, H., Arai, F., Chiba, T., 1965. Behavior of Bubbles in Gas Solid Fluidized Bed. *Chemical engineering*, **29**.

Kunii, D., Levenspiel, O. (1969). Fluidization engineering. New York, Wiley.

Leonard, B.P., 1979. A stable and accurate convective modelling procedure based on quadratic upstream interpolation. *Computer Methods in Applied Mechanics and Engineering*, **19**: 59-98.

Leva, M. (1959). Fluidization. New York, McGraw-Hill.

Loha, C., Chattopadhyay, H., Chatterjee, P.K., 2012. Assessment of drag models in simulating bubbling fluidized bed hydrodynamics. *Chemical Engineering Science*, **75**: 400-407.

Loha, C., Chattopadhyay, H., Chatterjee, P.K., 2013. Euler-Euler CFD modeling of fluidized bed: Influence of specularity coefficient on hydrodynamic behavior. *Particuology*, **11**: 673-680.

Loha, C., Chattopadhyay, H., Chatterjee, P.K., 2014. Effect of coefficient of restitution in Euler–Euler CFD simulation of fluidized-bed hydrodynamics. *Particuology*, **15**: 170-177.

Lu, W.-Z., Teng, L.-H., Xiao, W.-D., 2004. Simulation and experiment study of dimethyl ether synthesis from syngas in a fluidized-bed reactor. *Chemical Engineering Science*, **59**: 5455-5464.

Mathiesen, V., Solberg, T., Hjertager, B.H., 2000. An experimental and computational study of multiphase flow behavior in a circulating fluidized bed. *International Journal of Multiphase Flow*, **26**: 387-419.

McAuley, K.B., Talbot, J.P., Harris, T.J., 1994. A comparison of two-phase and well-mixed models for fluidized-bed polyethylene reactors. *Chemical Engineering Science*, **49**: 2035-2045.

Mori, S., Wen, C.Y., 1975. Estimation of bubble diameter in gaseous fluidized beds. *AIChE Journal*, **21**: 109-115.

Muzaferija, S., Peric, M., Sames, P., Schellin, T., 1998. A Two-Fluid Navier–Stokes Solver to Simulate Water Entry In: Proceedings of the 22nd Symposium on Naval Hydrodynamics. *Washington, DC, USA*.

Nikrityuk, P.A., Ungarish, M., Eckert, K., Grundmann, R., 2005. Spin-up of a liquid metal flow driven by a rotating magnetic field in a finite cylinder: A numerical and an analytical study. *Physics of Fluids*, **17**: 067101.

Olowson, P.A., Almstedt, A.E., 1990. Influence of pressure and fluidization velocity on the bubble behaviour and gas flow distribution in a fluidized bed. *Chemical Engineering Science*, **45**: 1733-1741.

Poulopoulos, S.G., Inglezakis, V.J. (2006). Adsorption, ion exchange and catalysis: design of operations and environmental applications, Elsevier.

Rowe, P.N., 1976. Prediction of bubble size in a gas fluidised bed. *Chemical Engineering Science*, **31**: 285-288.

Samuelsberg, A., Hjertager, B.H., 1996. An experimental and numerical study of flow patterns in a circulating fluidized bed reactor. *International Journal of Multiphase Flow*, **22**: 575-591.

Sellakumar, K.M., Zakkay, V., 1988. Bubble Characterization in Pressurized Fluidized-Bed Combustors with Bed Internals. *Combustion Science and Technology*, **60**: 359-374.

Shi, H., Komrakova, A., Nikrityuk, P., 2019. Fluidized beds modeling: Validation of 2D and 3D simulations against experiments. *Powder Technology*, **343**: 479-494.

Simonin, C., Viollet, P.L., 1990. Predictions of an oxygen droplet pulverization in a compressible subsonic coflowing hydrogen flow. *Numerical Methods for Multiphase Flows*, **91**: 65-82.

Sit, S.P., Grace, J.R., 1981. Effect of bubble interaction on interphase mass transfer in gas fluidized beds. *Chemical Engineering Science*, **36**: 327-335.

Stroh, A., Alobaid, F., Hasenzahl, M.T., Hilz, J., Ströhle, J., Epple, B., 2016. Comparison of three different CFD methods for dense fluidized beds and validation by a cold flow experiment. *Particuology*, **29**: 34-47.

Syamlal, M., O'Brien, T., 1989. Computer simulation of bubbles in a fluidized bed. *AIChE Symposium Series*, **85**: 22-31.

Taghipour, F., Ellis, N., Wong, C., 2005. Experimental and computational study of gas–solid fluidized bed hydrodynamics. *Chemical Engineering Science*, **60**: 6857-6867.

Thonglimp, V., Hiquily, N., Laguerie, C., 1984. Vitesse minimale de fluidisation et expansion des couches fluidisées par un gaz. *Powder Technology*, **38**: 233-253.

Wen, C.Y. (1984). Flow regimes and flow models for fluidised bed reactors. Recent advances in the engineering analysis of chemically reacting systems. L. K. Doraiswamy. India, Wiley Eastern Limited**:** 256–287.

Wen, C.Y., Yu, Y.H., 1966. A generalized method for predicting the minimum fluidization velocity. *AIChE Journal*, **12**: 610-612.

Xue, J., Chen, F., Yang, N., Ge, W. (2017). A Study of the Soft-Sphere Model in Eulerian-Lagrangian Simulation of Gas-Liquid Flow. International Journal of Chemical Reactor Engineering. **15**.

Yasui, G., Johanson, L.N., 1958. Characteristics of gas pockets in fluidized beds. *AIChE Journal*, **4**: 445-452.

Zenz, F.A. (1982). State-of-the-art Review and Report on Critical Aspects and Scale-up Considerations in the Design of Fluidized-bed Reactors: Final Report on Phase II, U.S. Department of Energy.

Zhou, L., Zhang, L., Bai, L., Shi, W., Li, W., Wang, C., Agarwal, R., 2017. Experimental study and transient CFD/DEM simulation in a fluidized bed based on different drag models. *RSC Advances*, **7**: 12764-12774.

9. Conclusion and recommendations

9.1. Dissertation Overview

Fluidized bed adsorbers allow for efficient contact between solid and gas phases and are, therefore, good candidates for the treatment of gas streams with large flow rates at low pressure drops in various industries. The gas-solid interactions, along with the adsorption reactions in fluidized bed adsorbers, generate a large number of variables which are intricately connected and often difficult to measure. Modeling and simulation tools make it possible to handle difficult processes involved in the fluidized bed operation. This research aimed to develop modeling approaches and utilize simulation tools to understand the adsorptive and hydrodynamic behavior of fluidized beds to be able to improve their design and operation.

9.2. Summary of Findings

In Chapter 3, a two-phase model was developed and used to predict the removal efficiency for adsorption of TMB on BAC in a multistage countercurrent fluidized bed. The two-phase model was compared to the Equilibrium model, as well as the experimental data at different operating conditions. According to the results, the Equilibrium model had a good prediction of the experimental results only when the system was in an equilibrium state (achievable at low adsorbent feed rate and high initial concentration). The two-phase model generally matched the experimental data except at very high air velocities where the existence of a third phase (cloud or wake) was expected. Sensitivity analysis showed that the two-phase model was highly sensitive to the internal diffusion and interphase mass transfer coefficients, and quite insensitive to the external and surface diffusion coefficients. The adsorbent particle diameter was an important parameter in the calculations of removal efficiency and could be optimized to enhance the removal efficiency for

specific operating conditions. The impact of adsorption capacity on removal efficiency was different depending on the number of adsorption sites available and the proximity to the equilibrium state.

In Chapter 4, important characteristics of BAC (i.e. pore diameter, porosity, and adsorption capacity) were correlated to its apparent density to allow the two-phase model to predict the performance of lab- and industrial-scale fluidized beds running with adsorbents having different degrees of heel buildup (different service lives and apparent densities). Based on the results, the two-phase model could accurately capture the effect of operating conditions on the overall removal efficiency in the adsorption of a mixture of solvents on BAC in a lab-scale fluidized bed (R^2=0.91 and 0.96 depending on the assumption of mixed or plug flow for gas in emulsion phase, respectively). The model also predicted the performance of an industrial-scale fluidized bed adsorber with activated carbon of different levels of exhaustion very well (the calculated overall removal efficiencies were within absolute 10% of the measurements in almost all test cases).

In Chapter 5, the Manes method for describing the competitive adsorption of VOC-water vapor and the Van't Hoff relationship for describing the thermodynamics of the Langmuir isotherm were incorporated in the two-phase model to capture the effect of humidity and temperature on the adsorption of a VOC, TMB, onto BAC. The results showed that the effect of humidity on the adsorption of TMB on BAC started at RH=75% in the form of a reduction in overall removal efficiency. The highest reduction in overall removal efficiency was 7.6% at RHs close to 100%. The exothermic nature of the adsorption reaction yielded a small reduction (1.7%) in overall removal efficiency after increasing the temperature from 22 to 50˚C in dry condition. Increasing the temperature can also improve the removal efficiency by reducing the RH value in humid

condition. For example, increasing the temperature from 25˚C to 30˚C can reduce the RH of a humid stream from 95% to 71%, resulting in a 6.9% improvement in overall removal efficiency.

In Chapter 6, a modeling approach incorporating fast ideal adsorbed solution theory integrated with a two-phase model was introduced to predict the adsorption of TMB on zeolite in the presence of humidity in a multistage countercurrent fluidized bed. The model was then used to investigate the intensification process in fluidized bed operation. According to the results, increasing the adsorbent feed rate as a strategy to improve the removal efficiency was effective when more adsorption sites were needed (e.g. at high inlet concentrations) and quite ineffective when the adsorption process was limited by low solid-gas contact time (e.g. high air flow rates). Reducing air flow rate at constant VOC load was always effective especially when there were enough adsorption sites available (e.g. high adsorbent feed rate, and low VOC loads and RHs). Increasing the number of stages was effective only when the availability of adsorption sites was not an issue (e.g. at high adsorbent feed rates and low VOC inlet concentrations and RHs). It was shown that switching from 1 adsorber of 6 stages to 3 adsorbers of 2 stages could improve the removal efficiency up to 34.5% for the cases simulated. Also, an optimized arrangement of weir heights in descending order from the top to the bottom of the bed could maximize the removal efficiency.

In Chapter 7, the effect of different formulas on the performance of the two–phase model was studied and discussed. It was shown that proper choices of empirical and semi-empirical formulas in the calculations of the two-phase model were imperative especially when the estimations of bed voidage and interphase mass transfer coefficient were concerned. The top 20 sets of formulas that yielded the best performance of the two-phase model were presented for the adsorption of TMB on a polymeric adsorbent. Finally, a large dataset of fluidized bed adsorption experiments was

used to produce a generic set of formulas capable of predicting the behavior of fluidized beds under a wide range of design and operating conditions.

In Chapter 8, CFD simulation of one stage of a lab-scale fluidized bed was conducted in 3D using ANSYS® FLUENT™. Hydrodynamically-important variables (e.g. solid volume fraction and air turbulent viscosity, etc.) were presented and discussed. The results of different (semi)empirical formulas describing minimum fluidization velocity, bed voidage at minimum fluidization velocity, bubble diameter, and bubble velocity were compared with those obtained by CFD. According to the CFD results, minimum fluidization velocity and bed voidage at minimum fluidization velocity were measured 0.194 m/s and 0.476, respectively. High air turbulence was found mostly above the bed and inside the large bubbles within the bed. Higher mean bed heights and higher levels of air circulation were observed at higher air flow rates. Having analyzed the formulas for predicting bubble diameter and bubble velocity at different bed heights and air flow rates, it was found that Yasui-Johnson's formula for estimating the bubble diameter could produce results in good agreement with CFD simulations.

9.3. Recommendations for Future Work

The following topics are recommended for future work:

1. In this study, VOC stream either contains one component (TMB in Chapters 3, 5, 6, and 7) or a mixture of VOCs is treated as one component (SM in Chapter 2). Considering that different chemical species might exhibit different affinity towards a given adsorbent, investigating the competitive adsorption of VOC components might be of interest for some applications. For example, a fluidized bed adsorber followed by a sacrificial bed is a widely used configuration for capturing VOC emissions from automotive painting operations (Nayan, 2020). Knowing the exact components in the output of the fluidized bed (which is the input of the sacrificial bed) is essential for designing the sacrificial bed.

2. In Chapter 4, the effect of heel buildup on the adsorption process in fluidized bed systems was modeled. Finding the pattern of the changes in adsorbent characteristics during the cyclic adsorption, and establishing a relationship between the adsorbent regeneration and heel buildup would be recommended as the next steps. Said information makes it possible to model the long-term performance of the adsorption-regeneration systems and track the life cycle of adsorbents.
3. The impact of humidity and temperature on the adoption process in a fluidized bed was modeled and discussed in Chapter 5 while TMB and virgin BAC were chosen as the adsorbate and adsorbent, respectively. Since the effect of humidity and temperature depends on the adsorbate and adsorbent, further studies can be carried out incorporating different adsorbates (e.g. polar chemicals) and adsorbents (e.g. used BAC, zeolite, and polymeric adsorbent).
4. In Chapter 8, the hydrodynamic study of only one stage of the lab-scale fluidized bed was carried out using the Euler-Euler method. Future studies may consider simulating the whole bed (even in industrial scale) and including the adsorption process to be able to predict the adsorptive behavior of the bed. Moreover, the Euler-Lagrange method which provides more detailed information such as bubble positions, size distribution, and age distribution can be considered instead of the Euler-Euler method used in this study. Needless to say, computer processing is a bottleneck in the development of this type of study.

9.4. References

Nayan, N.F. (2020). Removal of Polar VOCs at Low Concentration Using a Sacrificial Carbon Bed Department of Civil and Environmental Engineering, University of Alberta. **Master of Science**.

Bibliography

Abasaeed, A.E., Al-Zahrani, S.M., 1998. Modeling of Fluidized Bed Reactors for the Polymerization Reaction of Ethylene and Propylene. *Developments in Chemical Engineering and Mineral Processing*, **6**: 121-134.

Adánez, J., Abanades, J.C., 1991. Minimum fluidization velocities of fluidized-bed coal-combustion solids. *Powder Technology*, **67**: 113-119.

Afrooz, I.E., Sinnathambi, C.M., Chuang, D.L., Karuppanan, S., 2017. CFD simulation of bubbling fluidized bed: Effects of bed column geometry on hydrodynamics of gas–solid mixing. *Materialwissenschaft und Werkstofftechnik*, **48**: 226-234.

Akanni, K.A., Evans, J.W., Abramson, I.S., 1987. Effective transport coefficients in heterogeneous media. *Chemical Engineering Science*, **42**: 1945-1954.

Almohammed, N., Alobaid, F., Breuer, M., Epple, B., 2014. A comparative study on the influence of the gas flow rate on the hydrodynamics of a gas–solid spouted fluidized bed using Euler–Euler and Euler–Lagrange/DEM models. *Powder Technology*, **264**: 343-364.

Almstedt, A.E., Zakkay, V., 1990. An investigation of fluidized-bed scaling-capacitance probe measurements in a pressurized fluidized-bed combustor and a cold model bed. *Chemical Engineering Science*, **45**: 1071-1078.

Amdebrhan, B.T. (2018). Evaluating the Performance of Activated Carbon, Polymeric, and Zeolite Adsorbents for Volatile Organic Compounds Control. Department of Civil and Environmental Engineering, University of Alberta. **Master of Science**.

Andrews, M.J., O'Rourke, P.J., 1996. The multiphase particle-in-cell (MP-PIC) method for dense particulate flows. *International Journal of Multiphase Flow*, **22**: 379-402.

Ansys (Release 19.2). Ansys fluent theory guide. USA, ANSYS Inc.

Arastoopour, H., Pakdel, P., Adewumi, M., 1990. Hydrodynamic analysis of dilute gas—solids flow in a vertical pipe. *Powder Technology*, **62**: 163-170.

Arnaldos, J., Casal, J., 1987. Study and modelling of mass transfer in magnetically stabilized fluidized beds. *International Journal of Heat and Mass Transfer*, **30**: 1525-1529.

ASTM International (2014). Standard Test Method for Apparent Density of Activated Carbon.

Azimi, E., Karimipour, S., Nikrityuk, P., Szymanski, J., Gupta, R., 2015. Numerical simulation of 3-phase fluidized bed particle segregation. *Fuel*, **150**: 347-359.

Baird, M.H.I., Davidson, J.F., 1962. Gas absorption by large rising bubbles. *Chemical Engineering Science*, **17**: 87-93.

Barreto, G.F., Yates, J.G., Rowe, P.N., 1983. The effect of pressure on the flow of gas in fluidized beds of fine particles. *Chemical Engineering Science*, **38**: 1935-1945.

Broadhurst, T.E., Becker, H.A., 1975. Onset of fluidization and slugging in beds of uniform particles. *AIChE Journal*, **21**: 238-247.

Cai, P., Schiavetti, M., De Michele, G., Grazzini, G.C., Miccio, M., 1994. Quantitative estimation of bubble size in PFBC. *Powder Technology*, **80**: 99-109.

Chapman, S., Cowling, T.G., Burnett, D. (1990). The mathematical theory of non-uniform gases: an account of the kinetic theory of viscosity, thermal conduction and diffusion in gases, Cambridge university press.

Chavarie, C., Grace, J.R., 1975. Performance Analysis of a Fluidized Bed Reactor. II. Observed Reactor Behavior Compared with Simple Two-Phase Models. *Industrial & Engineering Chemistry Fundamentals*, **14**: 79-86.

Cheng, X., Bi, X.T., 2013. Modeling and simulation of nitrogen oxides adsorption in fluidized bed reactors. *Chemical Engineering Science*, **96**: 42-54.

Chiang, B.-C., Wey, M.-Y., Yang, W.-Y., 2000. Control of Incinerator Organics by Fluidized Bed Activated Carbon Adsorber. *Journal of Environmental Engineering*, **126**: 985-992.

Chitester, D.C., Kornosky, R.M., Fan, L.S., Danko, J.P., 1984. Characteristics of fluidization at high pressure. *Chemical Engineering Science*, **39**: 253-261.

Choi, K.-B., Park, S.-I., Park, Y.-S., Sung, S.-W., Lee, D.-H., 2002. Drying characteristics of millet in a continuous multistage fluidized bed. *Korean Journal of Chemical Engineering*, **19**: 1106-1111.

Choung, J.-H., Lee, Y.-W., Choi, D.-K., Kim, S.-H., 2001. Adsorption Equilibria of Toluene on Polymeric Adsorbents. *Journal of Chemical & Engineering Data*, **46**: 954-958.

Cooke, M., Haris, W., Highley, J., Williams, O., 1968. *Tripartite Chem. Engng Conf. Symp. on Fluidisation I*: 14-20.

Darton, R.C., Lanauze, R.D., Davidson, J.F., Harrison, D., 1977. Bubble Growth Due To Coalescence in Fluidized Beds. *Transactions of the Institution of Chemical Engineers*, **55**: 274-280.

Davarpanah, M., Hashisho, Z., Crompton, D., Anderson, J.E., Nichols, M., 2020. Modeling VOC adsorption in lab- and industrial-scale fluidized bed adsorbers: Effect of operating parameters and heel build-up. *Journal of Hazardous Materials*, **400**: 123129.

Davarpanah, M., Hashisho, Z., Phillips, J.H., Crompton, D., Anderson, J.E., Nichols, M., 2020. Modeling VOC adsorption in a multistage countercurrent fluidized bed adsorber. *Chemical Engineering Journal*, **394**: 124963.

Davidson, J.F., Harrison, D. (1963). Fluidized Particles. New York, Cambridge University Press.

de Lasa, H. (2012). Chemical Reactor Design and Technology: Overview of the New Developments of Energy and Petrochemical Reactor Technologies. Projections for the 90's, Springer Science & Business Media.

Delage, F., Pré, P., Le Cloirec, P., 2000. Mass Transfer and Warming during Adsorption of High Concentrations of VOCs on an Activated Carbon Bed: Experimental and Theoretical Analysis. *Environmental Science & Technology*, **34**: 4816-4821.

Di Felice, R., 1994. The voidage function for fluid-particle interaction systems. *International Journal of Multiphase Flow*, **20**: 153-159.

Do, D.D. (1998). Adsorption Analysis: Equilibria And Kinetics. London, Imperial College Press.

Dolidovich, A.F., Akhremkova, G.S., Efremtsev, V.S., 1999. Novel technologies of VOC decontamination in fixed, moving and fluidized catalyst-adsorbent beds. **77**: 342-355.

Du, W., Bao, X., Xu, J., Wei, W., 2006. Computational fluid dynamics (CFD) modeling of spouted bed: Assessment of drag coefficient correlations. *Chemical Engineering Science*, **61**: 1401-1420.

Emmanuel, O.K. (2015). The impact of economic growth and trade on the environment: the canadian case. 33rd USAEE/IAEE North American Conference. Pittsburgh, PA, USA.

Ergun, S., 1952. Fluid flow through packed columns. *Chem. Eng. Prog.*, **48**: 89-94.

Fayaz, M., Jahandar Lashaki, M., Abdolrazzaghi, M., Zarifi, M.H., Hashisho, Z., Daneshmand, M., Anderson, J.E., Nichols, M., 2019. Monitoring the residual capacity of activated carbon in an emission abatement system using a non-contact, high resolution microwave resonator sensor. *Sensors and Actuators B: Chemical*, **282**: 218-224.

Foo, K.Y., Hameed, B.H., 2010. Insights into the modeling of adsorption isotherm systems. *Chemical Engineering Journal*, **156**: 2-10.

Gallas, J.A.C., Herrmann, H.J., Sokołowski, S., 1992. Molecular dynamics simulation of powder fluidization in two dimensions. *Physica A: Statistical Mechanics and its Applications*, **189**: 437-446.

Garnavi, L., Kasiri, N., Hashemabadi, S.H., 2006. Mathematical modeling of a continuous fluidized bed dryer. *International Communications in Heat and Mass Transfer*, **33**: 666-675.

Geldart, D., 1970. The size and frequency of bubbles in two- and three-dimensional gas-fluidised beds. *Powder Technology*, **4**: 41-55.

Geldart, D., 1973. Types of gas fluidization. *Powder Technology*, **7**: 285-292.

Ghoshal, A.K., Manjare, S.D., 2002. Selection of appropriate adsorption technique for recovery of VOCs: an analysis. *Journal of Loss Prevention in the Process Industries*, **15**: 413-421.

Gidaspow, D. (1994). Multiphase flow and fluidization: continuum and kinetic theory descriptions, Academic press.

Giraudet, S., Pré, P., Tezel, H., Le Cloirec, P., 2006. Estimation of adsorption energies using the physical characteristics of activated carbons and the molecular properties of volatile organic compounds. *Carbon*, **44**: 2413-2421.

Girimonte, R., Formisani, B., Testa, F., 2017. Adsorption of CO2 on a confined fluidized bed of pelletized 13X zeolite. *Powder Technology*, **311**: 9-17.

Goldschmidt, M.J.V., Kuipers, J.A.M., van Swaaij, W.P.M., 2001. Hydrodynamic modelling of dense gas-fluidised beds using the kinetic theory of granular flow: effect of coefficient of restitution on bed dynamics. *Chemical Engineering Science*, **56**: 571-578.

Government of Canada (2020). Canada's Air Pollutant Emissions Inventory Report 2020.

Grace, J.R., 1986. Contacting modes and behaviour classification of gas—solid and other two-phase suspensions. *The Canadian Journal of Chemical Engineering*, **64**: 353-363.

Grace, J.R. (1986). Modelling and Simulation of Two-Phase Fluidized Bed Reactors. Chemical Reactor Design and Technology: Overview of the New Developments of Energy and Petrochemical Reactor Technologies. Projections for the 90's. H. I. de Lasa. Dordrecht, Springer Netherlands**:** 245-289.

Grosso, W., Chiovetta, M., 2005. Modeling a fluidized-bed reactor for the catalytic polimerization of ethylene: particle size distribution effects. *Latin American applied research*, **35**: 67-76.

Haider, A., Levenspiel, O., 1989. Drag coefficient and terminal velocity of spherical and nonspherical particles. *Powder Technology*, **58**: 63-70.

Halasz, I., Kim, S., Marcus, B., 2002. Hydrophilic and hydrophobic adsorption on Y zeolites. *Molecular Physics*, **100**: 3123-3132.

Hall, K.R., Eagleton, L.C., Acrivos, A., Vermeulen, T., 1966. Pore- and Solid-Diffusion Kinetics in Fixed-Bed Adsorption under Constant-Pattern Conditions. *Industrial & Engineering Chemistry Fundamentals*, **5**: 212-223.

Hamed, A.M., Abd El Rahman, W.R., El-Emam, S.H., 2010. Experimental study of the transient adsorption/desorption characteristics of silica gel particles in fluidized bed. *Energy*, **35**: 2468-2483.

Harrison, D., Davidson, J.F., de Kock, J.W., 1961. On the nature of aggregative and particulate fluidization. *Transactions of the Institution of Chemical Engineers*, **39**: 202-211.

Harshe, Y.M., Utikar, R.P., Ranade, V.V., 2004. A computational model for predicting particle size distribution and performance of fluidized bed polypropylene reactor. *Chemical Engineering Science*, **59**: 5145-5156.

Hatzantonis, H., Yiannoulakis, H., Yiagopoulos, A., Kiparissides, C., 2000. Recent developments in modeling gas-phase catalyzed olefin polymerization fluidized-bed reactors: The effect of bubble size variation on the reactor's performance. *Chemical Engineering Science*, **55**: 3237-3259.

Hockman, J.N. (1981). A Study of Bubble Size in a Large Particle Fluidized Bed at Elevated Temperatures. Mechanical Engineering, Oregon State University. **Master of Science**.

Hoffmann, A.C., Yates, J.G., 1986. Experimental Observations of Fluidized Beds at Elevated Pressures. *Chemical Engineering Communications*, **41**: 133-149.

Huggahalli, M., Fair, J.R., 1996. Prediction of Equilibrium Adsorption of Water onto Activated Carbon. *Industrial & Engineering Chemistry Research*, **35**: 2071-2074.

Huilin, L., Yurong, H., Gidaspow, D., 2003. Hydrodynamic modelling of binary mixture in a gas bubbling fluidized bed using the kinetic theory of granular flow. *Chemical Engineering Science*, **58**: 1197-1205.

Hymore, K., Laguerie, C., 1984. Analysis and modelling of the operation of a counterflow multistage fluidized bed adsorber for drying moist air. *Chemical Engineering and Processing: Process Intensification*, **18**: 255-267.

Inglezakis, V.J., Poulopoulos, S.G. (2006). 6 - Reactors Scale-up. Adsorption, Ion Exchange and Catalysis. V. J. Inglezakis and S. G. Poulopoulos. Amsterdam, Elsevier**:** 523-550.

Jahandar Lashaki, M., Atkinson, J.D., Hashisho, Z., Phillips, J.H., Anderson, J.E., Nichols, M., 2016. The role of beaded activated carbon's pore size distribution on heel formation during cyclic adsorption/desorption of organic vapors. *Journal of Hazardous Materials*, **315**: 42-51.

Kampa, M., Castanas, E., 2008. Human health effects of air pollution. *Environmental Pollution*, **151**: 362-367.

Kamravaei, S., Shariaty, P., Hashisho, Z., Phillips, J.H., Anderson, J.E., Nichols, M., Crompton, D. (2016). Performance of a Multistage Fluidized Bed Adsorber Using Polymeric Adsorbent to Capture Volatile Organic Compounds. AIChE Annual Meeting. San Francisco, CA, USA.

Kamravaei, S., Shariaty, P., Jahandar Lashaki, M., Atkinson, J.D., Hashisho, Z., Phillips, J.H., Anderson, J.E., Nichols, M., 2017. Effect of Beaded Activated Carbon Fluidization on Adsorption of Volatile Organic Compounds. *Industrial & Engineering Chemistry Research*, **56**: 1297-1305.

Kamravaei, S., Shariaty, P. Jahandar Lashaki, M., Atkinson, J.D., Hashisho, Z., Phillips, J.H., Anderson, J.E., and Nichols, M (2016). Effect of Beaded Activated Carbon Fluidization on Adsorption of Volatile Organic Compounds. AIChE Annual Meeting. San Francisco, CA, USA.

Kamravaei, S., Shariaty, P. Jahandar Lashaki, M., Atkinson, J.D., Hashisho, Z., Phillips, J.H., Anderson, J.E., and Nichols, M. Crompton, D (2015). Effect of Operational Parameters on the Performance of a Multistage Fluidized Bed Adsorber. AIChE Annual Meeting. Salt lake City, UT, USA.

Kapoor, A., Ritter, J.A., Yang, R.T., 1989. On the Dubinin-Radushkevich equation for adsorption in microporous solids in the Henry's law region. *Langmuir*, **5**: 1118-1121.

Kato, K., Wen, C.Y., 1969. Bubble assemblage model for fluidized bed catalytic reactors. *Chemical Engineering Science*, **24**: 1351-1369.

Kawabata, J.I., Yumiyama, M., Tazaki, Y., Honma, S., Chiba, T., Sumiya, T., Endo, K., 1981. Characteristics of gas-fluidised beds under pressure. *JOURNAL OF CHEMICAL ENGINEERING OF JAPAN*, **14**: 85-89.

Keenan, J., Chao, J., Kaye, J., 1983. Gas Tables International Version-Thermodynamic Properties of Air, Products of Combustion and Component Gases. *Compressible Flow Functions*.

Khan, A.S.A. (2010). Installation and operation of autosorb-1-C-8 for BET surface area measurement of porous materials.

Khan, M.J.H., Hussain, M.A., Mansourpour, Z., Mostoufi, N., Ghasem, N.M., Abdullah, E.C., 2014. CFD simulation of fluidized bed reactors for polyolefin production – A review. *Journal of Industrial and Engineering Chemistry*, **20**: 3919-3946.

Kim, B.R., 2011. VOC Emissions from Automotive Painting and Their Control: A Review. *Environmental Engineering Research*, **16**: 1-9.

Kim, H.S., Matsushita, Y., Oomori, M., Harada, T., Miyawaki, J., Yoon, S.H., Mochida, I., 2013. Fluidized bed drying of Loy Yang brown coal with variation of temperature, relative humidity, fluidization velocity and formulation of its drying rate. *Fuel*, **105**: 415-424.

King, D.F., Harrison, D., 1980. The bubble phase in high-pressure fluidized beds. *Fluidization*: 101-108.

Kobayashi, H., Arai, F., Chiba, T., 1965. Behavior of Bubbles in Gas Solid Fluidized Bed. *Chemical engineering*, **29**.

Kuipers, J.A.M., van Duin, K.J., van Beckum, F.P.H., van Swaaij, W.P.M., 1993. Computer simulation of the hydrodynamics of a two-dimensional gas-fluidized bed. *Computers & Chemical Engineering*, **17**: 839-858.

Kunii, D., Levenspiel, O. (1969). Fluidization engineering. New York, Wiley.

Laskar, I.I., Hashisho, Z., Phillips, J.H., Anderson, J.E., Nichols, M., 2019. Competitive adsorption equilibrium modeling of volatile organic compound (VOC) and water vapor onto activated carbon. *Separation and Purification Technology*, **212**: 632-640.

Laskar, I.I., Hashisho, Z., Phillips, J.H., Anderson, J.E., Nichols, M., 2019. Modeling the Effect of Relative Humidity on Adsorption Dynamics of Volatile Organic Compound onto Activated Carbon. *Environmental Science & Technology*, **53**: 2647-2659.

Leonard, B.P., 1979. A stable and accurate convective modelling procedure based on quadratic upstream interpolation. *Computer Methods in Applied Mechanics and Engineering*, **19**: 59-98.

Leslie, G.B., 2000. Health Risks from Indoor Air Pollutants: Public Alarm and Toxicological Reality. *Indoor and Built Environment*, **9**: 5-16.

Leva, M. (1959). Fluidization. New York, McGraw-Hill.

Levenspiel, O. (1972). Chemical reaction engineering. New York, Wiley.

Liu, P., Long, C., Li, Q., Qian, H., Li, A., Zhang, Q., 2009. Adsorption of trichloroethylene and benzene vapors onto hypercrosslinked polymeric resin. *Journal of Hazardous Materials*, **166**: 46-51.

Lodewyckx, P., Vansant, E.F., 1999. Influence of Humidity on Adsorption Capacity from the Wheeler-Jonas Model for Prediction of Breakthrough Times of Water Immiscible Organic Vapors on Activated Carbon Beds. *American Industrial Hygiene Association Journal*, **60**: 612-617.

Loha, C., Chattopadhyay, H., Chatterjee, P.K., 2012. Assessment of drag models in simulating bubbling fluidized bed hydrodynamics. *Chemical Engineering Science*, **75**: 400-407.

Loha, C., Chattopadhyay, H., Chatterjee, P.K., 2013. Euler-Euler CFD modeling of fluidized bed: Influence of specularity coefficient on hydrodynamic behavior. *Particuology*, **11**: 673-680.

Loha, C., Chattopadhyay, H., Chatterjee, P.K., 2014. Effect of coefficient of restitution in Euler–Euler CFD simulation of fluidized-bed hydrodynamics. *Particuology*, **15**: 170-177.

Long, C., Li, A., Wu, H., Zhang, Q., 2009. Adsorption of naphthalene onto macroporous and hypercrosslinked polymeric adsorbent: Effect of pore structure of adsorbents on thermodynamic and kinetic properties. *Colloids and Surfaces A: Physicochemical and Engineering Aspects*, **333**: 150-155.

Lu, W.-Z., Teng, L.-H., Xiao, W.-D., 2004. Simulation and experiment study of dimethyl ether synthesis from syngas in a fluidized-bed reactor. *Chemical Engineering Science*, **59**: 5455-5464.

Lugg, G.A., 1968. Diffusion coefficients of some organic and other vapors in air. *Analytical Chemistry*, **40**: 1072-1077.

Manes, M. (1984). Estimation of the effects of humidity on the adsorption onto activated carbon of the vapors of water-immiscible organic liquids. Engineering Foundation Conference. Bavaria, West Ger, Fundamentals of Adsorption**:** 335-344.

Mathiesen, V., Solberg, T., Hjertager, B.H., 2000. An experimental and computational study of multiphase flow behavior in a circulating fluidized bed. *International Journal of Multiphase Flow*, **26**: 387-419.

McAuley, K.B., Talbot, J.P., Harris, T.J., 1994. A comparison of two-phase and well-mixed models for fluidized-bed polyethylene reactors. *Chemical Engineering Science*, **49**: 2035-2045.

Mineto, A., Souza, M., Silva, R., Cabézas-Gomes, L., Montagnoli, A., Navarro, H. (2008). Particle diameter influence on simulation ofgas–solid flow in bubbling fluidized bed. 7th Brazilian conference on dynamics, control and applications.

Missen, R.W., Mims, C.A., Saville, B.A. (1999). Introduction to chemical reaction engineering and kinetics, Wiley New York.

Mohanty, C.R., Adapala, S., Meikap, B.C., 2009. Removal of hazardous gaseous pollutants from industrial flue gases by a novel multi-stage fluidized bed desulfurizer. *Journal of Hazardous Materials*, **165**: 427-434.

Mohanty, C.R., Malavia, G., Meikap, B.C., 2009. Development of a Countercurrent Multistage Fluidized-Bed Reactor and Mathematical Modeling for Prediction of Removal Efficiency of Sulfur Dioxide from Flue Gases. *Industrial & Engineering Chemistry Research*, **48**: 1629-1637.

Mohanty, C.R., Meikap, B.C., 2009. Pressure drop characteristics of a multi-stage counter-current fluidized bed reactor for control of gaseous pollutants. *Chemical Engineering and Processing: Process Intensification*, **48**: 209-216.

Mohanty, C.R., Meikap, B.C., 2011. Modeling the operation of a three-stage fluidized bed reactor for removing CO2 from flue gases. *Journal of Hazardous Materials*, **187**: 113-121.

Mojtaba Hashemi, S., Jahandar Lashaki, M., Hashisho, Z., Phillips, J.H., Anderson, J.E., Nichols, M., 2019. Oxygen impurity in nitrogen desorption purge gas can increase heel buildup on activated carbon. *Separation and Purification Technology*, **210**: 497-503.

Mori, S., Wen, C.Y., 1975. Estimation of bubble diameter in gaseous fluidized beds. *AIChE Journal*, **21**: 109-115.

Muzaferija, S., Peric, M., Sames, P., Schellin, T., 1998. A Two-Fluid Navier–Stokes Solver to Simulate Water Entry In: Proceedings of the 22nd Symposium on Naval Hydrodynamics. *Washington, DC, USA*.

Myers, A.L., Prausnitz, J.M., 1965. Thermodynamics of mixed-gas adsorption. *AIChE Journal*, **11**: 121-127.

Na, K., Kim, Y.P., Moon, I., Moon, K.-C., 2004. Chemical composition of major VOC emission sources in the Seoul atmosphere. *Chemosphere*, **55**: 585-594.

Nayan, N.F. (2020). Removal of Polar VOCs at Low Concentration Using a Sacrificial Carbon Bed Department of Civil and Environmental Engineering, University of Alberta. **Master of Science**.

Nikrityuk, P.A., Ungarish, M., Eckert, K., Grundmann, R., 2005. Spin-up of a liquid metal flow driven by a rotating magnetic field in a finite cylinder: A numerical and an analytical study. *Physics of Fluids*, **17**: 067101.

O'Brien, J.A., Myers, A.L., 1985. Rapid calculations of multicomponent adsorption equilibria from pure isotherm data. *Industrial & Engineering Chemistry Process Design and Development*, **24**: 1188-1191.

O'Brien, J.A., Myers, A.L., 1988. A comprehensive technique for equilibrium calculations in adsorbed mixtures: the generalized FastIAS method. *Industrial & Engineering Chemistry Research*, **27**: 2085-2092.

Olowson, P.A., Almstedt, A.E., 1990. Influence of pressure and fluidization velocity on the bubble behaviour and gas flow distribution in a fluidized bed. *Chemical Engineering Science*, **45**: 1733-1741.

Papadikis, K., Bridgwater, A.V., Gu, S., 2008. CFD modelling of the fast pyrolysis of biomass in fluidised bed reactors, Part A: Eulerian computation of momentum transport in bubbling fluidised beds. *Chemical Engineering Science*, **63**: 4218-4227.

Papasavva, S., Kia, S., Claya, J., Gunther, R., 2001. Characterization of automotive paints: an environmental impact analysis. *Progress in Organic Coatings*, **43**: 193-206.

Parmar, G.R., Rao, N.N., 2008. Emerging Control Technologies for Volatile Organic Compounds. *Critical Reviews in Environmental Science and Technology*, **39**: 41-78.

Partridge, B., Rowe, P. (1965). Chemical reaction in a bubbling gas-fluidised bed, UK Atomic Energy Authority Research Group.

Peters, M.H., Fan, L.-S., Sweeney, T.L., 1982. Reactant dynamics in catalytic fluidized bed reactors with flow reversal of gas in the emulsion phaset. *Chemical Engineering Science*, **37**: 553-565.

Philippsen, C.G., Vilela, A.C.F., Zen, L.D., 2015. Fluidized bed modeling applied to the analysis of processes: review and state of the art. *Journal of Materials Research and Technology*, **4**: 208-216.

Poulopoulos, S.G., Inglezakis, V.J. (2006). Adsorption, ion exchange and catalysis: design of operations and environmental applications, Elsevier.

Qi, S., Hay, K.J., Rood, M.J., 1998. Isotherm equation for water vapor adsorption onto activated carbon. *Journal of Environmental Engineering*, **124**: 1130-1134.

Qi, S., Hay, K.J., Rood, M.J., Cal, M.P., 2000. Equilibrium and heat of adsorption for water vapor and activated carbon. *Journal of Environmental Engineering*, **126**: 267-271.

Ramos, M.E., Bonelli, P.R., Cukierman, A.L., Ribeiro Carrott, M.M.L., Carrott, P.J.M., 2010. Adsorption of volatile organic compounds onto activated carbon cloths derived from a novel regenerated cellulosic precursor. *Journal of Hazardous Materials*, **177**: 175-182.

Reichhold, A., Hofbauer, H., 1995. Internally circulating fluidized bed for continuous adsorption and desorption. *Chemical Engineering and Processing: Process Intensification*, **34**: 521-527.

Rhodes, M.J., Wang, X.S., Nguyen, M., Stewart, P., Liffman, K., 2001. Use of discrete element method simulation in studying fluidization characteristics: influence of interparticle force. *Chemical Engineering Science*, **56**: 69-76.

Richardson, J.F., Zaki, W.N., 1954. Sedimentation and fluidisation: Part I. *Transactions of the Institution of Chemical Engineers*, **32**: 35-53.

Rowe, P.N., 1976. Prediction of bubble size in a gas fluidised bed. *Chemical Engineering Science*, **31**: 285-288.

Roy, S., Mohanty, C.R., Meikap, B.C., 2009. Multistage Fluidized Bed Reactor Performance Characterization for Adsorption of Carbon Dioxide. *Industrial & Engineering Chemistry Research*, **48**: 10718-10727.

Ruthven, D.M. (1984). Principles of adsorption and adsorption processes, John Wiley & Sons.

Samuelsberg, A., Hjertager, B.H., 1996. An experimental and numerical study of flow patterns in a circulating fluidized bed reactor. *International Journal of Multiphase Flow*, **22**: 575-591.

Sanders, R.E., 2003. Designs that lacked inherent safety: case histories. *Journal of Hazardous Materials*, **104**: 149-161.

Saxena, S.C., Vadivel, R., 1988. Wall effects in gas-fluidized beds at incipient fluidization. *The Chemical Engineering Journal*, **39**: 133-137.

Scala, F., Cammarota, A., Chirone, R., Salatino, P., 2004. Comminution of limestone during batch fluidized-bed calcination and sulfation. *AIChE Journal*, **43**: 363-373.

Scala, F., Salatino, P., Boerefijn, R., Ghadiri, M., 2000. Attrition of sorbents during fluidized bed calcination and sulphation. *Powder Technology*, **107**: 153-167.

Schulzke, T., Westermeyer, J., Giani, H., Hornsby, C., 2018. Combustion of Refined Renewable Biomass Fuel (RRBF) in a bubbling fluidized bed. *Renewable Energy*, **124**: 84-94.

Seader, J.D., Henley, E.J. (2006). Separation process principles, John Wiley & Sons, Inc.

Sellakumar, K.M., Zakkay, V., 1988. Bubble Characterization in Pressurized Fluidized-Bed Combustors with Bed Internals. *Combustion Science and Technology*, **60**: 359-374.

Shi, H., Komrakova, A., Nikrityuk, P., 2019. Fluidized beds modeling: Validation of 2D and 3D simulations against experiments. *Powder Technology*, **343**: 479-494.

Shiau, C.-Y., Lin, C.-J., 1993. An improved bubble assemblage model for fluidized-bed catalytic reactors. *Chemical Engineering Science*, **48**: 1299-1308.

Silberberg, M.S., Venkateswaran, R., Amateis, P., Lavieri, S. (2016). Chemistry, McGraw-Hill Education.

Simonin, C., Viollet, P.L., 1990. Predictions of an oxygen droplet pulverization in a compressible subsonic coflowing hydrogen flow. *Numerical Methods for Multiphase Flows*, **91**: 65-82.

Sit, S.P., Grace, J.R., 1981. Effect of bubble interaction on interphase mass transfer in gas fluidized beds. *Chemical Engineering Science*, **36**: 327-335.

Snider, D.M., 2001. An Incompressible Three-Dimensional Multiphase Particle-in-Cell Model for Dense Particle Flows. *Journal of Computational Physics*, **170**: 523-549.

Snider, D.M., 2007. Three fundamental granular flow experiments and CPFD predictions. *Powder Technology*, **176**: 36-46.

Snider, D.M., O'Rourke, P.J., Andrews, M.J., 1998. Sediment flow in inclined vessels calculated using a multiphase particle-in-cell model for dense particle flows. *International Journal of Multiphase Flow*, **24**: 1359-1382.

Sommerfeld, M., 2001. Validation of a stochastic Lagrangian modelling approach for inter-particle collisions in homogeneous isotropic turbulence. *International Journal of Multiphase Flow*, **27**: 1829-1858.

Song, W., Tondeur, D., Luo, L., Li, J., 2005. VOC Adsorption in Circulating Gas Fluidized Bed. *Adsorption*, **11**: 853-858.

Souza, M. (2009). Numerical effects onthe simulation of gas–solid flow in bubbling fluidized bedusing the kinetic theory of granular flow, São Paulo State University.

Stroh, A., Alobaid, F., Hasenzahl, M.T., Hilz, J., Ströhle, J., Epple, B., 2016. Comparison of three different CFD methods for dense fluidized beds and validation by a cold flow experiment. *Particuology*, **29**: 34-47.

Sullivan, P.D., Rood, M.J., Dombrowski, K.D., Hay, K.J., 2004. Capture of Organic Vapors Using Adsorption and Electrothermal Regeneration. *Journal of Environmental Engineering*, **130**: 258-267.

Syamlal, M., O'Brien, T., 1989. Computer simulation of bubbles in a fluidized bed. *AIChE Symposium Series*, **85**: 22-31.

Syamlal, M., O'Brien, T.J., 1988. Simulation of granular layer inversion in liquid fluidized beds. *International Journal of Multiphase Flow*, **14**: 473-481.

Taghipour, F., Ellis, N., Wong, C., 2005. Experimental and computational study of gas–solid fluidized bed hydrodynamics. *Chemical Engineering Science*, **60**: 6857-6867.

Tang, M., Cox, R., Kalberer, M., 2014. Compilation and evaluation of gas phase diffusion coefficients of reactive trace gases in the atmosphere: volume 1. Inorganic compounds. *Atmospheric Chemistry and Physics*, **14**: 9233-9247.

Tefera, D.T., Hashisho, Z., Philips, J.H., Anderson, J.E., Nichols, M., 2014. Modeling Competitive Adsorption of Mixtures of Volatile Organic Compounds in a Fixed-Bed of Beaded Activated Carbon. *Environmental Science & Technology*, **48**: 5108-5117.

Thonglimp, V., Hiquily, N., Laguerie, C., 1984. Vitesse minimale de fluidisation et expansion des couches fluidisées par un gaz. *Powder Technology*, **38**: 233-253.

Toomey, R.D., Johnstone, H.F., 1952. Gaseous Fluidization of Solid Particles. *Chemical Engineering Progress*, **48**: 220-226.

Tsyurupa, M.P., Davankov, V.A., 2006. Porous structure of hypercrosslinked polystyrene: State-of-the-art mini-review. *Reactive and Functional Polymers*, **66**: 768-779.

van Deemter, J.J., 1961. Mixing and contacting in gas-solid fluidized beds. *Chemical Engineering Science*, **13**: 143-154.

van Lare, C.E.J. (1991). Mass transfer in gas fluidized beds: scaling, modeling and particle size influence, Technische Universiteit Eindhoven.

Wanderley, P. (2010). Modeling andsimulation of an oxychlorination reactor in fluidized bed forthe production of 1,2-dichloroethane., Universidade Federal de Alagoas.

Weast, R.C. (1981). CRC Handbook of chemistry and physics : a ready-reference book of chemical and physical data. Boca Raton, Fla, CRC Press.

Wen, C.Y. (1984). Flow regimes and flow models for fluidised bed reactors. Recent advances in the engineering analysis of chemically reacting systems. L. K. Doraiswamy. India, Wiley Eastern Limited**:** 256–287.

Wen, C.Y., Yu, Y.H., 1966. A generalized method for predicting the minimum fluidization velocity. *AIChE Journal*, **12**: 610-612.

Werther, J., Hartge, E.-U., 2004. Modeling of Industrial Fluidized-Bed Reactors. *Industrial & Engineering Chemistry Research*, **43**: 5593-5604.

Xue, J., Chen, F., Yang, N., Ge, W. (2017). A Study of the Soft-Sphere Model in Eulerian-Lagrangian Simulation of Gas-Liquid Flow. International Journal of Chemical Reactor Engineering. **15**.

Yamamoto, T., Kataoka, S., Ohmori, T., 2010. Characterization of carbon cryogel microspheres as adsorbents for VOC. *Journal of Hazardous Materials*, **177**: 331-335.

Yang, R.T. (1987). Gas Separation by Adsorption Processes, Butterworth-Heinemann.

Yang, W.-c. (2003). Handbook of fluidization and fluid-particle systems, CRC press.

Yasui, G., Johanson, L.N., 1958. Characteristics of gas pockets in fluidized beds. *AIChE Journal*, **4**: 445-452.

Yazbek, W., Pré, P., Delebarre, A., 2006. Adsorption and Desorption of Volatile Organic Compounds in Fluidized Bed. *Journal of Environmental Engineering*, **132**: 442-452.

Zenz, F.A. (1982). State-of-the-art Review and Report on Critical Aspects and Scale-up Considerations in the Design of Fluidized-bed Reactors: Final Report on Phase II, U.S. Department of Energy.

Zhang, X., Gao, B., Creamer, A.E., Cao, C., Li, Y., 2017. Adsorption of VOCs onto engineered carbon materials: A review. *Journal of Hazardous Materials*, **338**: 102-123.

Zhao, P., Snider, D., Williams, K. (2006). Computational particle-fluid dynamics simulations of a commercial-scale turbulent fluidized bed reactor. AIChE Annual Meeting.

Zheng, J., Song, W., Du, L., Wang, L., Li, S., 2020. Desorption of VOCs from polymer adsorbent in Multistage Fluidized bed. *Chinese Journal of Chemical Engineering*.

Zhou, L., Zhang, L., Bai, L., Shi, W., Li, W., Wang, C., Agarwal, R., 2017. Experimental study and transient CFD/DEM simulation in a fluidized bed based on different drag models. *RSC Advances*, **7**: 12764-12774.

Appendix A: Supplementary Information for Chapter 3

Table S1. Equilibrium adsorption data for adsorption of TMB on BAC (Amdebrhan, 2018).

C^* (ppm_v)	q^*(kg TMB/kg BAC)
0	0.000
10	0.357
20	0.408
50	0.423
100	0.428
200	0.430
500	0.433
1000	0.434

Table S2. EGPM and EGPF models outputs for adsorption of TMB on BAC in a six-stage countercurrent fluidized bed adsorber.

	EGPM							EGPF						
no.	C_1 (ppm_v)	C_2 (ppm_v)	C_3 (ppm_v)	C_4 (ppm_v)	C_5 (ppm_v)	C_6 (ppm_v)	RE (%)	C_1 (ppm_v)	C_2 (ppm_v)	C_3 (ppm_v)	C_4 (ppm_v)	C_5 (ppm_v)	C_6 (ppm_v)	RE (%)
1	73.3	48.6	30.5	18.6	11.3	6.7	93.3	74.9	49.3	30.4	18.1	10.6	6.1	93.8
2	61.7	37.5	22.5	13.4	8.0	4.7	95.2	59.0	34.2	19.7	11.3	6.5	3.7	96.2
3	59.8	35.5	21.1	12.5	7.4	4.4	95.6	58.1	33.4	19.2	11.0	6.3	3.6	96.3
4	59.5	35.2	20.8	12.3	7.3	4.3	95.7	57.7	33.1	18.9	10.8	6.2	3.5	96.4
5	50.1	21.5	8.7	3.4	1.3	0.5	99.5	48.8	19.1	6.98	2.3	0.8	0.2	99.7
6	66.4	38.8	21.0	10.8	5.4	2.7	97.3	68.4	39.1	20.3	10.0	4.7	2.2	97.7
7	73.3	48.6	30.5	18.6	11.2	6.6	93.3	75.0	49.3	30.4	18.1	10.6	6.1	93.8
8	82.2	62.2	44.8	30.9	20.9	14.0	86.0	84.5	64.4	46.2	31.5	20.9	13.8	86.1
9	32.0	19.9	12.3	7.5	4.49	2.7	94.7	30.9	18.5	10.9	6.3	3.6	2.1	95.7
10	73.3	48.6	30.5	18.6	11.2	6.7	93.3	74.9	49.3	30.4	18.1	10.6	6.1	93.8
11	145.4	132.2	104.8	72.2	45.6	27.6	81.6	149.0	144.6	128.5	93.9	58.9	34.4	77.0
12	199.8	198.7	193.2	170.6	121.7	74.9	62.5	199.9	199.5	196.7	179.4	128.3	76.9	61.5
13	300.0	299.9	299.2	292.1	244.1	154.4	48.5	300.0	299.9	299.6	295.7	254.1	157.2	47.5
14	115.2	66.8	30.7	12.8	5.3	2.0	98.6	142.8	116.1	64.9	26.4	9.3	3.0	97.9
15	88.1	53.9	29.3	15.4	8.0	4.0	96.7	101.4	68.8	39.2	20.3	9.9	4.6	96.1
16	73.3	48.6	30.5	18.6	11.2	6.6	93.3	74.9	49.3	30.4	18.1	10.6	6.1	93.8
17	65.8	48.1	33.5	22.9	15.6	10.5	87.8	66.8	48.8	33.7	22.7	15.2	10.1	88.1
18	59.1	44.8	33.4	24.5	17.7	12.9	82.7	59.4	44.9	33.3	24.2	17.5	12.6	83.1
19	54.6	43.3	33.9	26.2	20.1	15.4	76.9	54.8	43.4	33.8	26.0	19.8	15.1	77.3
20	80.9	63.7	49.6	38.1	29.2	22.2	77.8	78.9	60.8	46.4	35.2	26.5	19.9	80.0
21	73.3	48.6	30.5	18.6	11.2	6.7	93.3	74.9	49.3	30.4	18.1	10.6	6.1	93.8
22	74.9	47.4	26.9	14.4	7.5	3.7	96.2	93.5	77.1	50.8	28.6	14.8	7.5	92.4

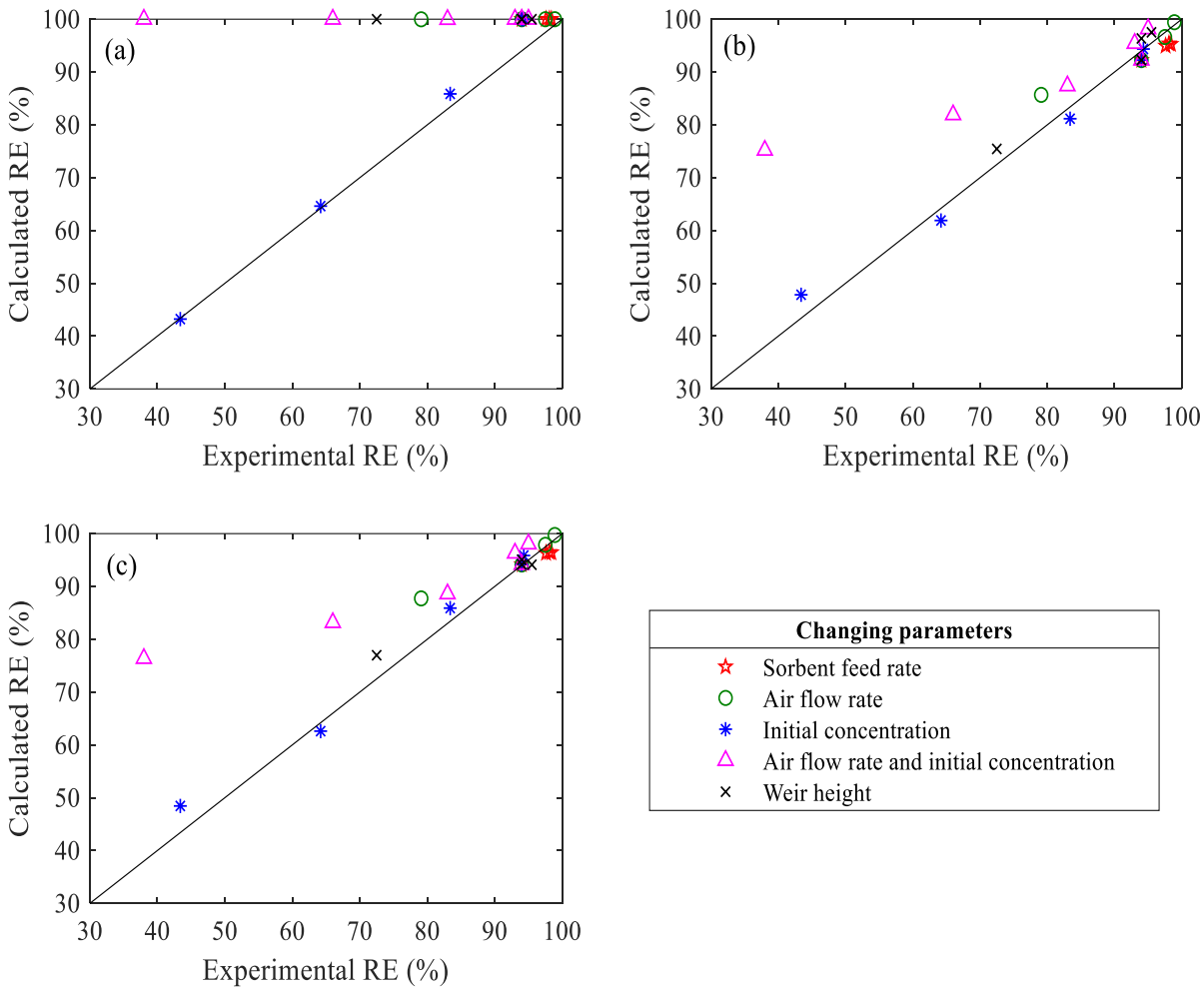

Figure S1. Experimental values of removal efficiency versus those predicted by (a) Equilibrium model, (b) two-phase model-EGPM, and (c) two-phase model-EGPF.

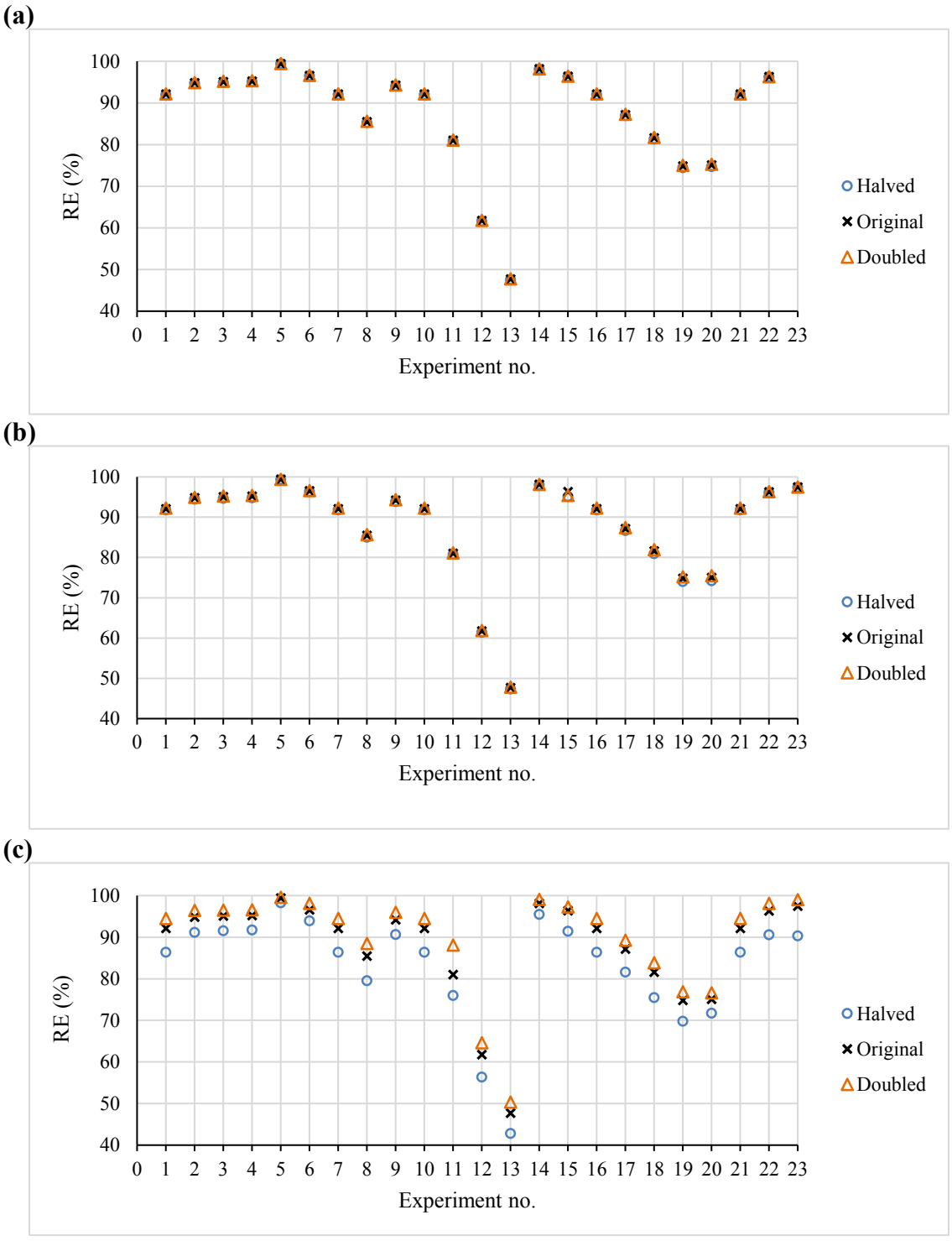

Figure S2. The sensitivity of EGPM model to (a) external diffusion coefficient, (b) surface diffusion coefficient, and (c) interphase mass transfer flow rate.

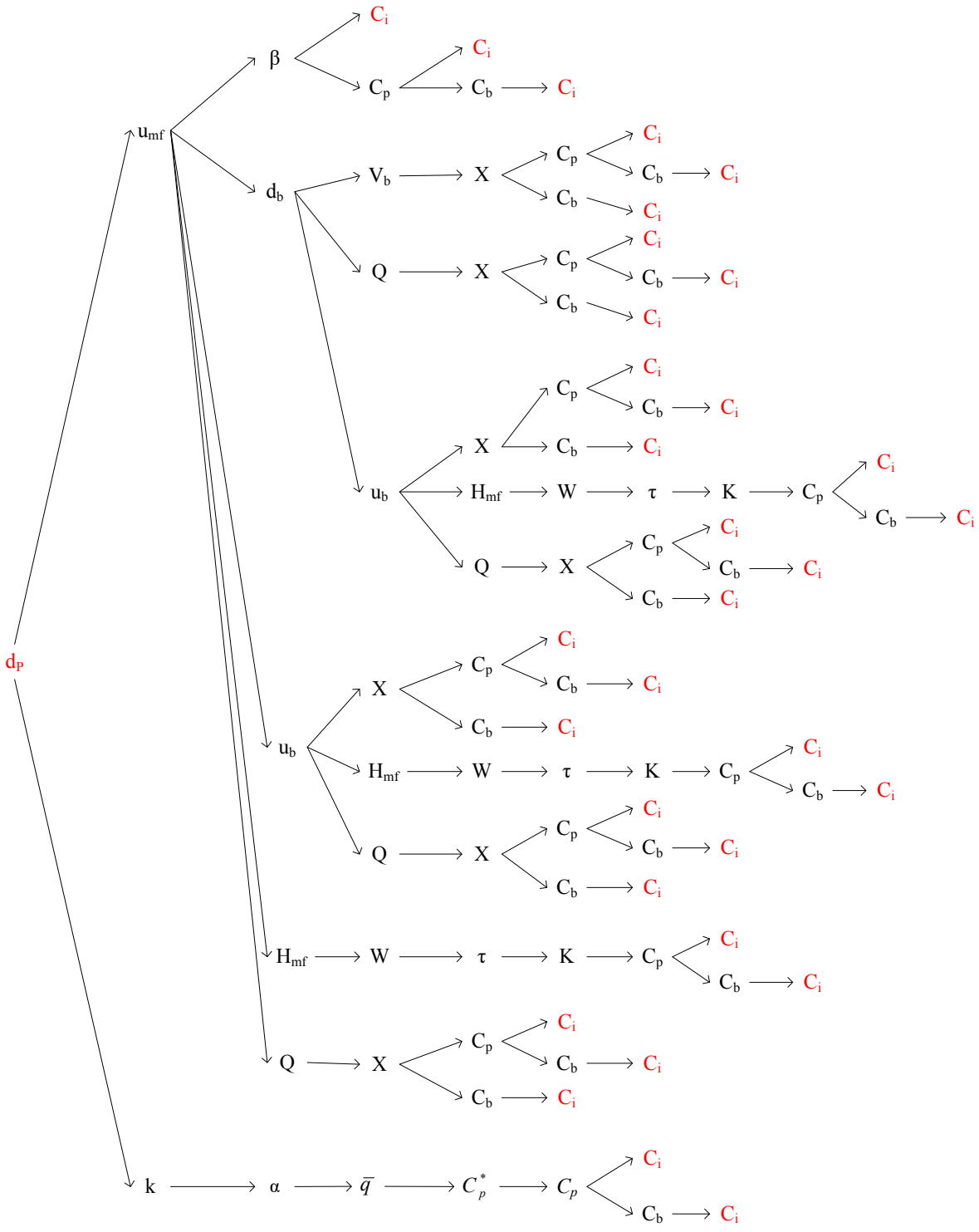

Figure S3. A demonstration of the effect of particle diameter variation on the concentration at the outlet of a multistage fluidized bed adsorber.

Reference for Apendix A

Amdebrhan, B.T. (2018). Evaluating the Performance of Activated Carbon, Polymeric, and Zeolite Adsorbents for Volatile Organic Compounds Control. Department of Civil and Environmental Engineering, University of Alberta. **Master of Science**.

Appendix B: Supplementary Information for Chapter 4

(a)

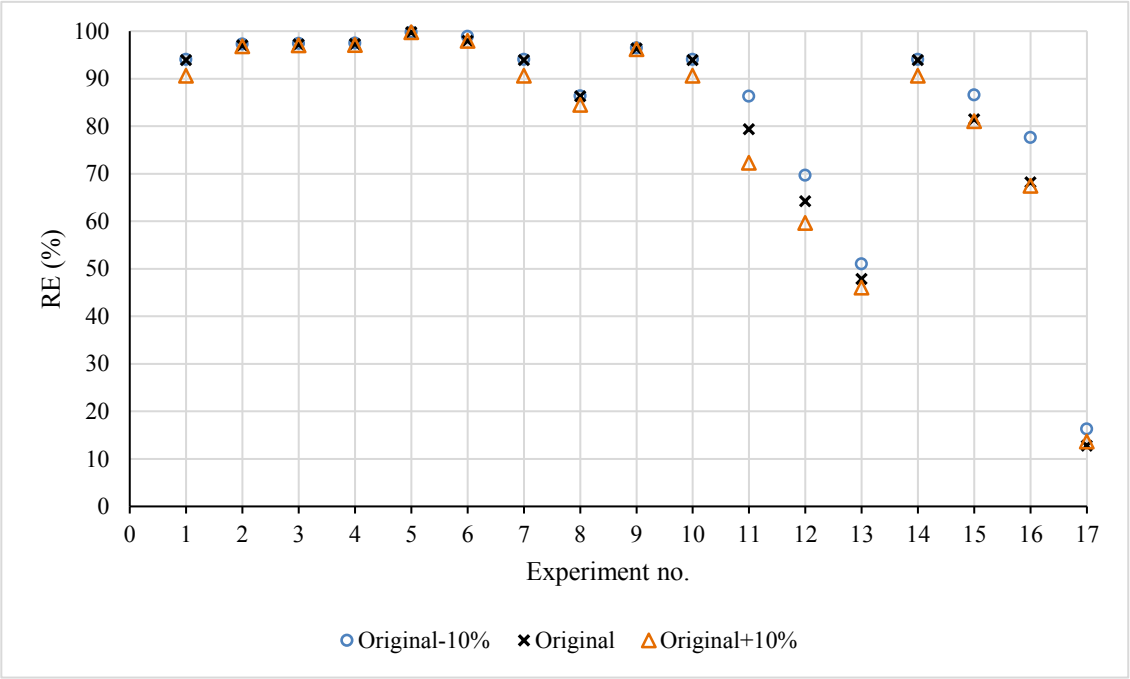

(b)

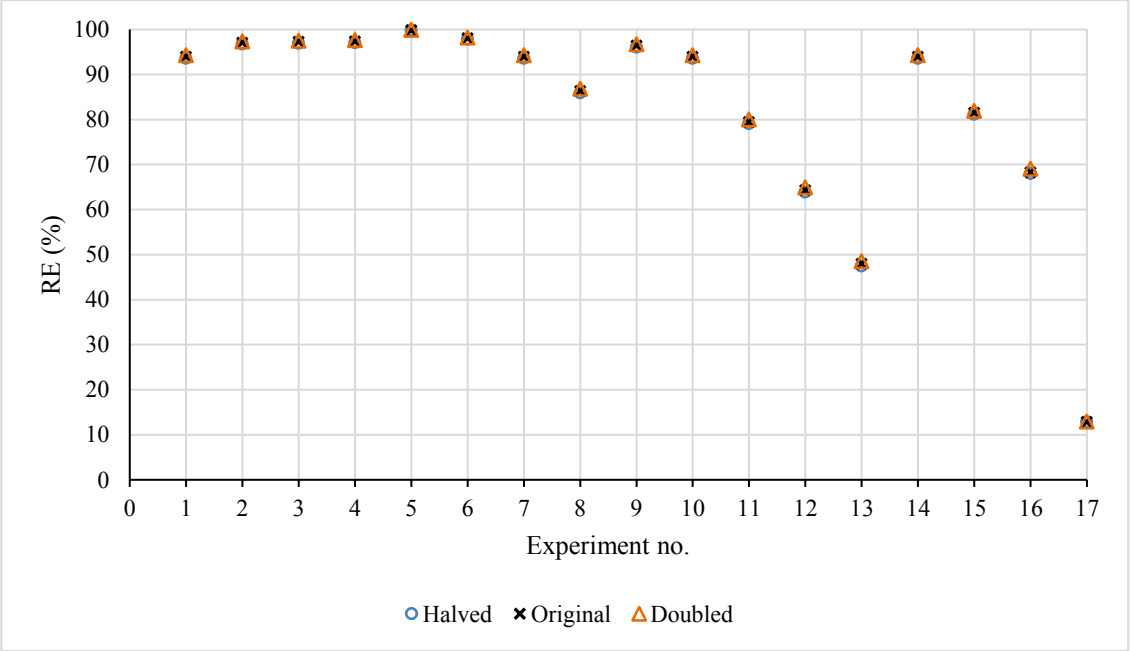

Figure S4. The sensitivity of EGPF to the values of (a) molecular weight and (b) air diffusivity. Experiment numbers are those listed in Table 4-2.

Table S3. Langmuir constants for the adsorption of SM on different adsorbents.

Adsorbent	Apparent density, ρ_p (kg m^{-3})	q_m (kg/kg)	b (kg/kg)	R^2
BAC-606	606	0.42	107584	0.98
BAC-707	707	0.25	100873	0.97
BAC-746	746	0.19	99613	0.98
BAC-807	807	0.01	96161	0.99

Table S4. The output of EGPM and EGPF models for the adsorption of SM on BAC in a six-stage countercurrent fluidized bed.

	EGPF							EGPM						
no.	C_1 (ppm_v)	C_2 (ppm_v)	C_3 (ppm_v)	C_4 (ppm_v)	C_5 (ppm_v)	C_6 (ppm_v)	RE (%)	C_1 (ppm_v)	C_2 (ppm_v)	C_3 (ppm_v)	C_4 (ppm_v)	C_5 (ppm_v)	C_6 (ppm_v)	RE (%)
1	80.5	54.7	33.4	19.4	11.1	6.1	93.9	76.4	51.5	32.0	19.1	11.3	6.4	93.6
2	57.6	32.2	17.8	9.8	5.4	2.9	97.0	59.3	34.3	19.7	11.3	6.4	3.6	96.4
3	56.0	30.9	16.9	9.3	5.1	2.8	97.2	58.0	33.2	18.9	10.8	6.1	3.4	96.5
4	55.3	30.3	16.6	9.0	4.9	2.7	97.3	57.4	32.7	18.6	10.5	6.0	3.4	96.6
5	51.4	19.2	6.4	1.9	0.6	0.2	99.8	51.0	21.1	8.1	2.9	1.0	0.4	99.6
6	74.0	43.5	22.1	10.3	4.6	2.0	98.0	62.2	33.1	16.8	8.4	4.0	1.9	98.1
7	80.5	54.7	33.4	19.4	11.1	6.1	93.9	76.4	51.5	32.0	19.1	11.3	6.4	93.6
8	87.4	67.4	47.7	32.5	21.2	13.6	86.3	83.5	63.2	44.8	30.8	20.5	13.5	86.5
9	31.0	18.2	10.6	5.9	3.3	1.8	96.4	31.3	18.8	11.2	6.4	3.7	2.1	95.8
10	80.5	54.7	33.4	19.4	11.1	6.1	93.9	76.4	51.5	32.0	19.1	11.3	6.4	93.6
11	148.5	142.7	124.3	88.8	54.4	30.9	79.4	140.0	118.8	86.4	55.7	33.4	19.3	87.1
12	199.9	199.4	196.2	177.4	124.1	71.4	64.3	199.6	197.9	190.6	164.9	114.7	68.3	65.8
13	300	299.9	299.7	296.4	258.6	156.2	47.9	300.0	299.9	299.2	292.0	245.1	151.9	49.4
1	80.5	54.7	33.4	19.4	11.1	6.1	93.9	76.4	51.5	32.0	19.1	11.3	6.4	93.6
2	98.7	93.7	78.5	55.7	33.4	18.2	81.8	92.6	76.7	56.5	36.5	21.9	12.7	87.3
3	100	99.6	97.6	87.25	59.8	33.8	66.2	99.1	95.5	83.2	62.1	39.0	22.4	77.6
4	100	99.9	99.5	95.93	77.3	47.7	52.3	100.0	99.7	98.1	90.5	67.6	41.3	58.7

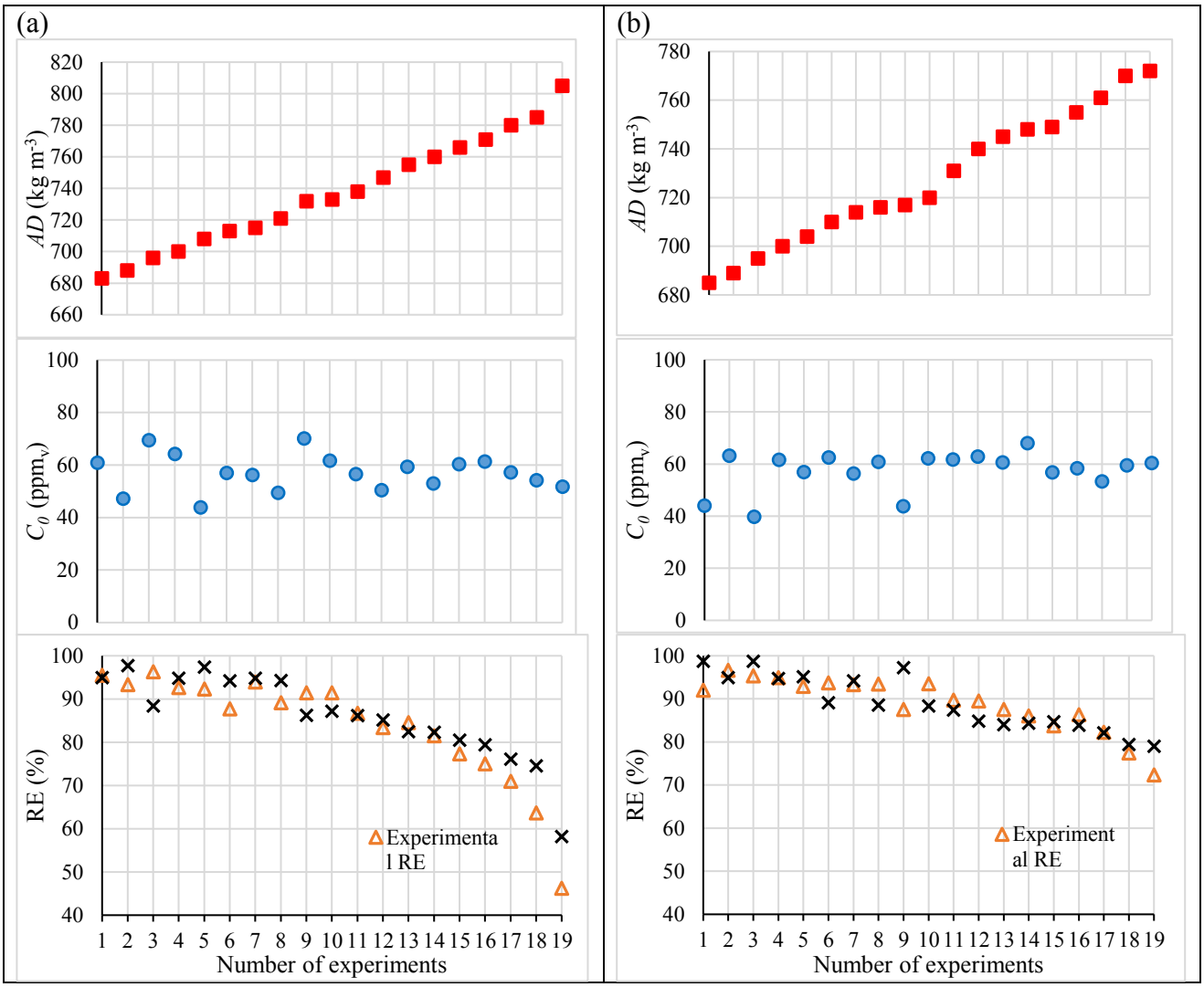

Figure S5. Apparent density, initial concentration, and experimental vs. calculated removal efficiencies for the adsorption of SM on BAC: (a) batch 1 and (b) batch 2.

Appendix C: Supplementary Information for Chapter 5

(a)

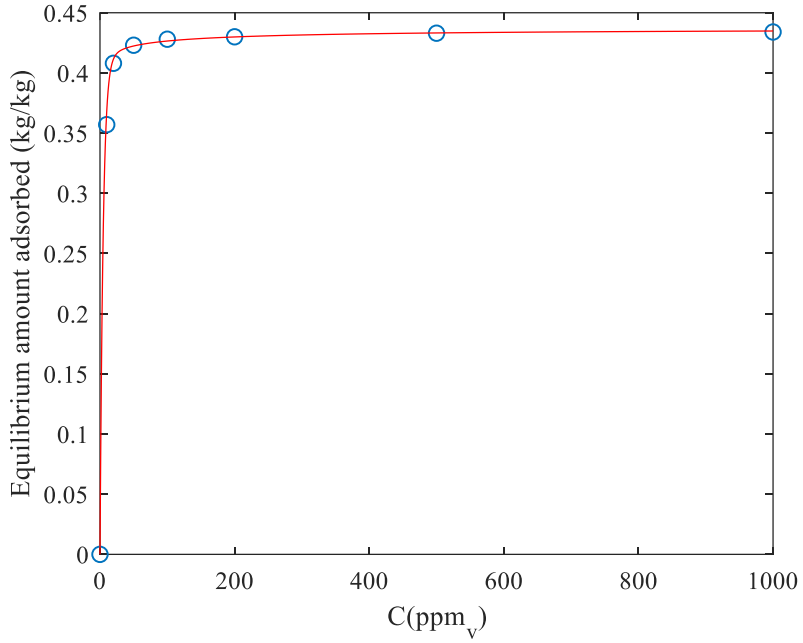

(b)

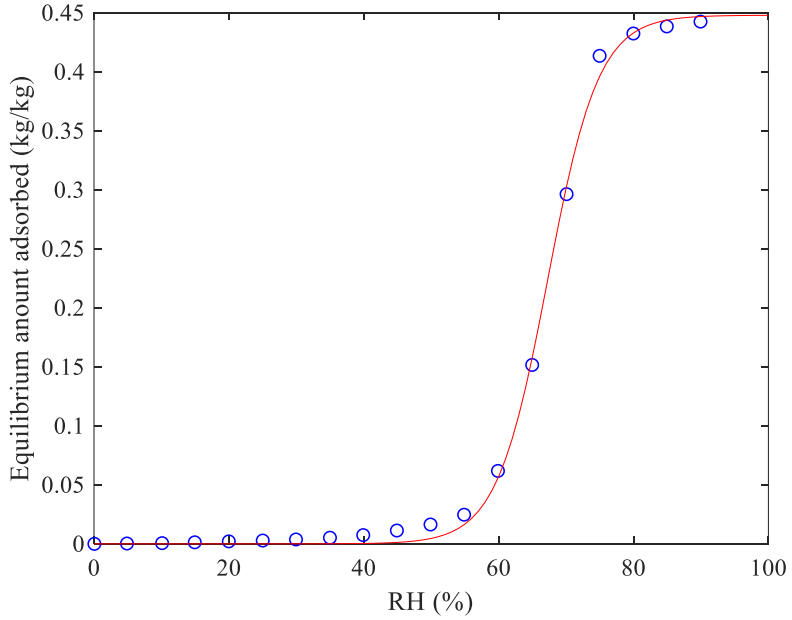

Figure S6. Measured values along with the MDR and QHR fits of the equilibrium adsorption isotherms of (a) TMB (Amdebrhan, 2018) and (b) water vapor (Laskar et al., 2019) on BAC at room temperature.

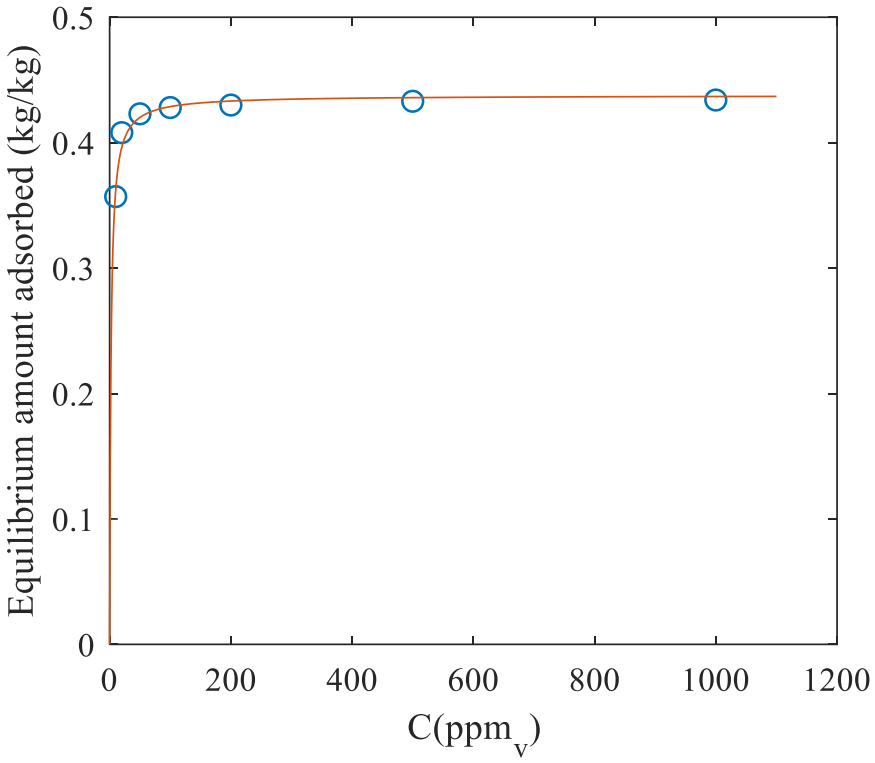

Figure S7. Measured data and Langmuir fit of the equilibrium adsorption isotherm of TMB on BAC at room temperature (Amdebrhan, 2018).

Table S5. The experimental and calculated concentration of TMB along the bed at different RH values.

	RH=0%		RH=28%		RH=55%		RH=75%		RH=85%		RH=93%	
	Exp.	Calc.	Exp.	Calc.	Exp.	Calc.	Exp.	Calc.	Exp.	Calc.	Exp.	Calc.
inlet	100	100	100	100	100	100	100	100	100	100	100	100
Stage 1	64.7	70.0	63.3	70.0	62.5	70.0	65.0	69.5	68.1	67.8	69.2	71.0
Stage 2	46.6	46.5	49.5	46.5	47.3	46.5	48.9	45.8	49.6	46.0	51.7	49.5
Stage 3	35.7	29.8	38.1	29.8	35.6	29.8	38.7	30.4	35.8	31.6	37.9	35.8
Stage 4	26.5	18.6	24.5	18.6	25.2	18.6	25.0	19.9	24.4	22.5	32.4	26.7
Stage 5	13.8	11.6	15.0	11.6	13.7	11.6	11.7	13.2	19.1	16.7	22.2	20.5
Stage 6	8.8	7.1	9.4	7.1	8.7	7.1	7.4	8.6	14.4	12.8	18.4	15.8

Table S6. The experimental and calculated concentration of TMB along the bed at different temperatures.

	T=22 ºC		T=40 ºC		T=50 ºC	
	Exp.	Calc.	Exp.	Calc.	Exp.	Calc.
inlet	100	100	100	100	100	100
Stage 1	71.1	73.2	77.1	68.9	78.2	71.8
Stage 2	42.9	49.3	66.2	46.0	73.4	50.2
Stage 3	21.2	31.7	27.3	29.9	39.5	34.2
Stage 4	12.1	20.0	19.8	19.0	28.1	22.8
Stage 5	7.2	12.5	7.6	11.9	12.3	15.0
Stage 6	6.0	7.7	8.5	7.3	11.4	9.5

References for Apendix C

Amdebrhan, B.T. (2018). Evaluating the Performance of Activated Carbon, Polymeric, and Zeolite Adsorbents for Volatile Organic Compounds Control. Department of Civil and Environmental Engineering, University of Alberta. **Master of Science**.

Laskar, I.I., Hashisho, Z., Phillips, J.H., Anderson, J.E., Nichols, M., 2019. Competitive adsorption equilibrium modeling of volatile organic compound (VOC) and water vapor onto activated carbon. *Separation and Purification Technology*, **212**: 632-640.

Appendix D: Supplementary Information for Chapter 6

Table S7. Experimental single-component adsorption isotherm of TMB and water vapor on zeolite (ZEOCAT F603) (Amdebrhan, 2018).

TMB			Water vapor		
Concentration (ppm)	Pressure (pa)	Equilibrium amount adsorbed (g/g)	RH (%)	Pressure (pa)*	Equilibrium amount adsorbed (g/g)
0.0	0.0	0.000	0.0	0.0	0.000
10.0	1.0	0.056	10.0	249.3	0.011
20.0	2.0	0.059	20.0	498.6	0.019
50.0	5.1	0.061	30.0	747.9	0.026
100.0	10.1	0.068	39.6	987.2	0.038
200.0	20.3	0.075	49.3	1229.0	0.050
500.0	50.7	0.092	60.0	1495.8	0.065
1000.0	101.3	0.106	70.0	1745.1	0.077
			80.7	2011.9	0.107
			93.6	2333.4	0.193

*water vapor saturated pressure= 2493 pa (at 21 °C)

(a)

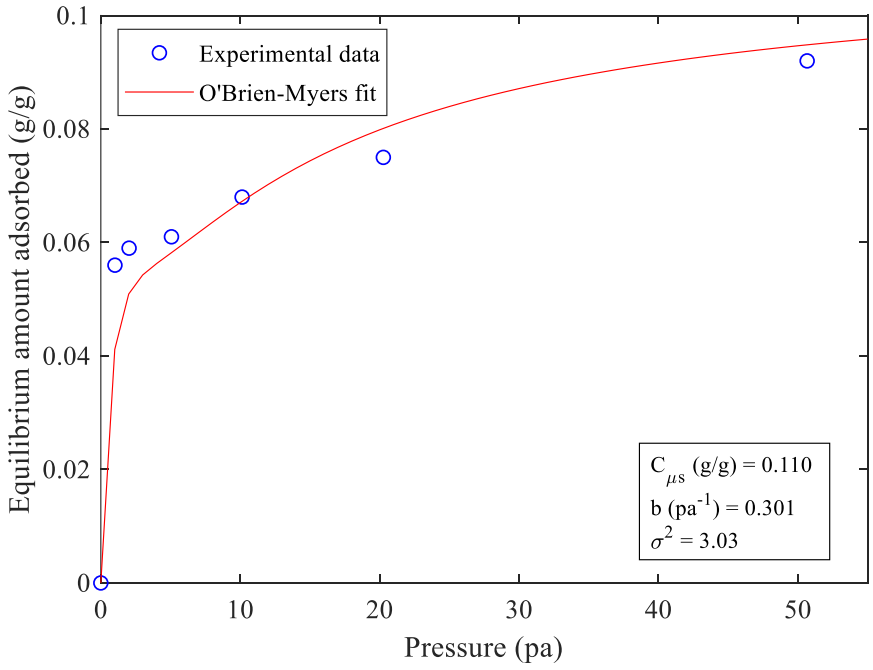

(b)

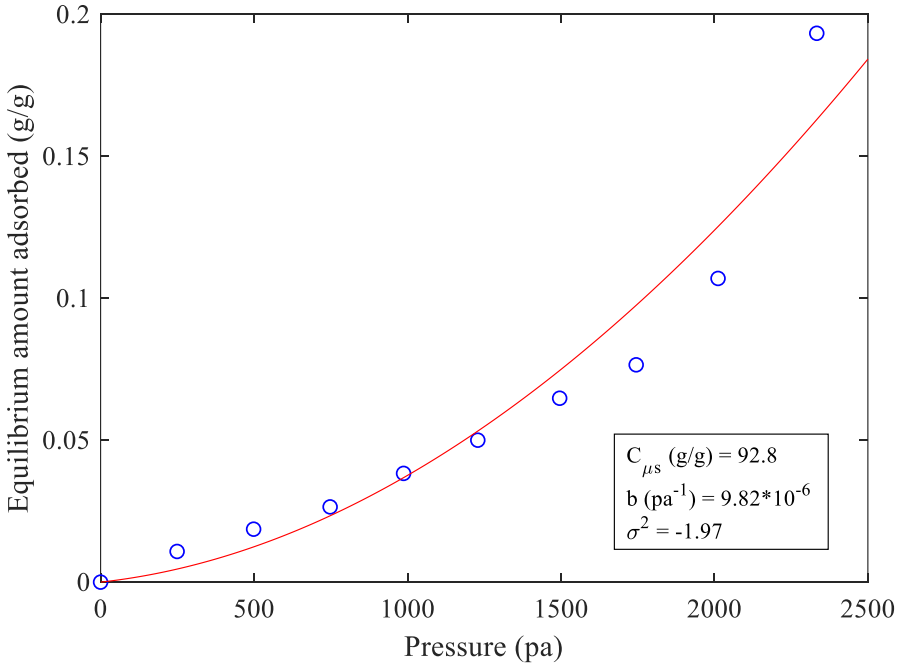

Figure S8. Measured values along with the O'Brien-Myers fits of the equilibrium adsorption isotherms of (a) TMB and (b) water vapor on zeolite (ZEOCAT F603).

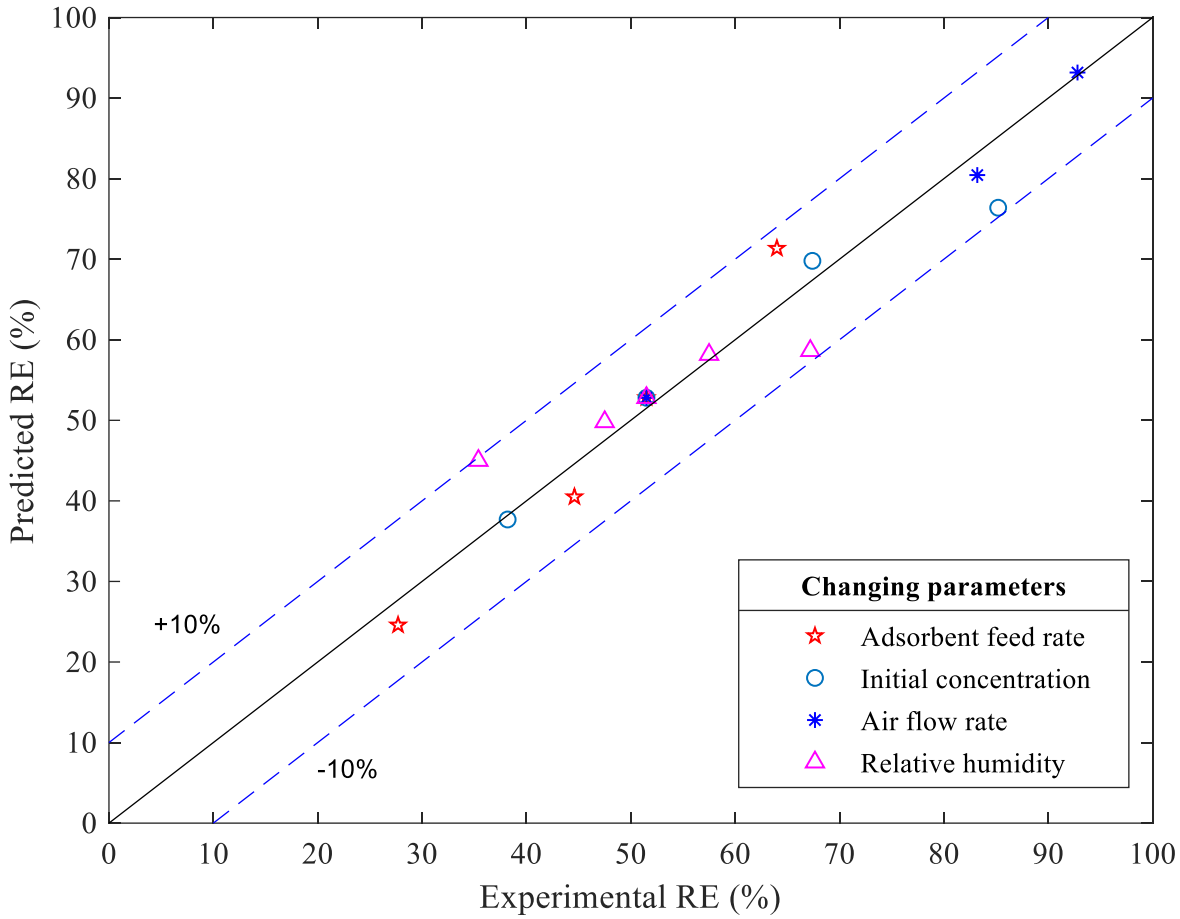

Figure S9. Experimental versus predicted removal efficiencies.

Table S8. The model output for adsorption of TMB on zeolite (ZEOCAT F603) in a six-stage countercurrent fluidized bed.

Changing parameter	no.	Concentration (ppm_v)						
		Inlet	Stage 1	Stage 2	Stage 3	Stage 4	Stage 5	Stage 6
Adsorbent feed rate	1	100	100	100	99	97	91	75
	2	100	99	98	95	89	78	60
	3	100	97	93	85	74	60	43
	4	100	91	80	68	54	41	29
Initial concentration	5	25	22	18	15	12	9	6
	6	50	45	40	34	28	21	15
	7	100	97	93	85	74	60	43
	8	150	149	148	145	137	122	93
Air flow rate	9	100	82	62	43	27	14	7
	10	100	92	81	67	51	34	20
	11	100	97	93	85	74	60	43
RH	12	100	96	90	82	71	57	41
	13	100	97	91	83	72	58	42
	14	100	97	93	85	74	60	43
	15	100	98	95	89	80	67	50
	16	100	98	94	89	81	68	52

Table S9. Removal efficiency at various experimental conditions using fluidized bed adsorbers with different stage configurations.

Exp. no.	Removal efficiency (%)			
	1 adsorber of 6 stages	2 adsorbers of 3 stages	3 adsorbers of 2 stages	6 adsorbers of 1 stage
1	24.6	48.1	58.5	57.9
2	40.5	70.0	71.1	67.4
3	52.8	76.7	81.2	72.3
4	71.4	86.2	86.9	78.2
5	76.4	87.5	90.4	83.4
6	69.8	84.5	86.4	79.7
7	52.8	76.7	81.2	72.3
8	37.7	65.3	72.2	66.0
9	93.2	96.3	94.9	NA*
10	80.5	92.5	89.5	79.1
11	52.8	76.7	81.2	72.3
12	58.7	77.8	81.9	73.3
13	58.2	77.6	81.9	73.1
14	52.8	76.7	81.2	72.3
15	49.8	75.4	80.1	71.3
16	48.4	73.7	78.7	70.3

* gas flow rate, in this case, is lower than that required for minimum fluidization.

Table S10. Removal efficiency at various experimental conditions using fluidized bed adsorbers with different weir heights (the same weir height across each adsorber).

Exp. no.	Removal efficiency (%)			
	H=2 mm	H=4 mm	H=20 mm	H=40 mm
1	23.6	24.6	25.4	25.5
2	39.6	40.5	42.3	42.5
3	50.4	52.8	54.0	54.1
4	61.1	71.3	80.9	81.4
5	61.6	76.4	85.6	86.3
6	59.3	69.8	76.7	77.3
7	50.4	52.8	59.2	59.4
8	36.9	37.7	39.4	39.6
9	89.2	93.2	97.6	97.7
10	72.1	80.4	84.1	84.3
11	50.4	52.8	59.2	59.4
12	51.5	58.6	61.3	62.2
13	51.3	58.2	58.4	58.4
14	50.4	52.8	59.2	59.4
15	46.9	49.8	52.1	52.7
16	45.5	48.3	50.6	51.1

Reference for Apendix D

Amdebrhan, B.T. (2018). Evaluating the Performance of Activated Carbon, Polymeric, and Zeolite Adsorbents for Volatile Organic Compounds Control. Department of Civil and Environmental Engineering, University of Alberta. **Master of Science**.

Appendix E: Supplementary Information for Chapter 7

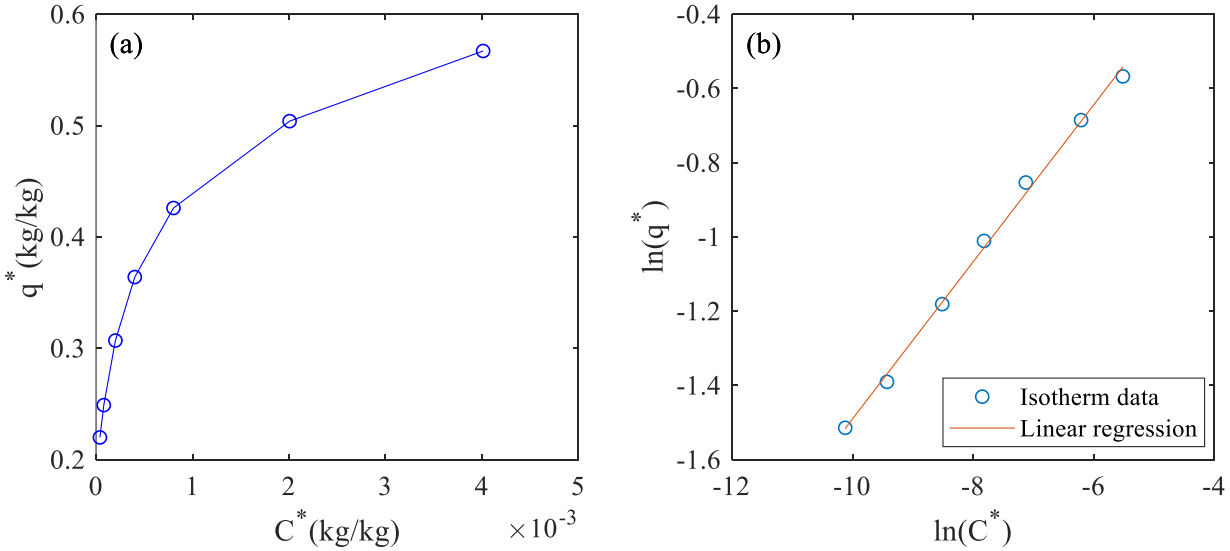

Figure S10. (a) Adsorption data and (b) Freundlich isotherm for adsorption of TMB on DOWEX.

Table S11. The results of the two-phase model for the adsorption of TMB on DOWEX in the lab-scale fluidized bed adsorber.

	EGPM							EGPF						
no.	C_1 (ppm_v)	C_2 (ppm_v)	C_3 (ppm_v)	C_4 (ppm_v)	C_5 (ppm_v)	C_6 (ppm_v)	RE (%)	C_1 (ppm_v)	C_2 (ppm_v)	C_3 (ppm_v)	C_4 (ppm_v)	C_5 (ppm_v)	C_6 (ppm_v)	RE (%)
1	91.3	80.8	68.5	55.8	43.7	33.6	66.4	94.1	85.7	74.3	61.0	47.3	35.7	64.3
2	78.9	61.4	47.4	36.5	27.1	21.5	78.5	78.4	60.2	45.6	34.4	25.9	19.4	80.6
3	77.2	59.4	45.6	35.0	26.9	20.7	79.3	75.8	57.2	43.0	32.3	24.3	18.3	81.7
4	76.9	59.0	45.3	34.8	26.7	20.5	79.5	75.3	56.6	42.6	32.0	24.0	18.1	81.9
5	42.5	35.1	28.0	22.0	17.0	13.1	73.8	43.4	36.3	29.0	22.6	17.2	12.9	74.2
6	91.3	80.8	68.5	55.8	43.7	33.6	66.4	94.1	85.7	74.3	61.0	47.3	35.7	64.3
7	142.5	131.9	117.3	99.5	79.6	61.4	59.1	146.7	140.8	130.9	114.9	93.7	71.3	52.5
8	194.2	184.9	170.3	149.5	122.8	95.3	52.4	197.8	193.4	184.6	167.9	141.5	108.7	45.6
9	38.5	29.6	22.7	17.4	13.4	10.3	79.5	37.7	28.3	21.3	16.0	12.0	9.0	81.9
10	77.2	59.4	45.6	35.0	26.9	20.7	79.3	75.8	57.2	43.0	32.3	24.3	18.3	81.7
11	117.0	90.4	69.6	53.5	41.0	31.5	79.0	115.4	87.7	66.2	49.8	37.5	28.2	81.2
12	157.1	122.0	94.1	72.3	55.5	42.6	78.7	155.7	119.1	90.2	67.9	51.1	38.4	80.8
13	82.2	63.2	45.2	29.6	18.2	10.9	89.1	88.9	73.7	54.6	35.7	21.1	12.0	88.0
14	88.0	74.1	58.7	43.9	31.4	22.0	78.0	92.5	81.9	67.6	51.7	36.4	24.8	75.2
15	91.3	80.8	68.5	55.8	43.7	33.6	66.4	94.1	85.7	74.3	61.0	47.3	35.7	64.3
16	92.7	83.7	73.2	62.0	51.1	41.7	58.4	95.5	89.0	80.1	68.7	56.5	45.4	54.6
17	60.4	36.2	21.7	13.0	7.8	4.7	95.3	57.1	32.4	18.3	10.4	5.8	3.3	96.7
18	70.6	49.6	34.8	24.4	17.1	12.0	88.0	68.8	46.9	31.9	21.6	14.7	10.0	90.0
19	77.2	59.4	45.6	35.0	26.9	20.7	79.3	75.8	57.2	43.0	32.3	24.3	18.3	81.7
20	81.8	66.7	54.3	44.2	36.0	29.3	70.7	80.6	64.8	51.9	41.6	33.3	26.6	73.4

Table S12.The experimental operating conditions used for finding the optimized set of formulas.

F_g (SLPM)	F_p (g/min)	C_0 (ppm)	q_0 (kg/kg)	H (mm)	No. of stages	AD (kg/m^3)	D (m)	d_p (m)
TMB on BAC-lab scale (Kamravaei, 2015, Kamravaei, 2016, Davarpanah et al., 2020)								
300	0.44	100	0	4	6	606	7.62E-02	7.50E-04
300	1.4	100	0	4	6	606	7.62E-02	7.50E-04
300	2.3	100	0	4	6	606	7.62E-02	7.50E-04
300	3.3	100	0	4	6	606	7.62E-02	7.50E-04
200	0.44	100	0	4	6	606	7.62E-02	7.50E-04
250	0.44	100	0	4	6	606	7.62E-02	7.50E-04
300	0.44	100	0	4	6	606	7.62E-02	7.50E-04
350	0.44	100	0	4	6	606	7.62E-02	7.50E-04
300	0.44	50	0	4	6	606	7.62E-02	7.50E-04
300	0.44	100	0	4	6	606	7.62E-02	7.50E-04
300	0.44	150	0	4	6	606	7.62E-02	7.50E-04
300	0.44	200	0	4	6	606	7.62E-02	7.50E-04
300	0.44	300	0	4	6	606	7.62E-02	7.50E-04
200	0.44	150	0	4	6	606	7.62E-02	7.50E-04
250	0.44	120	0	4	6	606	7.62E-02	7.50E-04
300	0.44	100	0	4	6	606	7.62E-02	7.50E-04
350	0.44	85.7	0	4	6	606	7.62E-02	7.50E-04
300	0.44	100	0	2	6	606	7.62E-02	7.50E-04
300	0.44	100	0	4	6	606	7.62E-02	7.50E-04
300	0.44	100	0	6	6	606	7.62E-02	7.50E-04
300	0.44	100	0	8	6	606	7.62E-02	7.50E-04
300	0.44	100	0	4	2	606	7.62E-02	7.50E-04
300	0.44	100	0	4	4	606	7.62E-02	7.50E-04
300	0.44	100	0	4	6	606	7.62E-02	7.50E-04
TMB on DOWEX- lab scale (Kamravaei et al., 2016)								

300	0.3	100	0	4	6	340	7.62E-02	1.00E-03
300	0.87	100	0	4	6	340	7.62E-02	1.00E-03
300	1.6	100	0	4	6	340	7.62E-02	1.00E-03
300	2.4	100	0	4	6	340	7.62E-02	1.00E-03
300	0.3	50	0	4	6	340	7.62E-02	1.00E-03
300	0.3	100	0	4	6	340	7.62E-02	1.00E-03
300	0.3	150	0	4	6	340	7.62E-02	1.00E-03
300	0.3	200	0	4	6	340	7.62E-02	1.00E-03
300	1.6	50	0	4	6	340	7.62E-02	1.00E-03
300	1.6	100	0	4	6	340	7.62E-02	1.00E-03
300	1.6	150	0	4	6	340	7.62E-02	1.00E-03
300	1.6	200	0	4	6	340	7.62E-02	1.00E-03
200	0.3	100	0	4	6	340	7.62E-02	1.00E-03
250	0.3	100	0	4	6	340	7.62E-02	1.00E-03
300	0.3	100	0	4	6	340	7.62E-02	1.00E-03
350	0.3	100	0	4	6	340	7.62E-02	1.00E-03
200	1.6	100	0	4	6	340	7.62E-02	1.00E-03
250	1.6	100	0	4	6	340	7.62E-02	1.00E-03
300	1.6	100	0	4	6	340	7.62E-02	1.00E-03
350	1.6	100	0	4	6	340	7.62E-02	1.00E-03
SM on BAC- lab scale (Kamravaei, 2015, Davarpanah et al., 2020)								
300	0.44	100	0	4	6	606	7.62E-02	7.50E-04
300	1.4	100	0	4	6	606	7.62E-02	7.50E-04
300	2.3	100	0	4	6	606	7.62E-02	7.50E-04
300	3.3	100	0	4	6	606	7.62E-02	7.50E-04
200	0.44	100	0	4	6	606	7.62E-02	7.50E-04
250	0.44	100	0	4	6	606	7.62E-02	7.50E-04
300	0.44	100	0	4	6	606	7.62E-02	7.50E-04
350	0.44	100	0	4	6	606	7.62E-02	7.50E-04

300	0.44	50	0	4	6	606	7.62E-02	7.50E-04
300	0.44	100	0	4	6	606	7.62E-02	7.50E-04
300	0.44	150	0	4	6	606	7.62E-02	7.50E-04
300	0.44	200	0	4	6	606	7.62E-02	7.50E-04
300	0.44	300	0	4	6	606	7.62E-02	7.50E-04
300	0.44	100	0	4	6	606	7.62E-02	7.50E-04
300	0.44	100	0	4	6	707	7.62E-02	7.50E-04
300	0.44	100	0	4	6	746	7.62E-02	7.50E-04
300	0.44	100	0	4	6	807	7.62E-02	7.50E-04
SM on BAC- industrial scale (Davarpanah et al., 2020)								
1416707	3439.4	60.88	0	12.7	6	683	5.44	7.50E-04
1416707	3464.5	44	0	12.7	6	685	5.44	7.50E-04
1416707	3504.8	47.16	0	12.7	6	688	5.44	7.50E-04
1416707	3525	63.23	0	12.7	6	689	5.44	7.50E-04
1416707	3565.3	39.78	0	12.7	6	695	5.44	7.50E-04
1416707	3590.4	69.45	0	12.7	6	696	5.44	7.50E-04
1416707	3600.5	64.32	0	12.7	6	700	5.44	7.50E-04
1416707	3630.7	61.56	0	12.7	6	700	5.44	7.50E-04
1416707	3686.1	56.9	0	12.7	6	704	5.44	7.50E-04
1416707	3691.2	43.89	0	12.7	6	708	5.44	7.50E-04
1416707	3716.3	62.53	0	12.7	6	710	5.44	7.50E-04
1416707	3761.7	56.99	0	12.7	6	713	5.44	7.50E-04
1416707	3801.9	56.41	0	12.7	6	714	5.44	7.50E-04
1416707	3827.1	56.22	0	12.7	6	715	5.44	7.50E-04
1416707	3857.3	60.9	0	12.7	6	716	5.44	7.50E-04
1416707	3882.5	43.84	0	12.7	6	717	5.44	7.50E-04
1416707	3927.8	62.15	0	12.7	6	720	5.44	7.50E-04
1416707	3953	49.44	0	12.7	6	721	5.44	7.50E-04
1416707	4053.7	61.84	0	12.7	6	731	5.44	7.50E-04

1416707	3449.4	70.23	0	12.7	6	732	5.44	7.50E-04
1416707	3469.6	61.74	0	12.7	6	733	5.44	7.50E-04
1416707	3499.8	56.61	0	12.7	6	738	5.44	7.50E-04
1416707	3525	62.85	0	12.7	6	740	5.44	7.50E-04
1416707	3545.1	60.64	0	12.7	6	745	5.44	7.50E-04
1416707	3575.3	50.42	0	12.7	6	747	5.44	7.50E-04
1416707	3595.5	68	0	12.7	6	748	5.44	7.50E-04
1416707	3605.5	56.8	0	12.7	6	749	5.44	7.50E-04
1416707	3610.6	59.41	0	12.7	6	755	5.44	7.50E-04
1416707	3625.7	58.39	0	12.7	6	755	5.44	7.50E-04
1416707	3681.1	53.02	0	12.7	6	760	5.44	7.50E-04
1416707	3726.4	53.31	0	12.7	6	761	5.44	7.50E-04
1416707	3751.6	60.3	0	12.7	6	766	5.44	7.50E-04
1416707	3766.7	59.51	0	12.7	6	770	5.44	7.50E-04
1416707	3771.7	61.28	0	12.7	6	771	5.44	7.50E-04
1416707	3801.9	60.36	0	12.7	6	772	5.44	7.50E-04
1416707	3832.2	57.18	0	12.7	6	780	5.44	7.50E-04
1416707	3877.5	54.17	0	12.7	6	785	5.44	7.50E-04
1416707	3887.5	51.82	0	12.7	6	805	5.44	7.50E-04
Water vapor on Alumina- bench scale (Hymore and Laguerie, 1984)								
360.5	33.3	13311.6	0.007	75	5	1670	0.2	3.62E-04
514.9	31.7	13810.8	0.007	75	5	1670	0.2	3.62E-04
360.5	65	13810.8	0.005	75	5	1670	0.2	3.62E-04
515.6	65	13727.6	0.007	75	5	1670	0.2	3.62E-04
357.8	35	20799.4	0.007	75	5	1670	0.2	3.62E-04
512.9	33.3	19468.3	0.007	75	5	1670	0.2	3.62E-04
357.8	66.7	19135.5	0.007	75	5	1670	0.2	3.62E-04
512.9	66.7	19634.7	0.006	75	5	1670	0.2	3.62E-04
434.0	50	16639.5	0.007	75	5	1670	0.2	3.62E-04

435.3	51. 7	16473.1	0.007	75	5	1670	0.2	3.62E-04
435.3	50	17138.7	0.007	75	5	1670	0.2	3.62E-04

References for Apendix E

Davarpanah, M., Hashisho, Z., Crompton, D., Anderson, J.E., Nichols, M., 2020. Modeling VOC adsorption in lab- and industrial-scale fluidized bed adsorbers: Effect of operating parameters and heel build-up. *Journal of Hazardous Materials*, **400**: 123129.

Davarpanah, M., Hashisho, Z., Phillips, J.H., Crompton, D., Anderson, J.E., Nichols, M., 2020. Modeling VOC adsorption in a multistage countercurrent fluidized bed adsorber. *Chemical Engineering Journal*, **394**: 124963.

Hymore, K., Laguerie, C., 1984. Analysis and modelling of the operation of a counterflow multistage fluidized bed adsorber for drying moist air. *Chemical Engineering and Processing: Process Intensification*, **18**: 255-267.

Kamravaei, S., Shariaty, P., Hashisho, Z., Phillips, J.H., Anderson, J.E., Nichols, M., Crompton, D. (2016). Performance of a Multistage Fluidized Bed Adsorber Using Polymeric Adsorbent to Capture Volatile Organic Compounds. AIChE Annual Meeting. San Francisco, CA, USA.

Kamravaei, S., Shariaty, P. Jahandar Lashaki, M., Atkinson, J.D., Hashisho, Z., Phillips, J.H., Anderson, J.E., and Nichols, M (2016). Effect of Beaded Activated Carbon Fluidization on Adsorption of Volatile Organic Compounds. AIChE Annual Meeting. San Francisco, CA, USA.

Kamravaei, S., Shariaty, P. Jahandar Lashaki, M., Atkinson, J.D., Hashisho, Z., Phillips, J.H., Anderson, J.E., and Nichols, M. Crompton, D (2015). Effect of Operational Parameters on the Performance of a Multistage Fluidized Bed Adsorber. AIChE Annual Meeting. Salt lake City, UT, USA.

Appendix F: Supplementary Information for Chapter 8

Table S13. Governing equations used in modeling (Ansys, Release 19.2).

Definition	Formula
Continuity equation	$\frac{\partial}{\partial t}\left(\alpha_q \rho_q\right)+\nabla\left(\alpha_q \rho_q \vec{\upsilon}_q\right)=0$
Momentum equations	$\frac{\partial}{\partial t}\left(\alpha_g \rho_g \vec{\upsilon}_g\right)+\nabla\left(\alpha_g \rho_g \vec{\upsilon}_g \vec{\upsilon}_g\right)=-\alpha_g \nabla p+\nabla \cdot \bar{\bar{\tau}}_g+\alpha_g \rho_g \vec{g}+K_{sg}\left(\vec{\upsilon}_s-\vec{\upsilon}_g\right)$
	$\frac{\partial}{\partial t}\left(\alpha_s \rho_s \vec{\upsilon}_s\right)+\nabla\left(\alpha_s \rho_s \vec{\upsilon}_s \vec{\upsilon}_s\right)=-\alpha_s \nabla p-\nabla p_s+\nabla \cdot \bar{\bar{\tau}}_s+\alpha_s \rho_s \vec{g}+K_{sg}\left(\vec{\upsilon}_g-\vec{\upsilon}_s\right)$
Stress tensor	$\bar{\bar{\tau}}_q=\alpha_q \mu_q\left(\nabla \vec{\upsilon}_q+\nabla \vec{\upsilon}_q^T\right)+\alpha_q\left(\lambda_q-\frac{2}{3}\mu_q\right)\nabla \cdot \vec{\upsilon}_q \bar{\bar{I}}$
Drag function	$K_{sg}=\frac{3}{4}\frac{\alpha_s \alpha_g \rho_g}{\upsilon_{r,s}^2 d_s} C_D\left\lvert\vec{\upsilon}_s-\vec{\upsilon}_g\right\rvert$
	$C_D=\left(0.63+\frac{4.8}{\sqrt{\mathrm{Re}_s / \upsilon_{\tau,s}}}\right)^2$
	$\mathrm{Re}_s=\frac{\rho_g d_s\left\lvert\vec{\upsilon}_s-\vec{\upsilon}_g\right\rvert}{\mu_g}$
	$\upsilon_{\tau,s}=0.5\left(A-0.06\,\mathrm{Re}_s+\sqrt{\left(0.06\,\mathrm{Re}_s\right)^2+0.12\,\mathrm{Re}_s\left(2B-A\right)+A^2}\right)$
	$A=\alpha_g{}^{4.14}, B=0.8\alpha_g{}^{1.28}$ For $\alpha_g \le 0.85$
	$A=\alpha_g{}^{4.14}, B=\alpha_g{}^{2.65}$ For $\alpha_g \ge 0.85,$
Transport equation	$\left(-p_s \bar{\bar{I}}+\bar{\bar{\tau}}_s\right):\nabla \vec{\upsilon}_s-\gamma_{\Theta_s}+\varphi_{gs}=0$
Solid pressure	$p_s=\alpha_s \rho_s \Theta_s+2\rho_s\left(1+e_{ss}\right)\alpha_s^2 g_{0,ss}\Theta_s$
Radial distribution coefficient	$g_{0,ss}=\left[1-\left(\frac{\alpha_s}{\alpha_{s,\max}}\right)^{\frac{1}{3}}\right]^{-1}$

Collision dissipation of energy	$\gamma_{\Theta s} = \frac{12\left(1-e_{ss}^2\right)g_{0,ss}}{d_s\sqrt{\pi}}\rho_s\alpha_s^2\Theta_s^{3/2}$
Transfer of kinetic energy	$\varphi_{gs} = -3K_{gs}\Theta_s$
Solid shear viscosity	$\mu_s = \mu_{s,\text{col}} + \mu_{s,\text{kin}} + \mu_{s,fr}$
Solid collisional viscosity	$\mu_{s,\text{col}} = \frac{4}{5}\alpha_s\rho_s d_s g_{0,ss}\left(1+e_{ss}\right)\left(\frac{\Theta_s}{\pi}\right)^{1/2}$
Solid kinetic viscosity	$\mu_{s,kin} = \frac{\alpha_s\rho_s d_s\sqrt{\Theta_s\pi}}{6\left(3-e_{ss}\right)}\left[1+\frac{2}{5}\left(1+e_{ss}\right)\left(3e_{ss}-1\right)\alpha_s g_{0,ss}\right]$
Solid frictional viscosity	$\mu_{s,fr} = \frac{p_s\sin\phi}{2\sqrt{I_{2D}}}$
Bulk viscosity	$\lambda_s = \frac{4}{3}\alpha_s\rho_s d_s g_{0,ss}\left(1+e_{ss}\right)\left(\frac{\Theta_s}{\pi}\right)^{1/2}$
Granular Temperature	$\Theta_s = \frac{1}{3}\upsilon_s^2$
k-ε model	$\frac{\partial}{\partial t}\left(\alpha_g\rho_g k_g\right)+\nabla.\left(\alpha_g\rho_g\vec{\upsilon}_g k_g\right) = \nabla.\left(\alpha_g\alpha_k\mu_{eff}\nabla.k_g\right)+\alpha_g G_{k,g}+$ $\alpha_g G_{b,g}-\alpha_g\rho_g\varepsilon_g-\alpha_g Y_M$
	$\frac{\partial}{\partial t}\left(\alpha_g\rho_g k_g\right)+\nabla.\left(\alpha_g\rho_g\vec{\upsilon}_g\varepsilon_g\right) = \nabla.\left(\alpha_g\alpha_\varepsilon\mu_{eff}\nabla.\varepsilon_g\right)+$ $\alpha_g C_{1\varepsilon}\frac{\varepsilon_g}{k_g}\left(G_{k,g}+C_{3\varepsilon}G_{b,g}\right)-\alpha_g C_{2\varepsilon}^*\rho_g\frac{\varepsilon_g^2}{k_g}$
	$C_{2\varepsilon}^* \equiv C_{2\varepsilon}+\frac{C_\mu\eta^3\left(1-\eta/\eta_0\right)}{1+\beta\eta^3}$
	$\eta \equiv Sk/\varepsilon, \eta_0 = 4.38, \beta = 0.012$

Table S14. Nomenclature.

Parameter	Definition	Unit
A, B	coefficient in the Syamlal-O'Brien model	-
$C_{1\varepsilon}$, $C_{2\varepsilon}$, $C_{3\varepsilon}$, $C^{*}_{2\varepsilon}$	constants in k-ε model	-
C_D	drag coefficient	-
d	diameter	m
e_{ss}	coefficient of restitution	-
g	gravitational acceleration	m s^{-2}
$g_{0,ss}$	radial distribution coefficient	-
G_b	generation of turbulence kinetic energy due to buoyancy	-
G_k	generation of turbulence kinetic energy due to the mean velocity gradients	-
$\overline{\overline{I}}$	stress tensor dimensionless	-
I_{2D}	second invariant of the deviatoric stress tensor	-
k	turbulence quantities	-
K_{sg}	exchange coefficient	-
p	pressure	pa
Re	Reynolds number	-
S	mean rate-of-strain tensor	s^{-1}
v	velocity	m s^{-1}
$v_{\tau,s}$	terminal velocity correlation for the solid phase	-
Y_M	contribution of the fluctuating dilatation in compressible turbulence to the overall dissipation rate	-
Greek letters		
α	volume fraction	-
α_k, α_ε	inverse effective Prandtl numbers for k and ε	-
β	constant in k-ε model	-
$\gamma_{\Theta s}$	collisional dissipation of energy	-
ε	turbulence dissipation rate	m^2 s^{-3}
η,η_0	constants in k-ε model	-
Θ_s	granular temperature	m^2 s^{-2}
λ	bulk viscosity	kg s^{-1} m^{-1}
μ	viscosity	pa s
ρ	density	kg m^{-3}
ϕ	angle of internal friction	-
$\overline{\overline{\tau}}$	stress tensor	pa
φ_{gs}	solid–fluid energy exchange coefficient	-
subscript* or *superscript		
col	collisional	
eff	effective	

fr	frictional
g	gas
kin	kinetic
max	maximum
q	phase
s	solid
T	stress tensor
τ	terminal velocity

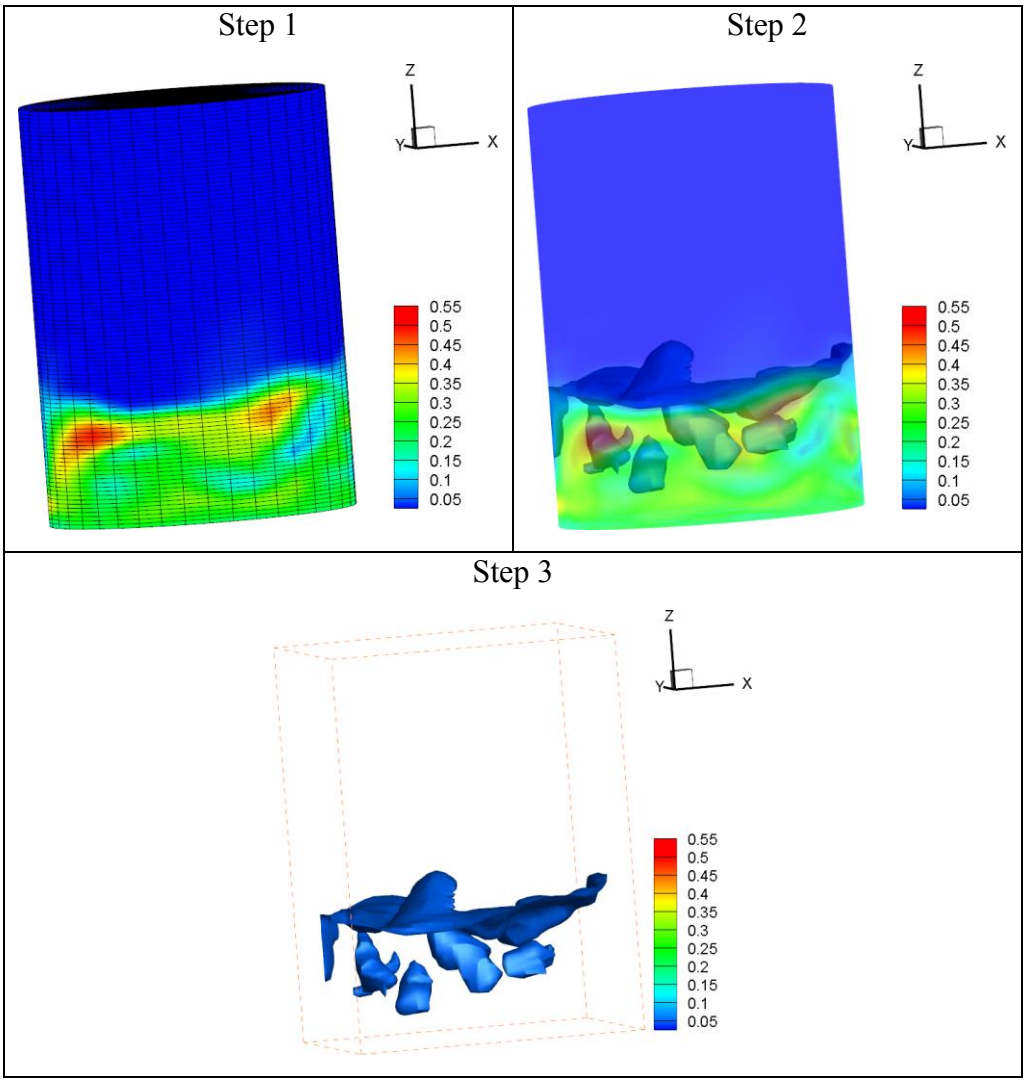

Figure S11. Steps in the extraction of bubble properties in the 3D visualization of simulation no. 8 (H = 12 mm and F_g = 300 SLPM). Snapshots were taken at t = 3.54 s.

Reference for Apendix F

Ansys (Release 19.2). Ansys fluent theory guide. USA, ANSYS Inc.